University of Tennessee, Knoxville

TRACE: Tennessee Research and Creative Exchange

Doctoral Dissertations

Graduate School

8-2019

Nanobrazing of Inconel 718 and Ti-6Al-4V

Denzel Bridges
University of Tennessee, dbridg10@vols.utk.edu

Follow this and additional works at: https://trace.tennessee.edu/utk_graddiss

Recommended Citation

Bridges, Denzel, "Nanobrazing of Inconel 718 and Ti-6Al-4V. " PhD diss., University of Tennessee, 2019.
https://trace.tennessee.edu/utk_graddiss/5600

This Dissertation is brought to you for free and open access by the Graduate School at TRACE: Tennessee Research and Creative Exchange. It has been accepted for inclusion in Doctoral Dissertations by an authorized administrator of TRACE: Tennessee Research and Creative Exchange. For more information, please contact trace@utk.edu.

To the Graduate Council:

I am submitting herewith a dissertation written by Denzel Bridges entitled "Nanobrazing of Inconel 718 and Ti-6Al-4V." I have examined the final electronic copy of this dissertation for form and content and recommend that it be accepted in partial fulfillment of the requirements for the degree of Doctor of Philosophy, with a major in Mechanical Engineering.

Anming Hu, Major Professor

We have read this dissertation and recommend its acceptance:

Seungha Shin, Peter K. Liaw, Sudarsanam Suresh Babu, Raymond Xu

Accepted for the Council:

Dixie L. Thompson

Vice Provost and Dean of the Graduate School

(Original signatures are on file with official student records.)

Nanobrazing of Inconel 718 and Ti-6Al-4V

A Dissertation Presented for the
Doctor of Philosophy
Degree
The University of Tennessee, Knoxville

Denzel Aaron Bridges
August 2019

© by Denzel Aaron Bridges, 2019

All Rights Reserved.

Dedication

When you pass through the waters, I will be with you; and when you pass through the rivers, they will not sweep over you. When you walk through the fire, you will not be burned; the flames will not set you ablaze

-Isaiah 43:2 NIV

Acknowledgments

I would like to express my sincere gratitude to Dr. Anming Hu for his guidance and support during my Ph. D. tenure. Special thanks to Dr. Seungha Shin, Dr. Sudarsanam Suresh Babu, Dr. Peter K. Liaw, and Dr. Raymond Xu for serving on my dissertation committee. I want to thank Dr. Zhili Feng for his advice and support during my graduate school career. Thanks to my fellow group members Yongchao Yu, Suhong Zhang, and Lingyue Zhang for their assistance and support. I also want to thank Dr. Ruozhou Li, Chaoli Ma, and Ying Ma for their direct support in different stages of my research. I want to thank all of my friends at the University of Tennessee and in Knoxville for their friendship, support, and prayers. I want to thank my family and my future wife, Emily Starnes, for their love, support, and prayers.

The research in Chapter 2 were jointly supported by Institute of Public Service, University of Tennessee through IUCRC project of National Science Foundation, a seed grant from Oak Ridge National Laboratory, Department of Energy, USA, and and the Priority Academic Program Development of Jiangsu Higher Education Institutions (PAPD), P. R. China. Chris Wetteland and Maneel Bharadwaj assisted in the collection of EDS and microhardness measurements. John Dunlap, Maulik Patel, and the Joint Institute of

Advanced Materials permitted use of their electron microscopy facilities and X-ray diffraction equipment provided the training needed to operate those devices.

Chapter 3 was jointly supported by Institute of Public Service, University of Tennessee through IUCRC project of National Science Foundation and a seed grant from Oak Ridge National Laboratory. John Dunlap, Maulik Patel, and the Joint Institute of Advanced Materials permitted use of their electron microscopy, EDX, and X-ray diffraction equipment.

Chapter 4 research jointly supported by a subcontract with the Jet Propulsion Laboratory/California Institute of Technology, the National Aeronautics and Space Administration (NASA) and a Department of Energy (DOE) Office of Science User Facility project at the Center for Nanophase Materials, Oak Ridge National Laboratory. John Dunlap, Maulik Patel, and the Joint Institute of Advanced Materials permitted of their electron microscopy, EDX, and X-ray diffraction equipment and trained me in the use of it.

Chapters 5 and 6 supported by Rolls-Royce Corporation through a research grant. John Dunlap, Michael Koehler, and the Joint Institute of Advanced Materials permitted use of their electron microscopy, EDX, and X-ray diffraction equipment, and Suhong Zhang, Zhili Feng, and Oak Ridge National Laboratory for hardness mapping and vibratory polishing. Lastly, Dr. Sudarsanam Suresh Babu and Michael Haines for assistance with Thermo-Calc.

Abstract

For high temperature brazing applications of Ti and Ni alloys, several design considerations must be evaluated including metallurgical compatibility, mechanical stability, wettability, etc. One of the obstacles to high temperature brazing is minimizing the melting temperature of the brazing material without sacrificing high operating temperature. Traditionally, this is accomplished by adding melting point depressants such as boron and silicon. However, adding boron and silicon exposes the base material to the formation of brittle intermetallic phases and/or low melting eutectic phases. Nanomaterials experience size-dependent melting point depression without the use of melting point depressants via the Gibbs-Thomson effect. Until the studies discussed in this dissertation, nanomaterials as the sole brazing material are seldom investigated. In this dissertation, we discuss nanomaterial brazing (nanobrazing) material performance when joining Inconel 718 and Ti-6Al-4V.

In the dissertation studies, we compare the mechanical strength of Cu-Ag and Ag nanomaterials and high entropy alloy nanoparticles for laser brazing Inconel 718 to their bulk counterparts. It was found that the Cu-Ag nanomaterials (243 MPa) outperformed a commercially available bulk Cu-Ag brazing alloy (110 MPa) due to Hall-Petch strengthening. The bulk high entropy alloy produced a stronger brazing joint (220 MPa) but higher threshold brazing temperature (1100 °C) than the nanoparticles (155 MPa, 959 °C). Ni/Al reactive multilayer films are investigated as a self-powered brazing material for joining Ti-6Al-4V. A lack of interdiffusion between BAlSi-4 and the reactive multilayer film prevents the joint from achieving high strength (> 100 MPa). In our study of Ni nanomaterials, we established that Ni can outperform BNi-2 commercial brazing material under the same vacuum brazing conditions. Increasing the heating rate and maximum temperature, and high diffusivity ($>1 \times 10^{-7}$ cm^2/s) were identified as critical factors in the nanobrazing process of Ni nanomaterials.

Through these studies, we provide evidence for two hypotheses: (1) Surface melting and diffusion are critical processes for successful nanojoining (2) (Sub)Grain boundary strengthening is an important mechanism for high bonding strength. Furthermore, the research in this dissertation provides a firm foundation for future nanobrazing studies and provides valuable insight to fundamental investigations and technical improvements for optimizing nanobrazing procedures.

Table of Contents

1 Introduction **1**

1.1 Effect of Microstructure on High-temperature Mechanical Properties 1

1.1.1 Crystal structure 1

1.1.2 Grain Strengthening 2

1.1.3 Dispersion Strengthening and Precipitation Strengthening 4

1.1.4 Fracture Mechanisms 6

1.2 High Temperature Alloys 8

1.2.1 High temperature Stainless Steels 9

1.2.2 Nickel-based Superalloys 11

1.2.3 Titanium Alloys 13

1.2.4 High Entropy Alloys 15

1.3 Materials Joining Technologies 17

1.3.1 Welding 17

1.3.2 Brazing 19

1.3.3 Diffusion Bonding 26

1.3.4 Additive Manufacturing 27

1.3.5 Nanoparticle-enhanced Welding and Brazing 28
1.3.6 Microjoining and Nanojoining 29
1.4 Research Objectives and Hypotheses 39
2 Laser Brazing of Inconel 718 using Cu-Ag and Ag Nanomaterials 43
2.1 Motivation and Background 45
2.2 Experiments and Methods 48
2.2.1 Materials 48
2.2.2 Preparation of Ag NP paste 49
2.2.3 Preparation of Ag Nanowire Paste 50
2.2.4 Preparation of Cu-Ag core-shell nanowire paste 50
2.2.5 Laser Brazing 51
2.2.6 Wettability 52
2.2.7 Mechanical Testing and Characterization 52
2.3 Results and Discussion 53
2.3.1 Characterization of Nanopaste 53
2.3.2 Brazing Simulation and Modeling 56
2.3.3 Ag Diffusion Behavior 58
2.3.4 Wettability of Ag Nanoparticles and Ag Nanowires 62
2.3.5 Cu-Ag CSNW Diffusion Behavior 65
2.3.6 Hardness 69
2.3.7 Bonding Strength 70
2.3.8 Fractography 73

2.4 Conclusions 75

3 High Entropy Alloys 77

3.1 Motivation and Background 79

3.2 Experimental Procedure 80

3.2.1 Bulk HEA Fabrication 80

3.2.2 HEA Nanofabrication 81

3.2.3 Laser Brazing 81

3.2.4 Characterization 82

3.3 Results and Discussion 83

3.3.1 HEA characterization 83

3.3.2 Mechanical Properties 84

3.3.3 Diffusion Behaviors 88

3.4 Conclusions 91

4 Self-powered Brazing 93

4.1 Motivation and Background 95

4.2 Experiments and Methods 97

4.2.1 RMF fabrication 97

4.2.2 Self-Powered Brazing 99

4.2.3 Reaction Temperature Measurement 100

4.2.4 Characterization 102

4.3 Results and Discussion 103

4.3.1 Characterization of RMF and BAlSi-4-Coated Ti64 103

4.3.2 Elemental Profiles and Temperature Evolution 104
4.3.3 Mechanical Properties 113
4.4 Conclusions 116

5 Ni Nanoparticle Transient Liquid Phase Bonding 117

5.1 Motivation and Background 119
5.2 Experiments and Methods 120
5.2.1 Materials 120
5.2.2 Nickel Nanoparticle Filler Metal Preparation 120
5.2.3 Transient Liquid Phase Bonding 121
5.2.4 Microstructure Characterization 122
5.2.5 Mechanical Performance Evaluation 123
5.3 Results and Discussion 124
5.3.1 Nanoparticle Characterization 124
5.3.2 Joint Microstructural Characterization 129
5.3.3 Mechanical Properties 135
5.4 Conclusions 142

6 Wettability and Diffusion of Ni nanomaterials 144

6.1 Introduction 144
6.2 Experimental and Analytical Methods 145
6.2.1 Ni Nanoparticle Synthesis 145
6.2.2 Ni Nanowire Synthesis 146
6.2.3 Contact Angle Measurement 146

6.2.4 Diffusion Analysis 147

6.3 Results and Discussion 148

6.3.1 Ni Nanomaterial Characterization 148

6.3.2 Wettability 149

6.3.3 Diffusion 152

6.4 Conclusions 157

7 Conclusions and Outlook **159**

7.1 Conclusions 159

7.2 Outlook 161

References **166**

Appendices **180**

A Acronyms **181**

B Denzel Bridges Publication list **183**

C MATLAB Codes **186**

D Gibbs-Thomson Derivation **194**

Vita **196**

List of Tables

1.1 Mechanical properties of selected Stainless steels 11

1.2 Mechanical properties of selected nickel super alloys 14

1.3 Mechanical properties of selected Ti alloys 16

1.4 Summary of different nanojoining techniques 40

2.1 Composition of the alloys and fluxes used in this study 49

2.2 Description of the nanopastes used in this laser brazing study 51

2.3 Summary of the Ag diffusion length and overall diffusion zone thickness of joints using Ag NPs and Ag NWs 63

2.4 Summary of the diffusion lengths of major elements in CSNW-joined IN718 at 300 W 67

2.5 Crystallite size (in nm) after brazing of Cu-Ag BFMs based on the Scherrer formula. recall that α is the Cu-rich phase and β is the Ag-rich phase 72

3.1 Chemical composition of IN718 81

3.2 Scherrer crystallite size according to the XRD patterns in Figure 3.3 84

4.1 List of Al-based RMF reaction characteristics [241] 98

4.2 Elemental composition of Ti64 and BAlSi-4 99

4.3 Layer-wise Additive Manufacturing Predictions and Simulations (LAMPS ©) simulation parameters. T.C. is thermal conductivity and H.C. is heat capacity [232] 102

4.4 Phase summary of the EDS point analysis shown in Figure 4.11 [233] 110

5.1 Ni NP surface melting range as a function of temperature 129

5.2 The crystallite size of Ni-42 and at the end of the heating cycle as a function of heating rate (T_{max} = 1050 °C) 131

5.3 DAZ thickness of Ni-42 joints as a function of heating rate 132

5.4 EDX areal composition analysis of the three principal elements (at%) of Ni-29 joint from Figure 5.8 in the areas marked by red boxes 132

5.5 Grain diameter summary according to EBSD measurements 134

6.1 Diffusion prefactor (D_0, cm^2/s), activation energy (E_A, kJ/mol), and Vibrational entropy (S_{vib}, J/mol-K) used for calculated bulk and nano diffusion coefficients 148

6.2 Contact angle for Ni nanomaterials heated to 1100 °C 152

List of Figures

1.1 (a) face-centered cubic (FCC), (b)body-centered cubic (BCC), (c) hexagonal closed-packed (HCP) unit cells and (d) bulk metallic glass ”unit cell” 3

1.2 (a) typical polycrystalline structure in metal with a single grain outlined in red, (b)schematic of a grain boundary, (c) graphical representation of grain boundary strengthening 4

1.3 Hardness and $\gamma\prime$ and $\gamma\prime\prime$ grain size in IN718 as a function of aging time at 750 °C (The data from this figure was adapted from Slama et al. 2000) [13] . . . 6

1.4 Schematic showing the procedural difference between (a) precipitation strengthening and (b) dispersion strengthening 7

1.5 Diagram illustrating (a) microvoid coalescence, (b) cleavage, and (c) intergranular fracture mechanisms/surfaces 8

1.6 Ashby plot of high temperature strength of selected high temperature alloys [16] 9

1.7 Typical structure of (a) austenite (304 Stainless steel) and (b) martensite (Fe-31wt%Ni-0.02wt%C steel) [23] 10

1.8 Fe-C phase diagram [20] 11

1.9 This figure was modified from Mignanelli et al. [36]. The effect of heat treatment time at 700 °C (following solution treatment) on the room temperature Vickers hardness and the microstructure of the IN718. (a) The variation in room temperature hardness, (b) the microstructure after 1 hour at 700 °C, (c) the microstructure after 10 hours at 700 °C, (d) the microstructure after 100 hours at 700 °C and (e) the microstructure after 1000 hours at 700 °C. Errors were calculated as the standard deviation of 10 individual measurements of the alloy hardness. 13

1.10 This figure was modified from Shi et al. [50]. Typical microstructure of Ti-6Al-4V 15

1.11 Crystal structures of (a) face-centered cubic (FCC) and (b)body-centered cubic (BCC) HEAs 17

1.12 Diagram of a basic (a) butt joint, (b) lap joint, (c) tee joint, (d) corner joint, and (e) edge joint 19

1.13 Photograph of turbine crack 22

1.14 (a)Visual representation of Young's equation and the contact angle. (b) Schematic of the different wetting conditions of a crack being repaired by capillary force-assisted brazing (c)Application of Young's equation for capillary force-assisted brazing 23

1.15 Schematic representation of TLP bonding. ISZ is the isothermally solidified zone 28

1.16 Schematic of directed energy deposition with powder stream for crack repair 29

1.17 Illustration of three primary diffusion types lattice diffusion (D$_{Lattice}$), grain boundary diffusion (D$_{GB}$), and surface diffusion (D$_{Surface}$) 33

1.18 General logarithmic plot of D vs $1/T$ 34

1.19 Melting point depression diagram of Au NPs [115] 35

1.20 (a) Working concept of a ball milling process (b) Ball-powder interaction concept for ball milling 36

1.21 Schematic of the growth mechanisms in wet chemical synthesis of NPs. Growth method 1 is chemical reduction of the precursor and growth method 2 is Ostwald ripening 37

1.22 This figure is modified from Li et al. [91]. Ag NWs (a) before sintering, after (b) photonic sintering (ambient temperature is room temperature) and (x) thermal sintering at 250 °C for 5 min. The white scale bars indicate 150 nm and the yellow arrows indicate places where NW-NW joining has occurred. . 38

1.23 Schematic of NP sintering with (a) a thick/complete organic shell and (b) a thin/partially covering organic shell [110] 39

2.1 Microstructure of the BNi-2 filler metal (a) General optical microscope and (b) SE, BSE image (SEM), and EDS analysis [77] 46

2.2 General packaging structure of a power semiconductor module [201] 47

2.3 This figure is modified from Liu et al. (2017). SEM cross-section of Cu-Ag joined Cu (a) 120× (b) 4000× and (c)10000× magnification [171] 48

2.4 (a) Schematic of the laser brazing set up and (b) laser power curve [144] . . 52

2.5 SEM images of a) Cu NWs, b) Cu-Ag CSNWs, c) magnified view of Cu-Ag CSNWs, d) Ag NWs, and e) Ag NPs; f) the UV-vis spectra of each nanomaterial [144]. 54

2.6 XRD pattern of a) Cu NWs, b) Cu-Ag CSNWs, c) Ag NWs and d) Ag NPs an inlet of each nanomaterial solution is included [144] 55

2.7 (a) COMSOL model of the lap joint used in this study with a finite element mesh (b) Thermal distribution after a 5 second ramp and 10 seconds of heating at 300 W (c) Global maximum, minimum and average temperatures as a function of time [144] 56

2.8 (a) Locations of the cross-sectional thermal distributions taken for parts d,e, and f, (b) average temperature of the brazing layer as a function of time. Thermal distribution of (c) xz-plane cross-section in the middle of the laser brasing region (d) the surface top plate, (e) interface between the top plate and the brazing layer, (f) interface between the bottom plate and the brazing layer [144] 57

2.9 EDS line scans of a brazing joint using Ag NWs (a-b) are for a line scan of the entire joint; (c-d) are for the interfacial area. The solid red arrow indicates the location of the line scan. The dotted lines in (d) are boundaries for the diffusion layer [144] 59

2.10 EDS line scan for (a-c) Ag NPs at 250 W, (d-f) Ag NPs at 300 W, (g-i) Ag NWs at 250 W, and (j-l) Ag NWs at 300 W. The red line in (a), (d), (g), and (j) indicates the location of the line scan. The space between the vertical dashed line in (b), (e), (h), and (k) shows the location of the diffusion zone (DZ) and the black box shows the section of the graph shown in (c), (f), (i), and (l) respectively. The black circles show the concentration humps of different IN718 elements [195] 61

2.11 The normalized silver EDS line scan for the samples in Figure 2.10 at (a) 250 W and (b) 300 W. The black solid vertical line and red dotted vertical line mark the end of the Ag diffusion range for Ag NPs and Ag NWs, respectively. The blue dotted line marks the beginning measuring point. [195] 62

2.12 (a) Change in area of Ag NPs heated to a 550 and 800 °C and Ag NWs at 550 °C. The optical images were taken before and after laser irradiation heating for Ag NPs 550 °C (b and e), Ag NPs 800 °C (c and f), and Ag NWs 500 °C (d and g). The blue and red shaded areas show the area covered by the nanopaste before and after brazing, respectively [144] 64

2.13 EDS line scans of a brazing joint using Cu-Ag CSNWs (a-b) are for a line scan of the entire joint; c-d are for the interfacial area. The solid red line is the location of the line scan. The black dotted line in (c) is the boundary between the IN718 and the brazed joint. The dotted lines in (d) and (f) indicate where the locations of the diffusion layers. (e-f): the local line scan performed on a Ag rich region adjacent to an α region as indicated by a short arrow bar in (e) [144] 66

2.14 XRD patterns after laser joining at 300 W for (a) BAg-8brazing alloy, (b) Cu-1, (c) Cu-3, and (d) Cu-2 [144]. 68

2.15 Vickers hardness of 300 W brazed joints within the brazing region (BR) and 50 m outside the brazing region (BR) using a) Ag-2 and b) Cu-1. The side of laser incidence is labeled. The red dotted line is the average hardness of IN718 prior to brazing [144] 70

2.16 Bonding strength vs laser power for the NPAs and the BAg-8 alloy [144] . . 71

2.17 Typical Stress-Strain curve of a Cu-3 joint (a) and a BAg-8 joint (b). The yield strength (σ_y) is also shown on each curve. This stress-strain curve was generated on an MTS-3 testing frame [144] 73

2.18 (a) SEM image of the surface of bare IN718. Fracture surface of IN718 bonded at 300 W using (b) Ag-1, (c) Ag-2, (d) Cu-1, (e) Cu-2, and (f) Cu-3 74

3.1 Schematic showing the design concept for HEA-based dissimilar joining. . . . 80

3.2 Schematic of the laser brazing setup [52]. 82

3.3 XRD pattern on HEA (a) As-synthesized bulk material (b) NPs, and (c) After brazing [52]. 83

3.4 SEM images of the HEA powder (a) after initial powderization (b) after low energy ball milling, and (c) after high energy ball milling. 84

3.5 Shear strength (left axis, bar graph) and brazing temperature (right axis, red solid line) as a function of laser power. The shear strength of BNi-2 is also shown by a black dotted line. The red and blue dotted lines are the solidus and liquidus temperatures, respectively [52]. 85

3.6 Hardness maps of brazing joints using (a) 350 W, (b) 400 W, and (c) 450 W laser power. The black arrow shows the direction of laser irradiation. The bottom of the hardness map lines up with the end of the joint overlap. (d) The average hardness of the IN718 and the HEA before brazing (BB) and after brazing. The average hardness after brazing was calculated by taking the average of all the hardness map values [52]. 87

3.7 An HEA fracture surface using (a) 350 W, (b) 400 W, and (c) 450 W laser power. Cr distribution on the fracture surface using (d) 350 W, (e) 400 W, and (f) 450W laser power. Arrows point to secondary cracks [52]. 88

3.8 (a) EDS line scan for brazed joints using the HEA brazing material at laser power (a-b) 350 W, (c-d) 400 W, and (e-f) 450 W. The dotted lines show the location of the diffusion zone. (g) Diffusion zone thickness of each element at each laser power [52]. 90

3.9 EDS of a bulk HEA joint (a-b) and HEA NPA joint (c-d) at 350 W andbulk HEA joint (e-f) and HEA NPA joint (g-h) at 400 W. 91

4.1 Schematic of the S4 process 96

4.2 Diagram showing (a) the self-propagating reaction of RMFs and (b) Heat flow of self-powered brazing 97

4.3 (a) Photograph of a Multiplaz 3500 plasma torch and (b) Schematic of the plasma coating process 98

4.4 (a) Schematic of e-beam evaporator (side view) (b) Schematic of multi-target crucible holder (top-view) 100

4.5 (a) Schematic of the configuration used in brazing experiments. (b) Schematic of lab shear testing [232]. 101
4.6 SEM image showing (a) the total as-fabricated RMF thickness and (b) the bilayer thickness for the 1.5:1 Ni:Al ratio. SEM image showing (c) the total as-fabricated RMF thickness and (d) the bilayer thickness for the 1:1 Ni:Al ratio (white is Ni and grey is Al) [232, 233]. 104
4.7 XRD pattern of the Ni/Al RMF (a) as-fabricated and (b) post ignition [232]. 105
4.8 DSC measurement of (a) 1.5:1 Ni/Al RMFs and (b) 1:1 Ni/Al RMFs [232, 233].105
4.9 High speed camera measurement of the RMF reaction with 1:1 Ni:Al ratio [232].106
4.10 EDS line scan of (a,b) the entire brazed joint, (c,d) the Ti64-BAlSi-4 interface, and (e,f) BAlSi-4-RMF interface with select point analysis [232]. 108
4.11 Brazing interface between BAlSi-4 and the 1.5:1 Ni/Al RMF [233]. 109
4.12 XRD pattern of the brazed joint [232]. 110
4.13 Snapshots of the LAMPS ©simulation, showing the temperature evolution and distribution in the brazed joint at various time steps. The places of high heat outside the joint are due to the heating of stagnant air around the lap joint [232]. 111
4.14 Temperature as a function of time simulated by LAMPS©(red, blue, and magenta lines) and measured using the highspeed camera (black solid line) [232]. 112
4.15 (a) Bonding strength as a function of applied pressure (RMF thickness kept constant at 66 μm). (b) Bonding strength as a function of total RMF thickness (Applied pressure = 20 MPa). 113

4.16 Fracture surfaces of RMF-brazed joints, with an RMF thickness of (a) 66 μm, (b) 99 μm, (c) 132 μm, and (d) 165 μm. 114

4.17 Hardness map of a 300 μm × 300 μm section of the brazed joint [232]. 115

5.1 TLP heating profile and lap joint configuration (inlet) [254]. 122

5.2 SEM and size distribution (histogram and distribution curve) of Ni NPs synthesized at 120 °C with the sodium borohydride added (a-b) rapidly, (c-d) dropwise added approximately 1 mL/min and (e-f) dropwise added approximately 0.03 mL/min. The mean and standard deviation (S.D.) are also listed in the figure [254]. 125

5.3 Typical UV-vis spectrum for Ni NPs 126

5.4 TEM micrograph of Ni NPs with the organic layer thickness labeled (red dotted line) from (a) Ni-22, (b) Ni-29, and (c) Ni-42 [254]. 126

5.5 FTIR of (a) as-synthesized (AS) Ni NPs and (b) Ni NP pellet heated to T_{max} =1050 °C at a heating rate of 15 °C/min [254]. 127

5.6 (a) The melting point as approximated by the Gibbs-Thompson (GT) and Liquid drop (LD) models, SM melting point calculated by the Chernyshev model as a function of particle diameter with the bulk melting point (M.P. indicated by a green dotted line. The blue shaded region is the temperature range where nano-TLP bonding is theoretically possible. The light brown region is the region where only solid-state sintering (SS) can occur. (b) zoomed region with some molecular dynamics calculations of the melting and SM temperature from Zhang et al. [260] and Wang et al. [102]. 128

5.7 (a) XRD patterns for as synthesized Ni-29 NPs and bonded Ni NPs at the end of the heating cycling. (b) The temperature profile of the high temperature XRD test (black line, left axis) and the crystallite size calculated by the Scherrer equation (scatter plot, right axis). (c) Ni NP pellet before heating and (d) after heating [254]. 130

5.8 (a) SEM image of the Ni-29 NP joint bonded at T_{max} = 1000 °C with heating rate of 10°C/min. The blue area is the diffusion affected zone (DAZ) and the red arrow shows the location of the line scan. The red boxes are areas used for area composition analysis (b) The EDX line scan of the Ni NP-IN718 interface. (c) room temperature Ni-Fe-Cr phase diagram [254]. 132

5.9 (a) EBSD inverse pole figure of a Ni-42 joint joined at 1050 °C and 15 °C/min. (b) Low angle (<15°) and high angle (>15°) grain boundary distribution based on region. The grain size distribution for (c) the IN718 side of the DAZ and (d) the Ni layer based on distance from the Ni-IN718 interface [254]. 134

5.10 Hardness map on the Vickers scale of a Ni-42 joint processed at a heating rate of 15 °C/min with T_{max} of (a) 950 °C, (b) 1000 °C, and (c) 1050 °C [254]. . 135

5.11 Bonding strength as a function of (a) particle diameter (T_{max} = 1050 °C and heating rate = 15 °C/min), (b) heating rate (Ni-42 and T_{max} = 1050 °C), and (c) T_{max} (Ni-42, heating rate = 15 °C/min). The BNi-2 foil (BNi-2 F) and BNi-2 325 mesh powder (BNi-2 M) are also included [254]. 137

5.12 DIC results for Ni-29 pellet joined at T_{max} =1000 °C and heating rate = 15 °C/min under 50 MPa of load. (a) The original image with the analyzed region under 10x magnification indicated by the white box, the analyzed region under 50x magnification is indicated by the red box. The loading condition is indicated by the red arrows. (b-c) are the normal strain in the x and y direction respectively and (d) is shear strain under 10x magnification. (e-f) are the normal strain in the x and y direction respectively and (g) is shear strain under 50x magnification. Circles are used to indicate areas of high tensile or compressive strain [254]. 138

5.13 Fracture surface of lap shear joints joined at T_{max} =1050 °C and heating rate = 15 °C/min (a-c) Ni-22, (d-f) Ni-29, and (g-i) Ni-42. The red arrow indicates the loading direction of the sample [254]. 140

5.14 Fracture surface of lap shear joints joined at T_{max} =1050 °C using Ni-42 pellets (a-c) 2 °C/min, (d-f) 5 °C/min, (g-i) 10 °C/min, (j-l) 15 °C/min. The red arrow indicates the loading direction of the sample. [254]. 141

5.15 Cross-section of a Ni-42 (T_{max} =1050 °C and heating rate = 15 °C/min) joint (a) before fracture and (b) after fracture [254]. 142

6.1 Schematic of how wettability experiments are conducted. 147

6.2 SEM and size distribution (histogram and distribution curve) of Ni NPs synthesized at 120 °C with the sodium borohydride added (a-b) rapidly, (c-d) dropwise added approximately 1 mL/min and (e-f) dropwise added approximately 0.03 mL/min. The SEM and size distribution of Ni NWs is also included (g-h). The mean and standard deviation (S.D.) are also listed in the figure. 150

6.3 Example of the contact angle measurements for Ni NP powder (a) and pellet (c). As well as for Ni NWs (b) powder and (d) pellet 151

6.4 Liquid drop model for spherical Ni NPs according to Nanda et al (Equation 1.18) and NWs with different cross-sectional shapes according to Qi et al. [102, 103] 152

6.5 Example of (a) an EDS line scan and (b) the fitting of the raw EDS data for Sauer-Friese analysis 153

6.6 Ni interdiffusion coefficients (a) as a function of particle diameter as calculated by Jiang et al.'s equation [112] as well as the experimentally calculated interdiffusion coefficients for Ni NPs and Ni NWs joined at 1050 °C and 15 °C/min. The bulk interdiffusion coefficients for Ni are also shown for 1050 °C. (b) Ni interdiffusion coefficients as a function of temperature for Ni-42 NPs is also shown 156

6.7 Calculated interdiffusion coefficients of key elements (Ni, Cr and Fe) in Ni-42 joints, processed with the three (3) different nano-brazing heating rates. These calculations are based on Sauer-Friese analysis of EDS data 157

7.1 Schematic of showing how the initial density of a pure Ni NW pellet (left) can be increased by adding Ni NPs (right). 163

7.2 Flow chart of the input parameters and projected output of the proposed phase field modeling. 164

7.3 Suggested embedded RMF joining schematic; arrows indicate where the adjacent BAlSi-4 surfaces would fuse together [232]. 165

Chapter 1

Introduction

1.1 Effect of Microstructure on High-temperature Mechanical Properties

1.1.1 Crystal structure

High temperature properties are vastly important in the aerospace, automotive, defense, and power generation industries. From a materials perspective, high temperature refers to temperatures more than two-thirds the material's melting temperature ($> \frac{2}{3}T_m$). In application, high temperature properties are typically investigated at roughly more than $0.4T_m$. Key high temperature mechanical properties include yield strength, ultimate tensile strength, hardness, low/high cycle fatigue resistance, and creep resistance. Fatigue refers a type of material failure that occurs due to cyclic loading conditions. Creep is a type of deformation that occurs under loading conditions less than or equal to yield stress (σ_y) at high temperature ($> 0.4T_m$). Metals are typically the materials that satisfy high temperature demands. Mechanical properties of metals is based on several key factors including crystal structure and microstructure. The combination of these factors give rise to the mechanical properties of materials and their suitability under certain operating conditions. First, crystal structure, in this context, refers to the way that atoms are arranged in a lattice. Most metals naturally occur in face-centered cubic (FCC) (Figure 1.1a) and body-centered cubic (BCC) (Figure 1.1b) form. Occasionally, some metals form hexagonal closed-packed (HCP) structures (Figure 1.1c). FCC metals tend to be ductile (i.e., sustains more permanent deformation before fracture) while BCC and HCP metals tend to be brittle. This is due to the number and interactions between slip systems in the crystal structure. Slip systems are the crystallographic family of planes and associated family of directions in which dislocations can easily move. FCC metals have 12 slip systems, BCC metals have up to 48 slip systems, and HCP metals have only 3 slip systems. Typically more slip systems mean a more ductile material, however, BCC metals essentially have too many interacting slip planes that impede dislocation motion. The only exception is at high temperature where the atoms have enough thermal energy to difuse each other [1].

1.1.2 Grain Strengthening

Microstructure features thus include grain size, grain shape, inclusion morphology, and phase distribution. Grains are single entities in a microstructure in which all the atoms are arranged in a periodic fashion, defining crystals. The incidence where two grains of different crystallographic orientation are merged together is called a grain boundary (Figure 1.2a). Most metals are polycrystalline materials (Figure 1.2b); significant effort is required to produce single crystalline metals. According to the Hall-Petch relation, as grain size (d)

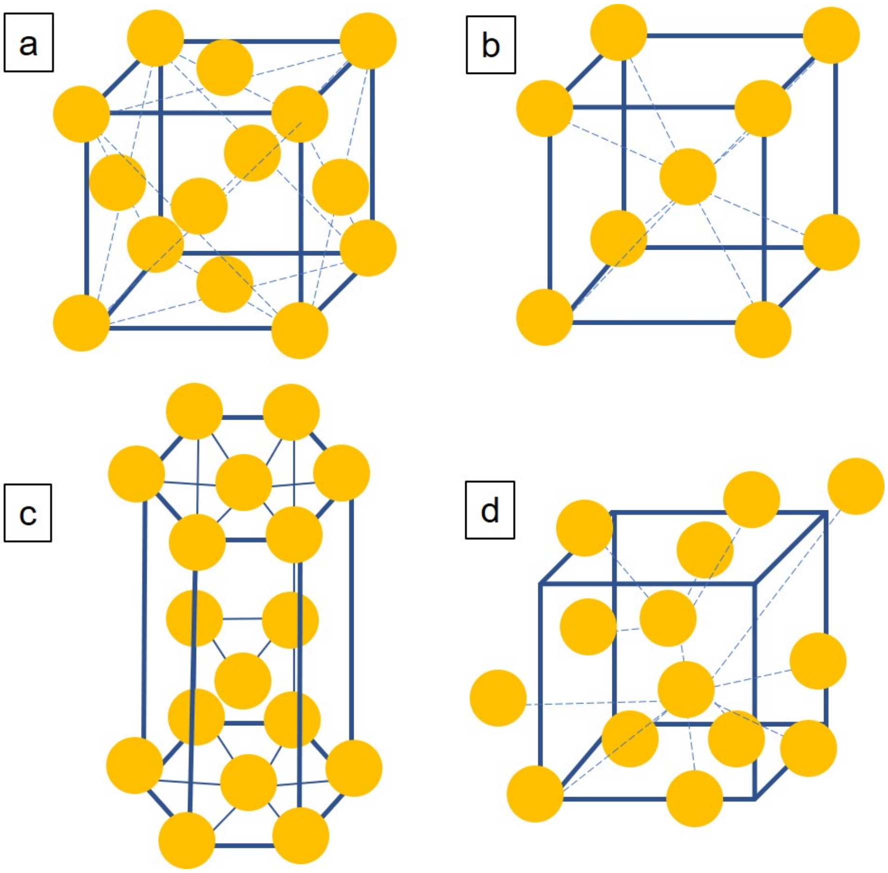

Figure 1.1: (a) face-centered cubic (FCC), (b)body-centered cubic (BCC), (c) hexagonal closed-packed (HCP) unit cells and (d) bulk metallic glass ”unit cell”

decreases yield strength σ_y increases (Equation 1.1). σ_0 is a material constant for the onset stress for dislocation movement and k_y is the Hall-Petch coefficient [2].

$$\sigma_y = \sigma_0 + \frac{k_y}{\sqrt{d}} \tag{1.1}$$

Essentially when grain size decreases, the grain boundary density increases. Grain boundaries serve as sites for dislocation pile-up and hindrances for dislocation motion required for deformation. Smaller grains are able to have fewer dislocations pile-up at the grain boundary than larger grains due to the shorter grain boundary length (Figure 1.2c), so more stress is required to move dislocations across grain boundaries and further deform the material.

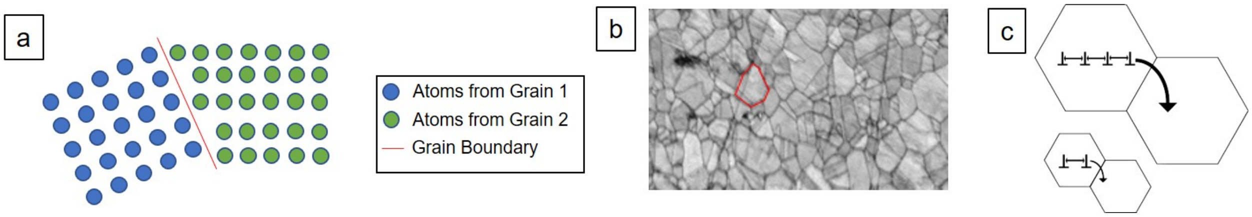

Figure 1.2: (a) typical polycrystalline structure in metal with a single grain outlined in red, (b)schematic of a grain boundary, (c) graphical representation of grain boundary strengthening

The range for the Hall-Petch relation is generally several hundred micrometers to 10-30 nm, depending on the material [3, 4]. Below a critical breakdown grain size (<10-20 nm), the material experiences no increase in strength. Hall-Petch strengthening, also known as grain boundary strengthening, is also suspected to occur at the subgrain level through the subgrain (i.e., crystallite) structure [5, 6]. If the grains are equiaxed (i.e., grains have principal axes of equal or near-equal length), metals with a finer microstructure can have a ≥100% increase in yield strength and ultimate tensile strength, but the material also becomes more brittle [7]. Brittleness in structural applications is a significant hazard, therefore structural materials must retain a level of ductility. One of the best options for structural and high temperature applications is to have a mixed nanocrystalline and microcrystalline structure to combine the ductility of a microcrystalline material and the Hall-Petch strengthening effect of a nanocrystalline material [8, 9].

1.1.3 Dispersion Strengthening and Precipitation Strengthening

Dispersion/precipitation strengthening is a very popular option for strengthening pure metals and alloys. Dispersion strengthening introduces hard particles such as metal oxides [10] into the molten metal prior to forming or incorporating the dispersant particles into a metal matrix by ball-milling or hot consolidation of the metal and dispersant powders [11]. Precipitation strengthening controls the heat treatment during manufacturing to precipitate hard intermetallic phases [12] in the metal/alloy matrix without adding foreign particles. The difference between the two procedures is schematically shown in Figure 1.4. For example, Figure 1.3 shows the effect of precipitate size on hardness as a function of aging time. Aging is essentially a form of isothermal heat treatment done to induce growth or phase precipitation [13]. When dislocations interact with the hard dispersions/precipitates, the dislocations must either "bow" around the hard particles via the Orowan mechanism or cut through the hard particles [1]. The stress required for bowing is shown in Equation 1.2 where G is the shear modulus, b is the magnitude of the Burgers vector, L is the distance between strengthening particles and r is the strengthening particle radius. If the particles are too soft, dislocations can penetrate and cut the strengthening particle. The general form of this equation is shown in Equation 1.3. A is a constant that varies depending on the type of particle strengthening, ϵ is a dimensionless mismatch factor that is dependent on shear modulus and the strengthening mechanism, and f is the particle volume fraction [14, 15].

$$\tau = \frac{Gb}{L - 2r} \tag{1.2}$$

$$\tau = AG\epsilon^{\frac{3}{2}}\sqrt{\frac{fr}{b}} \tag{1.3}$$

The strengthening particles whether they are dispersions or precipitates typically have a dissimilar crystal structure than the matrix material. Given the basics of the connection

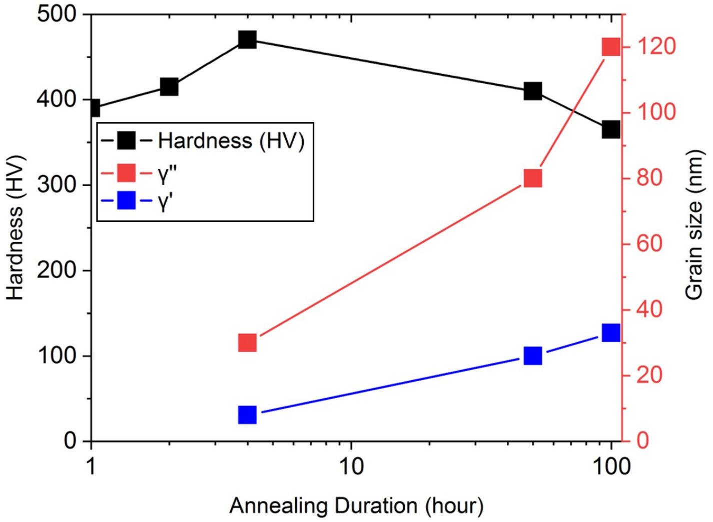

Figure 1.3: Hardness and $\gamma\prime$ and $\gamma\prime\prime$ grain size in IN718 as a function of aging time at 750 °C (The data from this figure was adapted from Slama et al. 2000) [13]

between mechanical properties and microstructure, we will now discuss some alloys used for high temperature applications.

1.1.4 Fracture Mechanisms

Aside from stress-strain relationships, one of the ways to evaluate the strengthening mechanisms and suitability of materials for certain applications is examining the fracture mechanisms. There are three primary and fundamental methods of fracture in engineering materials (i.e. metals, ceramics, high strength polymers etc.): microvoid coalescence, cleavage fracture, and intergranular fracture. Microvoid coalescence is primarily observed in metals, polymers and other ductile materials. Microvoid coalescence occurs due to formation of microvoids under tensile or shear loading conditions due to breaking of chemical bonds or prexisting porosity. Due to mechanically-induced plastic (i.e. permanent deformation) flow of the material around the microvoids, these microvoids grow larger and until large cracks form, eventually leading to complete fracture (Figure 1.5a). The main fracture surface

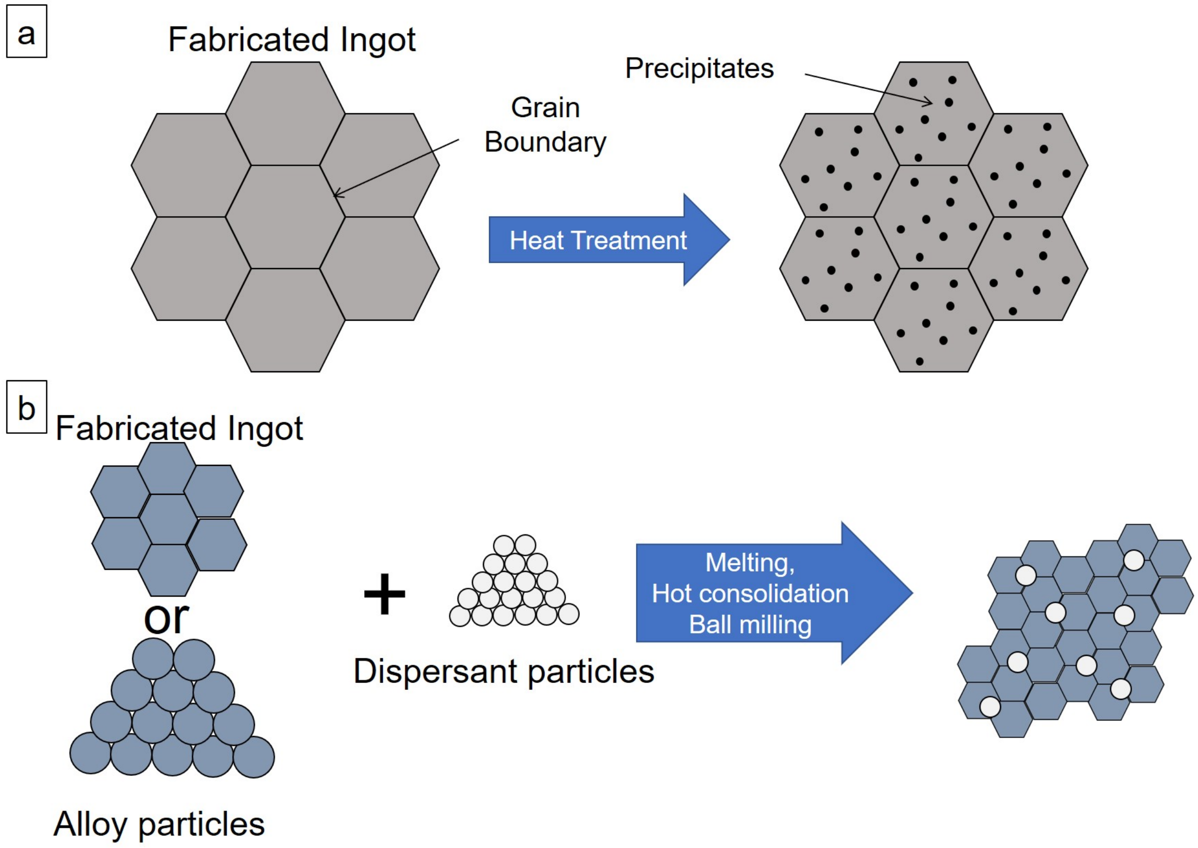
a
Fabricated Ingot
Grain
Boundary
Precipitates
Heat Treatment
b
Fabricated Ingot
or
Alloy particles
+
Dispersant particles
Melting,
Hot consolidation
Ball milling

Figure 1.4: Schematic showing the procedural difference between (a) precipitation strengthening and (b) dispersion strengthening

feature of a sample that failed due to microvoid coalescence are dimples. Cleavage fracture is a low energy fracture mechanism that is characterized by parallel ledge-like morphology (Figure 1.5b). Typically, this kind of fracture occurs when a material is subjected to certain environmental conditions, triaxial stress condition, or high strain rate. Intergranular fracture is easily recognizable as fracture occurs on the grain surfaces. These grain surfaces are typically flat and exactly resemble the grain morphology of the material (Figure 1.5c). Causes for intergranular fracture include grain boundary contamination of organic, metal oxide or otherwise brittle nature, stress corrosion cracking, or microvoid coalescence around secondary phase particles that occupy the grain boundaries. Microvoid coalescence is the

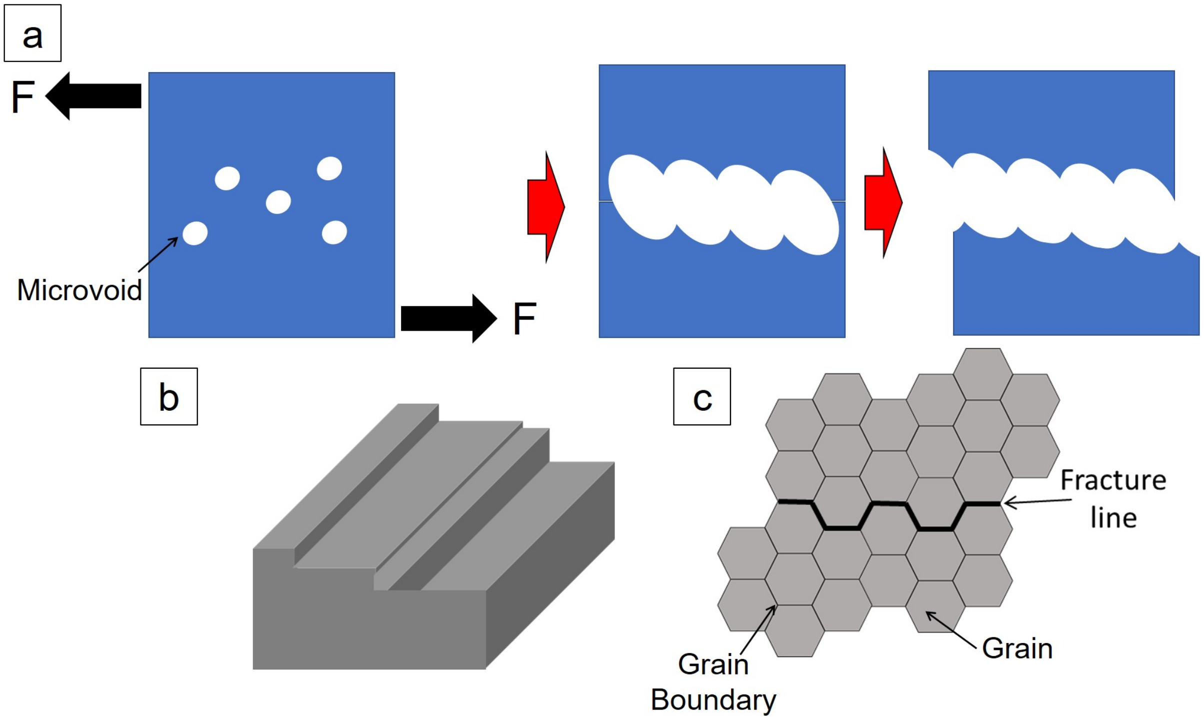

Figure 1.5: Diagram illustrating (a) microvoid coalescence, (b) cleavage, and (c) intergranular fracture mechanisms/surfaces

most ductile fracture mechanism folloed by cleavage fracture and intergranular fracture is the most brittle fracture mechanism.

1.2 High Temperature Alloys

Among the most common high temperature alloy types are high temperature stainless steels, cobalt alloys, nickel alloys, and titanium alloys. An emerging class of high temperature alloys is high entropy alloys (HEAs). HEAs are an emerging class of multi-principal component alloys having a high mixing entropy and containing five or more elements. The high temperature strength of selected alloys is shown in the Ashby plot in Figure 1.6 [16].

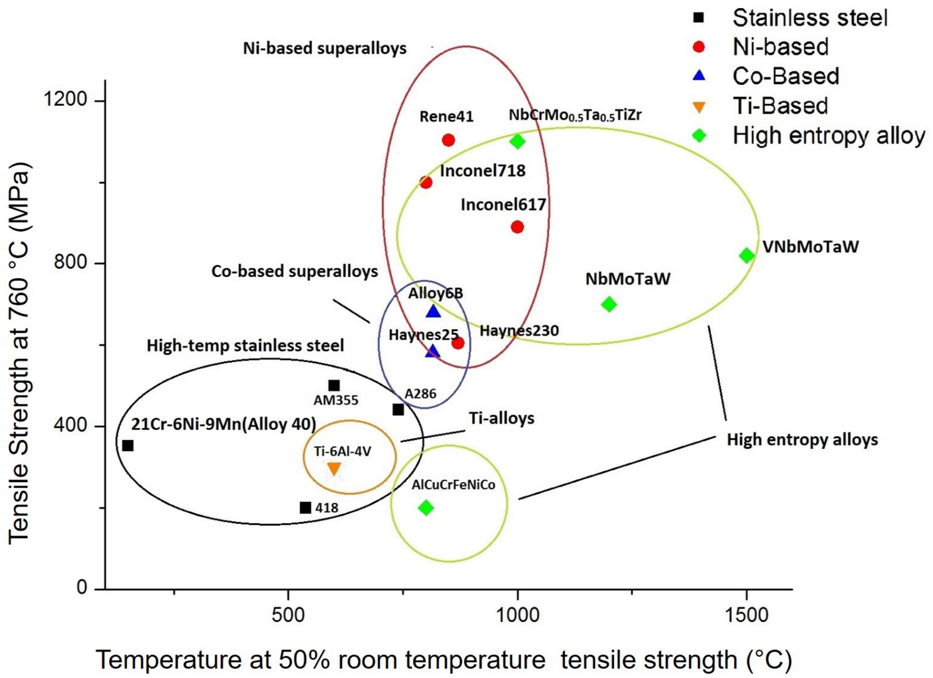

Figure 1.6: Ashby plot of high temperature strength of selected high temperature alloys [16]

1.2.1 High temperature Stainless Steels

Iron and steels are one of the most important structural metals both historically and in modern times. Steel has been used for such a long time that their metallurgy is well understood, and production of steel is inexpensive compared to many other alloys due to a much higher abundance in the Earths Crust [17].All stainless steels contain at least 10.5 wt% chromium and up to 1.5 wt% carbon [18]. Other elements such as Ni and Mn are added to improve the strength, corrosion resistance or change the microstructure morphology of the steel in question [19].

The most common steel types for high temperature applications are austenitic stainless steel, martensitic stainless steel, austenitic-martensitic stainless steel and duplex (austenitic-ferritic) stainless steel. Austenite, also known as γ-Fe is the face-centered cubic

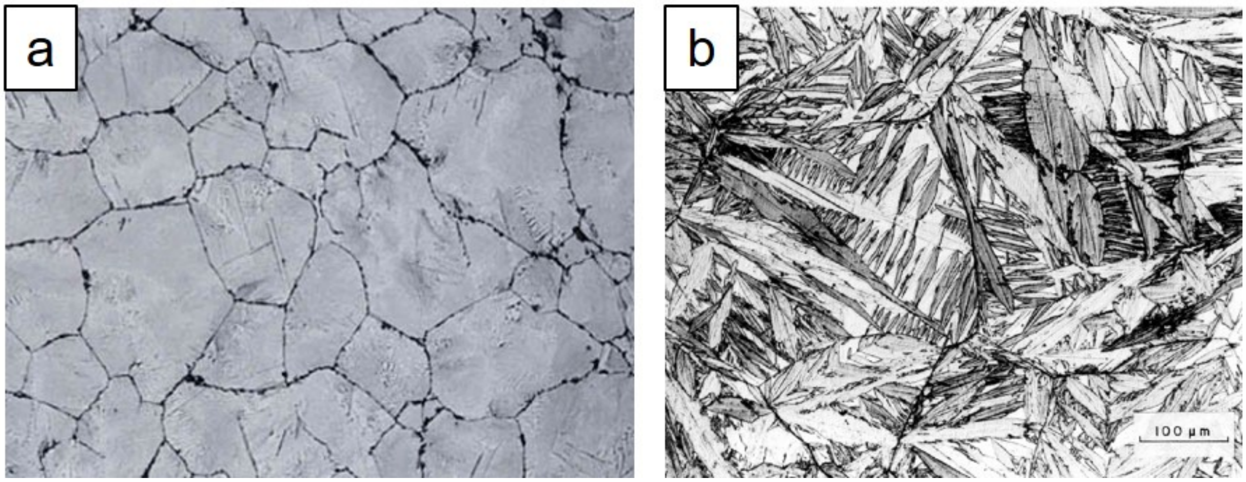

Figure 1.7: Typical structure of (a) austenite (304 Stainless steel) and (b) martensite (Fe-31wt%Ni-0.02wt%C steel) [23]

(FCC) allotrope of iron. Martensite is a body-centered tetragonal metastable phase that forms as a result of quenching austenite below at several hundred degrees Celsius per second. An example of a martensitic microstructure is shown in Figure 1.7. Since martensite is metastable, it does not appear in an equilibrium Fe-C phase diagram (Figure 1.8) [20]. Ferrite, also known as α- Fe is the body-centered cubic (BCC) allotrope of Fe. Table 1.1 shows the typical strength of selected steel types. Martensitic stainless steel is often tempered or cooled at a slightly lower rate because as-quenched martensite is too brittle for most applications, not just high temperature [18]. In austenitic-martensitic and duplex steels, martensite and ferrite, respectively, serve as strengthening phases in austenitic steels which tend to be softer [21]. Additionally, the weldability and manufacturing of the aforementioned steels is relatively well understood, however, as seen in Figure 1.6 the strength of stainless steels is lower and iron has significantly lower oxidation resistance, compared to nickel and cobalt. Additionally, the high weight of steels becomes a detriment to aerospace and automotive applications where lightweight is a powerful asset [22].

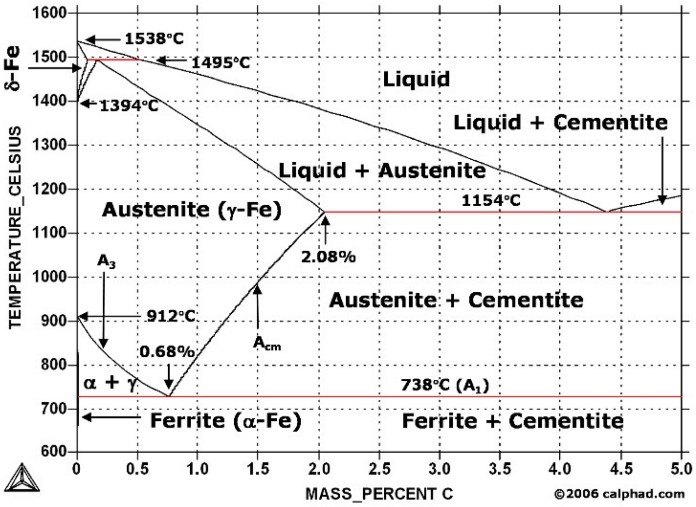

Figure 1.8: Fe-C phase diagram [20]

1.2.2 Nickel-based Superalloys

Table 1.1: Mechanical properties of selected Stainless steels

Steel type	Young's Modulus (GPa)	0.2% Yield Strength (MPa)	Tensile Strength (MPa)
304	200	215	505
416	200	275	200
21Cr-6Ni-9Mn	197	483	793
X46Cr13	220	657	782

For high temperature applications, the nickel alloys employed are known as superalloys due to their ability to retain high strength at elevated temperatures (650-1200 °C). Nickel superalloys such as Inconel, Haynes, Hastelloy, and René are composed of at least 40% Ni, plus Cr and one other element such as Fe, Co, or Mn. Even tungsten is used as a principal alloying element in Haynes 230 superalloy [24]. Most nickel alloys are either precipitation-hardened (e.g. Inconel 718 (IN718)) or solution-hardened (e.g. Hastelloy X)[25, 26]. To utilize one of these strengthening mechanisms an alloying element such as Al, Mo, Nb, or

Ti is added to produce hardening precipitates such as the γ' and γ'' phases [27–29]. In the case of IN718, the alloy is solution annealed at 1010-1065 °C for 18-20 hours followed by aging at 787 °C for 6-8 hours [30]. As seen from Figure 1.6, nickel superalloys have much better high temperature performance than stainless steels, but are certainly more expensive. Additionally, due to the presence of hardening precipitates, the weldability of several nickel superalloys is a hindrance due to strain age cracking, liquation cracking, hot cracking, and alloying element segregation (e.g. Nb) [31, 32].

The Inconel family of nickel superalloys such as IN718 (Figure 1.9) are some of the most popular nickel superalloys. They are austenitic (γ) Ni-Fe-Cr alloys that are solution strengthened by face-centered cubic (FCC) γ' precipitates ($Ni_3(Ti,Al)$) and metastable body-centered tetragonal γ'' precipitates (Ni_3Nb). Inconel alloys are typically aged at 600-750 °C for several hours to form the strengthening precipitates. The typical maximum operating temperature for the Inconel family of alloys is 650-750 °C because of the instability of the γ' and γ'' phases. γ' is unstable at temperatures between 600 °C and 800 °C and transforms into the η phase and/or grain growth which also reduces the strength [12, 33].γ'' is unstable at temperatures exceeding 650 °C transforming into the chemically similar, but more brittle δ phase[13, 34, 35]. Haynes and Hastelloy alloys are Ni-Cr-based but also may contain Fe as the third principal element. The Haynes and Hastelloy Ni alloys are primarily γ' strengthened but Haynes and Hastelloy alloys typically contain more Mo, W, and other high temperature elements. Haynes and Hastelloy alloys also have typically higher maximum operating temperatures (950-1200 °C) compared to Inconel (700-980 °C). René alloys have some of the uppermost high temperature tensile strength (around 1100 MPa at 760 °C) among nickel alloys due to high concentrations of alloying elements. Howvever, this

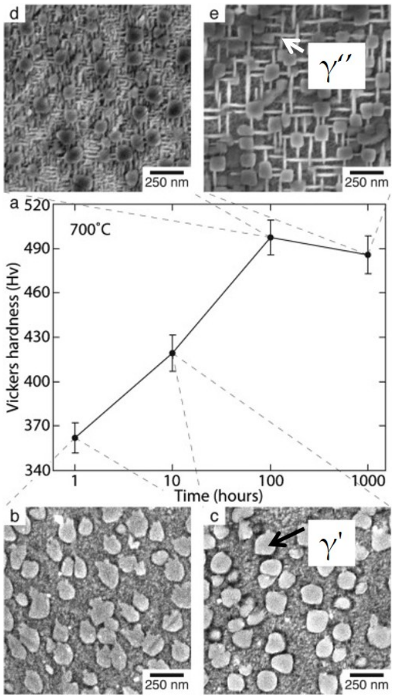

Figure 1.9: This figure was modified from Mignanelli et al. [36]. The effect of heat treatment time at 700 °C (following solution treatment) on the room temperature Vickers hardness and the microstructure of the IN718. (a) The variation in room temperature hardness, (b) the microstructure after 1 hour at 700 °C, (c) the microstructure after 10 hours at 700 °C, (d) the microstructure after 100 hours at 700 °C and (e) the microstructure after 1000 hours at 700 °C. Errors were calculated as the standard deviation of 10 individual measurements of the alloy hardness.

does, however, make their weldability especially poor due to redistribution of those alloying elements and loss of strengthening precipitates [29]. Some typical properties for selected Ni superalloys are listed in Table 1.2.

1.2.3 Titanium Alloys

Titanium alloys have similar high temperature capabilities as stainless steels. However, the most significant advantage that Ti alloys have over steel and nickel alloys is the high strength-to-density ratio. Due to the lightweight, Ti alloys are sought for aerospace and automobile applications [37, 38]. As a side note, Ti has excellent biocompatibility, so they are great for biomedical applications [39]. The most popular titanium alloy is Ti-6Al-4V.

Table 1.2: Mechanical properties of selected nickel super alloys

Alloy	Young's Modulus (GPa)	0.2% Yield Strength (MPa)	Tensile Strength (MPa)
Inconel 600	207	290	660
Inconel 718	208	1172	1407
Hastelloy X	205	340	760
Haynes 242	229	845	1290
Rene 41	218	1062	1420

However, the fusion joining (joining via melting of workpieces) of Ti alloys is challenging because of workpiece distortion and solid-state joining of Ti alloys is challenging because Ti forms a thick, stable oxide on the surface of the metal and a reducing atmosphere or high vacuum is required for many joining applications. Ti alloys are sometimes not the sole structural material in aerospace applications; a great deal of research is dedicated to dissimilar joining with other components such as aluminum alloys [40], magnesium alloys [41], and stainless steel [42–44].

Ti64, in particular is an $\alpha + \beta$ titanium alloy. α and β titanium are FCC and body-centered cubic (BCC) allotropes, respectively. α titanium has higher strength but is not heat treatable and more brittle than β titanium. α titanium is stabilized by typically adding Sn, Zr, Al. β titanium is generally unstable at room temperature unless a β-stabilizer such as V, Mo, and Si is added. There are five main categories of Titanium alloys: α, near-α, $\alpha - \beta$, near-β, and β. Near-α alloys consist of mostly α phase Ti with a small amount β-stabilizers to serve as a strengthening phase. Near-β alloys consist of mostly β phase Ti with a small amount α-stabilizers. $\alpha - \beta$ Ti alloys contain both α- and β-stabilizers such as Ti-6Al-4V in Figure 1.10 [45, 46]. Due to the more ductile nature and resistance to creep deformation of α-phase-containing Ti alloys, α, near-α, and $\alpha - \beta$ alloys are preferred for high

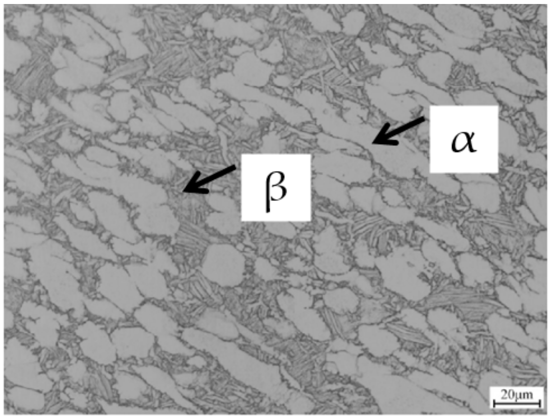

Figure 1.10: This figure was modified from Shi et al. [50]. Typical microstructure of Ti-6Al-4V

temperature applications over β-Ti [47]. As seen from Table 1.3, the Young's modulus of Ti alloys does not vary greatly, but increasing yield strength and tensile strength is associated with increased β content [46, 48, 49].

1.2.4 High Entropy Alloys

HEAs can be fabricated by arc melting [51], induction melting [52], or mechanical alloying [53]. The elemental composition is typically equimolar or near-equimolar. HEAs are characterized by four core effects that give them unique properties: high entropy effect, sluggish diffusion kinetics, severe lattice distortion, and cocktail effect [51, 54, 55]. The high entropy effect can be described through Equation 1.4.

$$\Delta S_{mix} = \sum_{i=1}^{n} -RC_i lnC_i \qquad 1.4$$

HEAs tend to have sluggish diffusion in solid-state partially due to the severe lattice distortion induced by several elements sharing the same lattice space. They however may still have a normal lattice structure (Figure 1.11). The cocktail effect states that properties

Table 1.3: Mechanical properties of selected Ti alloys

Alloy type	Composition	Young's Modulus (GPa)	0.2% Yield Strength (MPa)	Tensile Strength (MPa)
α	Ti-5Al-2.5Sn	103	760	790
Near-α	Ti-6Al-2Sn-4Zr-6Mo	114	862	930
$\alpha-\beta$	Ti-6Al-4V	114	950	1020
Near-β	Ti-10V-2Fe-3Al	107	1220	1282
β	Ti-3Al-8V-6Cr-4Mo-4Zr	110	1346	1433

of a material are not only determined by interactions between dissimilar elements, similar to a complex solid solution. Through the cocktail effect even small variations in the chemical composition of a HEA can affect the mechanical and chemical properties [56]. The cocktail effect is one of the most critical design principles in the designing of high entropy alloys for both high temperature and cryogenic applications [57–59]. The cocktail effect arises at both the multielement, atomic level [60]and the multiphase, micro-level [61]. High entropy alloys are theoretically capable of being used as structural materials [62] as well as brazing filler materials (BFMs) [52, 63]. As one of the newest class of materials in the world, much has yet to be firmly established about the metallurgical properties of HEAs before their widespread applications [64]. As seen from Figure 1.6, high entropy alloys resemble a wide spread of mechanical properties and if several high melting temperature elements (e.g. W, Mo, and Cr) make up their constituents, then their maximum operating temperature tends to be higher.

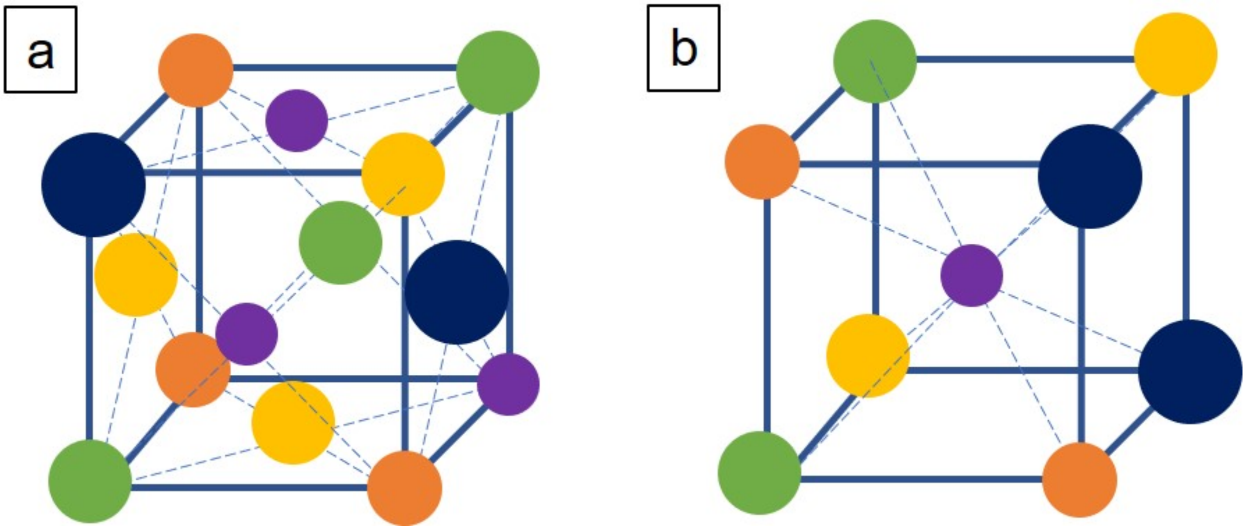

Figure 1.11: Crystal structures of (a) face-centered cubic (FCC) and (b)body-centered cubic (BCC) HEAs

1.3 Materials Joining Technologies

1.3.1 Welding

The joining of high temperature alloys is critically important to the manufacturing, fabrication, and assembly of high temperature components. The first and most widely used joining technique for metal-metal joining is fusion welding. Fundamentally, welding involves melting the joining surfaces, forming a molten pool and when the pool solidifies, the metal surfaces fuse together. There is a multitude of welding techniques that are differentiated by the type of input energy used to generate heat. The most popular welding category is arc welding which uses a metal electrode to generate an electrical arc that will provide enough heat to form a molten pool between the two pieces. There are several different types of arc welding based on the electrode material and the method of arc generation including but not limited to tungsten inert gas (TIG) welding [32], metal inert gas (MIG) welding, and plasma-arc welding [65]. Arc welding techniques typically incorporate a shielding gas or plasma to protect the workpieces from oxidation. Flux may also be used for protecting the workpieces; however, many fluxes are a source of joint contamination and produce harmful vapors when used [18]. Arc welding is one of the most thoroughly understood joining methods. However, arc welding is not suitable for joining metals that are prone to phase separation in a molten state such as Nb segregation in Inconel 718 [66] and Cu/Cr segregation in CoCrCuFeNi HEAs [67].

Like arc welding, laser welding also generates a molten pool between the two surfaces except laser irradiation is the heat source for this method. Due to the small spot size of the laser, it is possible to weld more precisely with laser welding compared to arc welding. Additionally, for some metals, an inert gas is not necessary for laser welding, though a vacuum or inert environment is required for oxidation-sensitive metals such as aluminum and titanium [68, 69].

Some welding techniques such as friction stir welding and ultrasonic welding are performed in solid-state [37]. In friction stir welding, metal surfaces are pressed together with a rotating tool head and the friction induced by the tool head produces heat that softens and mechanically intermixes the material. Ultrasonic welding operates on a similar principal as friction stir welding, except an ultrasonic tool head is used instead of a rotating tool head. Heat is still generated to form a mechanically mixed joint. Ultrasonic welding is capable of melting plastic base materials (BMs), but not metals due to limited processing temperatures. The two most popular types of welding joints are butt joints and lap joints. Butt joints are formed by welding two ends of the BM together (Figure 1.12a). Lap joints are formed by welding two or more overlapping pieces of the BM (Figure 1.12b). There are several other basic joint types such as tee joints (Figure 1.12c), corner joints (Figure 1.12d), and edge joints (Figure 1.12e), however, they appear almost exclusively in real life engineering structures and seldomly in fundamental joining research.

1.3.2 Brazing

Brazing, the focus of my dissertation, involves the melting and reflow of molten brazing filler material (BFM) into a gap between joined surfaces. Unlike welding, the BM is not melted during brazing, but sometimes a reaction occurs between the BM and the BFM. Keeping the BM in a solid-state is highly advantageous for joining materials that experience unfavorable phase segregation during welding and/or repairing components with complex geometries without destroying the component. For example, this is an important procedure for repairing service cracks in turbine blades [70–72]. Dissimilar material joining can be a challenge when using welding due to the formation of brittle intermetallic compound and incompatibility of certain elements. By using a brazing BFM, dissimilar material joining

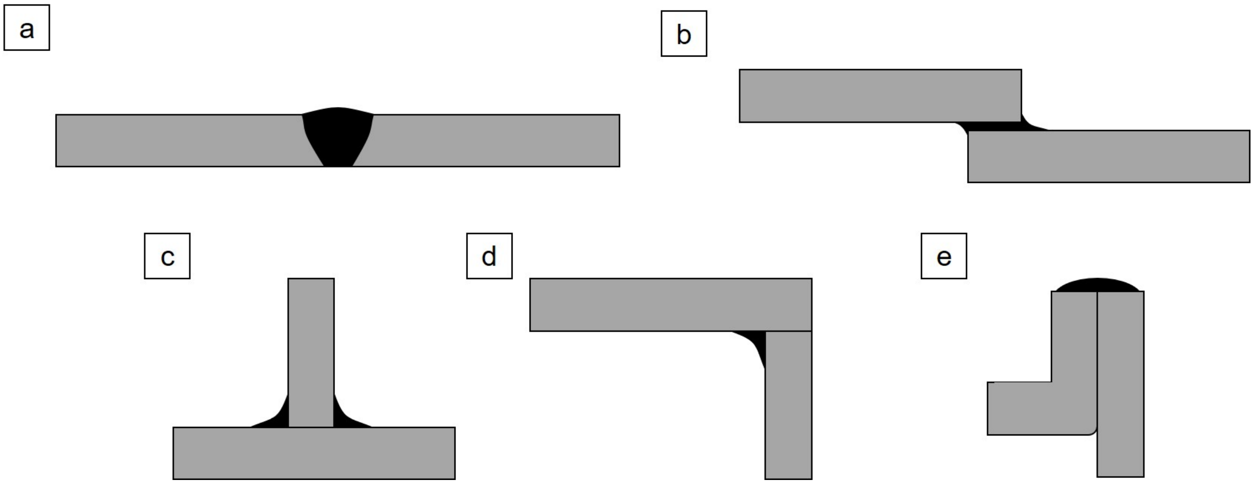

Figure 1.12: Diagram of a basic (a) butt joint, (b) lap joint, (c) tee joint, (d) corner joint, and (e) edge joint

becomes significantly easier. The challenge is finding an BFM that is compatible with both BMs and will form little to no intermetallic compounds [42, 73, 74]. Traditional brazing procedures use an inert gas (e.g. Ar), vacuum, or brazing flux to protect the BM and/or BFM from oxidation. The joints discussed in the previous section can also be applied to brazing. Most of the welding techniques can be applied to brazing, but welding arcs are potentially less favorable to lasers because lasers are typically more precise than welding arcs.

Demands of High temperature Brazing

High temperature brazing joints must satisfy two overarching conditions: metallurgical compatibility and mechanical compatibility. Metallurgical compatibility is a form of chemical compatibility in metals that is governed by the kinetics and thermodynamics of the materials system. The first way to evaluate metallurgical compatibility is to study the relevant equilibrium phase diagram(s) of the proposed system. The phase diagram can reveal the possible equilibrium phases, the melting point of those phases, and the potential phase transformations at elevated temperatures. The equilibrium phase diagram only considers the thermodynamics of the materials system. For other materials systems, especially the Fe-C system, only a limited amount of information can be obtained from only studying the phase diagram. For understanding the metallurgy of steels, several diagrams such as the time-temperature-transformation (TTT) diagram and the continuous-cooling-transformation (CCT) diagrams will show how specific heat treatments will change the microstructure and properties of the material [18]. Additionally, as the number of elements increases, the less likely that an all-inclusive, experimentally-verified phase diagram exists. Lack of predictability in welding and brazing is an obstacle when choosing a brazing filler material (BFM). For instance, copper-silver brazing materials are good for brazing several types of steel and nickel superalloys. However, for high temperature applications, especially those approaching 700 °C where some of these alloys begin to melt [75]. BAg-8 has questionable suitability for brazing nickel superalloys for turbine blade repair due to the low melting temperature of 780 °C (Figure 1.13).

Brazing materials must also have comparable tensile strength, fatigue strength, coefficient of thermal expansion (CTE), creep resistance, etc. In the case of nickel alloys, steels, and most refractory alloys, a copper-silver brazing filler material (BFM) is a compatible BFM, however, the joint will have lower hardness and Young's modulus than the BM [76]. Even conventional nickel-based BFMs may produce harder joints than the Inconel 718 (IN718) BM [77].

A thermal mismatch is also a potentially critical flaw that brazed/welded joints can have. Thermal mismatch comes from the difference in the CTE of the joined materials. When the material temperature changes, the resulting difference in thermal expansion/contraction of the two or more materials results in thermal stress. Most metals do not have significantly different CTEs so this usually does not come into play in any major way. However, it is specifically an issue for dissimilar material joining such as polymer-metal and ceramic-metal joining or in certain composite materials. Some CTE mismatch is acceptable in some materials because the particulate reinforcements induce a plastic dislocation region around the particulates that helps hinder dislocation movement at high temperatures, thereby enhancing high temperature strength [15].

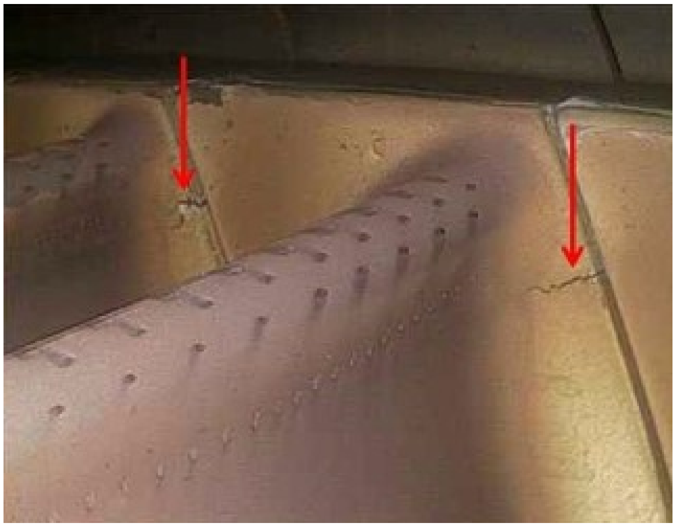

Figure 1.13: Photograph of turbine crack

Wettability

Wettability is the capacity of a liquid (i.e, a molten metal in this context) to spread and/or adhere a surface. The wettability of a molten metal in a welding or brazing scenario is quantifiable by measuring the contact angle (θ) and areal spreading (i.e. how much does the area of the BFM increase after spreading). The fundamental forces that determine wetting of a surface are the solid-vapor (γ_{sv}, solid-liquid (γ_{sl}, liquid-vapor (γ_{lv} interfacial energies and the contact angle is calculable by Young's equation (Equation 1.5). A conceptual representation of Young's equation and the contact angle is shown in Figure 1.14a. Different types of surface preparation can enhance wettability. For example, Hebda et al. reports that Ni plating has the best wettability performance compared to polishing with abrasive paper with different gradations when using a gold brazing material to wet AM 5510 stainless steel [78].

$$cos\theta = \frac{\gamma_{sv} - \gamma_{sl}}{\gamma_{lv}} \qquad 1.5$$

For good wetting, $\theta \leq 90°$. The ability of the molten BFM to wet the surface is not only important for robust joining, but also for crack repair and other narrow-gap joining (gap $< 400\mu m$). For narrow gap joining, penetration of the gap by the BFM is aided by the capillary pressure (P) as seen in Figure 1.14c and quantified in Equation 1.6).

$$P = \frac{\gamma_{sl} + \gamma_{lv}cos\theta - \gamma_{sv}}{r} \tag{1.6}$$

Many of the cracks in aerospace and other industries have small openings and are very deep, only a BFM with good wettability can successfully complete the the repair task Figure 1.14b-c [16, 70, 72]. The most common method to measure the contact angle is the sessile drop method which will be used to measure later in Chapter 6. The sessile drop method can be performed in-situ using a goniometer [79] or ex-situ by polishing the cross-section of a solidified BFM on the surface of a BM [80].

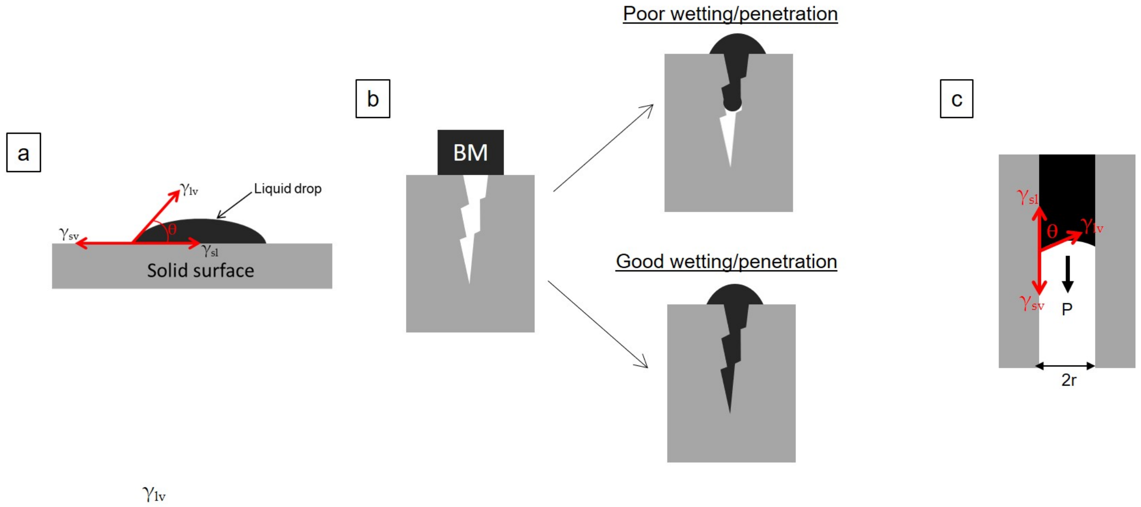
Poor wetting/penetration
b
c
a
BM
γ_{lv}
Liquid drop
γ_{sv}
θ
γ_{sl}
Solid surface
Good wetting/penetration
γ_{sl}
θ
γ_{lv}
γ_{sv}
P
2r
γ_{lv}

Figure 1.14: (a)Visual representation of Young's equation and the contact angle. (b) Schematic of the different wetting conditions of a crack being repaired by capillary force-assisted brazing (c)Application of Young's equation for capillary force-assisted brazing

Diffusion

Diffusion is a key phenomenon in materials science and joining technologies. Many of the phase transformations in the formation and heat treatment of alloys are diffusion driven. For example, limiting diffusion time with a high cooling rate prevents Fe_3C formation in steels[18]. For joining, diffusion helps ensure that the BM and the BFM are intermixed in order for a sound metallurgical bond to form. However, excessive diffusion can also be bad if the diffusion of one species significantly outpaces the other, resulting in Kirkendall voids. Also, one of the objectives of brazing is to avoid unnecessary changes to the BM and significant diffusion can result in the nucleation of unfavorable composition changes that may result in new phases. Diffusion is utilized heavily in diffusion bonding (Section 1.3.3) as the name implies. Most studies of diffusion tend to obey Fick's first (Equation 1.7) and second laws (Equation 1.8).

$$J_i = -\frac{Dc_i}{RT}\nabla\mu_i \tag{1.7}$$

$$\frac{\partial c}{\partial t} = -D\nabla^2 c \tag{1.8}$$

D is the diffusion coefficient, c is concentration, x is position, and t is time. A transformation of Fick's second law into a solvable original differential equation is the objective of the Boltzmann-Matano method [81]. The Boltzmann-Matano method produces an equation to solve for the concentration-dependent diffusion coefficient, helping to analyze real data (c^*).

$$\epsilon = \frac{x}{2\sqrt{t}}, \frac{\partial\epsilon}{\partial t} = \frac{\epsilon}{2t}, \frac{\partial\epsilon}{\partial x} = \frac{1}{2\sqrt{t}} \tag{1.9}$$

ϵ is a substitution term used to transform Fick's second law. Using this substitution, Fick's second law is transformed into the following form:

$$-2\epsilon\frac{\partial c}{\partial \epsilon} = \frac{\partial}{\partial \epsilon}[D(c)(\frac{\partial c}{\partial \epsilon})] \tag{1.10}$$

After integrating, this equation via Matano's method and isolating $D(c)$

$$-2\int_{c=c_2}^{c=c^*} \epsilon dc = \int_{c=c_2}^{c=c^*} d[D(c)(\frac{\partial c}{\partial \epsilon})] \tag{1.11}$$

$$D(c^*) = -\frac{1}{2t}\frac{\int_{c_2}^{c^*} xdc}{\frac{\partial c}{\partial x}_{c=c^*}} \tag{1.12}$$

Using the Boltzmann-Matano method, Fick's second law is solvable, however x must be quantified in reference to the average position weighted on the concentration (i.e. the Matano interface) [82]. The Matano interface is also difficult to accurately pinpoint so Sauer-Friese analysis is preferable because it is unnecessary to know the location of the Matano interface [81].

$$y_c = \frac{c(x) - c_L}{c_H - c_L} \tag{1.13}$$

$$D(c) = \frac{1}{2t\frac{\partial c}{\partial x}_{x*}}((1-y_c)\int_{-\infty}^{x*}(c(x) - c_L)dx + y_c\int_{x*}^{\infty}(c_H - c(x))dx) \tag{1.14}$$

$$D_{avg} = \frac{\int_{c_L}^{c_H} D(c)dc}{c_h - c_L} \tag{1.15}$$

Equation 1.14 can also be written as:

$$D(c) = \frac{1}{2t\frac{\partial c}{\partial x}_{x*}}(-(1-y_c)\int_{-\infty}^{x*} y_c dx + y_c\int_{x*}^{\infty}(1 - y_c)dx) \tag{1.16}$$

With Sauer-Friese analysis, the only values that are needed are an equation for concentration with respect to position, the maximum concentration (c_H) and the minimum concentration (c_L). There are other diffusion analysis techniques including Crank-Nicolson [83] and phase field analysis [84, 85].

Melting Point Depressants

As previously mentioned, brazing involves the melting and reflow of BFMs to join BMs together. For high temperature materials such as Ni, the full melting and reflow of the BFM can prove difficult since the melting point of pure Ni and some Ni alloys is higher or close to the solidus, liquidus, or melting temperatures of the BMs they are trying to join. The melting point of these BFMs may also be close to the phase/microstructure transition temperatures. For example, IN718 experiences significant grain growth above 1000 °C which can lead to lower strength [86]. Traditionally, refractory metal-based BFM contain melting point depressant (MPD)s such as boron, silicon, and phosphorus to lower the melting point such that the melting or unintentional altering BM is avoided. MPDs such as boron and silicon have a tendency to form brittle and/or low melting intermetallic phases within the BM after brazing.

1.3.3 Diffusion Bonding

As the name implies, diffusion bonded joints are formed by diffusion between either dissimilar metal surfaces or with an interlayer material present. The most active elements in diffusion bonding should have a sufficiently high diffusion coefficient to be most effective (10-100 times higher than self-diffusion coefficients of principal elements). A reactive interlayer material such as a reactive multilayer film (RMF) can significantly decrease the required bonding temperature through added exothermic heat and reaction with the BM [87].

Transient Liquid Phase Bonding

An important subset of diffusion bonding is transient liquid phase (TLP) bonding. In TLP bonding, a melting point depressant (MPD)-containing filler metal is heated to the point of melting, then the MPDs as well as other metallic elements diffuse from the BFM to the BM and the BFM solidifies isothermally due to depletion of the MPDs. The resulting joint area is a MPD-depleted isothermally solidified zone (ISZ) at the interface as demonstrated in Figure 1.15. The center of the joint may still contain higher amounts of MPDs. This technique is most common for high temperature brazing alloys such as BNi-2 which has a liquidus temperature of 999 °C. Without the MPDs, boron and silicon, the melting point of the BNi-2 (Ni 89%,Cr 8%, Fe 3%) would be approximately 1350 °C [88, 89]. Homogenization of the joint through diffusion is also possible if the BFM is chemically similar to the BM such as the BNi series materials and nickel superalloys.

1.3.4 Additive Manufacturing

Several innovations and applications of existing joining techniques have been made. One of the most major innovations is additive manufacturing. Metal additive manufacturing essentially combines powder metallurgy with various welding techniques, especially laser welding and electron beam welding. The most commonly used techniques are powder bed and directed energy deposition techniques. Powder bed techniques uses thin layers of powder spread across a surface and a laser or electron beam melts only a selected area. After the area is melted, another layer of powder is spread across the powder bed and a selected area

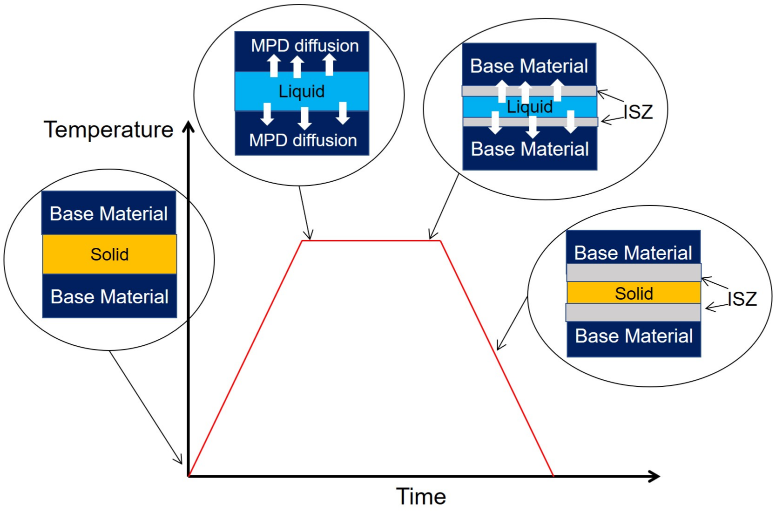
MPD diffusion
Liquid
MPD diffusion
Base Material
Liquid
Base Material
ISZ
Temperature
Base Material
Solid
Base Material
Base Material
Solid
Base Material
ISZ
Time

Figure 1.15: Schematic representation of TLP bonding. ISZ is the isothermally solidified zone

is melted again. This process repeats until the part has been manufactured. Direct energy deposition simultaneously uses incorporates a powder stream with a beam energy source such as an electron beam or laser such as the one seen in Figure 1.16. Directed energy deposition can also be performed with a wire feedstock instead of powder [90]. Additive manufacturing is also applicable to flexible electronics [91, 92] and bottom-up construction of electrodes and other components [93, 94]. Innovations in additive manufacturing have also allowed up to 100 nm resolution where the previous restriction was on the microscale [95].

1.3.5 Nanoparticle-enhanced Welding and Brazing

Another joining innovation is nanoparticle (NP)-assisted welding and brazing. NPs are essentially used in these studies to modify the melting behavior or phase evolution of welding and brazing joints. For example, Sokoluk et al. added TiC NPs to the welding filler metal for 7075 aluminum alloy to enable the alloy to be arc welded when it was previously

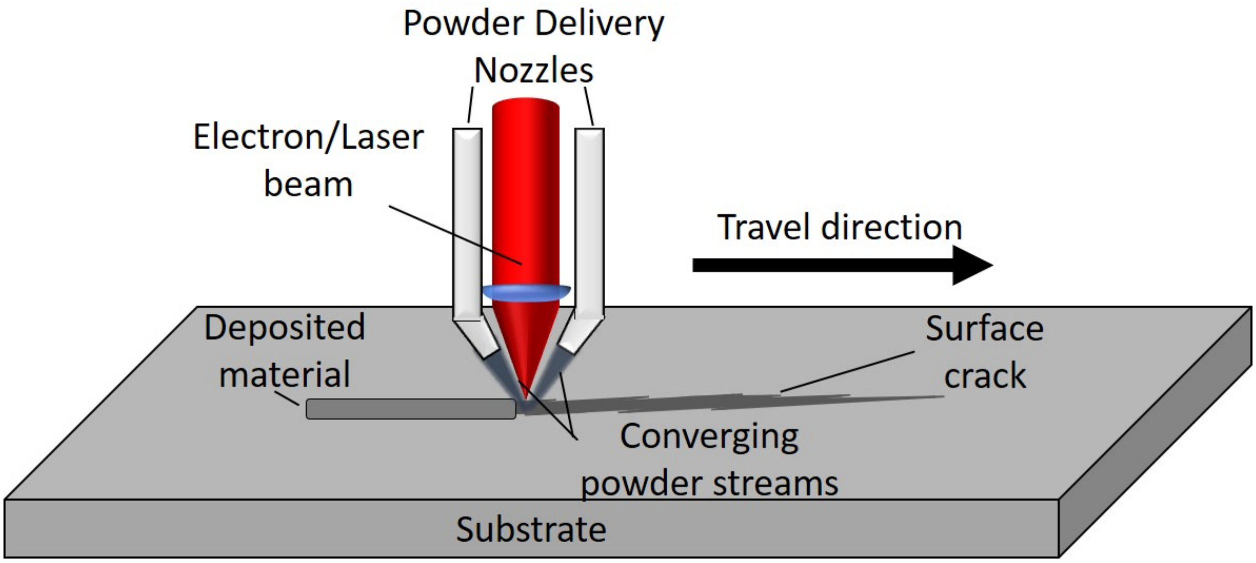
Powder Delivery
Nozzles
Electron/Laser
beam
Travel direction
Deposited
material
Surface
crack
Converging
powder streams
Substrate

Figure 1.16: Schematic of directed energy deposition with powder stream for crack repair

"unweldable" [96]. In 2014, Hdz-García et al. added Si NPs to BNi-9 bonded stainless steel joint resulting in an even lower melting point for the BFM. As a consequence, several eutectic phases formed in the melting zone of the joint [97]. In 2016, Hdz-García et al. incorporated W NPs in BNi-9 bonded Inconel 725. The addition of W resulted in the formation of finer intermetallic and eutectic phases due to the suppression of Ni and Cr diffusion [98].

1.3.6 Microjoining and Nanojoining

Microjoining and nanojoining involves the use of mircoparticles (<100 μm) and NPs (<100 nm) as a filler metal, respectively. Particle-based joining allows additional freedom when working with processes such as additive manufacturing, printable electronics, and crack repair [22]. Nanoparticles have been so attractive for high temperature electronics due to the size-dependent melting point depression of NPs seen in Figure 1.19. This melting point depression is caused by the Gibbs-Thomson effect [99]. The equation governing the Gibbs-Thomson effect (Equation 1.17) describes the melting point for an isolated spherical particle

(T_{MP}) with a diameter, d. At the time of this dissertation, there has not been a firmly established Gibbs-Thomson equation for nanowires, nanoplates, and other non-spherical nanomaterials [100].

$$T_{MP}(d) = T_{mB}(1 - \frac{4\sigma_{sl}}{H_f \rho_s d}) \qquad 1.17$$

T_{mB} is the bulk melting temperature, σ_{sl} is the solid-liquid interface energy, H_f is the bulk enthalpy of fusion and ρ_s is the molar volume of the solid. The Gibbs-Thomson equation was derived by equating the chemical potential of a liquid at T_m is equal to the chemical potential of a solid at T_m and a change in chemical potential occurs when the melting point changes. Please see reference [101] and Appendix D for the full derivation completed by Gibbs. The liquid drop model is another method used to approximate the melting point of NPs.

$$T_{MP}(d) = T_{mB}(1 - \frac{6\nu_o \gamma_{sv}}{0.0005736 T_{mB} d}) \qquad 1.18$$

ν_o is the atomic volume and γ_{sv} is the solid-vapor interfacial energy [102].Makkonen et al. discusses several methods for determining the different surface energies in the Gibbs-Thomson and liquid drop models [100]. Qi et al. use a model based on the liquid drop model that takes particle shape into account [103].

$$T_{MP}(d) = T_{mB}(1 - \frac{6\alpha r}{d}) \qquad 1.19$$

r is the atomic radius. In addition to lower melting temperature, NPs also can experience surface melting, where the surface layer of atoms is in a liquid or quasi-liquid state [99]. According to most computational studies, elemental NPs melt starting with surface followed by the NP core [104–106]. Many computational studies utilize the Lindemann criterion to determine the melting temperature. The Lindemann criterion is a theory for the melting transition based on the vibration of atoms in a material. As the temperature increases, the amplitude of thermal vibrations increase. When the amplitude of thermal vibrations exceed a threshold value (typically 10% of the nearest neighbor distance of atoms in a lattice), melting occurs [107]. When the According to the Chernyshev model, surface melting can occur several hundred Kelvin below even the T_{MP} (Equations 1.20 to 1.23).

$$T_{SM}(r) = T_{mB}[1 + y(r)exp(-y(r))](0.75\alpha)^{-1} \quad 1.20$$

$$\alpha = \frac{2S_{vib}}{3R} + 1 \quad 1.21$$

$$y(r) = \frac{\alpha - 1}{\frac{r}{r_c} - 1} \quad 1.22$$

$$r_c = 3h(1 + (\frac{0.75\alpha - 1}{\alpha - 1})^{-1}) \quad 1.23$$

S_{vib} is the bulk vibrational entropy of melting, R is the ideal gas constant, r_c is the critical radius under which surface melting does not occur, and h is the atomic diameter. This model assumes the surface layer is three atomic layers thick and that surface melting occurs when the NP surface is in a quasi-liquid state. Chernyshev's model is is unresponsive to particles ¡10 nm in diamter [108]. Even lower than the surface melting temperature, NPs have a sintering temperature that can be 10-30% of the bulk melting temperature as seen in Equation 1.24 [109, 110]

$$T_s(r) = 0.3T_{mB}exp[-\frac{2S_m^{bulk}}{3k(\frac{r}{3h} - 1)}] \quad 1.24$$

T_s is the sintering temperature, S_m^{bulk} is the bulk melting entropy, and h is the atomic diameter [111]. Sintering is a process in which adjacent particles are coalesce through solid-state (solid-state sintering) and/or liquid state diffusion (liquid-phase sintering). Note that sintering is an ongoing process once the minimum sintering temperature is reached and effective particle radius will continue to grow, thereby increasing the sintering temperature. When most researchers refer to sintering, they are referencing solid-state sintering unless otherwise stated.

Lastly, due to the lower activation energy required for diffusion in NPs, the diffusion coefficient for nanoparticles increases nonlinearly as particle size decreases. The Arrhenius-type equation that describes this as follows:

$$D(r,T) = D_o exp[\frac{-E_r}{RT}] \tag{1.25}$$

$$E(r) = E_{bulk} exp[\frac{-2S_{vib}}{3R(\frac{r}{r_s}-1)}]] \tag{1.26}$$

D_o is the pre-exponential factor, $E(r)$ is the activation energy of diffusion as a function of radius (r), R is the ideal gas constant, E_{bulk} is the bulk activation energy of diffusion and r_s is the radius of a NP if all atoms are located on the surface [112]. This relationship applies to lattice diffusion, grain boundary diffusion, and surface diffusion which are illustrated in Figure 1.17. The normal Arrhenius-type equation for bulk diffusion is expressed in Equation 1.27.

$$D(r,T) = D_o exp[\frac{-E_bulk}{RT}] \tag{1.27}$$

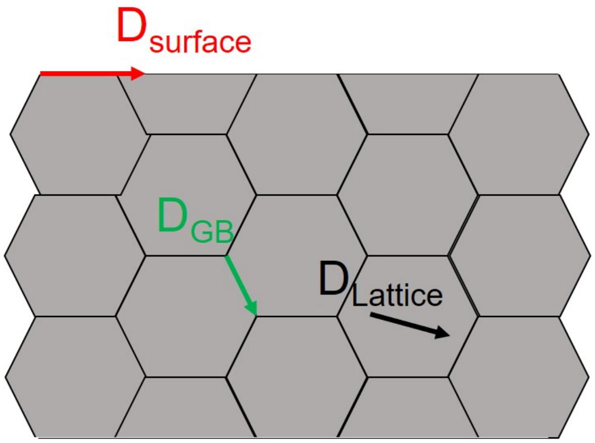

Figure 1.17: Illustration of three primary diffusion types lattice diffusion ($D_{Lattice}$), grain boundary diffusion (D_{GB}), and surface diffusion ($D_{Surface}$)

D_o and E_{bulk} are typically determined by plotting the natural logarithm of the measured diffusion coefficient versus the reciprocal of the temperature in Kelvin. The y-intercept and and slope multiplied by R of this plot are the D_o and E_{bulk}, respectively (Figure 1.18).

Due to the Gibbs-Thomson effect, the prevalence of surface melting, higher diffusion coefficient, and low sintering temperature of NPs, the minimum processing temperature of NPs is significantly lower than for microparticles. Note that surface melting and solid-state sintering cannot be simultaneously exploited. Once adjacent particles are joined, the melting temperature returns to its bulk value as seen in Figure 1.19 which contains theoretical and experimental data [109, 113–115].

There are two basic approaches to metal nanomaterial synthesis: the top-down approach and the bottom-up approach. In a top-down approach, a bulk or microscale form of the desired material is broken down into nanosized particles. Some examples of these approaches include ball milling (Figure 1.20) [116–119], laser ablation [120–124], exploding wire method [125–129], and vaporization-condensation [130, 131]. Most of these methods

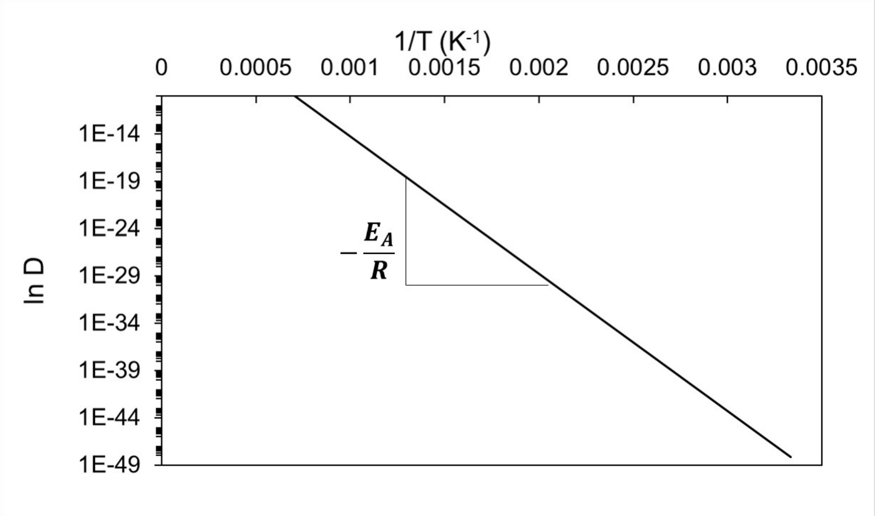

Figure 1.18: General logarithmic plot of D vs $1/T$

are performed in either a liquid media or under vacuum. Vacuum or inert gas atmosphere is typically preferable in order to avoid contamination from the atmosphere or from a liquid media [132]. Ball milling contains an additional concern because there is a possibility of contamination from the milling balls or milling jar lining. In our own experience, zirconia milling balls produce significant contamination when milling metals such as Ni and Cu. For micro- and nanojoining, contamination from a foreign substance can significantly hinder its joining capabilities especially if the foreign substance is ceramic or another non-metal substance with a high melting temperature. Ways to avoid contamination from these kind of foreign substances include using a proper process control agent to avoid cold welding between the particle and the milling balls and using sufficiently hard, but not brittle, milling balls/jar that will not fragment when milling certain hard materials. The most popular milling jar and milling ball materials are tungsten carbide and hardened stainless steel [133].

Top-down approaches are the method of choice for most large-scale synthesis applications and for fabricating multielement (i.e., more than two elements) NPs [134–136],

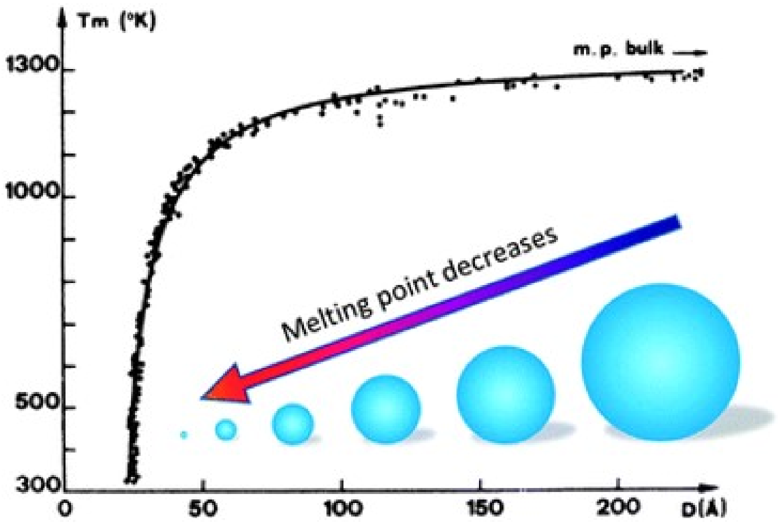

Figure 1.19: Melting point depression diagram of Au NPs [115]

however, they overall lack particle shape control capabilities in and size control to some extent. The bottom-up approach involves the reduction of an ionic compound via a reducing agent, in the presence of an electric field, or ultrasound. Wet chemical reduction is by far the most popular nanomaterial synthesis technique. Wet chemical reduction enables superior size [120, 137–140] and shape control [110, 141–144] compared to top-down approaches and can be carried out at ambient pressure and high pressure (e.g. solvothermal/hydrothermal synthesis) [92, 145–147]. Size and shape control is achieved typically by controlling the reactant concentration and introducing an organic capping agent to restrict the size or direction of growth [148–151]. The primary NM growth mechanisms in wet chemical reduction are (1) reduction of metal ions and deposition on existing particles/forming new nanocluster and (2) Ostwald ripening (Fig. 1.21). Ostwald ripening is when smaller particles dissolve in a media and the atoms redeposit on larger particles. [139]. Capping agents also help protect oxidation-prone NMs from oxidation [149, 152, 153]. Oxidation-resistant metals can also be used as a capping layer [154–157]. Wet chemical reduction is also the method

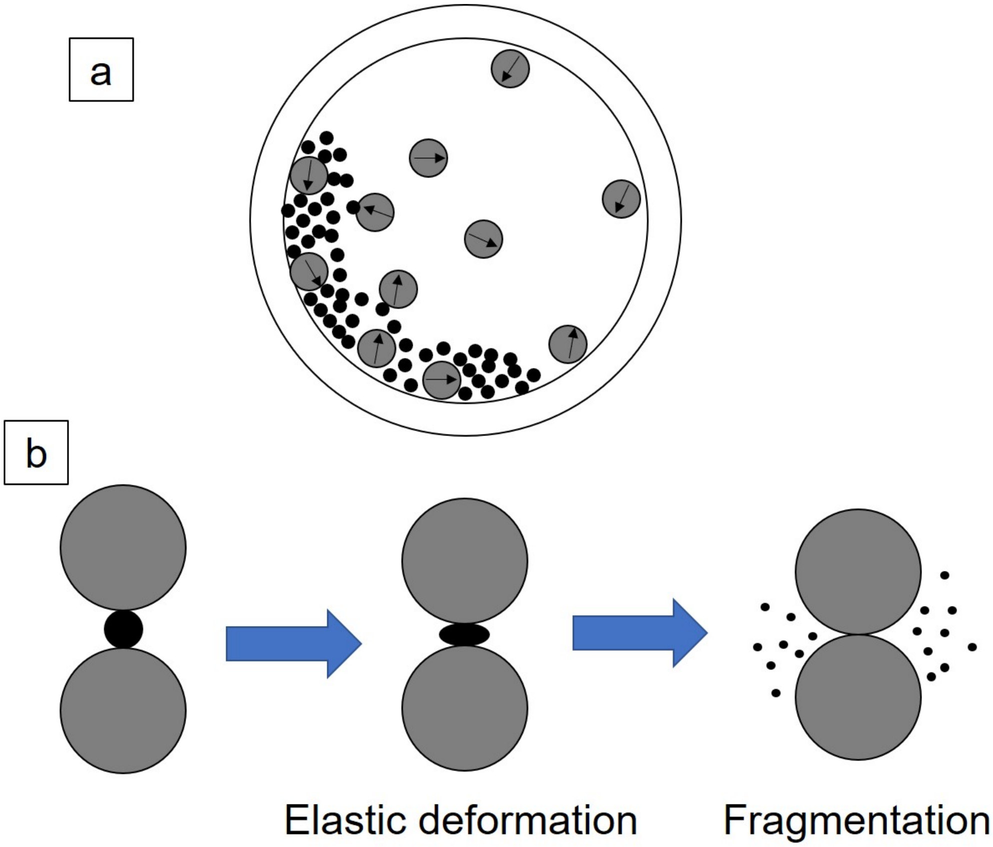

Figure 1.20: (a) Working concept of a ball milling process (b) Ball-powder interaction concept for ball milling

of choice for continuous synthesis techniques, usually with a microwave as the heat source [158–161]. Sonochemical synthesis uses ultrasound to generate the necessary heat to reduce the metal precursor in solution, but this technique tends to take longer than traditional chemical reduction [162–164]. Electrodeposition is used less frequently for fabricating NPs, but it can be used for fabricating aligned nanowires (NWs) [165–167]. Bottom-up techniques suffer from difficulties in fabricating large amounts of NMs but versatility and not requiring expensive equipment for laboratory-scale experiments are compensating qualities.

NPs have primarily been relegated to soldering and printable electronics applications [110, 168–174]. Being able to utilize the low processing temperature of NPs, damage to

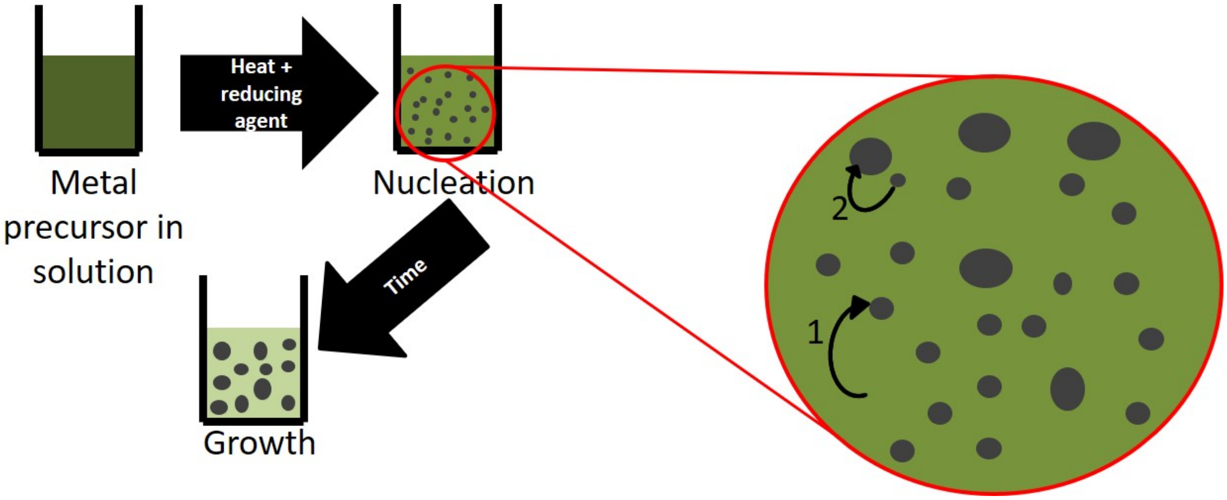

Figure 1.21: Schematic of the growth mechanisms in wet chemical synthesis of NPs. Growth method 1 is chemical reduction of the precursor and growth method 2 is Ostwald ripening

electronic components or polymeric substrates can be avoided. Cu-based and Ag-based NPs are among the most popular choices for soldering and electronic applications due to their high conductivity. For example, Li et al. have used silver nanoplates and nanowires (NWs) to fabricate flexible electronics and for wire bonding applications [91, 92, 141]. To avoid damaging temperature sensitive components in a SiC power electronic device, Manikam et al. mixed aluminum and silver nanoparticles for die attach applications and demonstrated its robustness under thermo-cycling conditions [175]. Nanowire-nanowire joining (Figure 1.22) is useful for different sensing applications such as sensing and flexible electronic applications since nanowire electronics have better flexibility than nanoparticle electronics [91]. Also, single nanowire devices have applications in high sensitivity detectors [176]. The bonding strength for low temperature nanojoining is typically limited to tens of MPa [177]. Additionally, low temperature nanojoining typically suffers from high porosity joints at the end of the heating cycle due to the presence of an organic shell on chemically synthesized NPs and/or from the organic vehicle in the paste. Organic content prevents

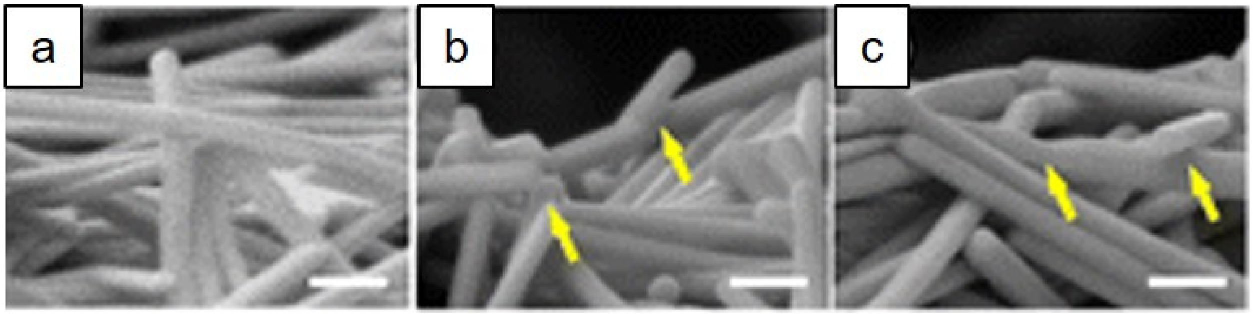

Figure 1.22: This figure is modified from Li et al. [91]. Ag NWs (a) before sintering, after (b) photonic sintering (ambient temperature is room temperature) and (x) thermal sintering at 250 °C for 5 min. The white scale bars indicate 150 nm and the yellow arrows indicate places where NW-NW joining has occurred.

intimate contact between adjacent NPs and hinders joining mechanisms as demonstrated in Figure 1.23 [110, 178]. Carbon can possibly reduce the melting temperature of some metallic NPs after decomposition of the organic layer, but presumably this is contingent on the dissolution C into the NP surface and interior.

Only a handful of studies have been done on high temperature joining as of 2019. Eluri et al. and Tiwari have used Ni NPs and Ag NPs (not mixed) on separate occasions for microchannel array applications [69, 179, 180]. Atieh et al. performed dissimilar TLP bonding of Ti-6Al-4V and Mg-AZ31 using Ni electroplating containing Ni and Cu NPs [41]. Most NPs are delivered as pastes in current state-of-art nanojoining techniques [181, 182]. These pastes typically consist of the dry nanopowder being dispersed in an organic vehicle. Using dry nanopowders for nanojoining is relatively uncommon [119]. Most of the high temperature nanojoining studies mentioned above still report joints that are porous after their brazing/diffusion bonding procedure and, compared to low temperature nanojoining, is not as thoroughly understood. A summary of different nanojoining techniques is shown in Table 1.4

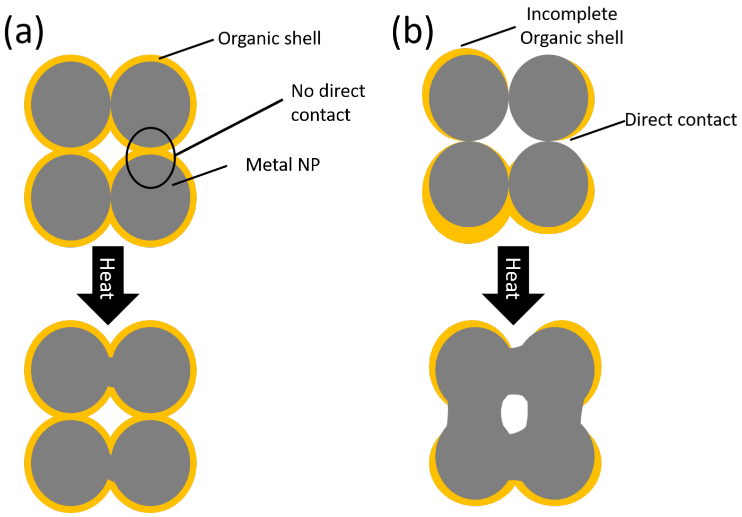

Figure 1.23: Schematic of NP sintering with (a) a thick/complete organic shell and (b) a thin/partially covering organic shell [110]

1.4 Research Objectives and Hypotheses

Due to the demand to remove MPDs from high temperature brazing materials, this dissertation investigates the possibility of using nanomaterials (NMs) as the sole BFM. The Gibbs-Thomson effect for NMs provides the necessary melting point depression without the use of problematic MPDs. By making use of the melting point depression effects, surface melting, and enhanced diffusion, the technique for using NMs as filler metals will be developed and its advantages will be speculated based on the findings. NMs, as a filler metal, are sought after as an alternative to conventional BFMs, therefore all BFMs are tested against existing conventional BFMs. According to the CALPHAD method performed by Soupousek et al. and Park and Lee, the melting point depression for NPs >20 nm is rather modest [193, 194]. However, the sintering and surface melting temperature are several hundred degrees lower than the bulk and particle melting temperatures, allowing for lower processing

Table 1.4: Summary of different nanojoining techniques

Method	**Temp. (°C)**	**Typical Bonding Strength (MPa)**	**Applications**	**References**
Nanosoldering	RT-450	10-50	Die attach, wire bonding, flexible electronics, printable electronics, hermetic sealing	[167, 173, 183–186]
Laser/photonic sintering	RT	10-40	Wire bonding, flexible electronics, printable electronics	[121, 187]
NW joining	RT	N/A	Sensing applications	[176, 188–190]
Nanobrazing	>450	75-150	HT assembly, crack repair, hermetic sealing	[180, 182, 191**?** , 192]

temperature range [106, 108, 109, 111]. I hypothesize that the following will be key aspects of nanomaterial brazing (nanobrazing) success and advantages over conventional materials:

1. Surface melting and diffusion will be more important processes than complete melting.
2. Grain boundary strengthening and/or subgrain boundary strengthening will be important mechanisms for high bonding strength of nanobrazed joints.

The first point will be tested by first using analytical calculations to determine the particle and surface melting temperatures. The microstructure characterization and mechanical properties of brazed samples can display if a surface melt induced diffusion can significantly improve the brazing properties without the complete melting. Brazing performance will be tested using brazing temperatures between the surface melting temperature and the particle melting temperature. Additionally, Energy Dispersive X-ray Spectroscopy (EDS) will be used to determine the elemental distribution in the nanobrazed joints and the concentration profile will be used to perform diffusion analysis, particularly Sauer-Friese analysis. These investigations can thus validate or falsify the first hypothesis. For the second point, tensile strength testing and digital image correlation (DIC) will be utilized to determine the strength and stress/strain distribution in the joint. SEM-electron backscattered diffraction (EBSD) analysis will be used to determine the grain size of the brazed joints and X-ray diffraction (XRD) will determine the subgrain entity (i.e. crystallite) size via the Scherrer formula (Eq. 1.28). The strength and (sub)grain measurements will be examined to see if there is a relationship.

$$\tau = 0.9\frac{\lambda}{\beta cos\theta} \tag{1.28}$$

τ is the mean grain size, λ is the x-ray wavelength, β is the full-width half maximum of an x-ray diffraction peaj, and θ is the Bragg angle. These investigations can validate if the strengthening mechanism is attributable to grain boundary strengthening. Ductility and brittleness will be qualitatively assessed by analysis of the fracture features.

This dissertation will be organized as follows. In Chapter 2, I will investigate copper-silver and silver nanomaterials, the effect of particle shape on mechanical, wetting and diffusion performance, and evaluation against a comparable bulk BFM on IN718. Chapter 2 will also address the importance of subgrain boundary strengthening in the differences between nanobrazing and traditional brazing bonding performance. In Chapter 3, HEA bulk materials and nanoparticles will be used as BFMs for IN718 and the melting and solidification behavior and differences in joining behavior of multielement nanobrazing materials will be eludicated. In Chapter 4, Ni/Al reactive multilayer films will be used to join Ti-6Al-4V and the effects of ultrashort brazing times on the diffusion behavior and mechanical strength of brazed joints. In Chapter 5, nickel NPs will be used to join IN718, the (sub)grain boundary strengthening effects will be discussed and the importance of temperature and heating rate on the diffusion and mechanical robustness will be elucidated. In Chapter 6, the diffusion and wetting behavior of Ni NPs and NWs will be thoroughly evaluated. Lastly, conclusions and outlook will be discussed.

Chapter 2

Laser Brazing of Inconel 718 using Cu-Ag and Ag Nanomaterials

Disclosure

This chapter is based on two publications. The first publication was originally published by Denzel Bridges, Chaoli Ma, Zane Palmer, Shutong Wang, Zhili Feng and Anming Hu in 2017:

[144] D. Bridges, C. Ma, Z. Palmer, S. Wang, Z. Feng, A. Hu. Laser brazing of Inconel 718 using Ag and Cu-Ag nanopastes as BFMs, Journal of Materials Processing Technology 249 (2017) 313-324.

Denzels contributions in the article: synthesized nanomaterials, conducted brazing experiments, analyzed the experimental data, wrote and revised the article.

Co-authors contributions are listed as follows: Chaoli Ma helped design the brazing procedure and assisted in data analysis. Zane Palmer helped collect hardness and Energy

Dispersive X-ray Spectroscopy (EDS) data. Shutong Wang designed the laser system used for brazing. Dr. Zhili Feng was consulted on the research direction. Dr. Anming Hu was the principal investigator (PI) on the research, assisted in data analysis and experiment design and revised the article.

The second publication was originally published by Denzel Bridges, Chaoli Ma, Suhong Wang, Songbai Xue, Zhili Feng and Anming Hu in 2017:

[195] D. Bridges, C. Ma, S. Zhang, S. Xue, Z. Feng, A. Hu. Diffusion and wetting behaviors of Ag NP and Ag nanowire pastes for laser brazing of Inconel 718, Welding in the World 62 (2017) 169-176.

Denzels contributions in the article: synthesized nanomaterials, conducted wetting and diffusion experiments, analyzed the experimental data, wrote and revised the article.

Co-authors contributions are listed as follows: Chaoli Ma assisted in data analysis. Suhong Wang helped revise the article. Dr. Songbai Xue and Dr. Zhili Feng were consulted on the research direction and revised the article. Dr. Anming Hu was the principal investigator (PI) on the research, assisted in data analysis and revised the article.

2.1 Motivation and Background

As mentioned in Chapter 1, Inconel 718 (IN718) is a precipitation-hardened austenitic nickel superalloy with excellent mechanical properties, structural stability and corrosion resistance at elevated temperatures. IN718 is strengthened by the $\gamma\prime$ and $\gamma\prime\prime$ phases. IN718 has several weldability issues due to Nb segregation, interdendritic liquid film formation, and formation of other low melting phases such as δ phase during welding-related melting and solidification. Ye et al. demonstrated these qualities in their study of hot cracking of IN718 welds [32]. Pouranvari et al. investigated diffusion brazing using a commercial BNi-2 (Ni7Cr4.5Si3.2B3Fe) brazing alloy to provide an alternative method of fabrication and repair of IN718 (571-725 MPa) [196]. By laser brazing, BNi-2 has a bonding strength of 200-500 MPa [77]. However, BNi-2 contains two melting point depressants (boron and silicon) which form brittle and/or low melting boride and silicide phases after brazing like those seen in Figure 2.1. These brittle phases can cause the concentration of internal stresses and result in cracking and mechanical failure. In contrast, BAg and BCu are suitable boron-free and silicon-free choices for brazing IN718 [76, 88, 197, 198].

Copper and silver based nanomaterials are popular nanomaterials for nanosoldering of printable and power electronics due to excellent mechanical, thermal, and electrical properties. the general structure of a power semiconductor module is shown in Figure 2.2. Power semiconductor modules have a high operating temperature (>200 °C), so the die attach and substrate attach materials must have a similar operating temperature which is not achievable for most traditional Pb-based soldering alloys. The die attach and substrate attach materials must also have a low processing temperature in order to not damage the

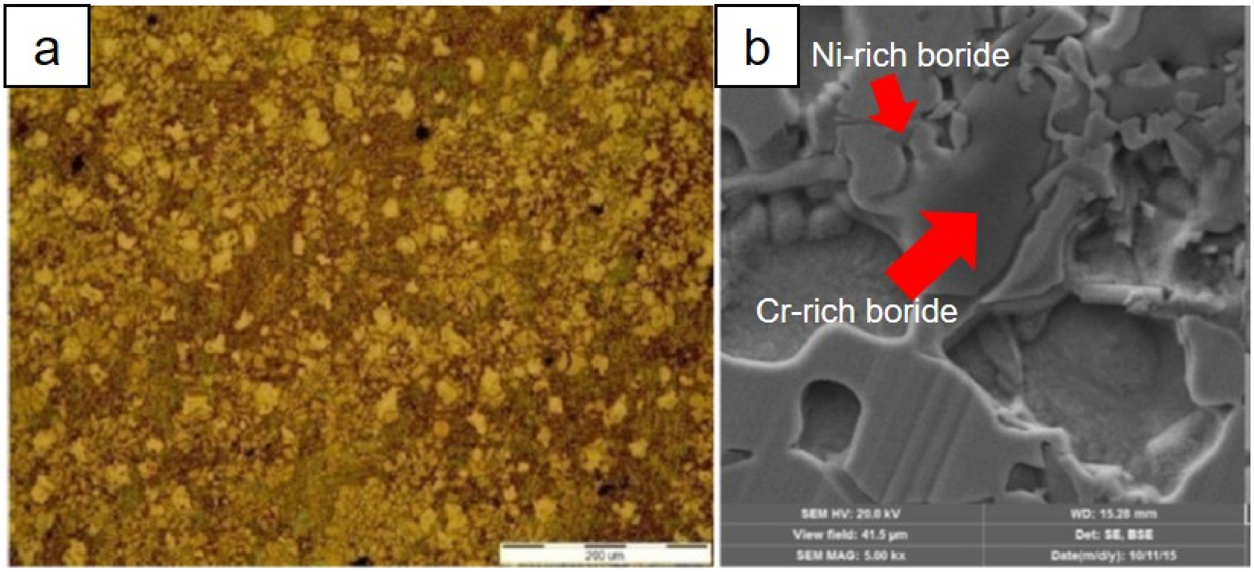

Figure 2.1: Microstructure of the BNi-2 filler metal (a) General optical microscope and (b) SE, BSE image (SEM), and EDS analysis [77]

temperature-sensitive semiconductor elements. The bonding using copper and silver-based nanomaterials can process at a low processing temperature and while operating at high operating temperatures after bonding. Fu et al. used silver nanopastes as a die attach material for large area (>100 mm^2) high temperature power electronics and demonstrated good bonding strength (50 MPa), good thermal conductivity (269 W/m-K), and thermal stability [174]. Good bonding strength for power electronics packaging must exceed 20 MPa in shear testing. Despite its good chemical stability and mechanical properties, the price of silver greatly cripples its widespread application in many industries. Copper (Young's modulus = 128 GPa) has higher mechanical strength and lower cost than silver (Young's modulus = 69 GPa) . Copper NPs are a nearly 10% (100× cheaper for the bulk material) cheaper alternative to silver for printable electronics and power electronics with comparable electrical properties [199, 200]. Copper NPs were combined with silver NPs by Liu et al. in order to lower the cost without sacrificing the benefits of silver for an alternative die attach material (Figure 2.3) [171]. However, at elevated temperatures, copper can easily be oxidized at the nanoscale (<100 °C). Organic capping layers or metallic coatings are often employed to stabilize copper nanomaterials in air. Metal coatings have the advantage over organic capping layers for high temperature applications because when organic capping layers decompose at high temperatures, decomposition byproducts and/or microvoids contaminate the joint and harm the mechanical, thermal, and electrical properties. Metal coatings do not produce any detrimental organic decomposition byproducts. Tsai et al. demonstrated this by showing that copper-silver core-shell NPs had better oxidation resistance compared to bare copper NPs because the noble metal oxidation resistance of the Ag shell protects the copper core [202]. Chen et al. used nickel to coat copper nanowires to prevent oxidation instead of an organic capping layer to fabricate transparent, flexible heaters [203]. Lee et al. demonstrated the potential of silver as a capping layer for copper NPs by using Cu-Ag core-shell NPs for printing applications, in their study Ag played a functional role in the

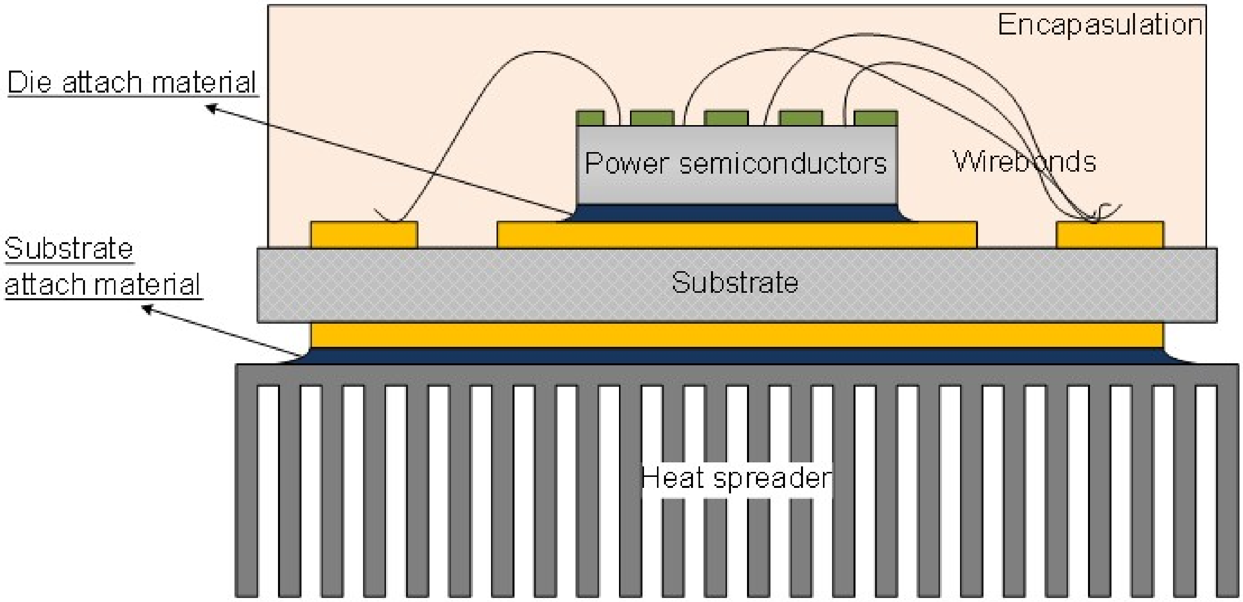

Figure 2.2: General packaging structure of a power semiconductor module [201]

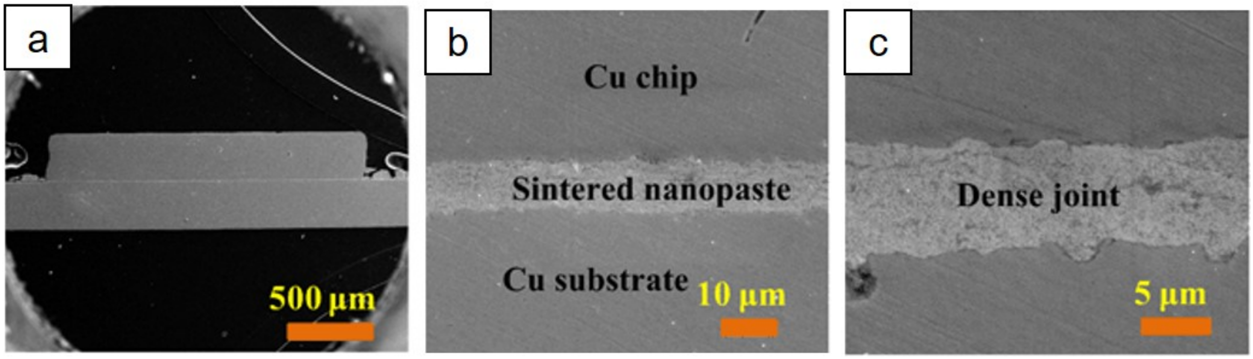

Figure 2.3: This figure is modified from Liu et al. (2017). SEM cross-section of Cu-Ag joined Cu (a) 120× (b) 4000× and (c)10000× magnification [171]

printed devices, whereas most organic capping layers do not [156]. However, brazing with Ag NPs, Cu NPs and Cu-Ag core-shell NPs as the BFM has not systematically studied yet.

The research in this chapter was used to investigate the mechanical viability of Cu-Ag nanobrazing materials compared to BAg-8, a commercial brazing material, as a BFM for IN718. As previously stated, Cu-Ag-based brazing materials are an MPD-free alternative to higher temperature brazing materials such as the BNi-2 series especially if there is no requirement for operating at the maximum temperature of IN718 (760 °C). The effect of Ag nanomaterial shape on strength, diffusion, and wetting will be discussed. By utilizing laser brazing in this investigation, we mitigate sintering prior to melting of the nanomaterials due to the high heating speed. Additionally, laser brazing allows us to precisely heat a select area of the joint without inadvertently melting the IN718 by controlling the laser power.

2.2 Experiments and Methods

2.2.1 Materials

Silver nitrate, L-ascorbic acid, and ethylene glycol (EG) were purchased from Sigma Aldrich. Polyvinylpyrrolidone (K-30 PVP; M.W. = 30,000) and sodium chloride were purchased from Alfa Aesar. Cupric nitrate was purchased from Fisher Scientific. K-85-90 PVP (M.W. = 1,300,000) was purchased from Acros Organics. 601 and 601B silver brazing flux were purchased from Superior Flux and Mfg. Co. All chemicals were used without further purification. IN718 was purchased from Rolled Alloys, Inc. BAg-8 is was purchased from McMaster-Carr (Table 2.1).

2.2.2 Preparation of Ag NP paste

Silver NPs were synthesized by a polyol wet chemical method [192]. 10 mL of EG-based $AgNO_3$ solution (0.9 M) and 190 mL of EG-based K-30 PVP (0.284 M) solution were prepared. All solutions were combined under magnetic stirring and heated to 150 °C for 15 min. After cooling naturally, Ag NPs were washed and concentrated using deionized (DI) water and centrifugation at 8000 rpm for 30 min two times and 12 min for the final centrifugation to remove EG and excess PVP. The concentration of the aqueous paste is approximately 50-60 % metal content.

.

Table 2.1: Composition of the alloys and fluxes used in this study

Material	**Elemental Composition (at%)**						
IN718	**Ni**	**Fe**	**Cr**	**Cu**	**Al**	**Si**	**C**
	53.10	18.40	18.30	0.05	0.49	0.07	0.05
	Mn	**B**	**Nb**	**Ti**	**S**	**Mo**	
	0.24	0.004	4.95	1.07	<0.002	3.06	
BAg-8	**Cu**	**Ag**					
	28	72					
601/601B Flux	**KBF_4**	**$K2B_4O_7$**	**H_3BO_3**	**$H_2B_2FO_2$**			
	20-40	15-25	30-40	7-15			

2.2.3 Preparation of Ag Nanowire Paste

Ag nanowires (NWs) were prepared by a similar polyol method as the Ag NPs. 10 mL of EG-based $AgNO_3$ solution (0.9 M), 6 mL of EG-based NaCl solution, and 184 mL of EG-based K-30 PVP (0.284 M) solution were prepared. All solutions were combined under magnetic stirring and heated to 180 °C for 15 min. After cooling naturally, Ag nanowires (NWs) were washed and concentrated using deionized (DI) water and centrifugation at 5000 rpm for 30 min, then again for 12 min for the final centrifugation to remove EG and excess PVP. This synthesis method has been modified based on the synthesis method used by [91]. he concentration of the aqueous paste is approximately 50-60 % metal content.

2.2.4 Preparation of Cu-Ag core-shell nanowire paste

Cu-Ag core-shell nanowires (CSNWs)) were synthesized by first making the copper core NWs, then coating with silver by a galvanic displacement reaction. The copper cores were fabricated by a facile hydrothermal method developed by Zhang et al. [204]. 0.181 g of $Cu(NO_3)_2$ and 0.15 g of L-ascorbic acid were dissolved in 30 mL ultrapure DI water (resistance = 18 MΩ). After 5 minutes, 0.38 g of K-85-90 PVP was added and magnetically stirred until fully dissolved. In this reaction, ascorbic acid co-acts as a reducing agent and capping layer and PVP as a structure-directing agent. The solution was then autoclaved in a 50 mL Teflon-lined stainless steel autoclave at 120 °C for 4 hours. After cooling, the Cu NWs were collected from the autoclave and centrifuged at 2000 rpm for 5 min to remove excess reducing agent [205]. After centrifuging, the NWs were redispersed in fresh ultrapure DI water. The silver coating solution which consists of 2.5 mL ultrapure DI water, 32 mg $AgNO_3$, and 75 mg K-85-90 PVP is based on the coating solution used by Zhao et al. [206].

Table 2.2: Description of the nanopastes used in this laser brazing study

Paste	**Cu(wt%)**	**Ag (wt%)**	**Description**
Ag-1	0	100	Silver NPs paste
Ag-2	0	100	Silver nanowire paste
Cu-1	80	20	Cu-Ag CSNWs paste
Cu-2	28	72	Cu-Ag CSNWs and Ag NPs composite paste
Cu-3	28	72	Cu-Ag CSNWs and Ag NWs composite paste

The silver coating solution was slowly added to the Cu NWs at room temperature under moderate magnetic stirring overnight. The nominal Cu:Ag atomic ratio is 4:1. The resulting solution was centrifuged and concentrated three times at 2000 rpm for 5 min. The nanopastes used for laser brazing are summarized in Table 2.2 where the metal content is 50-60%.

2.2.5 Laser Brazing

For nanopaste (NPA) samples, IN718 pieces (3 mm × 0.32 mm × 30 mm) were ultrasonically cleaned in acetone for 2 min then plasma cleaned using a PDC-001 Expanded Plasma Cleaner (Harrick Plasma) at low power for 2 min. Each NPA was applied to the IN718 and most of the water was evaporated by baking on a hot plate at 75 °C. Silver brazing flux was applied on top of the nanopaste. 601 silver brazing flux was used for laser power <250 W and 601B flux was used for laser power $\geq$ 250 W. The two IN718 plates were placed 9 cm from a 400 W continuous wave high energy diode laser ($\lambda = 806$ nm) on a 1 mm thick copper plate with an overlap of 34 mm as shown in Figure 2.4.

The laser intensity profile at the focal point is similar to a top-hat intensity profile with a size of 1 mm × 22 mm. The laser irradiated the top surface of the IN718 plate. The laser power was ramped to the target power in 5 seconds then held at the target power for 10 seconds/sample as seen in Figure 2.4b. No pressure was applied to the sample. A lap shear test was performed using a tensile testing machine on the brazed samples.

2.2.6 Wettability

The spreading capability of the Ag-1 and Ag-2 paste was determined by heating the paste and flux directly on a clean IN718 piece with a laser until the temperature reaches either 550 °C or 800 °C (5-10 seconds). 150 W and 200 W were the laser powers used to achieve 550 °C and 800 °C, respectively. The target laser power was reached in 5 seconds and maintained for 10 seconds. Direct irradiation of the Ag-2 paste at 800 °C resulted in the Ag NWs forming conglomerates, so this experiment is not included. This is well known that excessive laser fluence damage Ag NWs, causing the vaporization of Ag and formation of conglomerates [207].

2.2.7 Mechanical Testing and Characterization

For bonding strength evaluation, tensile tests were completed using a ZHIQUP Precision Instruments, 1500D force gauge with a constant displacement rate of 1 mm/min (5 acquisitions/second). The fracture area was measured via ImageJ software on the optical images of as-fracture samples Scanning electron microscopy (SEM) images were collected on a Zeiss Auriga Scanning Electron Microscope. X-ray diffraction measurements were conducted

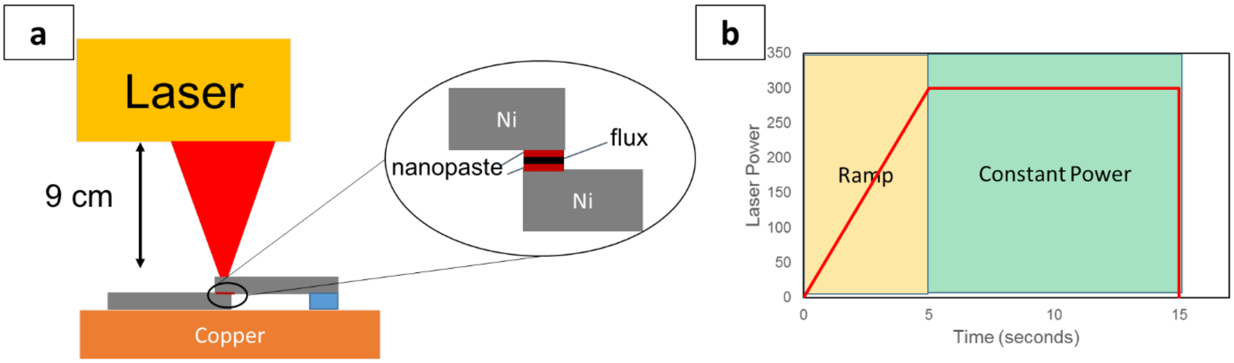

Figure 2.4: (a) Schematic of the laser brazing set up and (b) laser power curve [144]

on a Panalytical Empyrean X-ray Diffractometer, Energy Dispersive X-ray Spectroscopy (EDS) measurements were performed on samples brazed with 300 W laser power using a Phenom ProX energy-dispersive spectrometer. Vickers microhardness of 300 W brazed samples was measured using a Buehler MMT3 Microhardness Tester to make a diamond shaped indentation with 5 gram-force. The hardness was calculated using Equation 2.1 according to ASTM E384 - 10e2 standards.

$$Hardness = \frac{0.1891F}{d^2} \tag{2.1}$$

The hardness of IN718 prior to brazing was measured from a cross-sectional piece of IN718. For cross-sectional analysis, samples were embedded in an epoxy resin and the final polish step was conducted using colloidal silica (0.04 μm).

2.3 Results and Discussion

2.3.1 Characterization of Nanopaste

Figures 2.5a and 2.5b show the bare Cu NWs and the Cu-Ag CSNWs respectively. Cu NWs have a smooth surface with a rectangular cross-section and a 400-1000 nm diameter and 5-40 μm long. After the addition of $AgNO_3$, Ag nanocrystals nucleated and grew on the surface of the Cu NW giving it a rough surface morphology. The CSNWs became partially hollow due to the Kirkendall effect that occurs during the Ag galvanic displacement reaction [208, 209]. Essentially, the diffusion of Cu into the Ag shell is faster than diffusion of Ag shell atoms into the Cu core, resulting in the hollowing of the NWs. The CSNWs with a wall thickness of 40-80 nm and a pentagonal cross-section as seen in Figure 2.5c. The Ag

NWs have a smooth surface texture with a diameter of 40-50 nm and a length of 5-30 μm (Figure 2.5d). The Ag NPs are spherical and 55-75 nm in diameter (Figure 2.5e). As seen in Figure 2.5f, the UV-vis spectrum of Cu NWs show that the surface plasmon resonance (SPR) peak at 582 nm with high absorbance across the spectrum of 200 nm to 960 nm; Wang and Ruan report a similar spectrum [210]. After Ag coating, the SPR peak red shifts into the near-infrared/infrared range and the absorbance in the visible light range is greatly diminished. The Cu-Ag CSNWs reported in Wei et al.'s study exhibit similar behavior [211]. As expected, Ag NPs absorb light in the red and near-infrared spectrum (550-1000 nm) is absorbed very weakly like in the report by Podagatlapalli et al. [121]. Like Cu NWs, Ag NWs have a high absorbance across the spectrum except its SPR peak is located at 378 nm (unlike Ag NPs) and is consistent with the UV-vis spectrum in Tang and Tsuji [212].

XRD patterns for Cu NWs (Figure 2.6a) only show XRD peaks characteristic to copper and no copper oxides were identified. After the Ag coating, Cu peaks do not

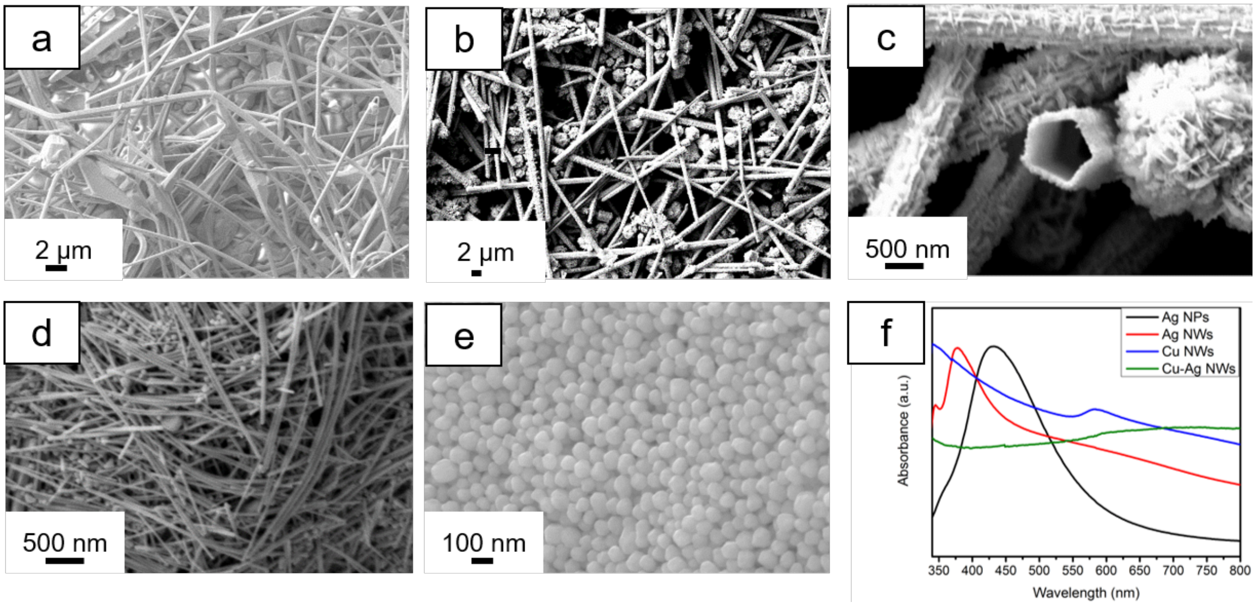

Figure 2.5: SEM images of a) Cu NWs, b) Cu-Ag CSNWs, c) magnified view of Cu-Ag CSNWs, d) Ag NWs, and e) Ag NPs; f) the UV-vis spectra of each nanomaterial [144].

disappear, but the peak intensity ratio for the Cu (111) and Cu (200) planes decrease from 3.44:1 to 2.85:1 (Figure 2.6b). The ratio between the Ag (111) and Ag (200) peak intensity is 7.02:1. It is worth noting that the CSNW XRD pattern shows distinct Cu peaks and distinct Ag peaks, and no detection of copper oxides. During the centrifugation step to remove the excess reducing agent, some of the organic capping layer (PVP) is also removed by washing. If the silver coating is not sufficient, the Cu NWs will easily develop an oxide layer on the surface in an aqueous environment and ambient atmosphere [154]. This indicates that CSNWs adopt a core-shell structure. The Ag NWs (Figure 2.6c) and Ag NPs (Figure 2.6d) have similar peak positions but the relative intensities for the (220) and (311) peaks are much stronger for Ag NPs than Ag NWs.

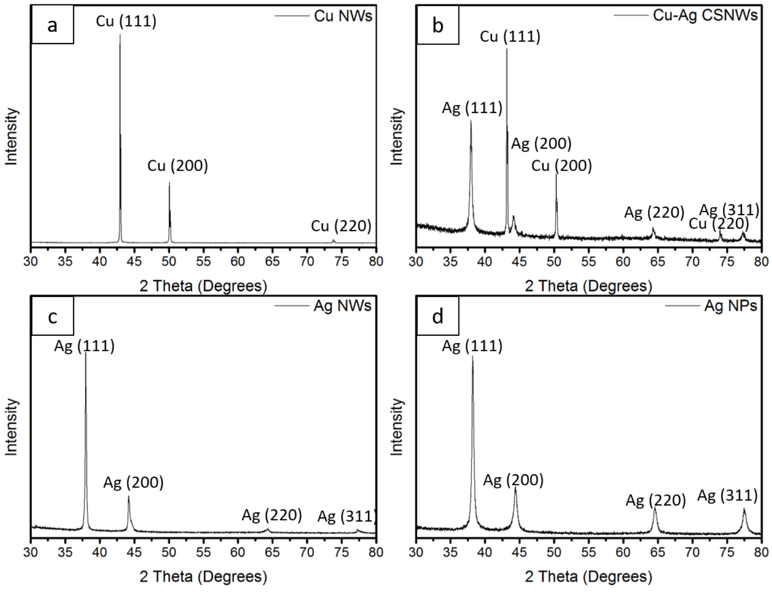

Figure 2.6: XRD pattern of a) Cu NWs, b) Cu-Ag CSNWs, c) Ag NWs and d) Ag NPs an inlet of each nanomaterial solution is included [144]

2.3.2 Brazing Simulation and Modeling

COMSOL Multiphysics Suite was used to estimate the temperature and temperature distribution of the laser brazing samples. For simplicity, the nanopaste material is treated as a dry powder with a thermal conductivity similar to a non-porous solid. The laser intensity is considered constant throughout the laser heated region due to the top-hat profile. At the end of the brazing process at 300 W, the temperature in the laser heated region is nearly 1000 °C as seen in Figure 2.7. A K-type thermocouple was used to measure the temperature of the top plate and validate the simulation results. The average temperature in the BFM increases to approximately 775 °C (the Cu-Ag eutectic temperature is 779 ∘C) during the brazing as seen in Figure 2.8b [75]. The average heating rate is approximately 50 °C/second. There was no significant temperature difference between the pure Ag paste and the Cu-Ag paste. According to Figure 2.8c, there is a temperature difference of 300 °C between the top plate and the bottom plate. The average surface temperature in the overlap area is 862 ± 56 °C (Figure 2.8d). Due to the low thickness of the BFM, the temperature is much more uniform. If the nanopaste layer was thicker, the nanopaste would be heated less uniformly.

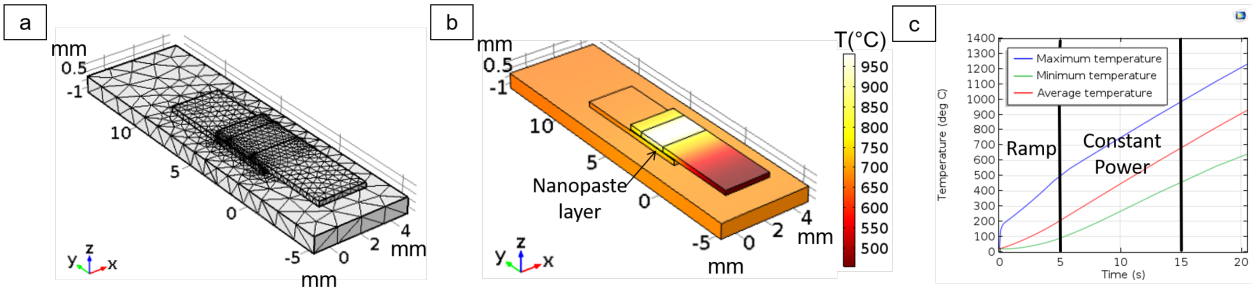

Figure 2.7: (a) COMSOL model of the lap joint used in this study with a finite element mesh (b) Thermal distribution after a 5 second ramp and 10 seconds of heating at 300 W (c) Global maximum, minimum and average temperatures as a function of time [144]

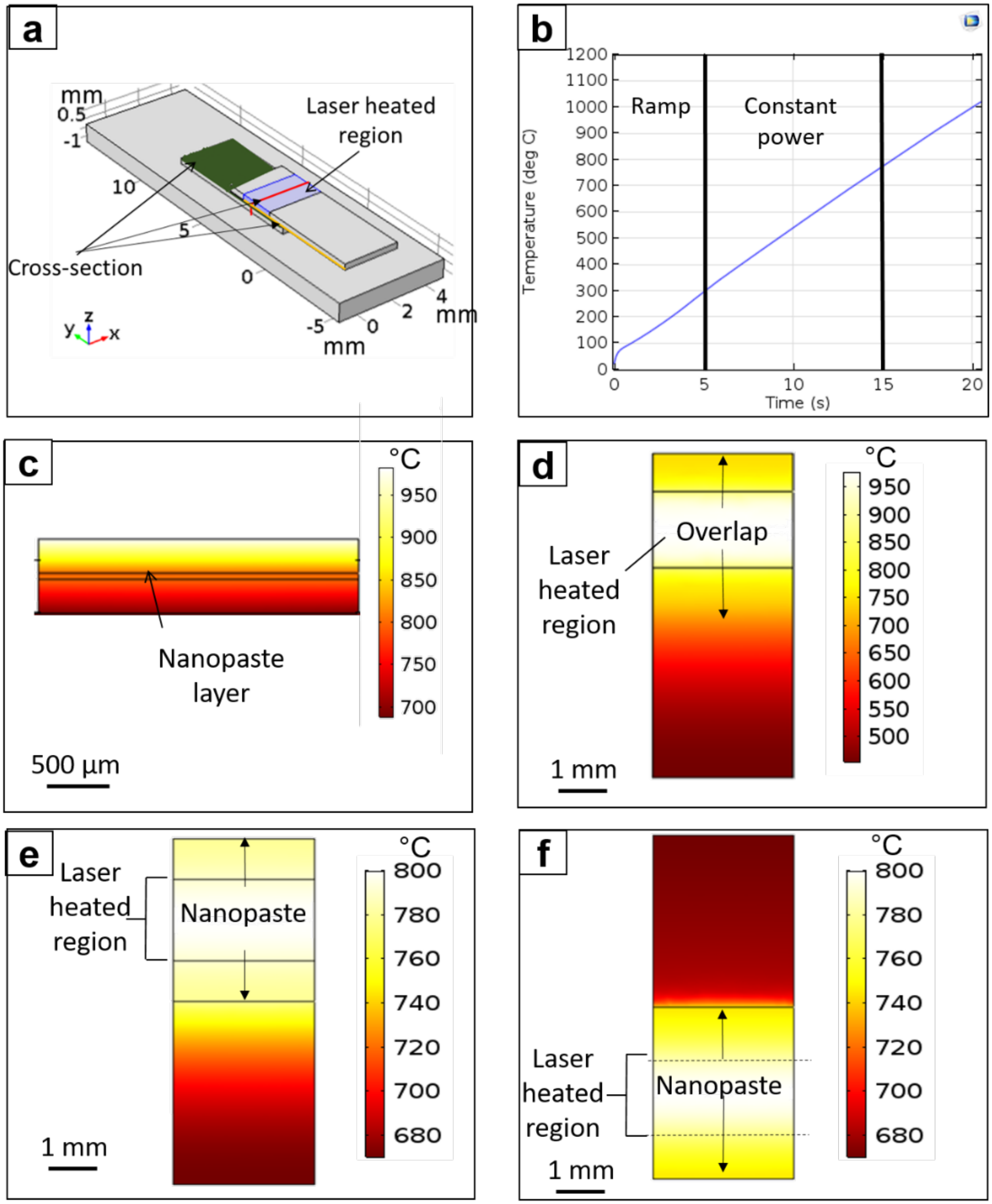

Figure 2.8: (a) Locations of the cross-sectional thermal distributions taken for parts d,e, and f, (b) average temperature of the brazing layer as a function of time. Thermal distribution of (c) xz-plane cross-section in the middle of the laser brasing region (d) the surface top plate, (e) interface between the top plate and the brazing layer, (f) interface between the bottom plate and the brazing layer [144]

According to Wang et al., the atoms at the Cu core of the nanostructure begin to melt at around 800-950 °C [104]. Once the filler material is melted, the atoms easily diffuse into the BM or participate in joining of nearby particles.

2.3.3 Ag Diffusion Behavior

The line scan in Figure 2.9b reveals a uniform concentration of Ni, Fe, and Cr in the BFM with the exception of a spike in Ni concentration (most likely a segregation of Ni in the joint) in the Ag filler metal. The line scan in Figure 2.9b reveal uniform dissolution of the BM (particularly Ni) into the Ag BFM and dissolution of Ag into the BM. The line scan reveals that there is a 3 μm diffusion layer between the BM and the BFM. The light spots in Figure 2.9c reveal the existence of secondary phases near the interface between the BM and BFM. The presence of the diffusion layer and dissolution of the BM into the braze indicates that metallurgical bonding has occurred at the interface.

Closer inspection reveals that the nanomaterial shape influences the diffusion behavior of the Ag NMs. The EDS line scans in Figure 2.10 show the elemental distribution across the joint interface. Figure 2.10b, 2.10e, 2.10h, and 2.10k present the EDS line scan as indicated by the red arrow in Fig 2.10a, 2.10d, 2.10g, and 2.10j, respectively. The space between the vertical dashed lines designates the location of the diffusion zone in the EDS line scan. The diffusion zone thickness is taken to be the maximum diffusion length out of all the elements measured. For Ag NPs, the diffusion zone thickness is 2.5 μm at 250 W and 2.6 μm at 300 W. Ag NWs exhibit a thicker diffusion zone with 3 μm at 250 W and 3.5 μm at 300 W. The box near the middle of the plot highlights the portion of the graph that is displayed in Fig 2.10c, 2.10f, 2.10i, and 2.10l. Interestingly, there are one or more

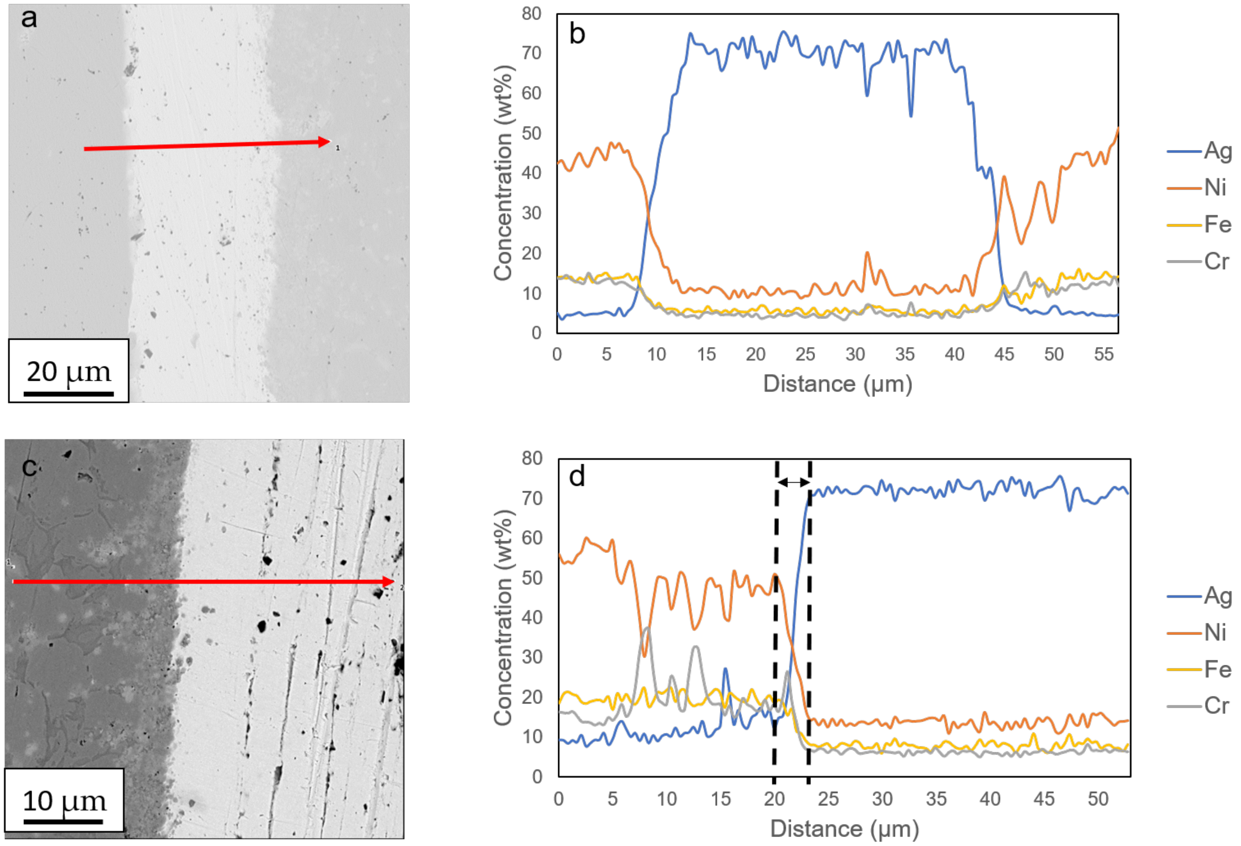

Figure 2.9: EDS line scans of a brazing joint using Ag NWs (a-b) are for a line scan of the entire joint; (c-d) are for the interfacial area. The solid red arrow indicates the location of the line scan. The dotted lines in (d) are boundaries for the diffusion layer [144]

concentration humps for some of the elements present in IN718. The black circles point out these concentration humps. The black dashed lines in Figure 2.10h and 2.10k display a visibly wider diffusion zone for Ag NW joints than Ag NP joints (Figure 2.10b and 2.10e). Additionally, the concentration humps are more noticeable when a higher laser power is used and/or when Ag NWs are the filler metal. At times, the concentration humps include other BM elements such as Cr (Figure 2.10i) and Fe (Figure 2.10l). The Ag NWs joint brazed at 300 W also has a significant increase in Nb and Mo concentrations.The concentration "humps" are most likely attributable to the difference in the bulk diffusion coefficient between Ag into Ni (4.21 $\times 10^{-12}$ cm^2/sec) [213] and Ni, Fe, and Cr into Ag (9.83 $\times 10^{-13}$ cm^2/sec, 7.08

$\times 10^{-13}$ cm^2/sec, and 3.07 $\times 10^{-10}$ cm^2/sec, respectively) [214, 215]. The diffusion coefficient value is even higher than Wazzan et al. reported because it is assumed in that publication that the diffusion is in pure, single crystal nickel, not polycrystalline nickel superalloy [213]. Most of the diffusion presumedly occurs during the constant laser power part. Additionally, the enhanced diffusion activity of the Ag NPs or NWs would be more than double the bulk value according to Equations 1.25 and 1.26.

Ag NWs produces greater Ag diffusion length than Ag NPs (Figure 2.11a and 2.11b). The more intriguing difference is between the Ag diffusion distance and the overall diffusion zone thickness. For Ag NPs, the Ag diffusion length is approximately 2.3 μm at 250 W and 1.8 μm at 300 W. For Ag NWs, the Ag diffusion length is approximately 3 μm and 2.5 μm using 250 W and 300 W, respectively. Clearly, there is a disparity in Ag diffusion length and overall diffusion zone thickness in all samples except Ag NWs brazed at 250 W as seen in Table 2.3. NWs and other non-spherical nanomaterials have been cited several times as having several types of crystallographic defects such as stacking faults, grain boundaries, and twin boundaries [216, 217]. Surface defects, depending on the type, are potential sites for initiating diffusion. Due to a higher surface-area-to-volume (SAV) ratio, Ag NWs (0.10 nm^{-1}) have increased surface diffusion activity in the early brazing stages compared to Ag NPs (0.08 nm^{-1}). Based on the Lindemann criterion, Ag NWs have more surface vibrational energy than Ag NPs which makes the surface less stable. A less stable NM surface is more prone to full melting and surface melting (since NM melting begins at the surface). Therefore, the Ag NWs have a lower melting temperature than Ag NPs. The higher vibrational energy of the Ag NW adatoms would facilitate diffusion into the IN718 [218]. Additionally, a higher percentage of atoms occupy the surface of the NWs that can

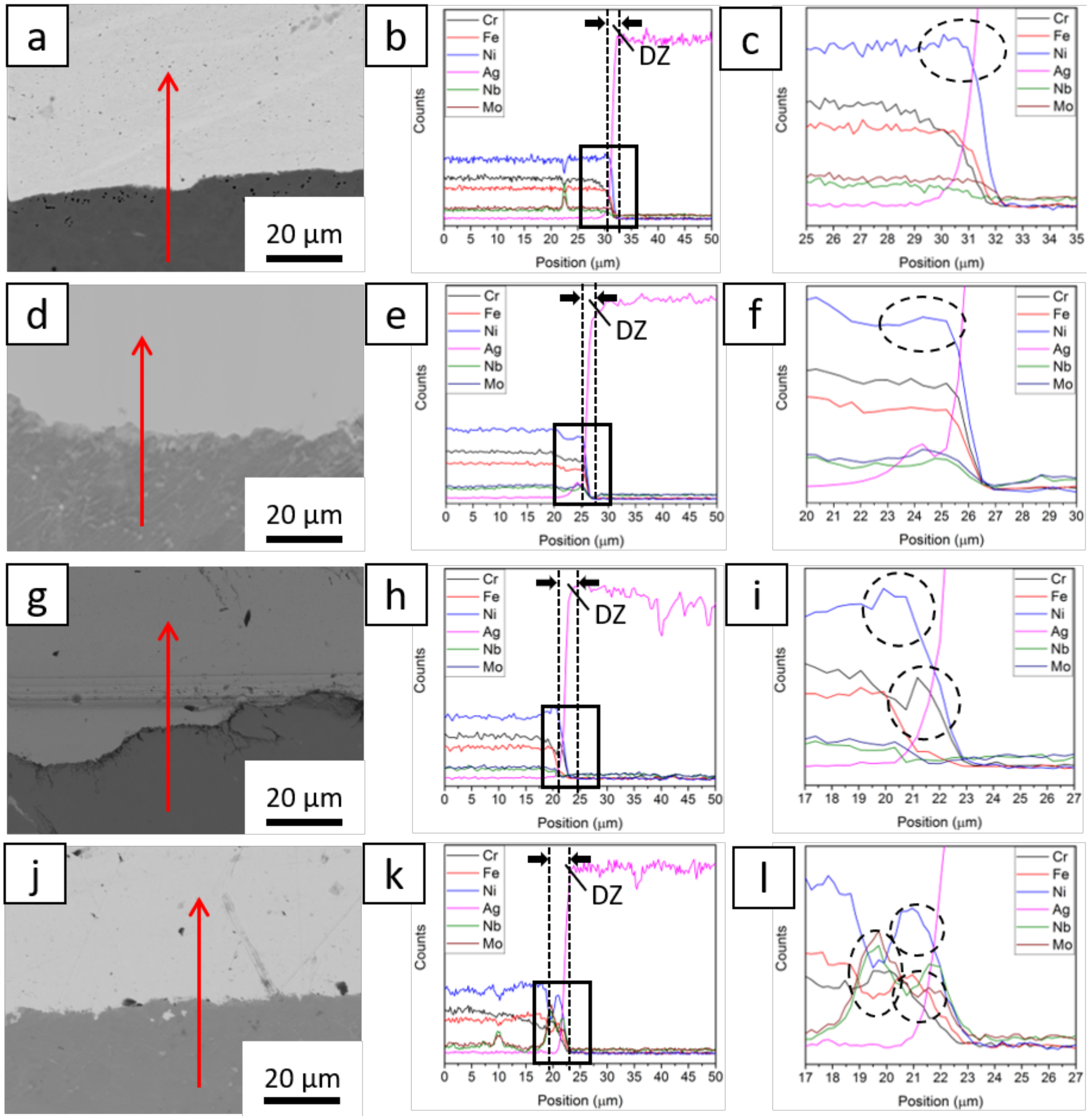

Figure 2.10: EDS line scan for (a-c) Ag NPs at 250 W, (d-f) Ag NPs at 300 W, (g-i) Ag NWs at 250 W, and (j-l) Ag NWs at 300 W. The red line in (a), (d), (g), and (j) indicates the location of the line scan. The space between the vertical dashed line in (b), (e), (h), and (k) shows the location of the diffusion zone (DZ) and the black box shows the section of the graph shown in (c), (f), (i), and (l) respectively. The black circles show the concentration humps of different IN718 elements [195]

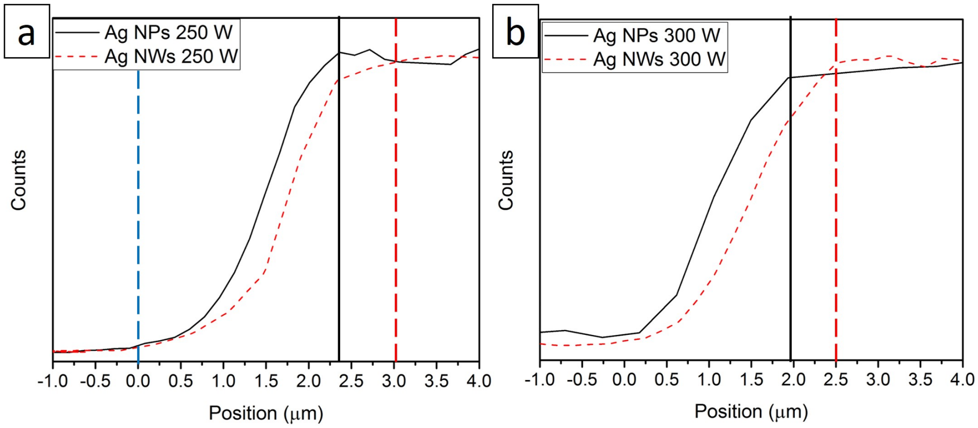

Figure 2.11: The normalized silver EDS line scan for the samples in Figure 2.10 at (a) 250 W and (b) 300 W. The black solid vertical line and red dotted vertical line mark the end of the Ag diffusion range for Ag NPs and Ag NWs, respectively. The blue dotted line marks the beginning measuring point. [195]

participate in diffusion which further facilitates the diffusion of Ag into the IN718 substrate or vice versa.

2.3.4 Wettability of Ag Nanoparticles and Ag Nanowires

The spreading behavior of Ag NPs provides some context to the diffusion behaviors of Ag NPs and Ag NWs. As seen in Figure 3a, the change in area is negative at 550 °C for both Ag NPs (Figures 2.12b and 2.12e) and Ag NWs (Figures 2.12d and 2.12g) and the areal change of Ag NPs at 800 °C reflects a substantial positive change in tjhe area (Figures 2.12c and 2.12f). The negative change in area is likely due to shrinkage in the nanopaste during heating. The shrinkage of the NP paste is naturally followed by accelerated wetting and spreading because of increasing temperature. Shrinkage in this context is the reduction of the area covered by the nanopaste after brazing. The shrinkage in nanopastes is caused by the fusing of adjacent NPs, evaporation of water and volatile compounds, and decomposition of the organic capping layer in the paste [104, 219]. The spreading at 800 °C is due to the

Table 2.3: Summary of the Ag diffusion length and overall diffusion zone thickness of joints using Ag NPs and Ag NWs

Laser Power	**250 W**	**300 W**
	Ag/DZ	Ag/DZ
Ag NPs	2.3/2.5	1.8/2.6
Ag NWs	3.0/3.0	2.5/3.5

wetting of the IN718 surface by molten silver. Ag NWs undergo 5% shrinkage at 550 °C which is remarkably lower than Ag NPs (10%). In between the shrinkage and wetting stages, the nanopaste undergoes full or near full densification of the NPs. The measured difference in shrinkage between Ag NPs and Ag NWs may be a result of a balance of shrinkage and wetting spreading, i.e., the Ag NWs undergo spreading after the densification process is completed due to a lower melting temperature. A lower melting temperature for Ag NWs, due to the shape effect, is supported by models constructed according to the Lindemann melting criterion [142, 220]. The Lindemann melting criterion is a theory that explains the melting mechanism of a material using the vibration of atoms in a crystal [221].

It should be noted that Ag does not typically wet a Ni-based surface based on the bulk Ag-Ni equilibrium phase diagram due to very limited solid solubility of Ag in Ni [216]. Bulk Ag is miscible with bulk Ni, Fe, Cr, Nb, or Mo only under these cases: (1) Ag is dissolved in solid Ni at up to 1 mol% Ag but Ag does not dissolve in solid Fe, Cr, Nb, and Mo in a significant amount (<<0.1 mol%); and (2) Ni, Cr, Fe, Nb, or Mo is dissolved in the silver-rich liquid (L) phase according to their respective phase diagrams [216]. Both cases in the bulk system are possible when the temperature is greater than the melting point of bulk silver (961.8 °C). However, this melting point is higher than the brazing temperature (500 °C-800 °C) of this study. If the melting temperature is lowered via the size effect, then it is

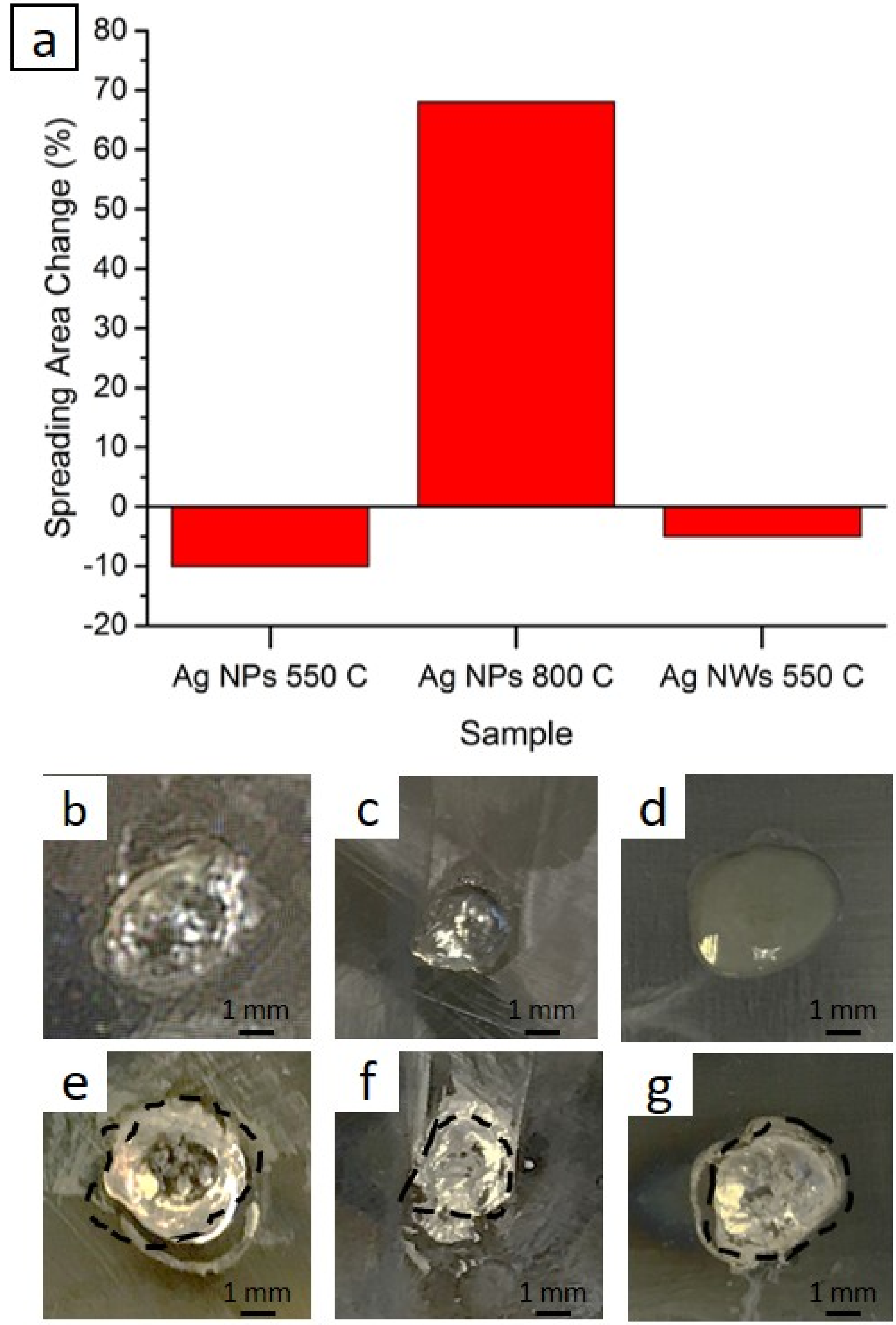

Figure 2.12: (a) Change in area of Ag NPs heated to a 550 and 800 °C and Ag NWs at 550 °C. The optical images were taken before and after laser irradiation heating for Ag NPs 550 °C (b and e), Ag NPs 800 °C (c and f), and Ag NWs 500 °C (d and g). The blue and red shaded areas show the area covered by the nanopaste before and after brazing, respectively [144]

possible for the second case at a lower temperature than the bulk case via transformation to the homogenous liquid phase (L) and/or L + liquid_2 (silver depleted liquid) phase. During brazing, the small amounts of Ni, Fe, Cr, Nb, or Mo can be solved into the molten silver, which most likely facilitates the wettability. The dissolved amount of Ni, Fe, Cr, Nb, and Mo in molten Ag increases as temperature increases, which enhances wettability at high temperature. When the temperature decreases below the liquidus line, some Ag can still diffuse into Ni which helps wettability. Ag is no longer soluble in Fe, Cr, Nb, and Mo below the liquidus line which means that these alloying elements will act as a diffusion barrier and wettability inhibitor during a cooling/solidification procedure. However, no phase diagram for the Ag-Ni, Ag-Fe, Ag-Cr, Ag-Nb, and Ag-Mo is available at the nanoscale, therefore, the current analysis is somewhat uncertain how much the nanoscale miscibility deviates from the bulk miscibility of these elements. Kinetic contributions cannot be ignored for determining the nanoscale miscibility of Ag in IN718.

2.3.5 Cu-Ag CSNW Diffusion Behavior

Figure 2.13 shows a brazing joint using the CSNWs. The EDS line scan for this joint shows that the dark colored regions are the extremely Cu-rich and are hence the α phase according to the Cu-Ag phase diagram (Figure 2.13d). These α regions contain on average 6 times more copper than silver. The light regions have a Cu:Ag ratio of 3:4. A higher resolution line scan (Figure 2.13e-f) shows that there is a smooth transition between the α phases and the Ag-rich β phases with a diffusion layer of approximately 1.6 m. The precipitation of α phases in a β matrix is not observed in the vacuum brazing experiments conducted by Ma et al. The phase separation is thermodynamically permissible due to the

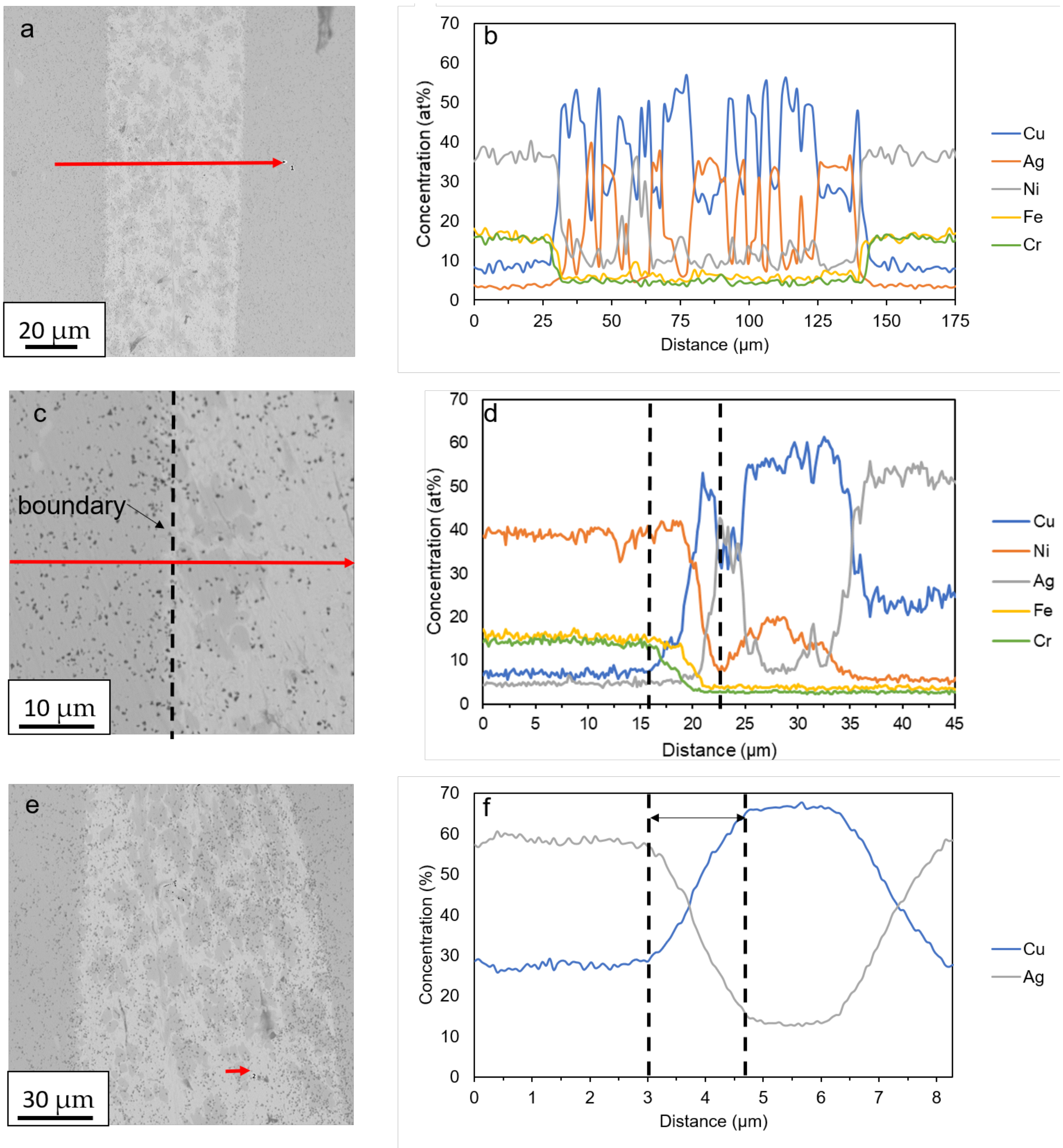

Figure 2.13: EDS line scans of a brazing joint using Cu-Ag CSNWs (a-b) are for a line scan of the entire joint; c-d are for the interfacial area. The solid red line is the location of the line scan. The black dotted line in (c) is the boundary between the IN718 and the brazed joint. The dotted lines in (d) and (f) indicate where the locations of the diffusion layers. (e-f): the local line scan performed on a Ag rich region adjacent to an α region as indicated by a short arrow bar in (e) [144]

miscibility gap in the Cu-Ag system. Additionally, the high heating/cooling speed of laser brazing technique inhibits homogenization of the brazed joint that is able to occur during vacuum brazing like in Ma et al.'s study [192]. Wang et al. displayed that at 727 °C the Ag shell will melt first before the Cu core melts (800-950 °C) and Cu-core remains intact until the Ag shell has completely melted. Once the entire NP has melted, the core-shell structure disappears, forming a homogenous liquid [104]. This is the widely understood behavior of pure and core-shell NM structures [106, 220]. Assuming the CSNWs fully melts and considering the nominal Cu:Ag ratio of the CSNWs is 4:1, the α grains form first as the BFM cools and the β matrix forms below the eutectic temperature. Even if the CSNWs did not fully melt, the Ag shell certainly melted even without the size-dependent melting point depression. The overall diffusion zone thickness for CSNWs is 5.5 μm which is more than any of the diffusion lengths listed in Table 2.4. The diffusion curve for each element reaches a steady state for Cu and Ni at different points which gives the diffusion zone a higher thickness. The Ag diffusion length is 2.0 μm which is similar to the diffusion lengths reported in Table 2.3 for both Ag NPs and Ag NWs. Table 2.3 also shows little correlation between Ag diffusion length and laser power.

XRD was performed on the Cu-Ag materials after brazing at 300 W (Figure 2.14).

Table 2.4: Summary of the diffusion lengths of major elements in CSNW-joined IN718 at 300 W

Element	**Diffusion Length (μm)**
Cu	5
Ni	3.5
Ag	2
Fe	2
Cr	3.5

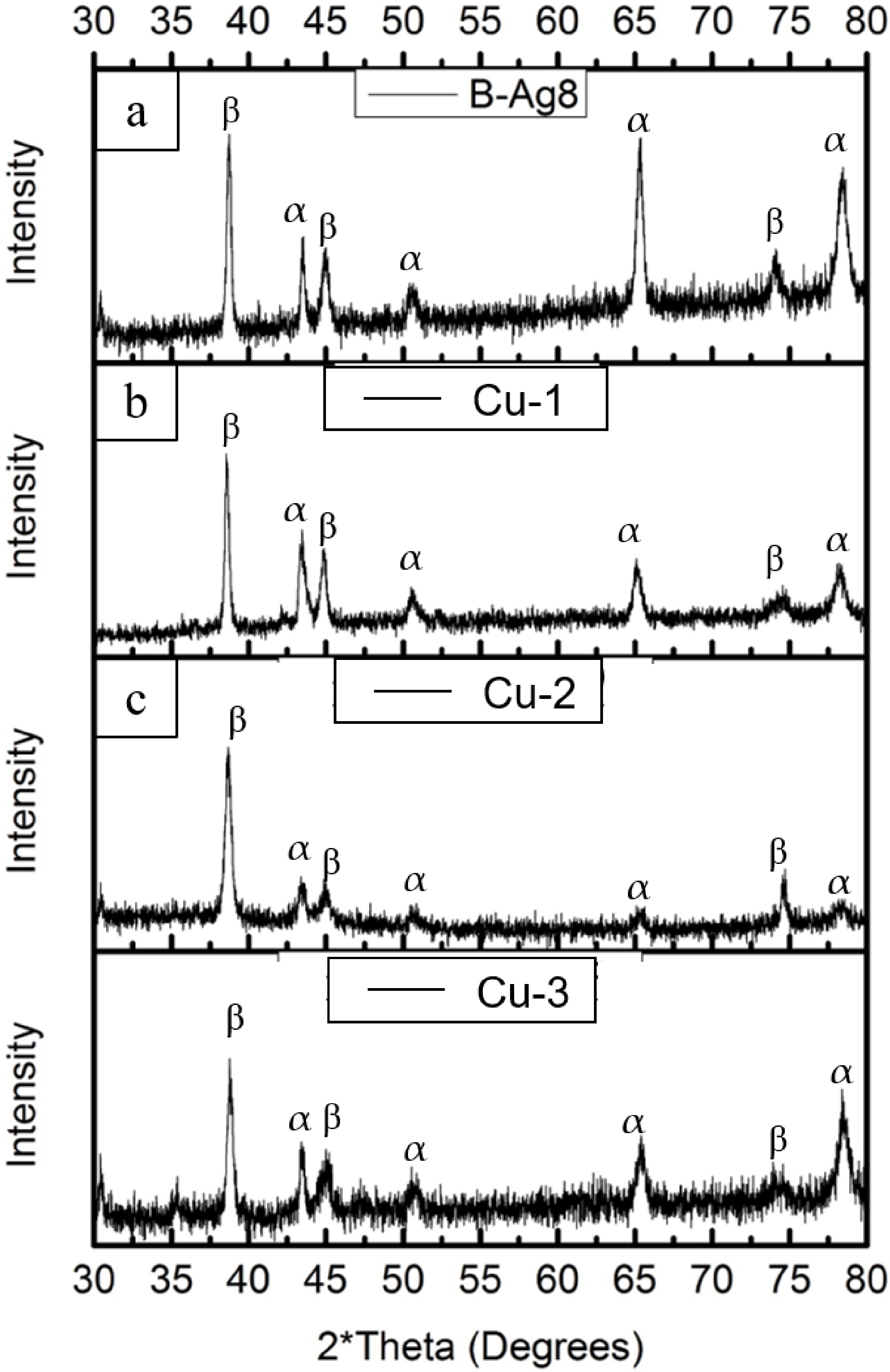

Figure 2.14: XRD patterns after laser joining at 300 W for (a) BAg-8brazing alloy, (b) Cu-1, (c) Cu-3, and (d) Cu-2 [144].

The relative intensity of the α peaks are significantly higher in the BAg-8 brazed joints than the α peaks in the Cu-1 and Cu-3 brazed joints. However, the relative intensities in the BAg-8 joint are very similar to the Cu-2 joint except for the α (220) peak (65.3°). Compared to the BAg-8 alloy, most of the major peaks from the NPA brazed joints were broader than those of the brazing alloy. Broader XRD peaks suggest that the final grain size is smaller for NPA brazed joint than BAg-8 brazed joints. The significance of this detail will be discussed later [144].

2.3.6 Hardness

The hardness profile of the Ag and Cu-Ag brazed joint is plotted in Figure 2.15. The Ag BFM (Figure 2.15a) has an average Vickers hardness of 71 HV within the brazing region. The plate that was directly irradiated by the laser is noted in the figure. The hardness of Ag-IN718 interface on the non-laser side is slightly greater than the hardness at the laser-irradiated interface. Hardness values for 100 μm outside the brazing region return to the original hardness value for IN718 on both sides of the brazing region. The Cu-Ag BFM is on average almost twice as hard as the Ag joint (Figure 2.15b). The hardness of the IN718, especially at the interface is much more greatly affected by the Cu-Ag CSNWs as well. This change in hardness is likely caused more significant compositional change when using Cu-1 compared to Ag-2 (as seen in Figures 2.9b and 2.13b). Like the Ag joint in Figure 2.15a, the laser irradiated interface has a lower hardness than the non-laser irradiated interface. On laser irradiated side, the hardness values regress to the original hardness of IN718 100 μm outside the brazing region. On the non-laser side, the hardness values regress to the

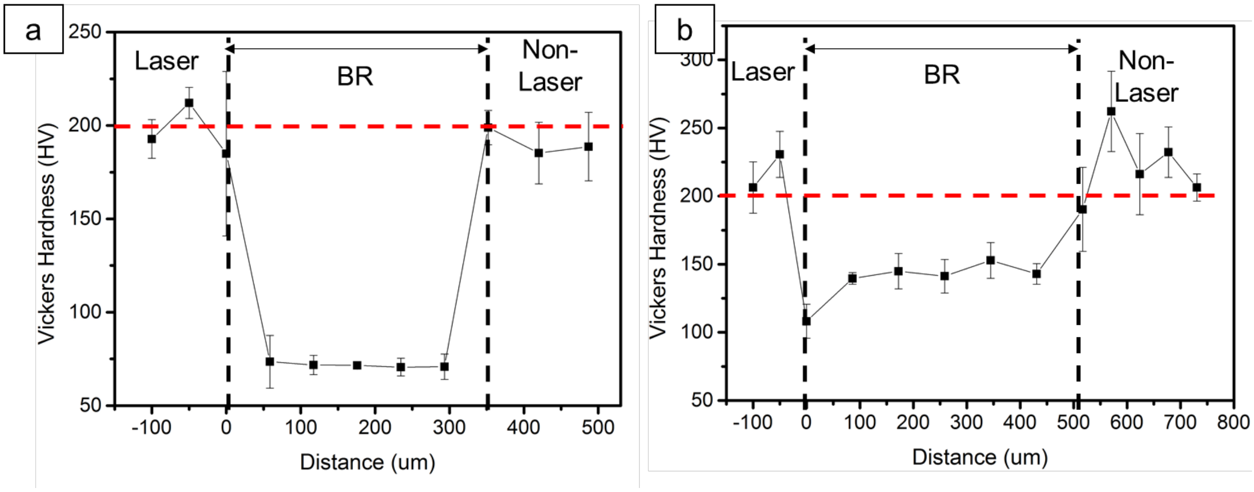

Figure 2.15: Vickers hardness of 300 W brazed joints within the brazing region (BR) and 50 m outside the brazing region (BR) using a) Ag-2 and b) Cu-1. The side of laser incidence is labeled. The red dotted line is the average hardness of IN718 prior to brazing [144]

original hardness of IN718 200 μm outside the brazing region. Nanoindentation can be used to determine the hardness of the individual α and β phases.

2.3.7 Bonding Strength

Figure 2.16 presents the bonding strength of each NPA as a function of laser power. High bonding strength (>100 MPa) was obtained for all NPAs except the Ag-1. Both silver NMs have a laser power threshold of 250 W, however, the Ag-2 NPA has superior bonding strength (116.3 MPa) compared to Ag-1 (49.1 MPa). The pure Cu-1 paste exhibits a steady increase in bonding strength as a function of laser power until it reaches a 224 MPa bonding strength at 300 W. The Cu-2 NPA has the highest bonding strength with a maximum bonding strength of 249.6 MPa. This bonding strength is not much higher than the pure CSNWs (Cu-1), but the error bars are noticeably smaller, suggesting that adding Ag NPs makes the joint more consistent. The slight increase in strength and consistency compared to the pure CSNWs is because the Ag NPs increase the green density of the

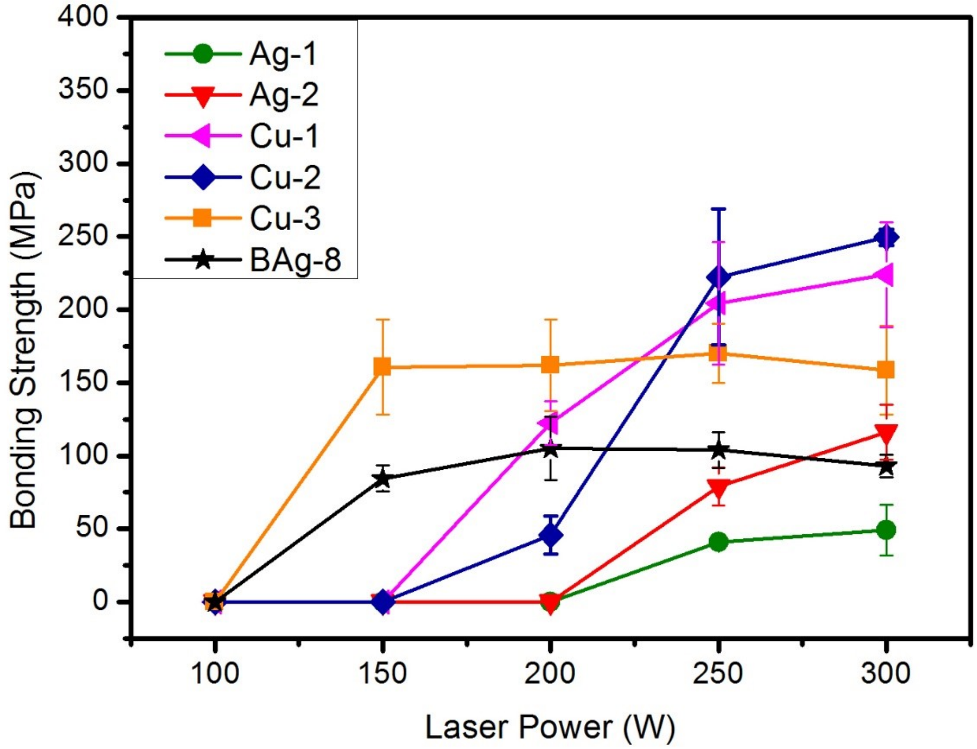

Figure 2.16: Bonding strength vs laser power for the NPAs and the BAg-8 alloy [144]

paste prior to brazing [222] and depress the melting temperature by pushing the Cu-Ag composition towards the eutectic composition which melts 220 °C lower than the Cu:Ag 80:20 composition in bulk. The large increase in bonding strength of the Cu-2 paste displays a between 200 W and 250 W corresponds with minimum laser power for joining of Ag NPs, suggesting that the NPs melting in the paste is a key occurrence that strengthens the Cu-Ag joint. Mixing Ag NWs into the CSNWs (Cu-3) effectively lowers the threshold laser power to 150 W. Cu-3 has a lower threshold laser power compared to Ag-1, Ag-2, and Cu-1 due to the Cu:Ag ratio shifting to the eutectic composition. The possible reason for why Cu-2 does not have the same bonding threshold as Cu-3 is that Ag NWs have been shown in numerous studies to have a lower minimum bonding temperature than Ag NPs via the shape effect.

Li et al. demonstrated that the bonding strength of Ag NWs becomes constant when a certain bonding temperature even when mixed with a differently shaped nanomaterial which is possibly why the laser power has very little effect on the bonding strength of the Cu-3 paste (160 MPa) [141]. The strengths of the Cu-Ag NPAs exceeds the strengths obtained when Cu-Ag NPAs were used to vacuum braze Ni200 (commercially pure Ni) [192] which may attributable to the faster heating rate inherent to laser brazing. The effect of heating rate on strength will be discussed in greater detail in Chapter 5. The Cu-Ag NPAs have higher bonding strength than the BAg-8 at least partially due to subgrain Hall-Petch strengthening. Using the Scherrer formula, the crystallite sizes were calculated based on the XRD peaks in Figure 2.6. The results of these calculations are presented in Table 2.5 [144].

For the NPAs, the calculated crystallite sizes are smaller than BAg-8 on average except for a couple of exceptions. The Cu-1 joint contains β (111) and α (220) oriented grains that are roughly the same size as the β (111) and α (220) oriented grains in the BAg-8 joint. Based on calculations of the β (311) peak, some of the β crystallites in the Cu-3 joint are larger than those found in the BAg-8 joint. The Cu-2 joint contains larger α grains than the BAg-8 joint based on the α (111) and α (311) peaks. Overall, the NPA brazed joints have much smaller grain sizes than BAg-8 brazed joints. Therefore, the superior bonding strength of the Cu-Ag NPAs can be heavily attributed to the Hall-Petch strengthening of

Table 2.5: Crystallite size (in nm) after brazing of Cu-Ag BFMs based on the Scherrer formula. recall that α is the Cu-rich phase and β is the Ag-rich phase

Material	**β (111)**	**α (111)**	**β (200)**	**α (200)**	**β (220)**	**α (220)**	**β (311)**
BAg-8	54.7	67.7	48.0	28.6	46.1	48.6	33.4
Cu-1	54.8	41.8	42.0	34.4	46.1	24.3	25.0
Cu-2	41.2	66.8	33.6	21.5	36.9	17.7	40.1
Cu-3	36.5	41.8	33.7	24.5	15.3	48.8	25.0

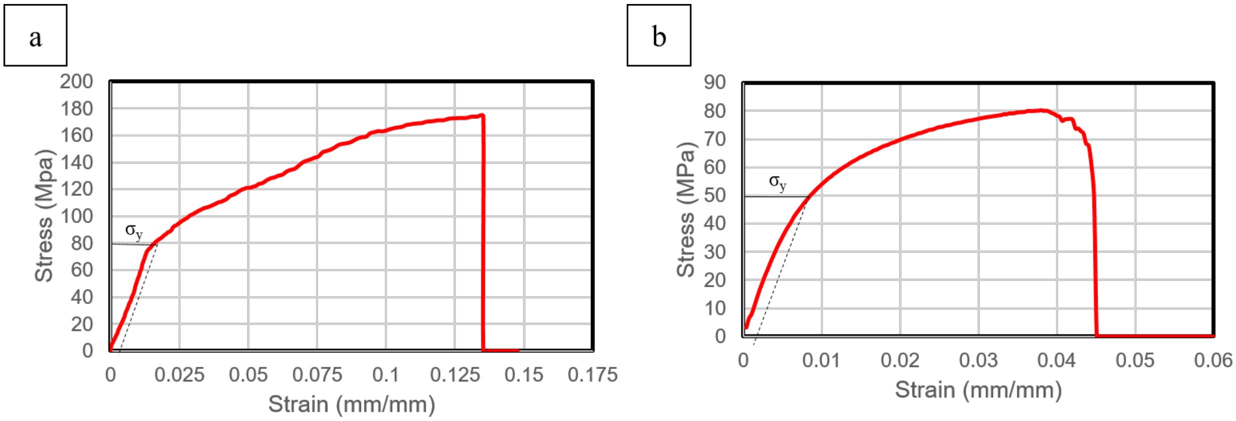

Figure 2.17: Typical Stress-Strain curve of a Cu-3 joint (a) and a BAg-8 joint (b). The yield strength (σ_y) is also shown on each curve. This stress-strain curve was generated on an MTS-3 testing frame [144]

the BFM on a subgrain level.

The higher yield strength was confirmed by the stress-strain curves in Figure 2.17. The Cu-3 brazed joint has an offset yield strength of 80 MPa and the BAg-8 brazed joint has an offset yield strength of 50 MPa. According to the stress-strain curve the BAg-8 joint experiences more necking during fracture than the CSNWs, implying a more ductile failure mechanism in the BAg-8 joint.

2.3.8 Fractography

The fracture surfaces shown in Figure 2.18 indicate that fracture occurs within the BFM, not at the interface between the braze material and the BM. The Ag joints (Figure 2.18b-c) have dimple fracture surface, indicating strong bonding. The dimples from the Ag-2 paste are much larger than the dimples in the Ag NP fracture surface. The Cu-1 joint (Figure 2.18d) has a dimple-cleavage fracture surface. The Cu-2 paste fracture surface (Figure 2.18e) is very similar to the fracture surface the Ag-1 paste (Figure 2.18b). The similarities in the Cu-2 paste and Ag-1 paste fracture surfaces further supports the conclusion that the addition

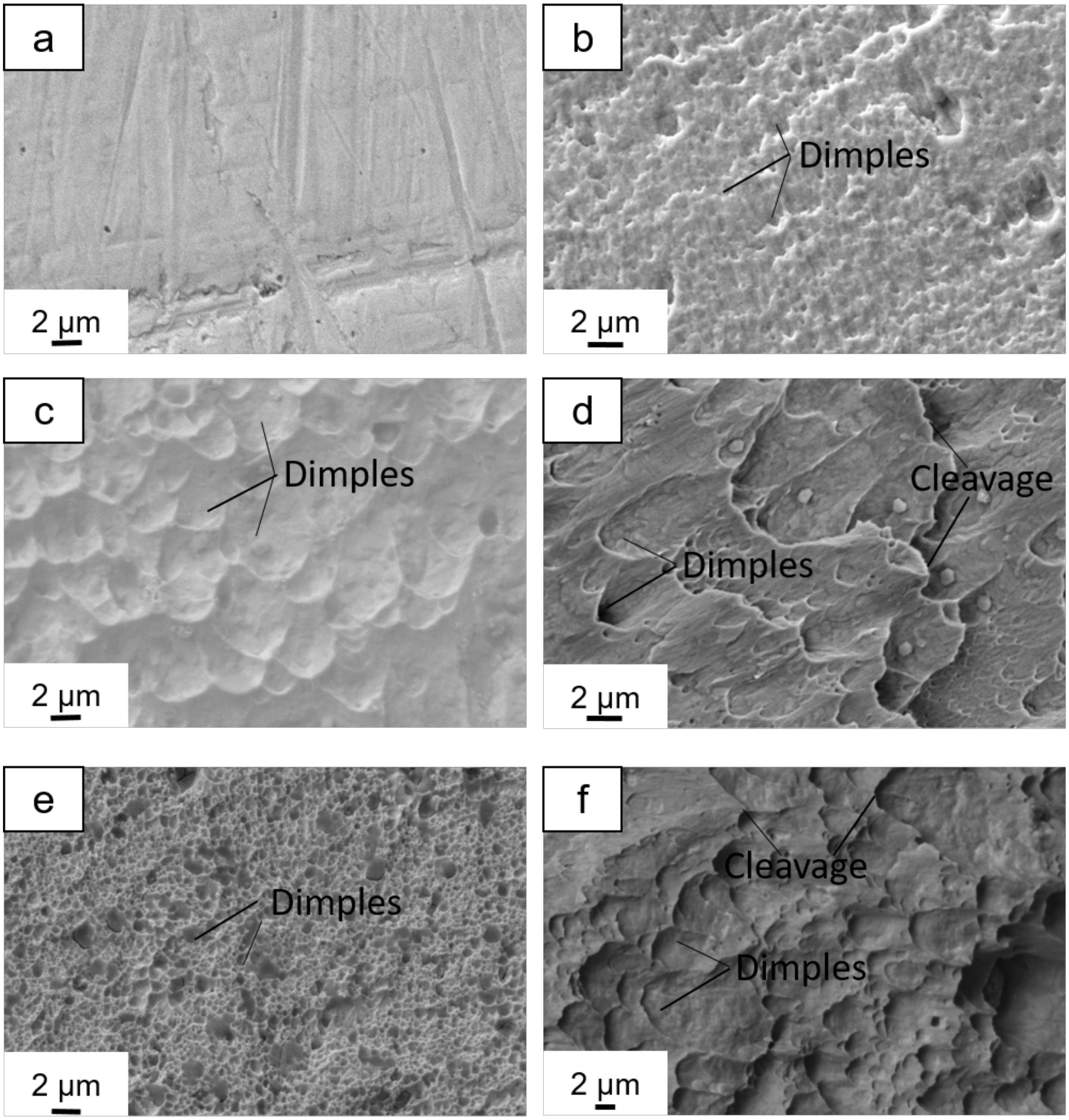
a
2 µm
b
Dimples
2 µm
c
Dimples
2 µm
d
Cleavage
Dimples
2 µm
e
Dimples
2 µm
f
Cleavage
Dimples
2 µm

Figure 2.18: (a) SEM image of the surface of bare IN718. Fracture surface of IN718 bonded at 300 W using (b) Ag-1, (c) Ag-2, (d) Cu-1, (e) Cu-2, and (f) Cu-3

of Ag NPs greatly influences the bonding behavior of Cu-Ag CSNWs. The main difference is that the fracture surface of the Cu-2 (Figure 2.18e) paste has larger, deeper dimples than the Ag-1 paste fracture surface (Figure 2.18b). The Cu-3 paste fracture surface (Figure 2.18f) primarily resembles the fracture surface of the CSNWs, however the dimple features become more apparent after Ag NWs are added to the CSNWs paste. The emphasized dimple features in the Cu-3 paste fracture surface demonstrate that the Ag NWs also have a dominant effect on the bonding/fracture of the Cu-Ag joint.

2.4 Conclusions

Cu-Ag and Ag nanomaterials exhibit high bonding strength and higher joint density than previous nanosoldering studies and higher strength compared to BAg-8 by laser brazing. For Cu-2 and Cu-3 nanopastes (eutectic Cu-Ag composition), the Ag NPs and Ag NWs play an important role in the bonding performance and fracture mechanism of joints fabricated by mixed Cu-Ag NPAs. The addition of Ag NPs seems to make the joint more reliable while the Ag NWs lower the laser power threshold. The superior bonding strength of Cu-Ag NPAs compared to the BAg-8 filler metal is attributed to Hall-Petch strengthening at a subgrain level. The differences in mechanical strength of Ag NW paste and Ag NP paste as a filler metal can be attributed to the diffusion behavior of each nanopaste. Ag NWs have superior strength and larger diffusion zone, but Ag NPs have a lesser effect on the BM. Additionally, Ag NWs have more favorable wetting behavior than Ag NPs. Brazing of both nanomaterial shapes resulted in oversaturation of the BM near the Ag-IN718 interface due to faster diffusion of IN718 principal elements compared to Ag. The implications of these findings reveal that the shape of the nanomaterials in a brazing paste can be manipulated to affect the strength and diffusion behavior of the brazed joint.

Chapter 3

High Entropy Alloys

Disclosure

This chapter based on a publication originally published by Denzel Bridges, Suhong Zhang, Samantha Lang, Minrui Gao, Zhenzhen Yu, Zhili Feng and Anming Hu in 2018:

[52] Bridges, D., Zhang, S., Lang, S., Gao, M., Yu, Z., Feng, Z., Hu, A. Laser brazing of a nickel-based superalloy using a Ni-Mn-Fe-Co-Cu high entropy alloy filler metal. Materials Letters 215, 11-14 (2018). This chapter is also based on a TMS poster presented by Samantha Lang at TMS 2018 titled "Laser Brazing of Nickel Superalloys with a Ni-Mn-Fe-Co-Cu High Entropy Alloy Nanopaste"

Denzels contributions in the article: fabricated bulk high entropy alloy used in this study, conducted some of the brazing experiments with bulk high entropy alloy brazing material, analyzed the experimental data, wrote and revised the article.

Co-authors contributions are listed as follows: Suhong Zhang helped revise the published article. Samantha Lang performed some of the bulk high entropy alloy brazing material and all experiments using the high entropy alloy nanoparticles under Denzel Bridges' guidance and supervision and subsequent EDS analysis. Minrui Gao and Dr. Zhenzhen Yu jointly designed the high entropy alloy composition and provided technical guidance on its utilization. Dr. Zhili Feng was consulted on the research direction and assisted in hardness mapping of the brazed joint. Dr. Anming Hu was the PI on the research, assisted in data analysi and experiment design and revised the article and the poster.

3.1 Motivation and Background

As previously mentioned, high entropy alloys (HEAs) are multi-principal component alloys with high mixing entropy and contain five or more elements in equimolar or near-equimolar quantities. Usually these alloys are single phase. Also recall that the four core effects of HEAs are the high entropy effect, sluggish diffusion kinetics, severe lattice distortion, and cocktail effect [223]. Due to the unique properties of HEAs, it is possible to increase or depress the melting temperature in the bulk state by adding different elements and without the addition of conventional MPDs, such as Si, P, and B. For instance, refractory elements such as Cr, V, and Mo can be added to increase the high temperature stability of HEAs [51]. This expands the potential of HEAs into being used not just as a structural material, but a BFM as well. Additionally, HEAs can be designed to have a comparable chemical composition as the BM which is a desirable requirement for brazing repair applications. Also HEAs can be designed to be compatible for dissimilar materials joining with different elements to match both sides of dissimilar BMs as demonstrated in Figure 3.1. The melting point can be even further controlled through nanofabrication of the bulk material.

Minrui Gao and Zhenzhen Yu designed a Ni-Mn-Fe-Co-Cu HEA (20% Ni, 35% Mn, 5% Fe, 20 % Co, 20 % Cu) to have a combination of high strength and good ductility and to be compatible with Ni superalloys. Ni, Mn, Fe, Co, and Cu were chosen by Gao and Yu because the five element have similar atomic radii, mechanical properties, and chemical properties. According to a Thermo-Calc phase diagram calculation it forms a simple FCC structure and an acceptable melting range of 1080-1150 °C at a composition of (20% Ni,

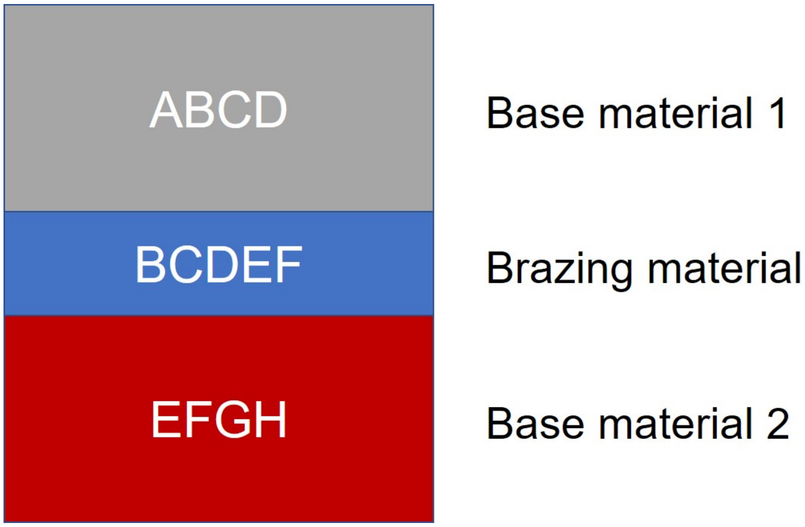

Figure 3.1: Schematic showing the design concept for HEA-based dissimilar joining.

35% Mn, 5% Fe, 20 % Co, 20 % Cu). The thermal expansion coefficient of this HEA (16.6×10^{-6}/K) is similar to Inconel 600 (13.3×10^{-6}/K) and IN718 (13.0×10^{-6}/K) [224]. In this work, we demonstrate the potential of this Ni-Mn-Fe-Co-Cu HEA for laser brazing of IN718 and the effect of nanofabrication on the brazing performance. We will elucidate the mechanical properties of HEA-brazed IN718 and discuss the lattice distortion, diffusion kinetics, and cocktail effect on the mechanical properties.

3.2 Experimental Procedure

3.2.1 Bulk HEA Fabrication

For HEA fabrication, nickel, copper, cobalt, iron, and manganese powders at a nominal composition of (20% Ni, 35% Mn, 5% Fe, 20 % Co, 20 % Cu) were mixed by mortar and pestle. The powder mixture was then melted with an SP-25VIM vacuum induction melting system for 2 minutes at an output current of 900 A in a graphite crucible, then cooled naturally under vacuum. The graphite crucible helps ensure a faster cooling rate and making sure that the HEA remains a single phase material [224].

3.2.2 HEA Nanofabrication

HEA NPA was fabricated by first grinding the as-fabricated HEA ingot from the previous step into micropowder using a diamond grinding wheel. The collected micropowder was then used then ball milled at 500 rpm for 12 hrs in terpineol using onyx milling balls and milling jar. The solution was then transferred to a high energy rotary vibrating ball mill and milled for 2 hours at 1200 rpm using stainless steel milling balls. The ball milling procedure crushes and fragments the micropowder until nanoparticles are obtained as shown in Figure 1.20. Stainless steel was chosen for high energy ball milling to avoid harmful contamination from ceramic milling balls. Also, the main elements in stainless steel would not introduce incompatible or significant contamination. The resulting solution was further concentrated by centrifugation at 8000 rpm until the paste has a glue-like consistency.

3.2.3 Laser Brazing

For laser brazing, IN718 (0.32 mm thick) is cut into 2 mm × 15 mm pieces (Table 3.1) and ultrasonically cleaned in acetone. The HEA filler metal was cold-rolled to a approximately 400 μm thick piece and placed between two IN718 pieces coated with 601B flux in a lap joint configuration with a 1.5 mm overlap. The lap joint rests on a 1 mm thick copper platform. Lap joints were brazed by combining two diode lasers (wavelength = 806

Table 3.1: Chemical composition of IN718

Ni	**Fe**	**Cr**	**Cu**	**Al**	**Si**	**C**	**Mn**	**B**	**Nb**	**Ti**	**S**	**Mo**
52.47	19.11	20.42	0.05	1.05	0.14	0.24	0.25	0.02	3.09	1.30	<0.004	1.86

nm), one 500 W laser (focal length = 20 cm) and one 400 W laser (focal length = 10 cm) as sen in Figure 3.2. The integration of two laser heads allowed safe and sustainable operation of each head at 200-300 W. A small part of the HEA filler metal is directly irradiated for 20 seconds. This was done because the solidus temperature of IN718 (1260 °C) is very close to the liquidus temperature of the HEA bulk filler metal. For the nanobrazing material, HEA NPA was applied to both IN718 chips and laser irradiated in the same way as the bulk material. BNi-2 foil (82.4% Ni, 7% Cr, 4.5% Si, 3.1% B, 3% Fe) was also used as a filler metal for comparison (solidus temperature = 971°C, liquidus temperature = 998 °C). The brazing temperature was measured with an Omega SAT-30-12 S-type thermocouple.

3.2.4 Characterization

For bonding strength evaluation, tensile tests were completed using a ZHIQUP Precision Instruments, 1500D force gauge with a constant displacement rate of 1 mm/min (5 acquisitions/second). For cross-sectional analysis, samples were embedded in an epoxy resin and polished using diamond paste up to 0.25 μm and colloidal silica solution (0.04 μm).

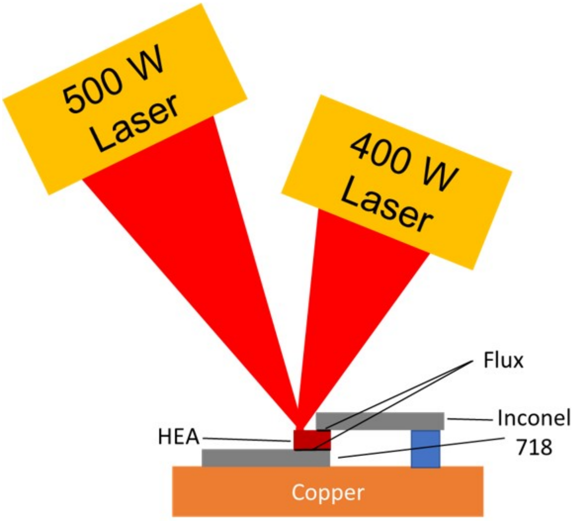

Figure 3.2: Schematic of the laser brazing setup [52].

Scanning Electron Microscopy (SEM) images were collected on a Zeiss Auriga Scanning Electron Microscope. Energy Dispersive X-ray Spectroscopy (EDS) measurements were performed using a Zeiss EVO SEM equipped with a Bruker xFlash ®6—30 detector. Vickers microhardness mapping was measured with a LECO LM100AT microhardness tester with a 25 gram-force indentation force. The hardness of Inconel 718 and the HEA prior to brazing were also measured. X-ray diffraction (XRD) measurements were conducted on a Panalytical Empyrean X-ray Diffractometer.

3.3 Results and Discussion

3.3.1 HEA characterization

It is confirmed from the XRD pattern in Figure 3.3a-b that the HEA is a single-phase FCC material in both the bulk and NP forms and appears to remain single phase after brazing (Figure 3.3c). In the bulk form the (200) peak is almost not visible which is unusual for an FCC material, showing that there is some alignment preference as-synthesized. The NPs do not have any atypical crystallographic alignment based on Figure 3.3b. However,

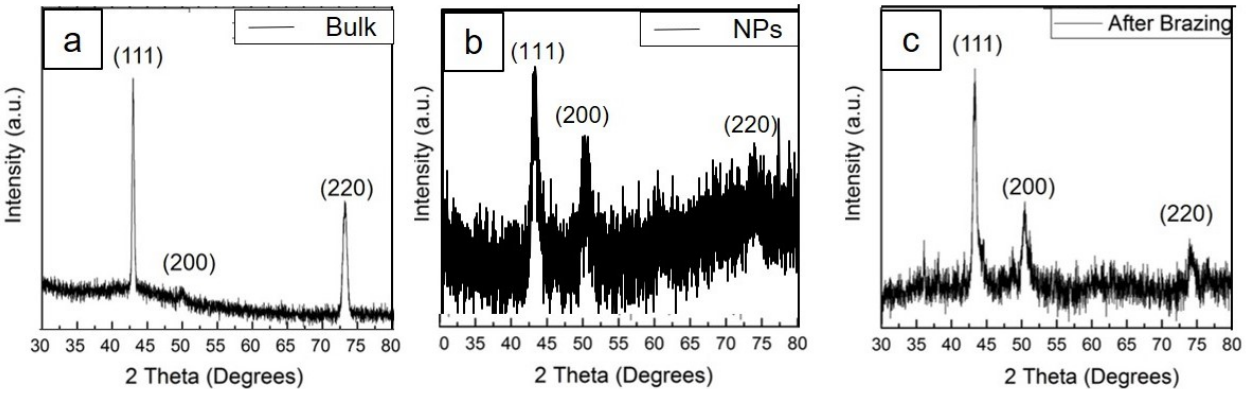

Figure 3.3: XRD pattern on HEA (a) As-synthesized bulk material (b) NPs, and (c) After brazing [52].

there is a very clear decrease in crystallite size as seen in Table 3.2. Undoubtedly, this is caused by a pulverization of the HEA material during ball milling [5, 116]. After brazing, the HEA appears to remain a single phase FCC material. As for the NP fabrication, the inital powderization on the grinding wheel produced particles approximately 60 μm in diameter (Figure 3.4a). After low energy ball milling the average particle size was reduced to 500 nm (Figure 3.4b). The low energy ball milling served to reduce the particle size to a smaller diameter prior to high energy ball milling and thereby increasing the efficiency of the high energy ball milling procedure. The high energy ball milling reduced the nanoparticles to 100 nm, the threshold for the nanoregime (Figure 3.4c).

3.3.2 Mechanical Properties

According to Figure 3.5, the maximum shear strength was obtained using the bulk HEA as a FM at 400 W laser power (220 MPa) which corresponds to 1165 °C (15 °C above the HEA liquidus temperature). Like nearly all brazing materials, the optimal brazing

Table 3.2: Scherrer crystallite size according to the XRD patterns in Figure 3.3

Plane	Bulk	NP	After Brazing
(111)	256.3	138.9	166.8
(200)	142.7	61.2	107.1
(220)	148.8	107.2	80.9

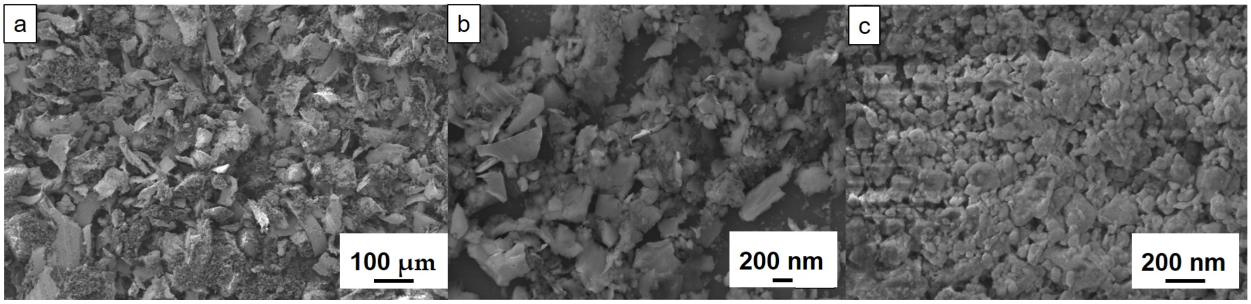

Figure 3.4: SEM images of the HEA powder (a) after initial powderization (b) after low energy ball milling, and (c) after high energy ball milling.

temperature for the HEA is slightly above the liquidus temperature to ensure that the brazing material remains liquid for significant metallurgical bonding, wetting, and diffusion. If the temperature is too low such as with 350 W laser power, the incomplete melting of brazing materials may result in shallow diffusion of certain elements into the BM and thereby a weak bonding [225]. In practical application, incomplete melting can affect the final microstructure and inhibit wetting and crack repairing. The brazing temperature of samples brazed at 450 W and 500 W is far above the liquidus temperature which detrimentally affects the strength. For the HEA NPA, it is shown to be effective at brazing using 250 W and 300 W laser power which corresponds to a maximum brazing temperature of 959 °C and 1021 °C, respectively. This thoroughly demonstrates that the brazing temperature of HEA NPs is far below that of

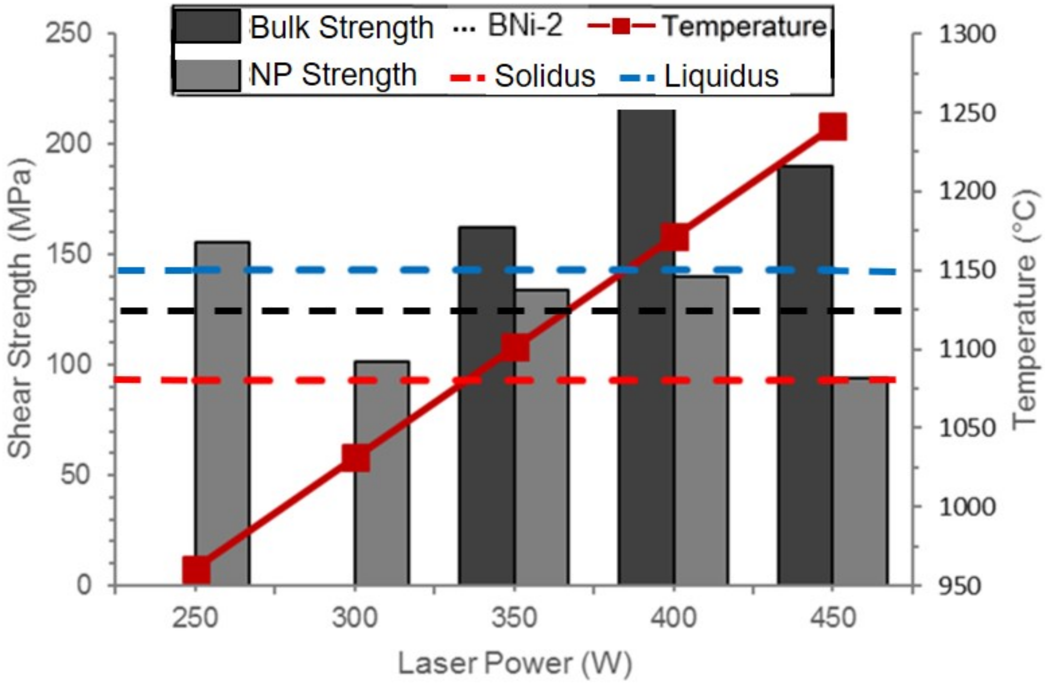

Figure 3.5: Shear strength (left axis, bar graph) and brazing temperature (right axis, red solid line) as a function of laser power. The shear strength of BNi-2 is also shown by a black dotted line. The red and blue dotted lines are the solidus and liquidus temperatures, respectively [52].

the HEA solidus temperature. The HEA NPs, however, exhibit a maximum strength of only 155 MPa, nearly 30% lower than the maximum strength of the bulk HEA BFM. The reasons why the strength is significantly lower is due to the significant phase separation that occurs in NPs but not in the bulk material under laser brazing conditions which will be discussed later.

Each hardness map of the bulk HEA in Figure 3.6 shows a spot with higher hardness than the rest of the joint close to the top plate interface. The average hardness before brazing of the HEA and IN718 on the Vickers hardness scale is 93 HV and 250 HV, respectively (Figure 3.6d). After brazing the hardness of the HEA more than quadruples compared to the initial value due to introduction of Cr into the HEA BFM (to be discussed later). The hardness of IN718 also increases. There is a significant decrease in hardness between 350 W (410 HV) and 400 W (304 HV) of the HEA material in contrast to the decrease in shear strength that occurs at 450 W. The average IN718 hardness experiences a similar hardness decrease between 400 W (351 HV) and 450 W (288 HV). The difference in hardness between the top half and bottom half of the joint (Figure 3.6a-c), is likely due to the variable temperature gradient (TG) and cooling rate (CR) in the transverse (i.e. perpendicular to the HEA-IN718 interface) and longitudinal directions (i.e. parallel to the HEA-IN718 interface). The CR is likely faster when the distance to the copper platform decreases due to heat sinking. But the TG is most likely largest in the transverse direction. Both the TG and the CR affect the grain nucleation and growth rate of the HEA material and the grain size and shape affect the hardness of the material. The most probable reason for the large hardness increase in the HEA is the changes in lattice distortion and cocktail effects induced by Cr atom introduction into the HEA lattice [226]. Detailed structural and elemental analysis

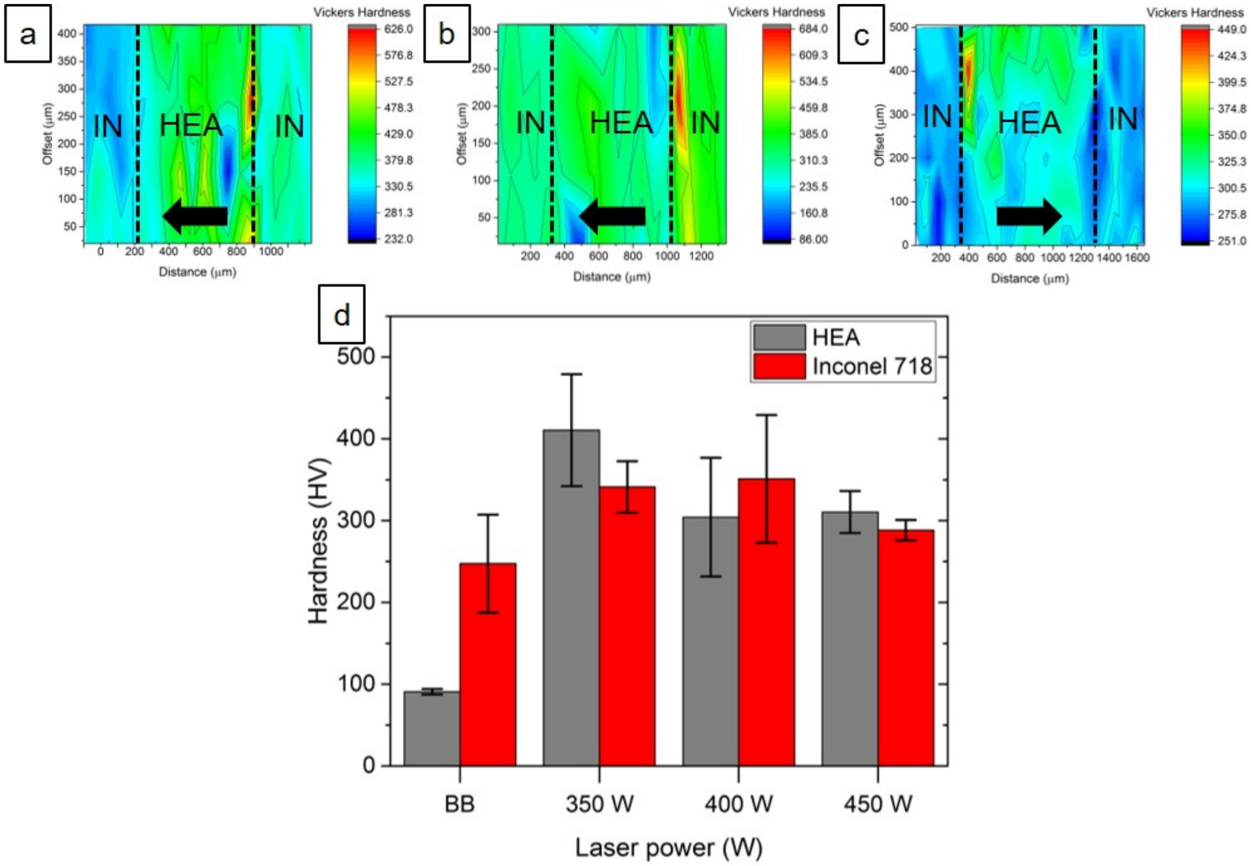

Figure 3.6: Hardness maps of brazing joints using (a) 350 W, (b) 400 W, and (c) 450 W laser power. The black arrow shows the direction of laser irradiation. The bottom of the hardness map lines up with the end of the joint overlap. (d) The average hardness of the IN718 and the HEA before brazing (BB) and after brazing. The average hardness after brazing was calculated by taking the average of all the hardness map values [52].

can help confirm this hypothesis. Unlike shear strength, the decrease in hardness at higher brazing temperature is not caused by excessive diffusion, but by a change in the cocktail effect via the composition change [227].

The fracture surfaces (Figures 3.7a-c) cleavage fracture characteristics [228]. Fracture occurs in the BFM. There no visible evidence of microvoid coalescence failure (i.e. dimpled fracture morphology). This atypical fracture behavior because predominantly cleavage fracture occurs primarily in BCC, HCP, and covalently bonded crystals and FCC materials under corrosive environmental conditions [1]. Cleavage is a low energy fracture mechanism and the presence of such fracture features implies low fracture toughness. However, the fracture surfaces of the joints also contain several secondary cracks, especially at 350 W and 400 W. Secondary cracks are cracks that branch off from the main fracture plane and usually indicate improved fracture toughness [229]. At 450 W, there are fewer secondary cracks, implying more brittle fracture compared to 350 W and 400 W. EDS mapping (Figure 3.5d-f) shows high Cr concentration on the fracture surface which increases with laser power. The high Cr concentration in the 450 W joint (Figure 3.7f) fracture surface implies that excessive Cr concentration leads to embrittlement of the HEA layer [52].

3.3.3 Diffusion Behaviors

As seen in Figure 3.8g, the diffusion zone (DZ) thickness increases with laser power. The dramatic increase in DZ thickness at 450 W correlates to the 12% strength decrease. The

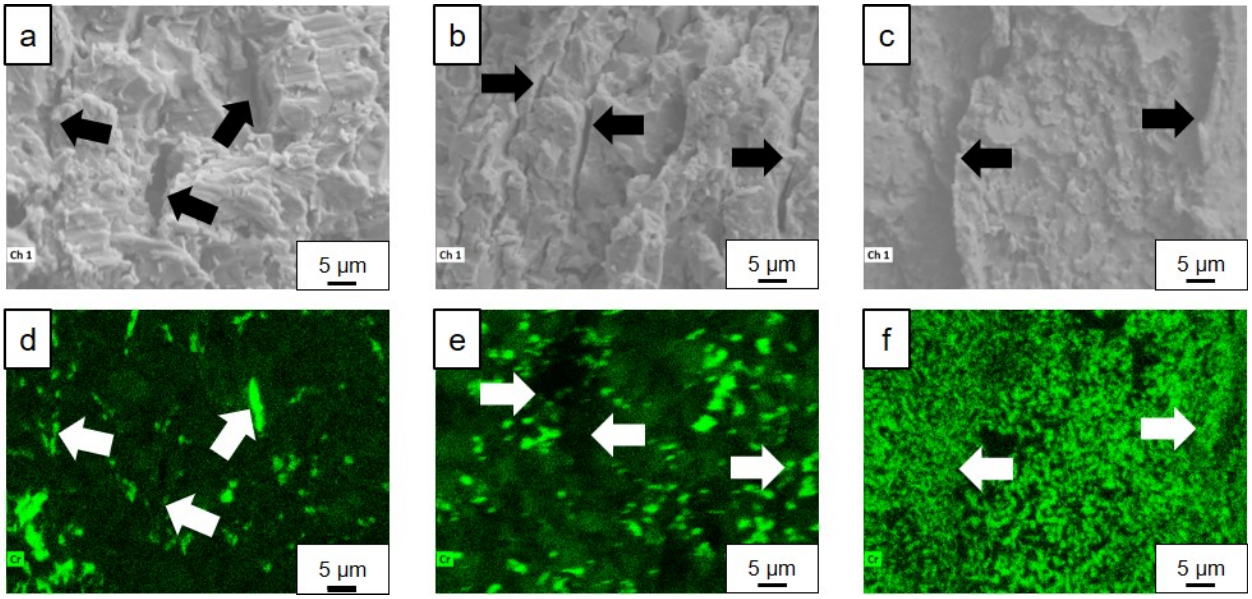

Figure 3.7: An HEA fracture surface using (a) 350 W, (b) 400 W, and (c) 450 W laser power. Cr distribution on the fracture surface using (d) 350 W, (e) 400 W, and (f) 450W laser power. Arrows point to secondary cracks [52].

change in composition that occurs because of interdiffusion is a likely cause of the change in shear strength and hardness via the cocktail effect. In HEAs, the cocktail effect constitutes atomic-scale multielement composite effects and microscale multiphase composite effects. When interdiffusion occurs, the alloy composition and mutual interaction between dissimilar elements change, thus changing the mechanical properties. For this HEA brazing material, Cr is introduced into the lattice and, as previously reported, small element concentrations can alter the mechanical properties of HEAs [230]. The XRD pattern after brazing (Figure 3.3c) also insinuates that the addition of Cr induces additional lattice distortion.For HEAs, severe lattice distortion arises from several different atoms occupying the same lattice. After brazing, six atom species occupy the HEA lattice instead of five. Due to the fast heating and cooling rates of laser brazing, the severe lattice distortion increases with respect to the as-fabricated HEA. This would cause the diffraction angle and relative peak intensity to shift due to a change in the lattice parameter after brazing [231].

Figure 3.9 shows a comparison between the 350 W and 400 W joints for the bulk HEA BFM and the HEA NPA. As seen in Figure 3.9e-h, we observe significant phase separation and broader diffusion zone in the nanobrazed joint (29 μm) compared to the bulk HEA (15 μm). The phase separation is only seen in the bulk HEA BFM under vacuum brazing conditions. Gao describes similar phase segregation under vacuum brazing conditions in his thesis based on the same HEA BFM, but this occurs over a much longer time scale than laser brazing [224]. For the bulk material, sufficient time is needed for the single phase HEA structure to segregate into multiple phases and laser brazing of the bulk HEA BFM is too fast in terms of heating and cooling rate. The mechanical advantages of HEAs are partially due to the lattice distortion caused by multiple elements occupying a lattice. This lattice

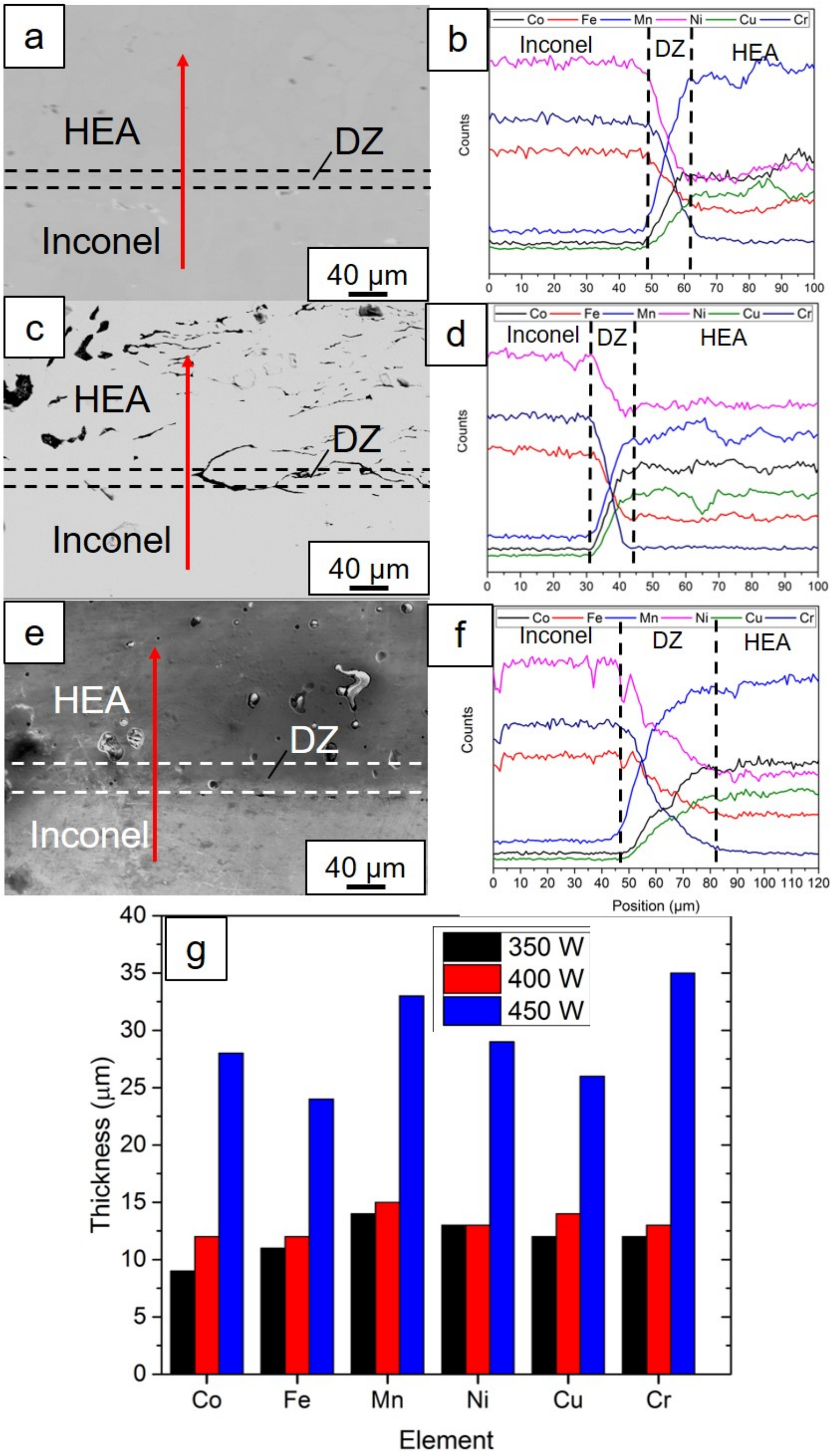

Figure 3.8: (a) EDS line scan for brazed joints using the HEA brazing material at laser power (a-b) 350 W, (c-d) 400 W, and (e-f) 450 W. The dotted lines show the location of the diffusion zone. (g) Diffusion zone thickness of each element at each laser power [52].

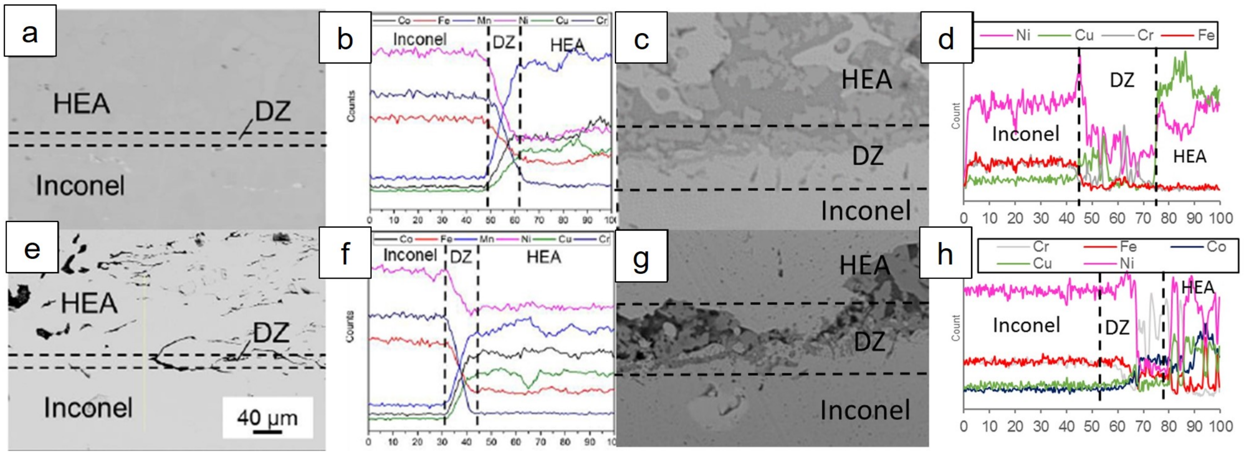

Figure 3.9: EDS of a bulk HEA joint (a-b) and HEA NPA joint (c-d) at 350 W andbulk HEA joint (e-f) and HEA NPA joint (g-h) at 400 W.

distortion significantly impedes dislocation motion and diffusion of atomic species in solid state. When the phases segregate, that advantage is lost and the material is much weaker. Remember, a relatively short cooling rate helps keep the HEA as a single phase material. The fact that the HEA NPs experience the significant phase separation even under laser brazing conditions is most likely due to the clearly increased diffusion activity in NPs compared to the bulk material (recall Equations 1.25 and 1.26). It should be noted that the solidification of the HEA NPs from a liquid or partially liquid state is a complicated thermodynamics and kinetics question and requires further investigation.

3.4 Conclusions

The Ni-Mn-Fe-Co-Cu HEA investigated in this paper demonstrates joining strength exceeding 200 MPa and hardness exceeding 275 HV when used as a brazing filler metal for IN718. Using a brazing temperature much greater than the liquidus temperature results in a loss of shear strength and hardness in the brazing material. This loss of strength and hardness is attributed to excessive interdiffusion between the BFM and IN718 and compositional changes in the brazing material, respectively [227]. The large increase in hardness after brazing is most likely caused by a combination of severe lattice distortion and microscale/atomic-scale cocktail effects. For the NPs, a clear decrease in minimum laser power/brazing temperature is demonstrated. However, due to the significant phase separation that occurs when using the NPs instead of the bulk material, the strength is significantly weaker than the strength obtained from the bulk HEA material.

Chapter 4

Self-powered Brazing

Disclosure

This chapter based on two publications. The first publication was originally published by Denzel Bridges, Christopher Rouleau, Zachary Gosser, Cary Smith, Zhili Zhang, Kunlun Hong, Jinquan Cheng, Yoseph Bar-Cohen, and Anming Hu in 2018:

[232] Bridges, D., Rouleau, C., Gosser, Z., Smith, C., Zhang, Z., Hong, K., Cheng, J., Bar-Cohen, Y., Hu, A. Self-powered brazing of Ti-6Al-4V using Ni/Al Reactive Multilayer Films. Applied Sciences 8, 985-998, (2018).

The second publication is a conference paper that was published by Denzel Bridges, Ying Ma, Christopher Rouleau, Zachary Gosser, Cary Smith, Zhili Zhang, Kunlun Hong, Jinquan Cheng, Yoseph Bar-Cohen, and Anming Hu in 2018:

[233] Bridges, D., Ma, Y., Rouleau, C., Gosser, Z., Smith, C., Zhang, Z., Hong, K., Cheng, J., Bar-Cohen, Y., Hu, A. PREPARTATION OF THICK NI/AL REACTIVE MULTILAYER

FILMS AND PROSPECTIVE USE FOR SELF-POWERED BRAZING OF TI-6AL-4V in International Manufacturing Science and Engineering Conference 2018. (ASME).

Denzels contributions in the article: Fabricated reactive multilayer films, performed brazing and strength testing and structural characterizations. Wrote and edited both articles

Co-authors contributions are listed as follows: Ying Ma assisted in fabricating reactive multilayer films and assisted in experimental design. Dr. Christopher Rouleau and Zachary Gosser maintained and designed the electron beam evaporation system used to fabricate the reactive multilayer films. Cary Smith and Dr. Zhili Zhang provided high speed camera imaging of the reaction propagation. Dr. Kunlun Hong performed differential scanning calorimetry on the reactive multilayer films. Dr. Jinquan Cheng performed LAMPS simulations of the self-powered brazing process. Dr. Yoseph Bar-Cohen served as the co-PI on the project, provided NASA funding, and revised both articles. Dr. Anming Hu was the PI on the research, assisted in data analysis and experiment design and revised the article.

4.1 Motivation and Background

In-space manufacturing covers a wide range of manufacturing and joining processes. For example, the Sealing, Seaming, Sterilization, and Separation (S^4) process was developed for potential application for Mars sample return missions (Figure 4.1) [234]. In addition, in-space repair is useful for a wider range of exploration mission capabilities, as well as personnel survival in human operated missions. These potential missions have requirements for an extremely high probability of success for full preservation of samples collected from space missions and for ensuring the safe handling of samples and planetary protection of samples and personnel when returned to Earth for analysis [234]. Brazing is one of the most effective methods of joining structures and supports both S4 and repair procedures, however, in-space manufacturing has several stringent requirements that are not considered for terrestrial manufacturing processes. For instance, brazing, generally, requires high input energy, which is traditionally delivered by large, cumbersome equipment, which have a large energy cost. So, one of the objectives of in-space manufacturing is to minimize the necessary input energy, the weight of components, and the total operating time. Failure to consider these parameters may prohibit application and would limit exploration missions to bodies, such as ocean worlds, distant moons, and planets in the solar system, including Europa, Enceladus, Ganymede, Callisto, Ceres, and Pluto, which are, increasingly, a potential target of proposed exploration.

Reactive multilayer films (RMFs) are comprised of alternating layers of materials that can be ignited electrically, thermally, by laser pulse, or mechanical striking, producing an exothermic heat release. The process of RMF-assisted joining has been demonstrated using

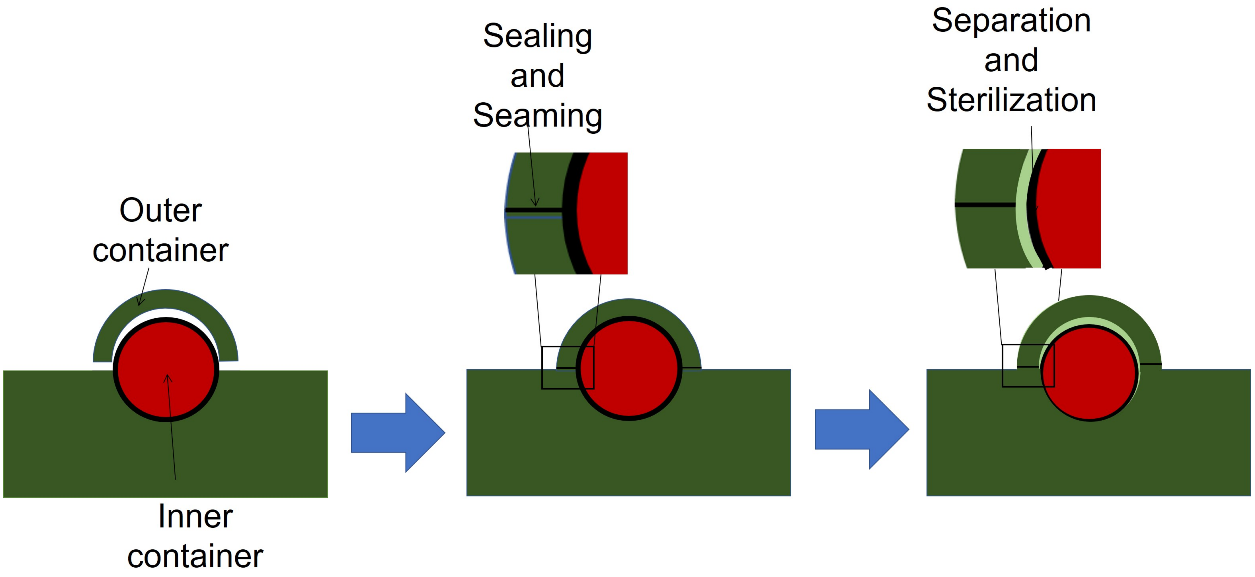

Figure 4.1: Schematic of the S4 process

several types, such as Ti/Al [235, 236], Ti/Ni [43, 87], and Ni/Al [74, 237, 238] in air, vacuum, and underwater for joining similar dissimilar metals, ceramics, and semiconductors [168, 238]. Most RMF joining studies have been performed on solder materials (melting point $\leq$450 °C) [119] or using furnace-based joining procedures [239, 240]. However, electrically ignited RMF joining for brazing applications (>450 °C) has been seldom explored. Self-powered brazing is a novel and innovative joining process in which the heat required for joining is generated almost entirely from the internal chemical energy of the brazing materials and only needs an inconsequentially small trigger to release the energy through an exothermic reaction (Figure 4.2). Ni/Al RMFs has one of the highest heat reactions among Al-based RMF types as seen in Table 4.1 [241]. Pd/Al and Pt/Al RMF have higher heat of reactions, however, Ni is significantly cheaper than palladium (Pd) and platinum (Pt) and the Ni/Al reaction is more stable. Using self-powered brazing via self-propagating reactions of Ni/Al RMFs offers an innovative solution that greatly reduces the significant power requirement

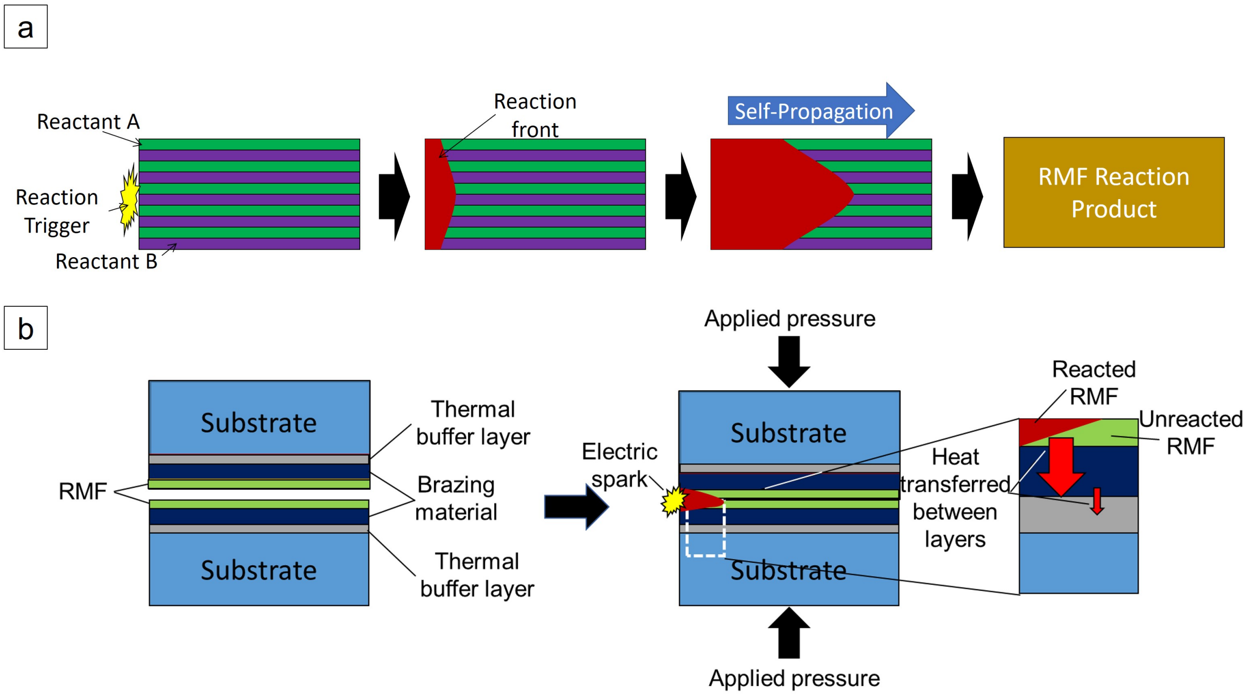
a
Reactant A
Reaction Trigger
Reactant B
Reaction front
Self-Propagation
RMF Reaction Product
b
Substrate
Thermal buffer layer
RMF
Brazing material
Substrate
Thermal buffer layer
Applied pressure
Electric spark
Substrate
Heat transferred between layers
Reacted RMF
Unreacted RMF
Substrate
Applied pressure

Figure 4.2: Diagram showing (a) the self-propagating reaction of RMFs and (b) Heat flow of self-powered brazing

for brazing and the weight of equipment transported into space. For this study, we will discuss, herein, the preparation of Ni/Al RMFs join Ti-6Al-4V (Ti64) coated with BAlSi-4 as the BFM and Ni/Al RMFs as the heat source and demonstrate the potential of this new technique, in addition to discussing the phase transformations associated with the bonding procedure.

4.2 Experiments and Methods

4.2.1 RMF fabrication

Ti64 was purchased from McMaster-Carr and cut into pieces that were 3 mm wide and 30 mm long. Ti64 pieces were coated with BAlSi-4 by melting a BAlSi-4 strip (liquidus temperature = 582 °C), purchased from Prince & Izant, directly on to Ti64 with a plasma

Table 4.1: List of Al-based RMF reaction characteristics [241]

Reactants and products	**Exothermic Heat of reaction (kJ/mol)**	**Adiabatic reaction temperature**
Ti + Al ⟶ TiAl	36	1227
Zr + Al ⟶ ZrAl	45	1480
Co + Al ⟶ CoAl	60	1639
Ni + Al ⟶ NiAl	59	1639
Pd + Al ⟶ PdAl	92	2380
Pt + Al ⟶ PtAl	100	2800

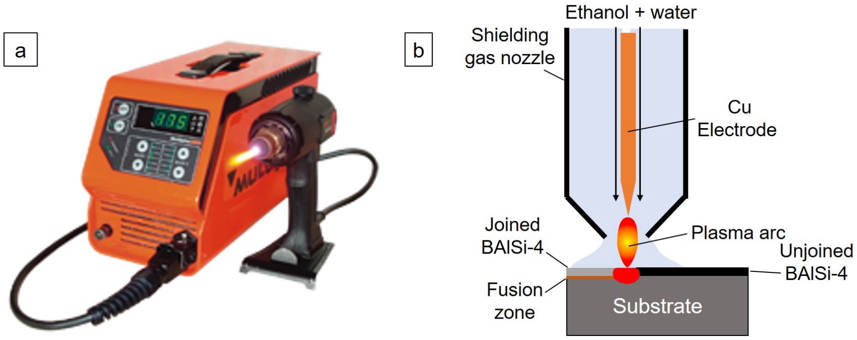

Figure 4.3: (a) Photograph of a Multiplaz 3500 plasma torch and (b) Schematic of the plasma coating process

welding torch (Figure 4.3). The composition of Ti64 and BAlSi-4 are included in Table 4.2. The thickness of BAlSi-4 was grinded down to 80-110 μm to optimize the temperature increase experienced by BAlSi-4 during the RMF reaction. The BAlSi-4-coated Ti64 was polished up to a mirror finish with 1 μm diamond paste. Ni/Al bilayers were deposited directly on to BAlSi-4-coated Ti64 and polyimide substrates using a modified Varian 3118 electron beam evaporator (Figure 4.4). The pressure inside the chamber was maintained $<5 \times 10^{-6}$ Torr. Ni/Al RMFs were fabricated using electron beam physical vapor (e-beam) deposition. A direct current DC power supply (Sorensen DC560-18E) was used to heat the substrate during growth, while a deposition controller (Leybold XTC/2) was utilized for rate (nominally 6.5 Å/s) and thickness control. Two RMF Ni:Al compositions were fabricated: 1.5:1 and 1:1. To produce a 1.5:1 ratio, each Ni and Al layer was 60 nm each. To produce

Table 4.2: Elemental composition of Ti64 and BAlSi-4

Material	Element Composition (at%)						
Ti64	Ti	Al	V				
	90	6	4				
BAlSi-4	Al	Si	Cu	Fe	Mg	Mn	Zn
	86.45	12.0	0.3	0.8	0.1	0.15	0.2

a 1:1 ratio, each Ni layer was 44 nm and each Al layer was 66 nm [87]. Note that 1:1 ratio is the stoichiometric ratio for this RMF reaction. A 60 nm-thick Ti layer was added as the bottom layer to help the film adhere to the BAlSi-4 substrate and 30 nm Ti interlayers were added intermittently to offset the internal stresses in as-deposited RMFs that cause the film to peel off the substrate or delaminate during deposition [242]. Ti was also chosen based on its ability to react with both Al and Ni their own respective exothermic reactions with the Ni/Al reaction [236, 241]. Ni was used as the final layer to mitigate oxidation when exposed to air. RMFs were also deposited on polyimide sheets so that the RMFs could be peeled off for SEM and XRD analysis [232].

4.2.2 Self-Powered Brazing

For brazing, the BAlSi-4-coated Ti64 pieces with the RMF were arranged in the configuration shown in Figure 1 with applied pressure and ignited using electrical heating via a 13 V DC power source (Figure 4.5a). Electrical heating was supplied by touching the side of the BAlSi-4 coating with 28-gauge Ni wire until the film reacted (within 3 s). The same ignition conditions were used for all RMF thicknesses because, based on the literature search, the ignition conditions affect the reaction initiation, but not the propagation [243]. Pressure was applied to ensure close contact between the RMFs and BAlSi-4. Extra RMFs were peeled off the polyimide substrate and added between the BAlSi-4, in addition to the

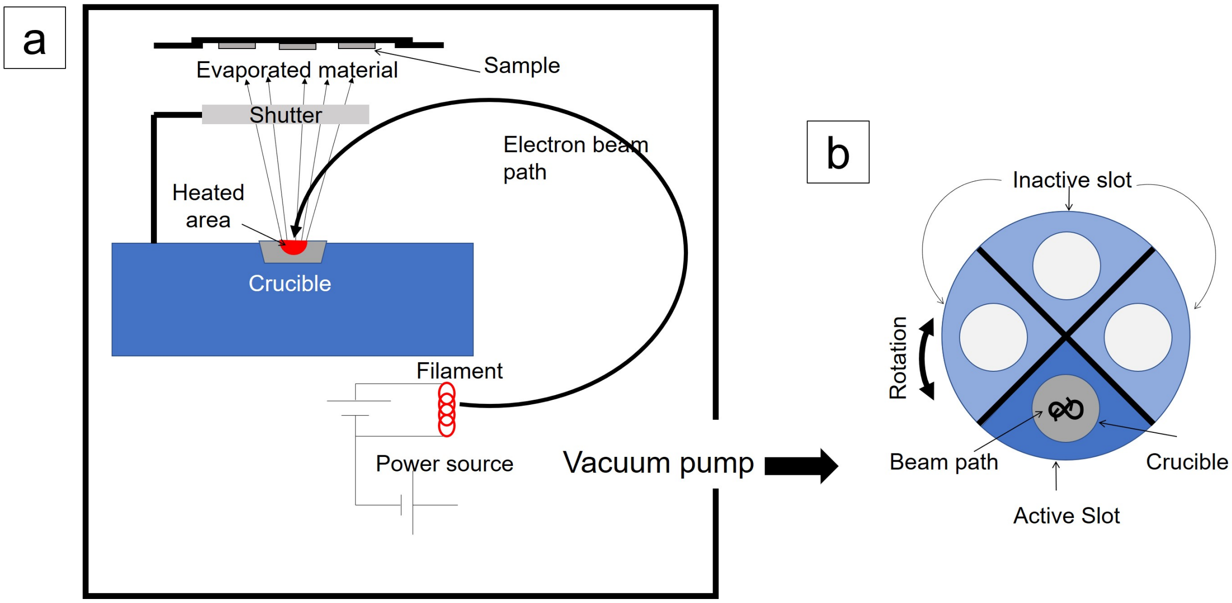
a
Sample
Evaporated material
Shutter
Electron beam path
Heated area
Crucible
Filament
Power source
Vacuum pump
b
Inactive slot
Rotation
Beam path
Crucible
Active Slot

Figure 4.4: (a) Schematic of e-beam evaporator (side view) (b) Schematic of multi-target crucible holder (top-view)

as-deposited amount to vary thickness. RMF thickness = 66 μm was used to test the effect of applied pressure on the bonding strength, then the applied pressure that yielded the highest bonding strength was used to test the effect of RMF thickness on bonding strength. Brazed joints underwent lap shear testing to determine the strength (Figure 4.5b). The free end of the Ti64 plate was cut shorter to prevent buckling during lap shear testing. The total brazing procedure can be completed within 1 min and had negligible cooling time. A microhardness map was obtained using Phase II 900-390 Micro Hardness Tester to test a 300 μm × 300 μm area (each point is 50 μm apart).

4.2.3 Reaction Temperature Measurement

The temperature achieved during RMF brazing was estimated computationally and measured experimentally. The temperature was determined computationally using the Layer-wise Additive Manufacturing Predictions and Simulations (LAMPS) ©software (from

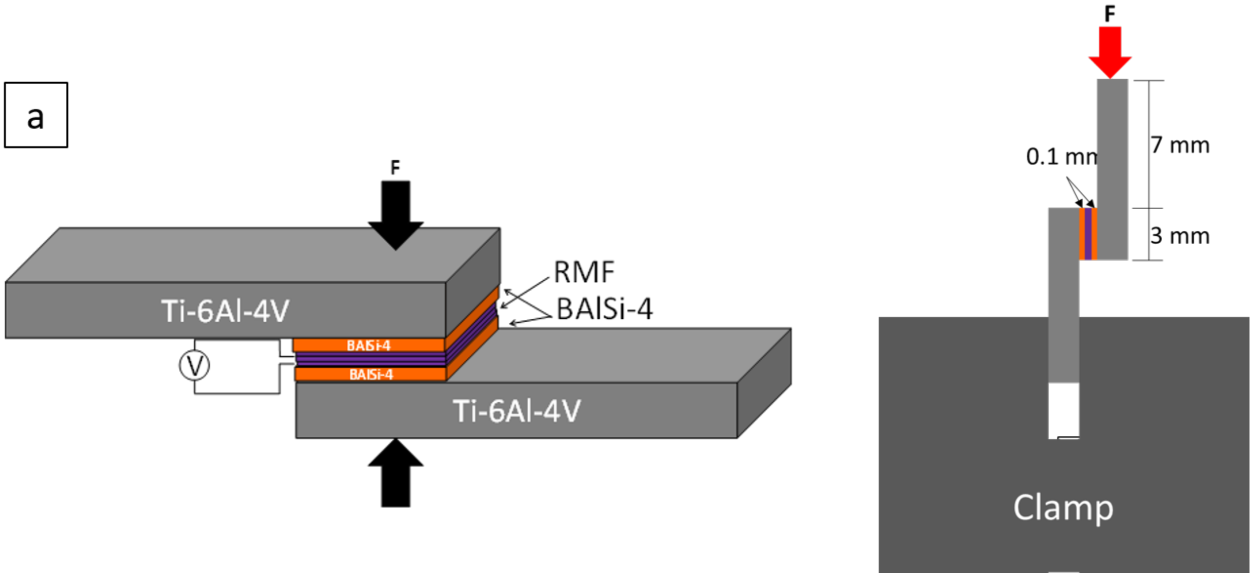

Figure 4.5: (a) Schematic of the configuration used in brazing experiments. (b) Schematic of lab shear testing [232].

Version 2.0, Composite Solutions and Digital Manufacturing LLC, Chandler, AR, USA, 2017) CS3DM. LAMPS ©is based on the analytical block technique that enables simulation of moving heat sources, such as the reaction propagation front in RMFs. The model had the parameters shown in Table 4.3. Thermal conductivity, the coefficient of thermal expansion, and heat capacity are assumed to be constant due to the short timescale of the reaction. It is reasonable for computations on the millisecond scale to assume that the thermophysical properties are temperature independent. Each frame is approximately 50 μs and the total simulation time was 3.44 ms. A slice of the cross-section was used for analysis of the temperature during brazing. The simulation time is shorter than the real reaction and cooldown procedure due to the computational limits of the LAMPS software.

To experimentally determine the brazing temperature, a PowerView HS-650 high-speed camera was used to capture several images of BAlSi-4 in a furnace heated to a known temperature. The average brightness of the area of interest was extracted using MATLAB

Table 4.3: Layer-wise Additive Manufacturing Predictions and Simulations (LAMPS ©) simulation parameters. T.C. is thermal conductivity and H.C. is heat capacity [232]

Material	Length (mm)	Width (mm)	Thickness (mm)	T.C. (W/m-K)	Density (g/cm^3)	CTE (10^{-6} K^{-1})	H.C. (J/g-K)
Ti-6Al-4V	30	3	0.44	6.7	4.43	8.6	0.526
BAlSi-4	3	3	0.1	205	2.66	21	0.9
RMF	3	3	0.135	76	4.91	12.5	0.536

(Version R2017b, MathWorks, Natick, MA, USA, 2017) at 20 °C, 735 °C, 785 °C, 835 °C, and 885 °C (confirmed by thermocouple) and fitted a function using MATLAB to obtain an equation for the temperature as a function of brightness. The same highspeed camera was used to record the brazing procedure from ignition to reaction extinction. MATLAB was, once again, used to extract the average brightness from the area of interest and, finally, the temperature was calculated using the derived equation. Note that the highspeed camera does not have the same time limitation as the LAMPS simulation, so the temperature of the entire brazing process can be measured. The MATLAB code used to perform this process is included in Appendix C.

4.2.4 Characterization

Cross-sectional analysis was evaluated by embedding a lap joint sample in epoxy and then polishing with SiC paper, then diamond paste and, finally, colloidal silica particles. SEM images were collected on a Zeiss Auriga Scanning Electron Microscope. X-ray diffraction measurements were conducted on a Panalytical Empyrean X-ray Diffractometer; the post-brazing XRD profile was obtained from the lap-joint cross-section embedded in epoxy the XRD beam line is perpendicular to the bond interface to detect all phases present in the joint. Lastly, EDS measurements were performed using a Zeiss MA15 EVO SEM equipped with a Bruker xFlash 6—30 detector. A PowerView HS-650 highspeed camera (1500 frames/s) was used to determine the reaction propagation speed of Ni/Al films. Differential scanning calorimetry (DSC) was performed using a Netzsch-Gertebau STA 449 C Jupiter Thermo-microbalance.

4.3 Results and Discussion

4.3.1 Characterization of RMF and BAlSi-4-Coated Ti64

The total thickness of the 1.5:1 ratio RMF achieved is 21 μm (Figure 4.6a) and the bilayer thickness of 120 nm is confirmed with each layer being 60 nm thick (Figure 4.6b). The total thickness of 1:1 ratio RMF achieved is 32.9 μm with a bilayer thickness of 110 nm as seen in Figure 4.6c. The average Ni layer thickness (white) is 44 nm and the average Al layer thickness is 66 nm, producing a 110 nm bilayer thickness (Figure 4.6d). The XRD pattern in Figure 4.7a shows that Ni and Al were deposited with no significant intermixing between the as-deposited layers. The post-ignition XRD scan was performed on a free-standing film that was peeled off the polyimide substrate. The post-ignition XRD scan detects only AlNi, indicating complete reaction of the RMF (Figure 4.7b). The total reaction heat is 1097 J/g for the 1.5:1 ratio (Figure 4.8a). The total reaction heat is 1275 J/g for the 1:1 ratio (Figure 4.8b). The reaction heat is lower for the off-stoichiometric ratio because some of the reaction heat is absorbed by the excess Ni. The reaction propagation speed is 4.36 m/s for the 1:1 ratio. For the 1.5:1 ratio, the propagation speed is almost half as fast at 2.31 m/s. As seen by the high-speed camera images (Figure 4.9), the RMF reaction completes very quickly (4.6 ms), but the film cools down over 30 times longer (169.5 ms) as indicated by the

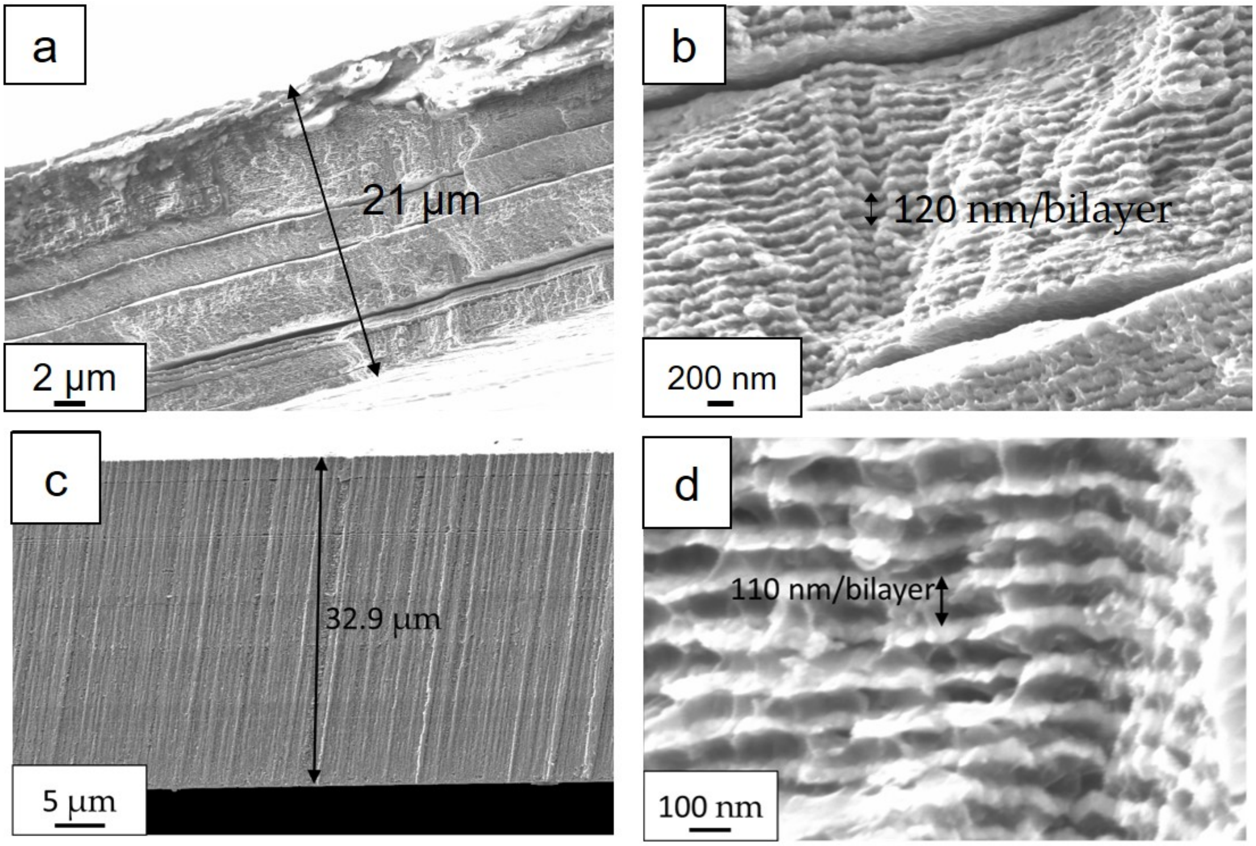

Figure 4.6: SEM image showing (a) the total as-fabricated RMF thickness and (b) the bilayer thickness for the 1.5:1 Ni:Al ratio. SEM image showing (c) the total as-fabricated RMF thickness and (d) the bilayer thickness for the 1:1 Ni:Al ratio (white is Ni and grey is Al) [232, 233].

diminishing light intensity. The Ni/Al reaction is known as a solid + liquid reaction [244]. In the context of the RMF reaction, first the Al layers melt, then, the solid Ni layers dissolve in the molten Al and this is concluded by crystallization of Ni-Al intermetallic compounds. Melting and dissolution occurs during reaction propagation and crystallization occurs after the end of the propagation phase [232, 245, 246].

4.3.2 Elemental Profiles and Temperature Evolution

The EDS line scan of the cross-section of a 1:1 RMF-brazed joint reveals the general distribution of elements in the joint. The dips and spikes in the Al and Si in the BAlSi-4

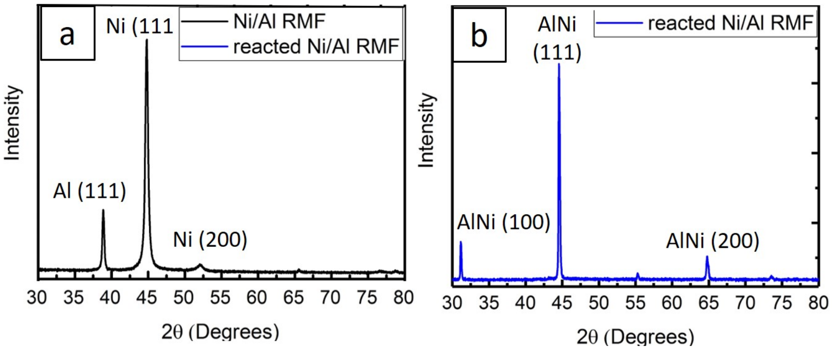

Figure 4.7: XRD pattern of the Ni/Al RMF (a) as-fabricated and (b) post ignition [232].

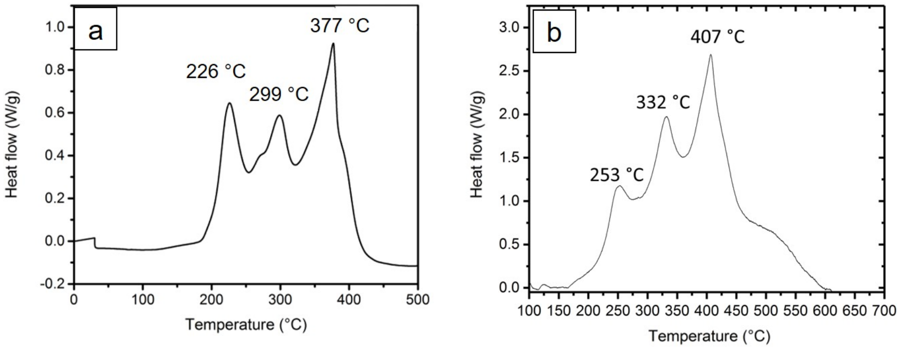

Figure 4.8: DSC measurement of (a) 1.5:1 Ni/Al RMFs and (b) 1:1 Ni/Al RMFs [232, 233].

region on both sides of the RMF is due to detection of Si-rich grains in an Al-rich matrix (Figure 4.10a,b). A high-resolution line scan of the Ti64-BAlSi-4 interface reveals a reaction zone produced during the plasma-arc coating (Figure 4.10c,d). Additionally, there is an increased concentration of Si detected at the Ti64-BAlSi-4 interface. Si has limited solubility in Ti in a solid state so, when Si attempts to diffuse into Ti from the molten brazing material, it stagnates at the Ti64 surface. Notice that there is a reaction zone at the Ti64-BAlSi-4 interface. EDS point analysis of this region reveals that this region is very Al-rich. Therefore, the formation of the reaction zone arises from Ti from the BM dissolving into the molten Al-Si and solidifying prior to the rest of the brazing material. Si is a melting point depressant so it is likely that the Al remained in its liquid state longer than normal, especially near the interface where the Si concentration was elevated [97]. If the Al is liquid for a longer

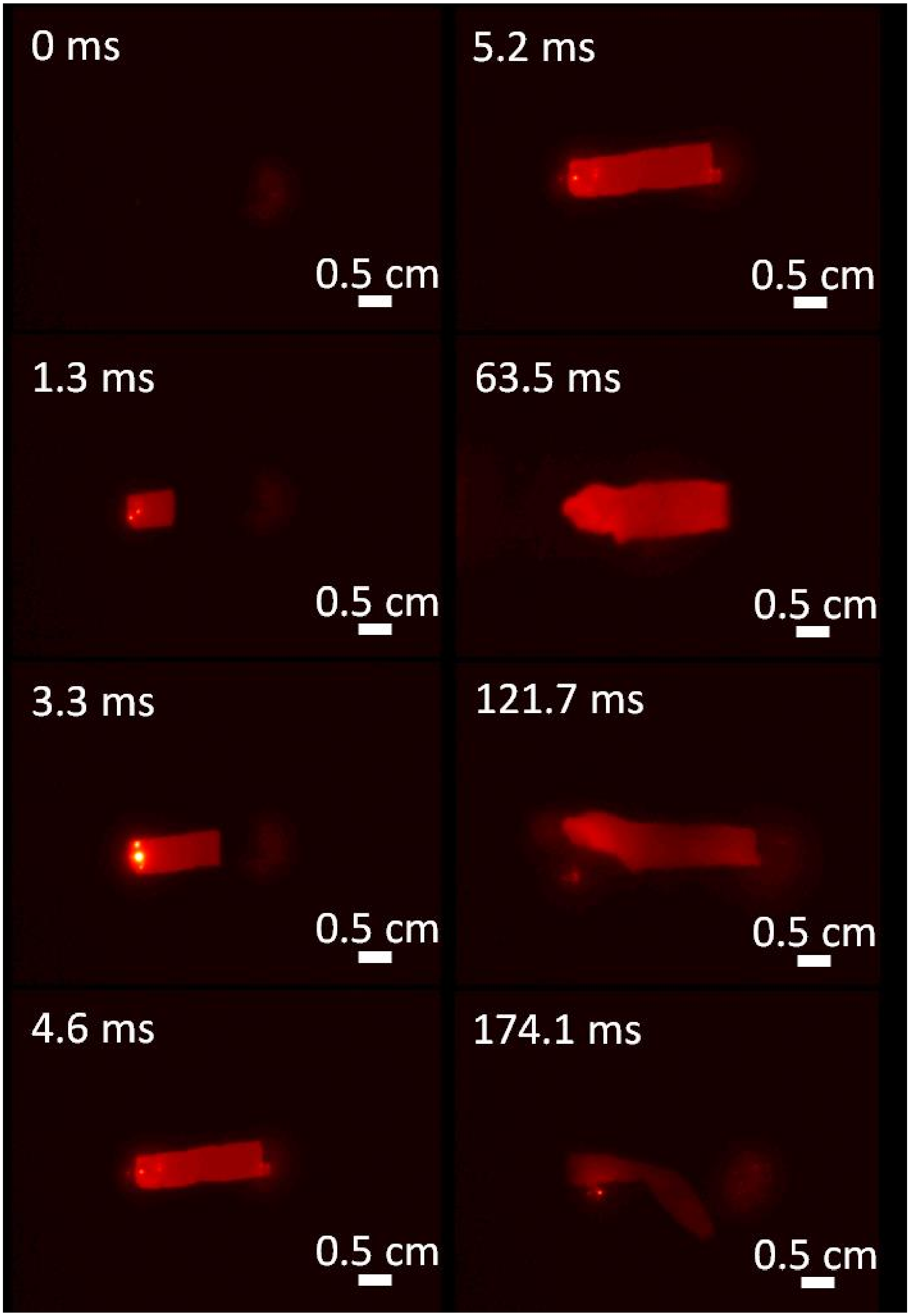
0 ms
5.2 ms
0.5 cm
0.5 cm
1.3 ms
63.5 ms
0.5 cm
0.5 cm
3.3 ms
121.7 ms
0.5 cm
0.5 cm
4.6 ms
174.1 ms
0.5 cm
0.5 cm

Figure 4.9: High speed camera measurement of the RMF reaction with 1:1 Ni:Al ratio [232].

time, it would allow more Ti to diffuse into the brazing material and expand the width of the reaction zone [232].

The RMF-BAlSi-4 interface also yielded interesting results. As seen in Figure 4.10e,f there are no obvious signs of a reaction zone, but there is a 1.6 μm thick Ni-rich zone 6.4 μm from the RMF-BAlSi-4 interface. The diffusion length for Al is approximately 2.0 μm and Ni is approximately 1.2 μm. No noticeable reaction zone forms for three primary reasons: (1) A lack of excess Ni (i.e., above the equiatomic amount), (2) short reaction time, and (3) the lower intrinsic diffusion coefficient of Ni compared to Al [247, 248]. During the reaction, virtually all the Ni is consumed in the RMF reaction and is largely unavailable for any significant reaction with the brazing material (i.e., not enough to produce a secondary phase in the reaction zone or on the interface). EDS indicates near-equiatomic amounts of Ni and Al at points 1, 3, and 4 (indicated in Figure 4.10e), with slight Al enrichment at point 4 and slight Ni enrichment at point 3. According to the Ni-Al phase diagram, these concentrations correspond to the AlNi phase. Point 2 detects almost two times the amount of Ni in this region compared to Al, which is characteristic of the Ni_5Al_3 phase.

This is in direct contrast to the 1.5:1 RMF, where the excess Ni reacted with the molten Al in the BAlSi-4 and formed a dendrite structure as seen in Figure 4.11. EDS point analysis was performed on points of interest and the results show that these dendrites (point 2) are the Al_3Ni intermetallic phase (Table 4.4). The formation of these dendritic structures is most likely caused excess Ni from the RMF diffusing into the molten brazing material and rapidly solidifying on the interface. XRD of the brazed joint (Figure 4.12) revealed several phases belonging to the parent structures, but the two particularly interesting peaks belong to Al3Ti and Ni_5Al_3, which, in conjunction with the EDS data, belong to the reaction zone

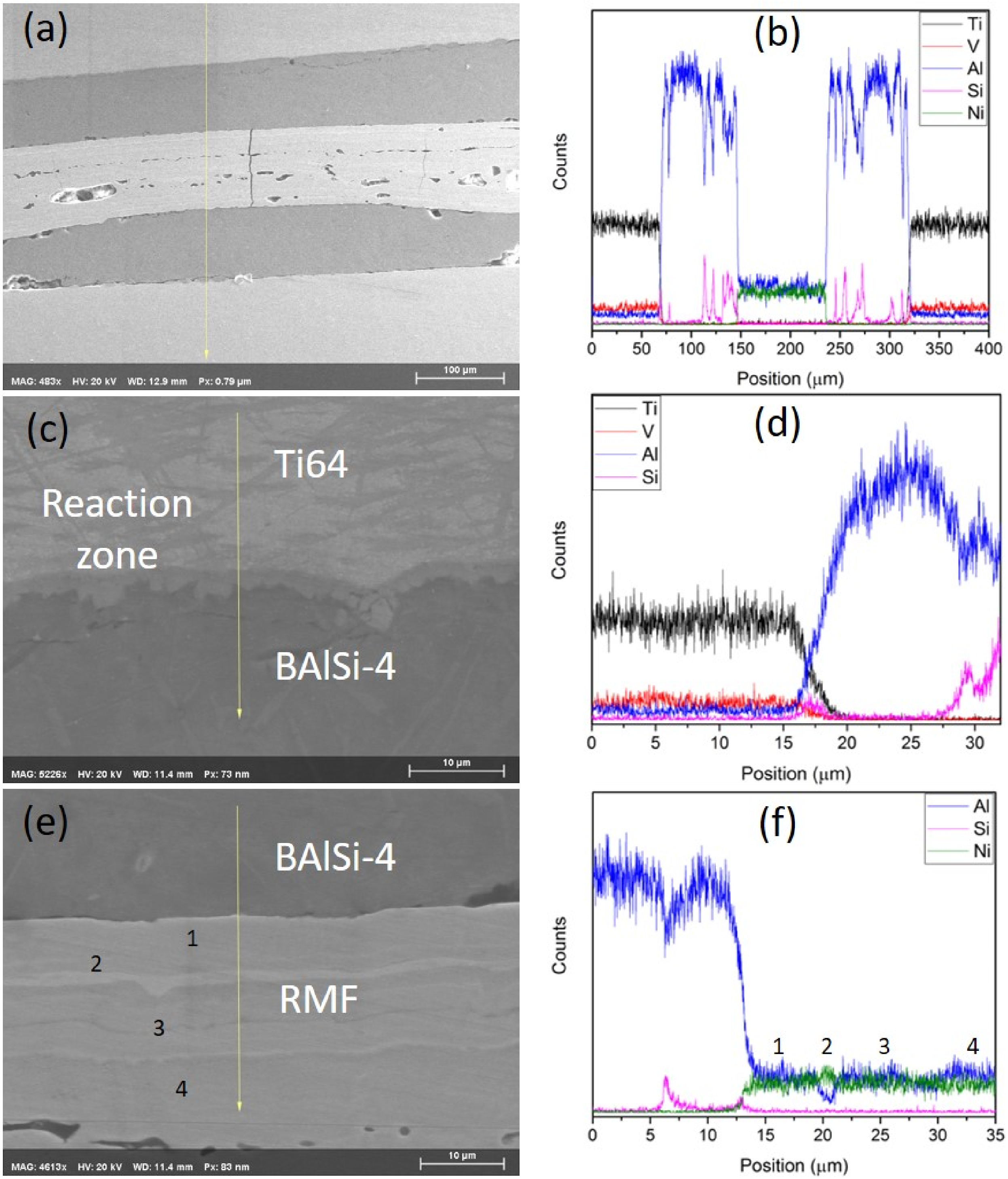

Figure 4.10: EDS line scan of (a,b) the entire brazed joint, (c,d) the Ti64-BAlSi-4 interface, and (e,f) BAlSi-4-RMF interface with select point analysis [232].

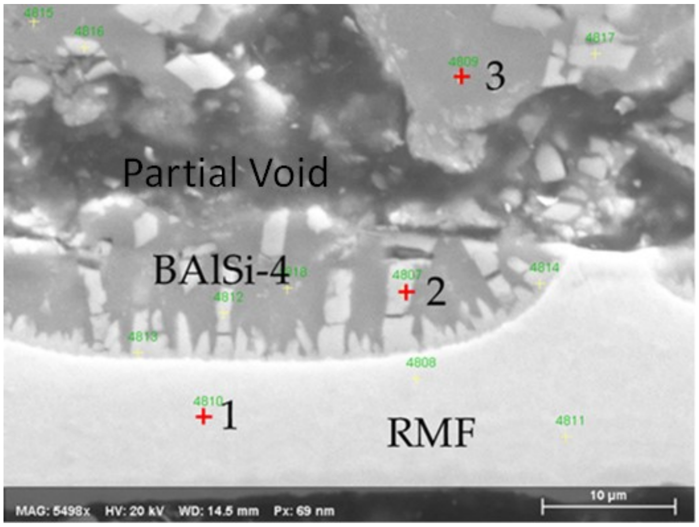
4815
4816
4809
3
4817
Partial Void
BAlSi-4
4818
4812
4813
4807
2
4814
4808
4810
1
RMF
4811
MAG: 5498x HV: 20 kV WD: 14.5 mm Px: 69 nm
10 μm

Figure 4.11: Brazing interface between BAlSi-4 and the 1.5:1 Ni/Al RMF [233].

at the Ti64-BAlSi-4 interface and the Ni-rich region in the RMF, respectively. The Al_3Ti phase was formed during the plasma coating process based on SEM observations prior to RMF brazing.

The temperature evolution of the joint as a function of time helps in understanding the most probable pathway to the nucleation of the Ni-rich phase in the brazing joint. The temperature distribution of the brazing joint cross section, according to LAMPS, is shown in Figure 4.13. The BAlSi-4 and RMF reach a maximum temperature of approximately 813 °C, which is far above the liquidus line of BAl. The LAMPS simulation shows that the temperature within the brazing region (i.e., the RMF and BAlSi-4) increases by 991 °C/ms. The temperature decreases at a rate of 32.9 °C/ms in the center of the RMF, 38.8 °C/ms at the RMF-BAlSi-4 interface, and 37.5 °C/ms at the Ti64-BAlSi-4 interface, as shown in Figure 4.14. The faster heat dissipation at the interface is due to heat sinking in the BAlSi-4 and Ti64. This simulation is further validated by the surface measurement

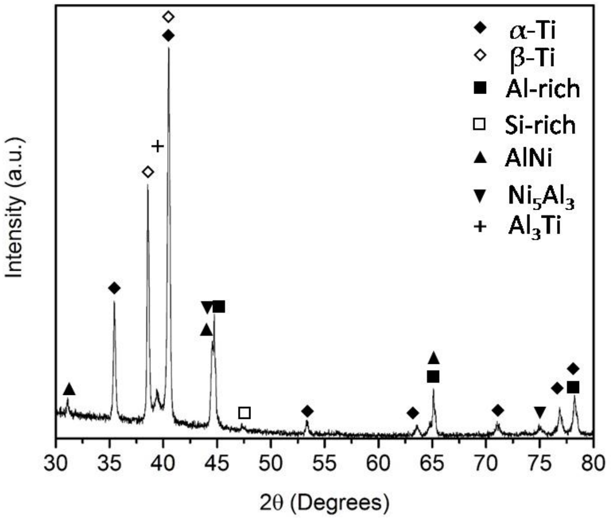

Figure 4.12: XRD pattern of the brazed joint [232].

Table 4.4: Phase summary of the EDS point analysis shown in Figure 4.11 [233]

Region	Ni	Al	Si	Identified Phases
1	69.3	30.8	0	AlNi+Al_3Ni_5
2	17.1	74.7	8.2	Al_3Ni
3	N.D.	98	N.D.	(Al)

of brazing materials with high speed imaging. The measurement indicates the maximum surface temperature reached is only 683 °C. The temperature increases by 125.5 °C/ms and decreases by 6.827.3 °C/ms, depending on how much time has elapsed after the maximum temperature is reached. The measured temperature is significantly lower than the simulated temperature because the LAMPS ©simulation is an idealized case of RMF brazing. For a real case, thermal conductivity and heat capacity are functions of temperature and, in the LAMPS simulation, it is assumed to be constant. Heat capacity increases with temperature for most materials, including Al [249–251], which means, as the temperature increases, more heat will be required to increase the temperature per degree Celsius. Convective heat loss is also not accounted for in the LAMPS ©simulation. Convective heat loss and higher heat capacity and higher temperatures will, certainly, decrease the maximum temperature

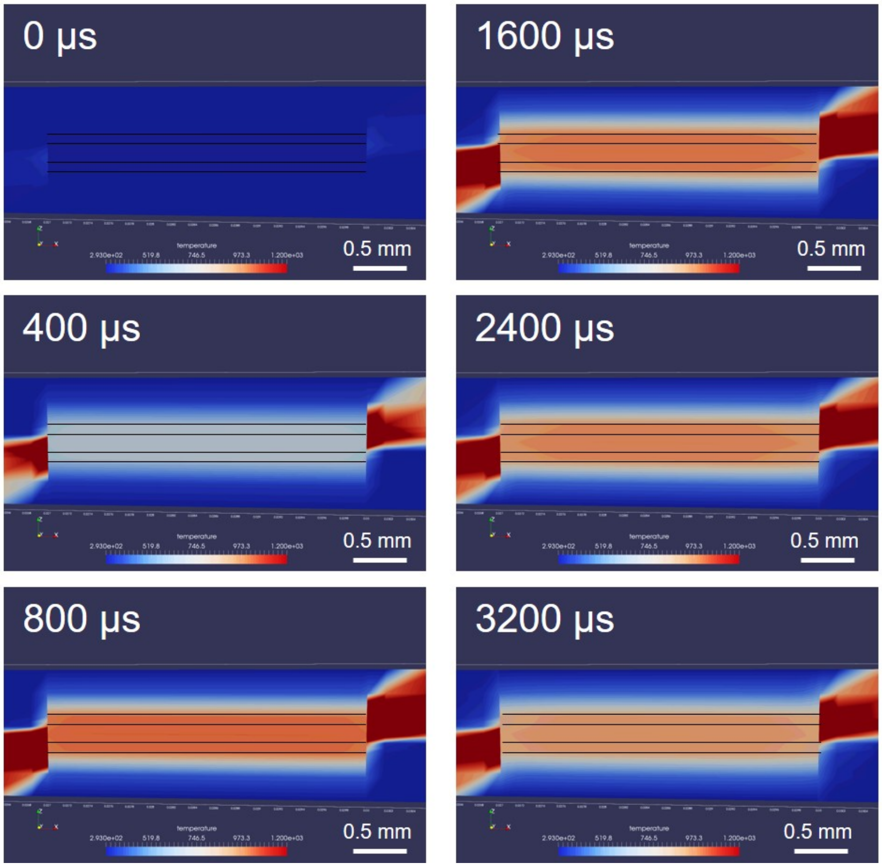

Figure 4.13: Snapshots of the LAMPS ©simulation, showing the temperature evolution and distribution in the brazed joint at various time steps. The places of high heat outside the joint are due to the heating of stagnant air around the lap joint [232].

attained during the RMF reaction. Lastly, we assume, in the LAMPS©simulation, that the RMF is defect free and perfectly flat. However, defects present in the real RMF [236], which are possibly introduced through applied pressure, can decrease the propagation efficiency of the film [252].

Based on the measured temperature, heating rate, and cooling rate and assuming nearly instantaneous melting, the BAlSi-4 would be in the liquid state for approximately 10 ms. Most of the interdiffusion occurs when the brazing material is in a molten state. When the brazing material and the RMF return to the solid state, diffusion slows down significantly. When the reaction occurs, Al diffuses into the RMF from the brazing material and Ni diffuses

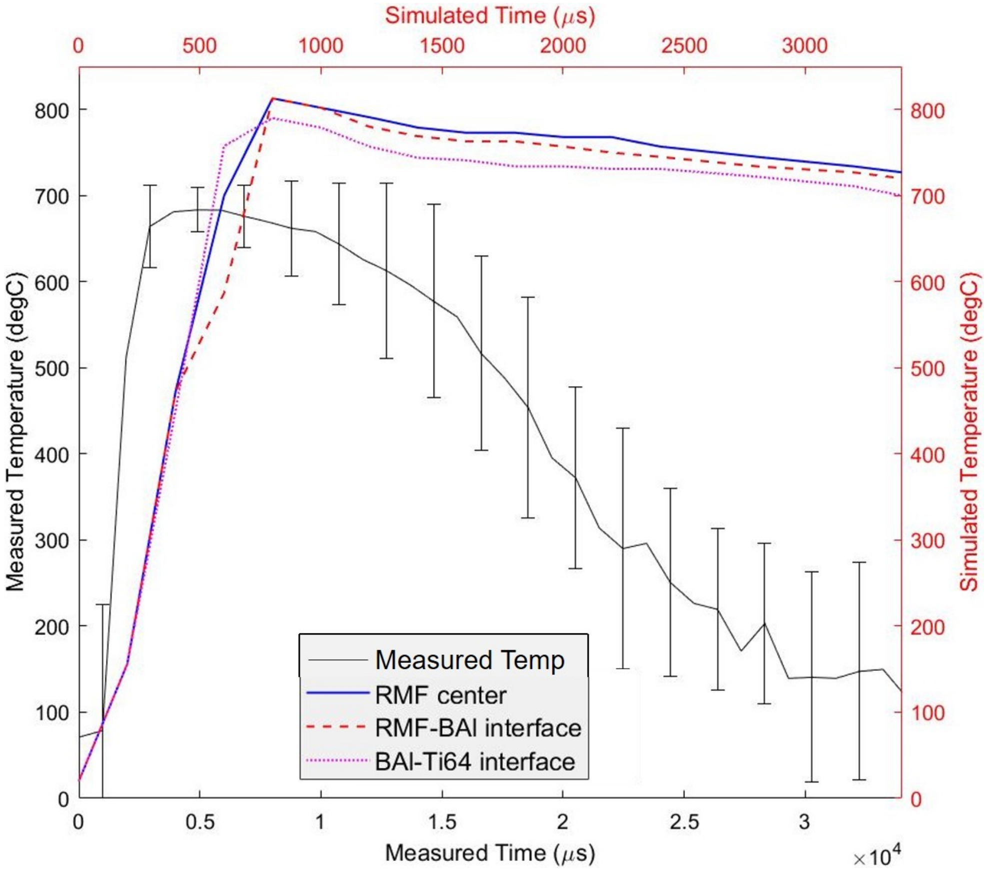

Figure 4.14: Temperature as a function of time simulated by LAMPS©(red, blue, and magenta lines) and measured using the highspeed camera (black solid line) [232].

into the brazing material. Since the temperature cools at the interface first, the braze and the RMF will become completely solid at the interface first. As the temperature decreases throughout the joint, the solubility of Ni in Al rapidly declines. Due to the temperature gradient that exists in the joint cross-section, there is also a Ni diffusivity gradient. When the Ni diffusivity and solubility drop below some critical value, the Ni will continue to diffuse from the center of the RMF, but the diffusion and dissolution rate of Ni will quickly slow down close to the interface due to the lower temperature. When the portion of the RMF that is 6.4 μm from the BAlSi-4-RMF interface has fully solidified, there is a build-up of Ni that has not diffused into the rest of the RMF layer or dissolved in the molten Al during the reaction propagation and, based on the Ni now present in this region, that portion of the RMF will crystallize into Ni_5Al_3.

4.3.3 Mechanical Properties

The shear strength of the brazed joint was evaluated as a function of pressure and the RMF thickness. Applied pressure serves an important role in RMF brazing because it ensures intimate contact between the RMF and the brazing material [253]. However, excessive pressure will cause the molten brazing material to be squeezed out of the joint, which is why the bonding strength decreases above 20 MPa applied pressure, as shown in Figure 4.15a. The RMF thickness was kept to 66 μm for the pressure investigation. The maximum bonding strength (10.6 MPa) was achieved using 20 MPa applied pressure and RMF thickness = 165 μm (Figure 4.15b). The effect of increasing the RMF thickness is, primarily, increasing the overall heat release, which increases the amount of molten liquid during brazing. The low bonding strength, despite the sufficient interface temperature, is

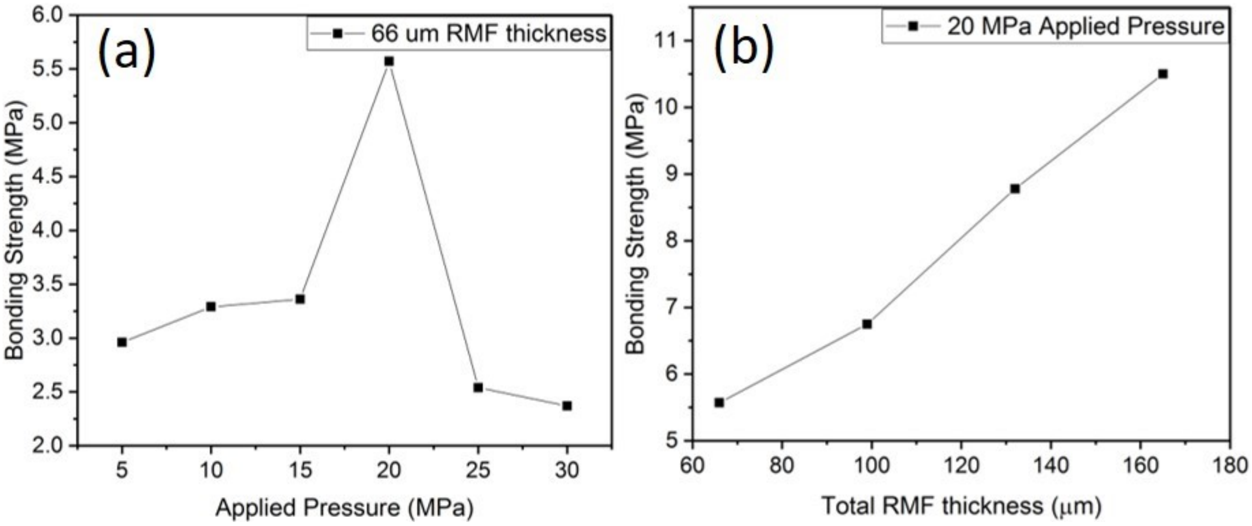

Figure 4.15: (a) Bonding strength as a function of applied pressure (RMF thickness kept constant at 66 μm). (b) Bonding strength as a function of total RMF thickness (Applied pressure = 20 MPa).

attributed to the limited metallurgical bonding and low reaction time. These two causes are related by diffusion. Low diffusion is a result of a short reaction time and limited metallurgical bonding is partially caused by low interdiffusion. Despite the clear reaction between the RMF and the BAlSi-4, the non-equimolar RMF produces significantly weaker bonding (0.59 MPa) than the equimolar RMF [233].

The fracture surfaces, shown in Figure 4.16, display some small cleavage fracture features. Several microcracks also appear in the surface as the RMF thickness increases. The appearance of microcracks and cleavage fracture features is partially due to the brittle nature of the AlNi and Ni_5Al_3 intermetallic compounds that comprise the RMF layer after

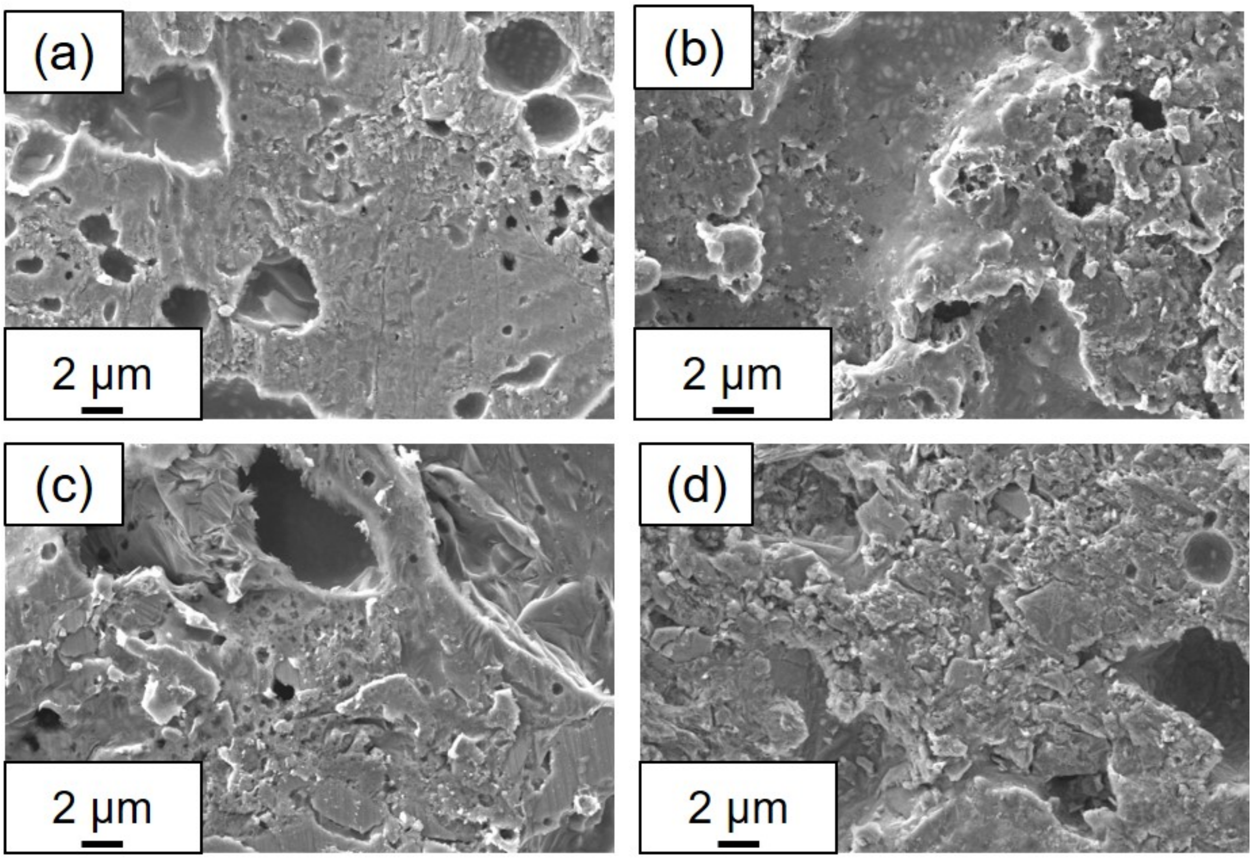

Figure 4.16: Fracture surfaces of RMF-brazed joints, with an RMF thickness of (a) 66 μm, (b) 99 μm, (c) 132 μm, and (d) 165 μm.

brazing. Also, as previously stated, the low interdiffusion between the brazing and RMF layers ensures that the brazed joint fails primarily at the RMF-BAlSi-4 interface due to a lack of strong metallurgical bonding. There is most likely a large amount of residual stress at the RMF-BAlSi-4 interface due to the large lattice mismatch between the Al matrix (lattice constant = 4.046 Å) and AlNi (lattice constant = 2.887 Å). Additionally, the hardness map, shown in Figure 4.17, shows that there is a very steep hardness gradient across the narrow RMF-BAlSi-4 interface, further indicating a lack of a reaction zone along that interface. Furthermore, the hardness is uniform within the RMF (524 HV) and BAlSi-4 (75 HV) layers of the brazed joint. The Ti64-BAlSi-4 interface, however, has a hardness gradient across the interface due to the presence of the Al_3Ti at the interface. The bonding strength can be further improved by using the AlNi product of the RMF reaction as a strengthening phase instead of a monolithic load bearing layer of the joint and altering the Ni:Al ratio at the top and bottom of the RMF to promote reaction between BAlSi-4 and the RMF. These improvements will be discussed in greater detail in Chapter 7.

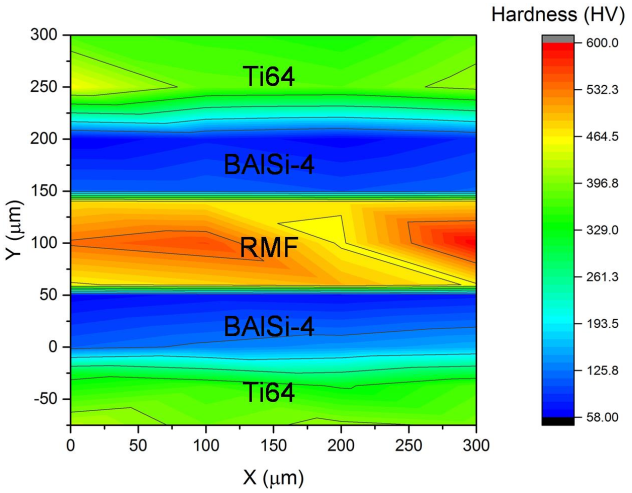

Figure 4.17: Hardness map of a 300 μm × 300 μm section of the brazed joint [232].

4.4 Conclusions

Self-powered brazing using Ni/Al RMFs has been demonstrated for quick brazing BAlSi-4-coated Ti64 without using a long brazing procedure, such as furnace brazing. The total heating and cooling time was less than 100 milliseconds. Due to a difference in the diffusivity of Ni and Al, Ni_5Al_3 nucleated in the RMF, in addition to the AlNi phase. However, no apparent reaction zone formed at the RMF-BAlSi-4 interface due to a lack of excess Ni and the extremely short brazing time. The short brazing time also sacrifices sufficient diffusion that is typically required for robust joining. The Ti64-BAlSi-4 interface, on the other hand, clearly had a reaction zone in which Al_3Ti was present. Applied pressure needs to be controlled to optimize bonding performance and there was a positive correlation between bonding strength and RMF thickness. Due to the local heating, the total operation can be completed within 1 min. This significantly simplifies the brazing technique.

Chapter 5

Ni Nanoparticle Transient Liquid Phase Bonding

Disclosure

This chapter based on two publications. The first publication was originally published by Denzel Bridges, Raymond Xu, and Anming Hu in 2018:

[254] Bridges, D., Xu, R. & Hu, A. Microstructure and mechanical properties of Ni nanoparticle-bonded Inconel 718. Mater Design 174, 107784, (2019).

Denzels contributions in the article: Fabricated Ni nanoparticles, performed transient liquid phase bonding experiments, carried out microstructure characterization and mechanical testing. Lastly, Denzel wrote and revised the article.

Co-authors contributions are listed as follows: Dr. Raymond Xu provided funding from the Rolls-Royce Corporation, provided guidance on the joining experiment design and revised the article. Dr. Anming Hu was the PI on the research, assisted in data analysis and experiment design and revised the article.

5.1 Motivation and Background

It has been previously discussed that Cu-Ag-based [76] and Ni-based [77] BMs are good choices for joining IN718 because they are metallurgically compatible, do not form intermetallic compounds, and/or have melting temperature lower that the BM. Although, sufficiently strong joining can be achieved using Cu-Ag-based nano-BMs, Cu-Ag alloys have melting points close to the maximum operating temperature of IN718 [255], thus they cannot be used at high temperature. Ni-based BMs, on the other hand, has much higher melting points which can be closer to that of most Ni superalloys. For example, an alloy containing 90% Ni and 10% Cr by weight has a melting point of approximately 1440 °C which is much higher than the solidification temperature of Inconel 718 (1250 °C) [256]. Therefore, to avoid melting or otherwise altering the base metal, MPDs are essential to lower the melting point below the melting point of most Ni superalloys [225]. To effectively use an MPD-containing BM, the MPD must be diffused from the BM into the BM so that brittle, low melting borides, silicides, etc. cannot form as discussed in Chapter 1. TLP bonding is sometimes used to sufficiently diffuse the MPD into the base metal [197]. However, traditional TLP bonding requires long heat cycles to ensure the MPD is not concentrated in the base metal or BFM. Additionally, prolonged exposure to temperatures exceeding the recommended operating temperature causes significant grain growth in nickel superalloys which reduces the mechanical strength and hardness due to loss of grain boundary strengthening [35, 86]. Grain growth and intermetallic compound formation can negatively affect the thermo-mechanical performance of IN718. Since Cu-Ag-based brazing materials do not have the necessary high-temperature compatibility with IN718, Ni NPs are a good alternative since Ni has a bulk melting point 671 °C higher than the eutectic Cu-Ag temperature and 370 °C higher than the melting point of pure Cu [75]. Ni NPs have been used by Hausner et al. to join NiCr stainless steel using up to 30 MPa of applied pressure and bonding temperature of 850 °C and obtained a joining strength of 120 MPa . Without applied pressure, the joint was noticeably weaker (100 MPa) [30]. Tiwari et al. also used Ni NPs to join 316 stainless steel and obtained a bonding strength of 140 MPa and void fraction ¡5 % [257]. In previous high-temperature NP joining (nano-joining) studies, the heating rate and NP size effects on the joint properties are seldom studied. Therefore, in this study, we will investigate Ni NPs as a high temperature MPD-free filler metal for joining IN718. The effects of bonding temperature, Ni NP size, and heating rate on the mechanical properties and microstructure of Ni NP-brazed IN718 will be elucidated. The underlying nano-joining mechanism is discussed.

5.2 Experiments and Methods

5.2.1 Materials

Nickel chloride hexahydrate was purchased from Acros Organics. All other chemicals were purchased from Fisher Scientific. An IN718 sheet was purchased from McMaster-Carr (AMS 5596). All polishing consumables were purchased from Allied High Tech.

5.2.2 Nickel Nanoparticle Filler Metal Preparation

0.7 grams of nickel chloride hexahydrate was dissolved in 70 mL of ethylene glycol, then 1.1 mL of pure hydrazine hydrate was added to the mixture. Mechanical stirring was used during the synthesis process because Ni NPs are magnetic. Once the solution reached 100 °C, 0.05 grams of sodium borohydride dissolved in 5 mL of deionized water was added as the primary reducing agent. The injection rate of sodium borohydride was adjusted to control the particle size. Sodium borohydride was added at three rates: (1) poured rapidly, (2) 1 mL/min, and (3) 0.03 mL/min. The temperature was further increased to 120 °C, held for 5 hours, then allowed to cool naturally. The black Ni NPs were then washed with ethanol and collected by centrifugation three times. The collected Ni NPs were dried using a freeze dryer. In preparation for TLP bonding, 30 mg of dry Ni NPs were loaded into a circular dry pellet press (inside diameter = 6 mm) without any binder material and uniaxially pressed under 2 GPa of pressure. The resulting pellet is 0.3 mm thick. A pressed pellet was used instead of an NP paste to increase the initial green density of the NP filler metal.

5.2.3 Transient Liquid Phase Bonding

For TLP bonding, 3 mm × 40 mm × 0.4 mm (W × L × T)specimens of IN718 were cut and cleaned ultrasonically in acetone followed by 50% HCl aqueous solution etching in preparation for Ni plating. Ni plating was done using a Woods nickel strike solution for 15 minutes (67 mA/cm^2) followed by a modified Watts nickel plating solution (0.684 M nickel sulfate hexahydrate, 0.467 M ammonium chloride, and 0.485 M boric acid) for 10 minutes. The resulting Ni plating was approximately 50 μm thick. The Ni NP pellet and the Ni-plated IN718 were arranged in a lap joint configuration (Figure 5.1) with a 2 mm overlap and held in place by a graphite clamp. The lap joints (Figure 5.1 inlet) are heated in an Across International STF1200 tube furnace according to the temperature profile in Figure 5.1. The vacuum level was about 7.5 × 10^{-4} Torr. Four heating rates of 2, 5, 10, and 15 °C/min were used to test the effect of the heating rates on the microstructure and mechanical properties, respectively. The first temperature plateau at 900 °C for 30 minutes

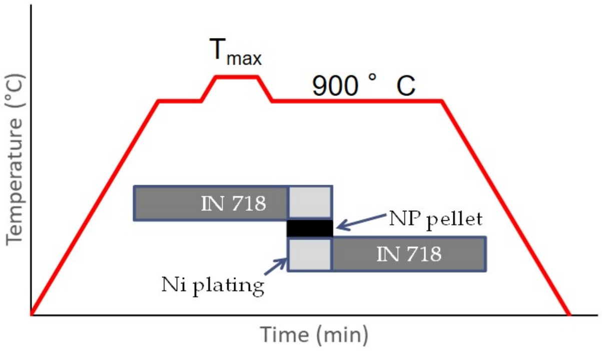

Figure 5.1: TLP heating profile and lap joint configuration (inlet) [254].

was added to homogenize the temperature of the lap joint prior to reaching the maximum temperature (T$_{max}$). T$_{max}$ was maintained for 40 minutes and the final temperature step (900 °C) was held for 2 hours. Three maximum temperatures T$_{max}$ of 950, 1000, and 1050 °C were investigated. The time spent at T$_{max}$ was kept short and T$_{max}$ was limited to $\leq$ 1050 °C to ensure that minimal grain growth occurred in the IN718 [35]. The final temperature step at 900 °C was held to encourage diffusion between the IN718 and Ni NPs [258]. Brazing was also carried out using AWS BNi-2 brazing filler metal foil (80 μm thickness) and BNi-2 325 mesh micro-sized powder.

5.2.4 Microstructure Characterization

A cross-sectional analysis was evaluated by embedding a lap joint sample in epoxy which was polished with SiC paper, and diamond paste up to 0.25 μm. Samples were then etched with aqua regia. An additional vibratory polishing step was done for EBSD samples using a Buehler VibroMet 2 vibratory polisher. Scanning Electron Microscopy (SEM) images of as-synthesized NPs and fracture surfaces of tested lap joints were collected on a Zeiss Auriga Scanning Electron Microscope using the secondary electron detector. Transmission Electron Microscopy (TEM) of as-synthesized NPs was conducted using a

Libra 200 transmission electron microscope. Ambient temperature X-ray diffraction (XRD) measurements were conducted on a Panalytical Empyrean X-ray Diffractometer. In-situ high-temperature XRD (HTXRD) measurements were also done with the Empyrean and the furnace used for in-situ heating was an Anton Paar HTK 1200N. The temperature was increased to 1000 °C under vacuum ($?<1\times10^{-4}$ Torr) at a rate of 10 °C/min, held for 30 min, and then decreased to 900 °C and held for 2 hours. Measurements were taken continuously throughout the heating process. FTIR analysis was conducted on a Ni NP pellet that was heated to 1050 °C at a rate of 15 °C/min to detect residual organic content. Lastly, energy dispersive x-ray spectroscopy (EDS) and electron backscatter diffraction (EBSD) measurements were performed using a Zeiss MA15 EVO SEM equipped with a Bruker xFlash ®6—30 detector and Bruker e- FlashFS EBSD detector, respectively. Thermo-Calc was used to produce a Ni-Fe-Cr ternary phase diagram at 293 K.

5.2.5 Mechanical Performance Evaluation

For bonding strength evaluation, tensile tests were completed using a ZHIQUP Precision Instruments, 1500D force gauge with a constant displacement rate of 1 mm/min (5 acquisitions/second). Three trials were conducted for each test condition to obtain an average strength at fracture. Hardness mapping was done with a LECO LM100 AT micro-hardness tester under 25-gram load. Samples were prepared for digital image correlation (DIC) measurements by polishing one surface of the lap joint up to 1 μm diamond paste followed by aqua regia etching. DIC was done using a 10MP AmScope microscope camera attached to an adjustable frame and coupled with a 10× or 50× microscope lens. Analysis of the images taken using the microscope camera was done using an open source MATLAB software called Ncorr [259]. All specimens used for Microstructure Characterization and Mechanical Testing were in as-TLP bonded condition without post-bonding heat treatment.

5.3 Results and Discussion

5.3.1 Nanoparticle Characterization

The diameter of the spherically-shaped nanoparticles was determined by SEM measuring of 200 NPs using ImageJ. When sodium borohydride is added all at once, the average particle diameter was found to be about 22 nm (Figure 5.2a-b). Figure 5.2c-d shows the SEM and the accompanying size distribution of Ni NPs with an average diameter of 29 nm that were synthesized using a 1 mL/min injection rate, and Figure 5.2e-f shows the SEM and the accompanying size distribution of Ni NPs (average diameter = 42 nm) synthesized using a 0.03 mL/min injection rate. Essentially, nanoparticle wet chemical synthesis is governed by two fundamental processes: nucleation of seed particles (<10 nm) and growth. Growth occurs via reduction of $NiCl_2$ or Ostwald ripening. Since the lower injection rate means less $NiCl_2$ is reduced, NPs grow through smaller particles dissolve and redeposit on larger particles (i.e. Ostwald ripening) and coalescense of smaller particles and reduced metal ions in the liquid. Faster injection rate means much more particles will nucleate and grow through consumption of reduced $NiCl_2$ [139]. The end result of the control of the injection rate is that the nucleation and growth steps are controlled [110]. Hereafter, the 22 nm NPs will be referred to as Ni-22, the 29 nm NPs will be referred to as Ni-29, and the 42 nm NPs will be referred to as Ni-42. Figure 5.3 shows that there is not a strong plasmonic response from these NPs, but the NPs do have moderate absorption across the visible spectrum.

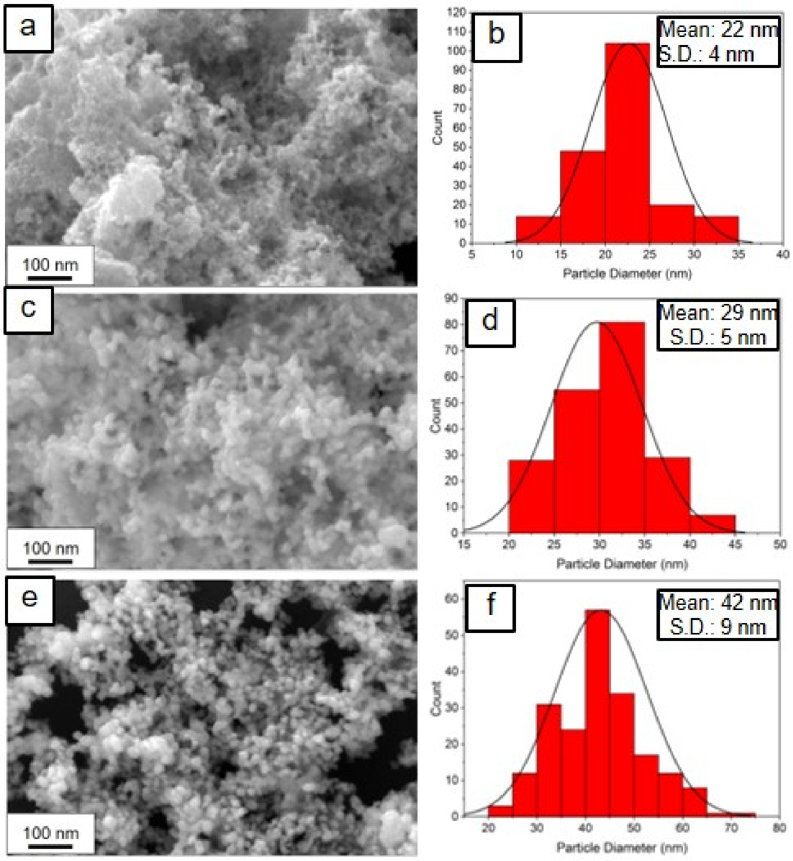

Figure 5.2: SEM and size distribution (histogram and distribution curve) of Ni NPs synthesized at 120 °C with the sodium borohydride added (a-b) rapidly, (c-d) dropwise added approximately 1 mL/min and (e-f) dropwise added approximately 0.03 mL/min. The mean and standard deviation (S.D.) are also listed in the figure [254].

TEM micrographs of each Ni NP samples reveal the presence of an organic shell (shown with red dotted line) around the NPs as seen in Figure 5.4. The Ni-22 NPs have an organic layer (3.7 nm) over twice the thickness of the Ni-29 (1.7 nm) and Ni-42 NPs (1.5 nm). The darkly colored regions are the Ni NPs and the lighter regions are the organic shell. In Figure 5.5, FTIR analysis shows that the Ni NPs respond more strongly when the average particle size is smaller both as-synthesized and after heating. This indicates more organic content. As synthesized, the Ni NPs have peaks at 1255-1280 cm^{-1} (C-O stretch bond), 890-905 cm^{-1} (-CH=CH-(trans)), and 750-840 cm^{-1} (=C-H bending bond). Post-heating

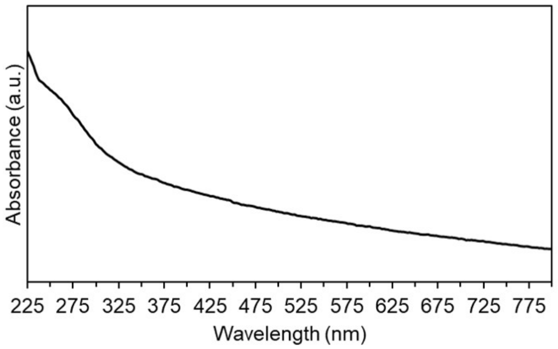

Figure 5.3: Typical UV-vis spectrum for Ni NPs

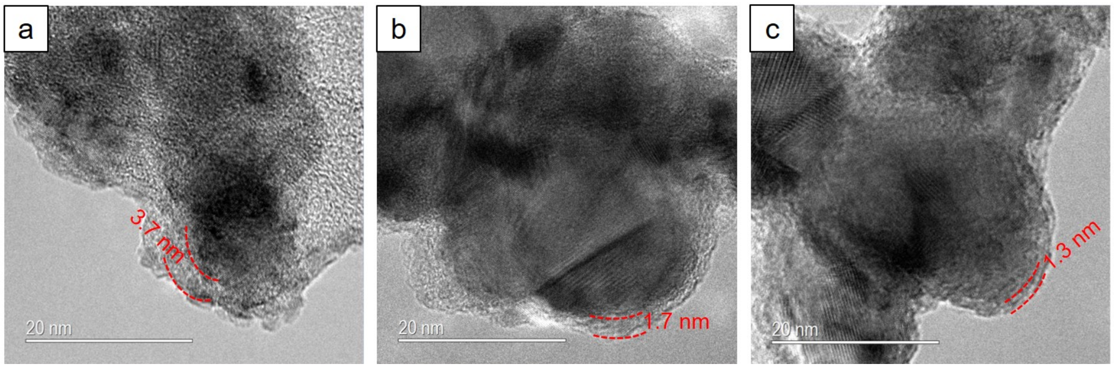

Figure 5.4: TEM micrograph of Ni NPs with the organic layer thickness labeled (red dotted line) from (a) Ni-22, (b) Ni-29, and (c) Ni-42 [254].

the C-O stretch bond remains in Ni-29 and Ni-42. Ni-22 shows a valley at 1025 cm^{-1} and a peak at 929 cm^{-1} which corresponds to an alkene type C-H stretch bond. Both types of bonds are characteristic to those found in ethylene glycol. Based on the FTIR scan, the organic layer around the Ni NPs is an organic complex produced by the Ni NP surface coated with the ethylene glycol molecules.

The Gibbs-Thomson (GT) equation (Eq. 1.17) was used to approximate the melting point of the Ni NPs synthesized [260]. The liquid-drop model is another method used to approximate the particle melting point Eq. 1.18 [102]. Considering that the bulk melting point of Ni is 1455 °C, the melting point depression is rather modest by the GT and LD approximations. For surface melting, we use the Chernyshev model (Eq. Equations 1.20

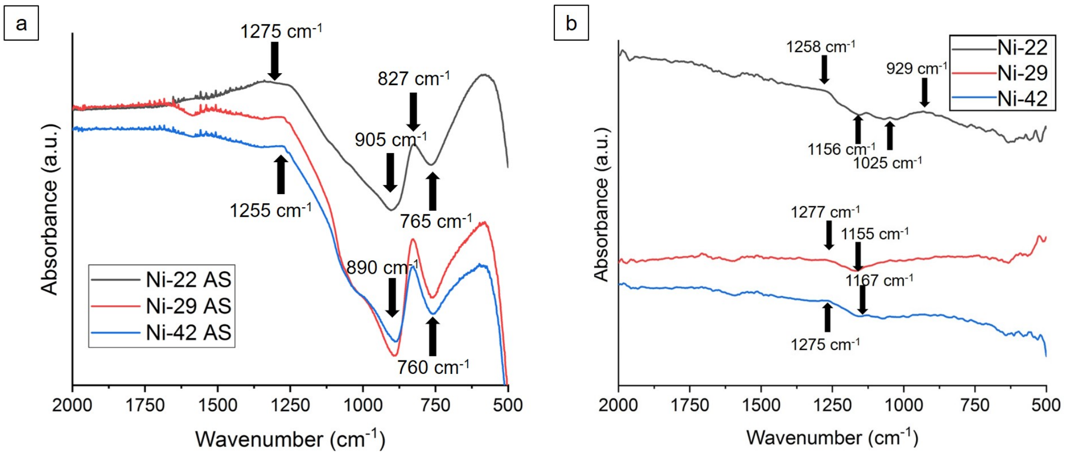

Figure 5.5: FTIR of (a) as-synthesized (AS) Ni NPs and (b) Ni NP pellet heated to T$_{max}$ =1050 °C at a heating rate of 15 °C/min [254].

to 1.23) for calculating the onset surface melting point (T$_{SM}$) which is based on the Lindemann melting criterion [108].

Recall that the Chernyshev model assumes the surface layer is three atomic layers thick and that surface melting occurs when the NP surface is in a quasi-liquid state. Chernyshev states that the surface melting point does not respond to particle diameters >10 nm and hence says it is unreliable for NPs >10 nm in diameter. A dotted line is used for the Cheryshev model for particle diameters >10 nm. T_{MP} and T$_{SM}$ as a function of temperature are plotted in Figure 5.6. Molecular dynamics calculations of the melting and SM temperatures from Zhang et al. [261] and Wang et al. [105] are slightly higher than calculated by the GT and LD models as seen in Figure 5.6b. In both manuscripts, the Lindemann criteria and embedded atom method potentials were used to determine the melting and surface melting temperatures. Note that molecular dynamics simulations have a much shorter time scale (picosecond to nanosecond time scale) than the brazing procedure used in this study, so the melting behavior may vary in real time and in a real vacuum environment. In fact, Wang et al. reports that T$_{SM}$ is nearly the same as the T_{MP} according

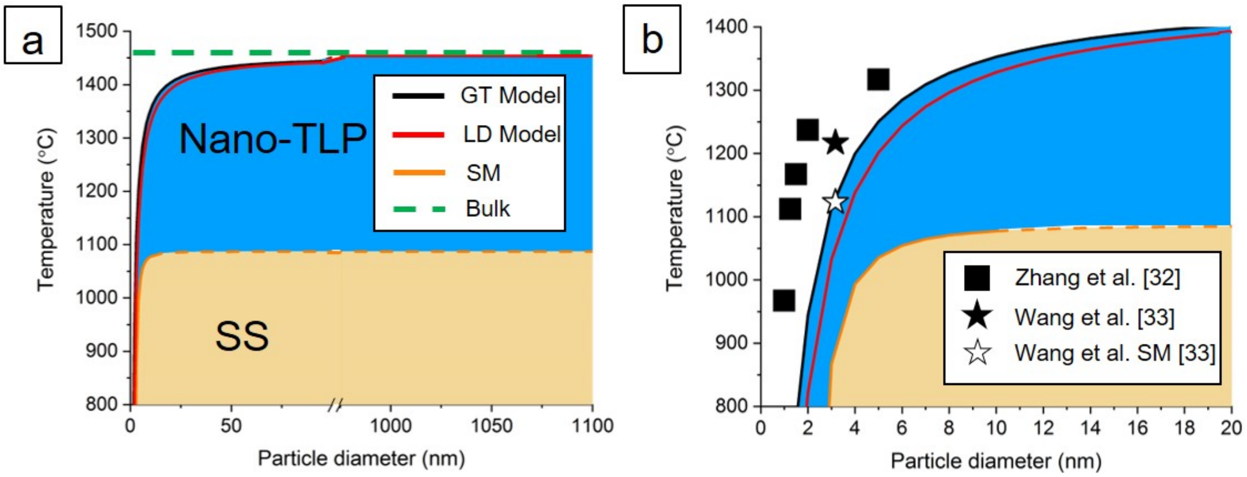

Figure 5.6: (a) The melting point as approximated by the Gibbs-Thompson (GT) and Liquid drop (LD) models, SM melting point calculated by the Chernyshev model as a function of particle diameter with the bulk melting point (M.P. indicated by a green dotted line. The blue shaded region is the temperature range where nano-TLP bonding is theoretically possible. The light brown region is the region where only solid-state sintering (SS) can occur. (b) zoomed region with some molecular dynamics calculations of the melting and SM temperature from Zhang et al. [260] and Wang et al. [102].

to the GT model. The differences in their founding arises from the algorithm used for energy minimization. Below T$_{SM}$, solid-state sintering (SS) can occur and between T_{MP} and T$_{SM}$, TLP bonding is theoretically possible. It should be noted that the Ni NP sets contain particles with below average diameters, so T_{MP} and T$_{SM}$ are also lower than average, creating a melting range for the NPs. Table 5.1 shows the theoretical surface melting range of the Ni NPs based on the particle size distributions in Figure 5.2 and calculated using Equations 1.17 and 1.18. Note that all surface melting approximations assume that no pressure is applied to the NPs during heating. Based on these calculations, the Ni NPs used in this study have a wide range temperature range in which SM is theoretically possible. A few atomic layers to a few nanometer-thick quasi-liquid layers can trigger a non-conventional TLP, i.e. a nano-TLP under the conditions outlined in section 5.2.3 although the NP melting

Table 5.1: Ni NP surface melting range as a function of temperature

Ni NP set	SM range (°C)
Ni-22	1036-1403
Ni-29	1083-1436
Ni-42	1085-1443

and SM melting point approximations/simulations of Ni nanoparticles at tens of nanometers in diameter still needed further experimental validation and theoretical investigation.

5.3.2 Joint Microstructural Characterization

Ambient temperature XRD results of Ni NPs as-synthesized and after heating to 1000 °C show pure Ni and no oxide formation (Figure 5.7a). After heating, the Ni peaks become significantly sharper, indicating significant a growth in crystallite size (as estimated by the Scherrer formula). Different from SEM imaging which displays the morphological grain size, HTXRD helps elaborate the crystallite growth behavior of Ni NPs through the calculation (1.19 Å/min). The HTXRD shows that at 250 °C the crystallites begin to grow rapidly (13.7 Å/min) until 1000 °C is reached as seen in Figure 5.7b. Once at the isothermal step at 1000 °C, the crystallite slows down by 60% (5.51 Å/min), then once the temperature decreases to 900 °C the crystallize growth decreases by over 83% (0.918 Å/min). The rapid grain growth at 250 °C corresponds to 30% of the bulk melting point of Ni (in Kelvin). The crystallite growth should be the synergistic results of both grain coarsening and sintering processes. According to the HTXRD results, most of the crystallite growth occurs during the non-isothermal parts of the heat cycle. If the ramp time is longer, there is a longer period of time for the crystallites to grow. Particle diameter and T$_{max}$ do not display a mathematically monotonous relationship to the crystallite size. Table 5.2 shows the Scherrer crystallite size after TLP processing dependence on the heating rate. For 5-15 °C/min, the

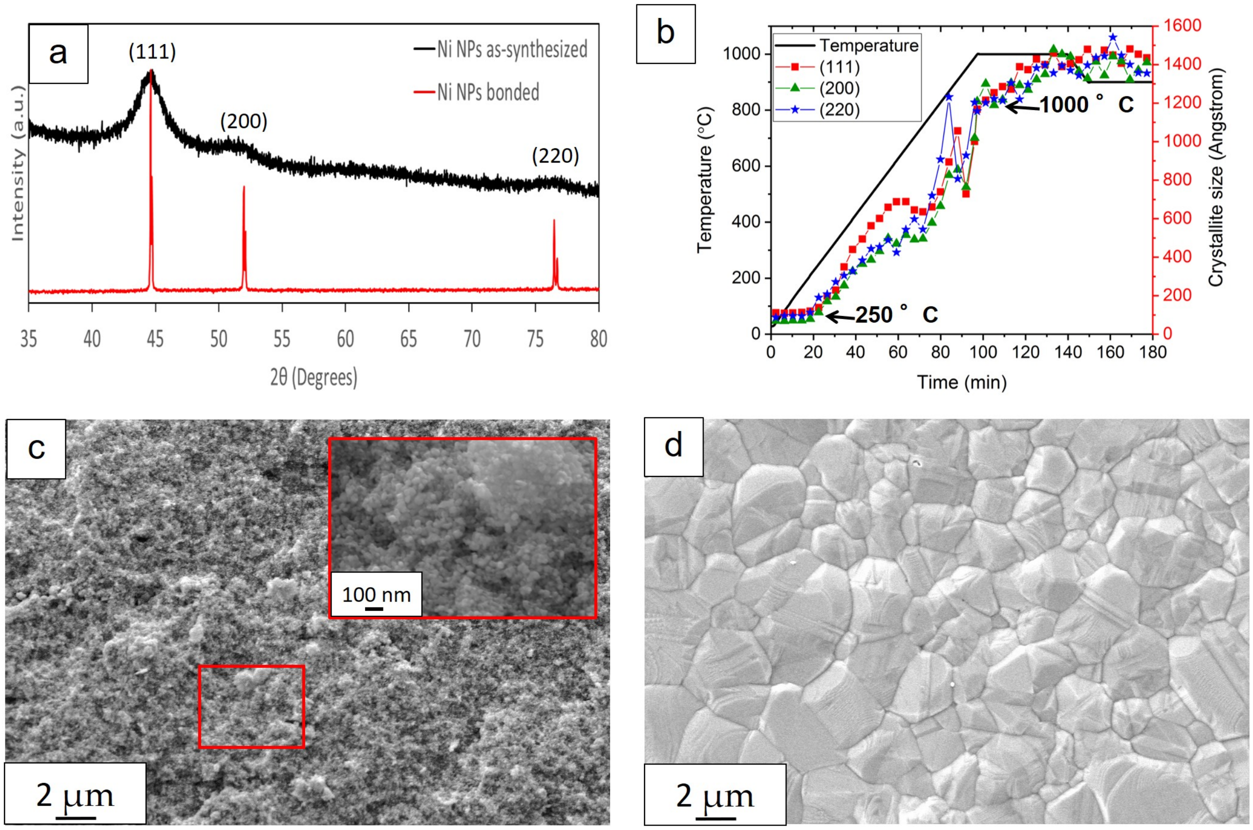

Figure 5.7: (a) XRD patterns for as synthesized Ni-29 NPs and bonded Ni NPs at the end of the heating cycling. (b) The temperature profile of the high temperature XRD test (black line, left axis) and the crystallite size calculated by the Scherrer equation (scatter plot, right axis). (c) Ni NP pellet before heating and (d) after heating [254].

crystallite size is inversely related to the heating rate although there are some differences among the calculations based on different diffraction peaks. The most likely cause of the inverse relationship is that the total heat cycle time is longer when the heating rate is lower [113].

The cross-section of the joint shows that the Ni NPs pellet has low porosity (Figure 5.8a). This sample was heated according to our temperature profile in Figure 5.1 to 1000 °C at a rate of 10 °C/min. The EDX line scan (Figure 5.8b) reveals a diffusion affected zone thickness of 25 μm. It is clear from the elemental profiles of Ni, Fe, and Cr (the primary elements in IN718) that Fe and Cr have the high diffusion lengths similar to diffusion-affected

Table 5.2: The crystallite size of Ni-42 and at the end of the heating cycle as a function of heating rate (T_{max} = 1050 °C)

Heating Rate (°C/min)	**Crystallite size (\AA)**		
	(111)	**(220)**	**(200)**
As-synthesized	129	108	164
5	1724	1541	1113
10	1338	1348	721
15	484	373	497

zone (DAZ) thickness. Ni only has a much shorter diffusion length of approximately 5 μm. This is most likely due to the higher concentration gradient-driven diffusion in Fe and Cr compared to Ni. This will be expanded upon in the next chapter. Local EDX analysis by point and areal scans of the DAZ show that the DAZ contains approximately 9% Fe and 3% Cr each and 90% Ni. This identifies our DAZ as the γ phase on the Ni-Fe-Cr phase diagram. The results of the elemental analysis of the principal elements (i.e. the most abundant elements Ni, Fe, and Cr) in these regions are listed in Table 5.4. Based on the principal element concentrations, the DAZ is primarily composed of γ phase Ni-Fe-Cr (Figure 5.8c) [111]. Compared to the primary phase of IN718 (γ phase), the DAZ γ phase obviously contains far less Fe and Cr. In addition, only trace amounts of Nb, Al, and Ti (key elements in the IN718 strengthening phases).

Table 5.3 shows the results of the DAZ thickness as a function of heating rate. The Ni DAZ thickness experiences a significant jump in between 10 and 15 °C/min. The higher DAZ thickness suggests stronger metallurgical bonding considering Ni appears to diffuse more deeply into IN718 when the heating rate increases to 15 °C/min. Higher DAZ thickness is indicative of good fusion of the metal surfaces and intimate contact between the surfaces [35]. When the heating rate increases, the amount of particle-particle sintering prior to reaching

T$_{max}$ is much lower due to the decreased time spent at lower temperatures [262].

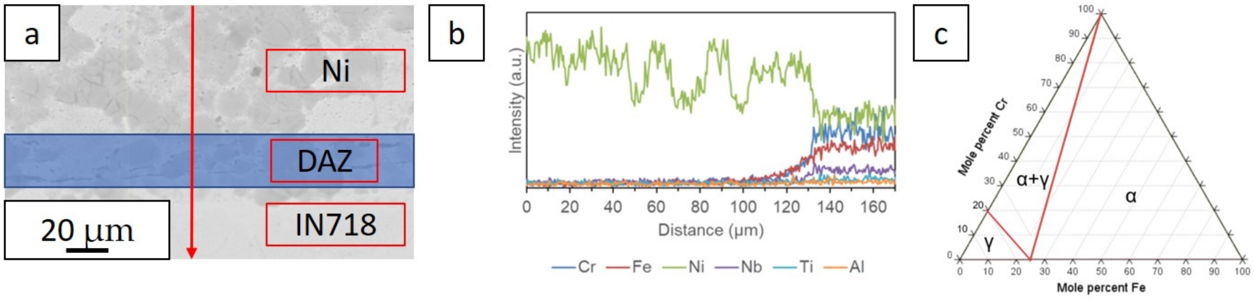

Figure 5.8: (a) SEM image of the Ni-29 NP joint bonded at T$_{max}$ = 1000 °C with heating rate of 10°C/min. The blue area is the diffusion affected zone (DAZ) and the red arrow shows the location of the line scan. The red boxes are areas used for area composition analysis (b) The EDX line scan of the Ni NP-IN718 interface. (c) room temperature Ni-Fe-Cr phase diagram [254].

Table 5.3: DAZ thickness of Ni-42 joints as a function of heating rate

Heating Rate (°C/min)	**DAZ thickness (μm)**		
	Ni	**Fe**	**Cr**
2	8	16	20
5	8	22	24
10	9	24	26
15	23	35	38

Table 5.4: EDX areal composition analysis of the three principal elements (at%) of Ni-29 joint from Figure 5.8 in the areas marked by red boxes

Element	**Ni**	**Fe**	**Cr**
Ni NP	98.7	0.5	0.5
DAZ	76.4	9.0	2.7
IN718	53.6	18.7	20.2

If particle-particle sintering is suppressed, the particle radius of curvature (ROC) is retained at higher temperatures and since the particle ROC is inversely related to the diffusion coefficient [106], nano-enhanced diffusion is still exploitable at higher temperatures. Additionally, less particle-particle sintering allows more surface melting to occur due to the percentage of surface atoms that can participate in surface melting.

The EBSD measurement shows that the grains in the Ni region are equiaxed and are visibly smaller near the Ni-IN718 interface and grow larger approximately 10 μm away from the interface (Figure 5.9a). The inverse pole figure assumes that the [111] direction is perpendicular to the surface. There appears to be no significant preferred grain orientation in this joint (i.e. randomly oriented). The grain boundaries are mostly high angle grain boundaries (>15°), but it should be noted that the percentage of high angle grain boundaries increases in Ni closer to the Ni-IN718 interface (Figure 5.9b). Of course, low angle grain boundaries are more populous in the center of the Ni BFM. There are also more high angle grain boundaries in the IN718 side of the DAZ, but only by approximately 2%. Low angle (<15°) and high angle grain boundaries are typically linked to ductile and brittle behavior of materials, respectively. The grain diameters of IN718 and the DAZ (Figure 5.9c) is are mostly >10 μm with an average of 9.60 μm for IN718 and 1.52 μm for the DAZ. Likewise, on the Ni size of the interface, the average grain size is 0.78 μm near the interface and continues to increase the further away the grains are from the Ni-IN718 interface (Figure 5.9d). The grain diameter results are summarized in Table 5.5. As seen in Table 5.5, the grain diameter tends to increase as heating rate decreases and as the distance from the Ni-IN718 interface increases. Diffusion is a possible cause, but a deeper understanding of the observed grain size trend requires a separate, thorough investigation.

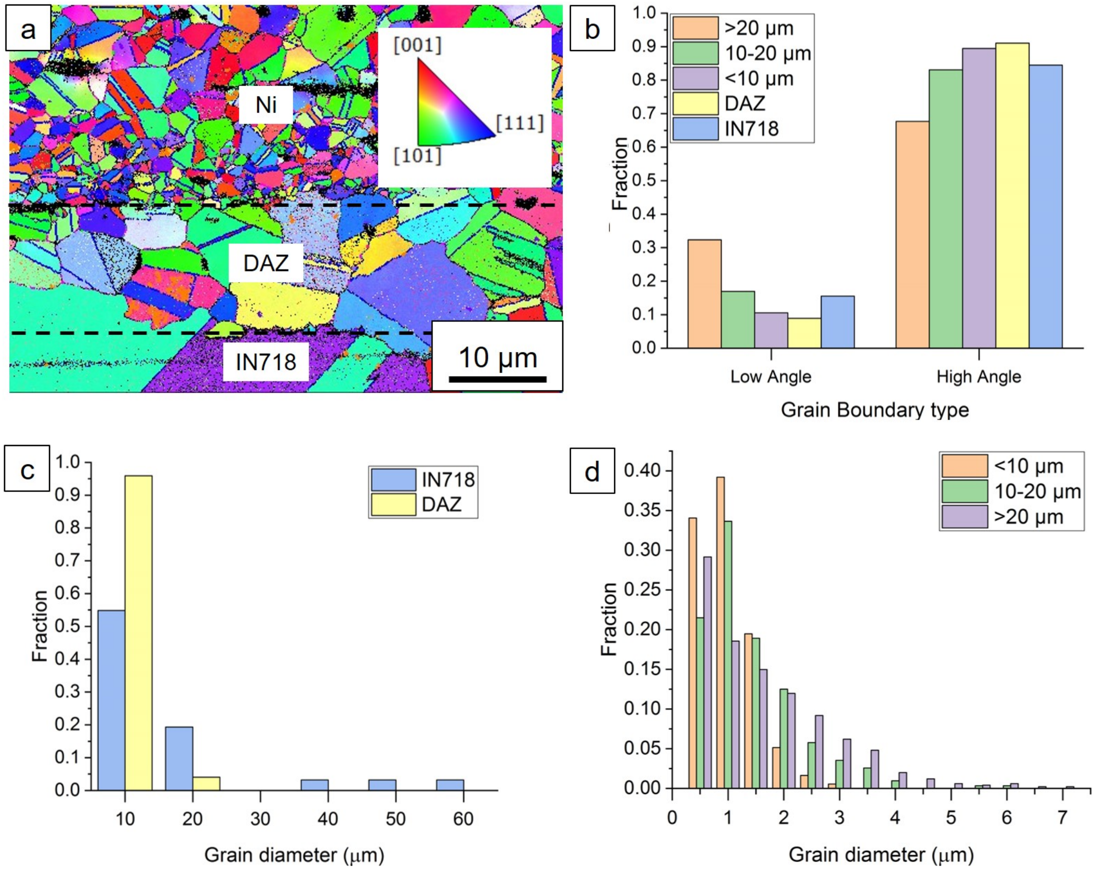

Figure 5.9: (a) EBSD inverse pole figure of a Ni-42 joint joined at 1050 °C and 15 °C/min. (b) Low angle (<15°) and high angle (>15°) grain boundary distribution based on region. The grain size distribution for (c) the IN718 side of the DAZ and (d) the Ni layer based on distance from the Ni-IN718 interface [254].

Table 5.5: Grain diameter summary according to EBSD measurements

	15 °C/min		**10 °C/min**		**2 °C/min**	
Region	**Mean grain diameter (μm)**	**Standard deviation**	**Mean grain diameter (μm)**	**Standard deviation**	**Mean grain diameter (μm)**	**Standard deviation**
>10 μm	0.78	0.44	1.24	0.62	1.81	0.64
10-20 μm	1.14	0.83	1.47	0.80	1.76	0.87
>20 μm	1.39	1.15	1.72	1.34	2.06	1.00

5.3.3 Mechanical Properties

A hardness map of Ni-42 joints is shown in Figure 5.10. The profile shows the middle of the joint is very soft compared to the rest of the joint. The average hardness of the Ni NP pellet is 123, 195, 231 HV for the joints brazed at $T_{max} = 950$, 1000, and 1050 °C, respectively. The hardness of the Ni NP pellet in the braze joints is lower compared to typical values of bulk Ni (>500 HV) partly due to the porosity of the joint. Another contributing factor is the higher amount of LAGBs in the middle of the joint compared to the regions closer to the interface [263]. The average hardness of the IN718 is approximately 440 HV at each T_{max} which is much higher than the initial 250 HV. The increase in hardness is attributed to age hardening during the bonding process [89].

According to Figure 5.11, the increasing of particle diameter, heating rate, and/or T_{max} increases the bonding strength. Improved strength by increasing T_{max} is unsurprising because of the better robustness of particle-particle joining at a higher temperature. Recall that our estimated particle melting point is only up to 52-64 °C lower than the bulk melting point according to the GT and LD approximations. Based on those calculations, we do not

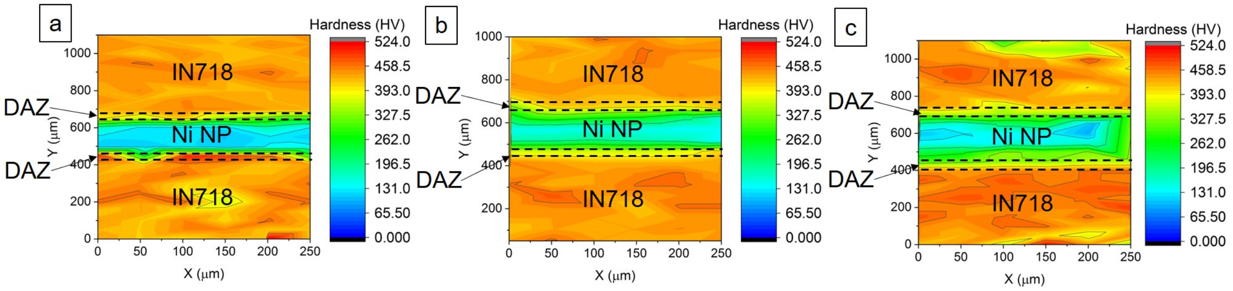

Figure 5.10: Hardness map on the Vickers scale of a Ni-42 joint processed at a heating rate of 15 °C/min with T_{max} of (a) 950 °C, (b) 1000 °C, and (c) 1050 °C [254].

fully melt the Ni NPs during the joining process, so the joining mechanism is either solid-state sintering or liquid phase sintering via surface melting. Also, recall that the crystallite size begins to grow for Ni-29 at 250 °C which we assume to be the onset for solid-state sintering. Despite of the higher melting point, the bonding strength surprisingly increases as particle size increases. Theoretically, the decreasing particle size should mean lower melting temperature and better chance of fusing to IN718 due to wetting processes, however the opposite is observed. The most likely reason for Ni-22 to have a lower bonding strength than Ni-29 and Ni-42 is that Ni-22 NPs have thicker organic layers than Ni-29 and Ni-42 NPs, according to TEM and FTIR (Figs. 3 and 4) [264]. At low temperature, these organic layers hinder joining because they prevent direct particle-particle or particle-surface contact. Although, these organic layers decompose at high temperatures, the decomposition byproducts may not fully volatilize in vacuum [265]. Therefore, any non-volatile byproducts will remain in the BFM. Based on the FTIR analysis (Figure 5.5) more organic byproducts are left behind after heating to 1050 °C for Ni-22 than Ni-29 and Ni-42. This organic residue will segregate to the grain boundaries of the Ni metal due to the tendency of carbon to diffuse along grain boundaries [13], providing contamination. This grain boundary contamination is what most likely causes intergranular fracture [92]. As the heating rate increases, so does the strength, though there is no significant difference between joints at 2 °C/min and 5 °C/min (Fig 10b). The strength unsurprisingly increases as T_{max} increases as seen in Figure 5.11c. The strength increases in the joints bonded at T_{max} from 1000 to 1050 °C could be a result of surface melting occurring in the NP filler. The maximum strength achieved is 234 MPa which is higher than the strength achieved using BNi-2 foil (150 MPa) or 325 mesh powder (64.2 MPa).

According to our DIC measurements, under 10× magnification (Figure 5.12b-d) shows that the strain is relatively evenly distributed throughout the joint with some areas of high strain near the Ni-IN718 interfaces, as indicated by the circles in Figure 5.11. Under 50× magnification (Figure 5.12f-h) this is even more apparent considering the areas of high strain are allocated at the Ni-IN718 interface. The high strain at the interface indicates this is where much of the load/stress is being concentrated according to the stress-strain response indicated by Hookes law. Normal strain in the x-direction shows a tensile strain condition at the interface but mostly low magnitude compressive strain in the areas surrounding the interface as a response to the tensile loading conditions at the interface. For the normal strain in the y-direction the strain is primarily tensile due to the tensile loading condition also being in the y-direction. The x-direction has more compressive strain, as previously mentioned, as conventional mechanics would predict via Poissons ratio [175]. For shear strain, the positive shear strain is in agreement with the shear loading condition of the specimen. The concentration of strain in the interface is reflected in the tendency of the joined samples to fail within the BFM, but closer to the interface. One of the reasons 15

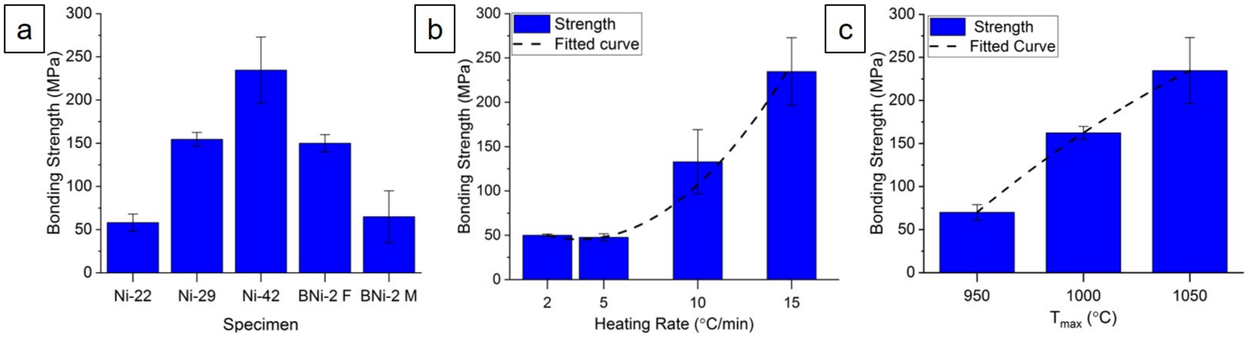

Figure 5.11: Bonding strength as a function of (a) particle diameter (T$_{max}$ = 1050 °C and heating rate = 15 °C/min), (b) heating rate (Ni-42 and T$_{max}$ = 1050 °C), and (c) T$_{max}$ (Ni-42, heating rate = 15 °C/min). The BNi-2 foil (BNi-2 F) and BNi-2 325 mesh powder (BNi-2 M) are also included [254].

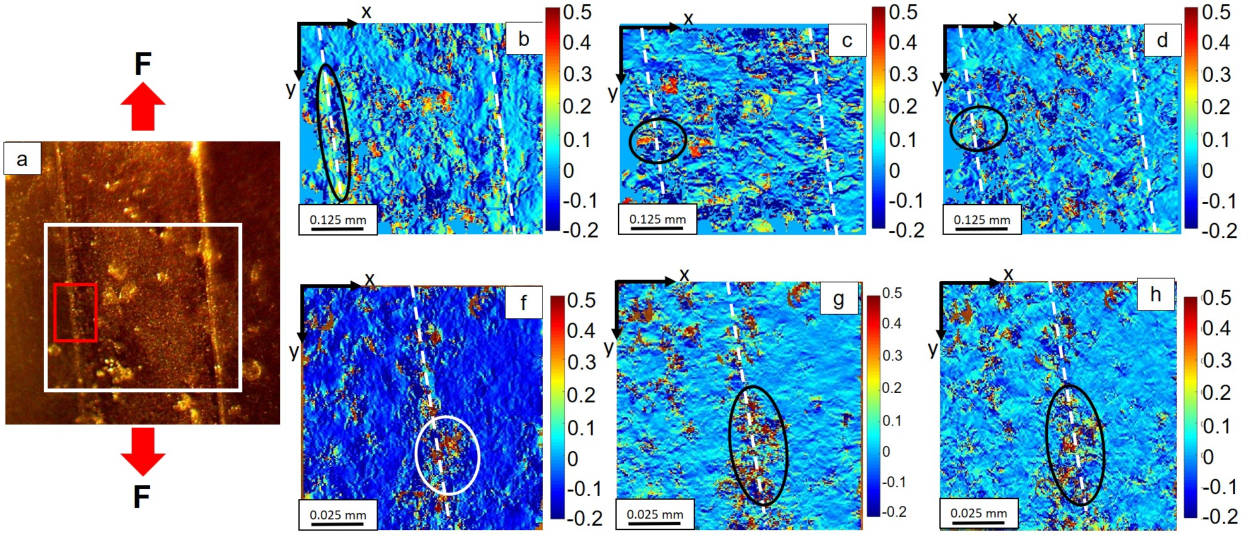

Figure 5.12: DIC results for Ni-29 pellet joined at T_{max} =1000 °C and heating rate = 15 °C/min under 50 MPa of load. (a) The original image with the analyzed region under 10x magnification indicated by the white box, the analyzed region under 50x magnification is indicated by the red box. The loading condition is indicated by the red arrows. (b-c) are the normal strain in the x and y direction respectively and (d) is shear strain under 10x magnification. (e-f) are the normal strain in the x and y direction respectively and (g) is shear strain under 50x magnification. Circles are used to indicate areas of high tensile or compressive strain [254].

°C/min samples have significantly higher strength than 10 °C/min or 5 °C/min samples is that smaller grain size near the interface (where stress is most concentrated) allows the joint to sustain higher stress due to Hall-Petch strengthening of the interface. Part of the reason for strain being concentrated at the interface is that there is some preexisting strain due to lattice strain. Ni has a lattice constant of 3.52 Å[266] and the γ matrix of IN718 is reported to be between 3.60-3.64 Å[1] which translates to a 2-3% lattice strain. As previously mentioned, the interfacial regions are more highly populated with high angle grain boundaries which are typically associated with high strain values (Figure 5.9b). Low angle grain boundaries are more populous in the center of the joint and generally reflect lower strain values.

For Ni-22, the tendency for strain concentration in the Ni-IN718 interface is particularly catastrophic as reflected in the tendency for Ni-22 joints to fracture at the Ni-IN718 interface. Ni-22 joint primarily fails by intergranular fracture occurring at the Ni-IN718 interface (Figure 5.13a-b). Presumably, intergranular fracture in Ni-22 joints occurs at the interface because the weakening of the grain boundary due to contamination works in tandem with the inherent lattice strain at the interface to manufacture a particularly brittle interface. Some dimpled morphology (bottom of Figure 5.13a-b) can be seen in random areas of the fracture surface. The intergranular features of fracture surface are also very morphologically similar to a NP pellet that was only heated without being configured in the lap joint configuration. Ni-29 and Ni-42 do not experience intergranular fracture. Ni-29 (Figure 5.13c-d) shows deep, slanted dimples with some cleavage fracture lines (dimple diameter=1.2-1.8 μm, dimple aspect ratio = 1.52). Dimple diameter is the diameter along the major axis of the elliptically-shaped dimples and was measured by ImageJ and the aspect ratio was calculated by the ratio between the major and minor diameters of the dimples. The dimples are clearly much deeper and circular (dimple aspect ratio = 1.38) for Ni-42 and the cleavage fracture lines have disappeared (dimple diameter = 1.5-3 μm, dimple aspect ratio = 1.38). Cleavage is a low energy fracture mechanism, so their absence from the Ni-42 fracture surface suggests higher toughness due to more deformation and higher strain sustained prior to fracture (Figure 5.13e-f) [92]. Fracture in the Ni-29 and Ni-42 NP joints occured within the filler metal.

The effect of heating rate on the fractography was also investigated. The fracture surfaces for Ni-42 joints processed at 1050 °C at different heating rates shows increasing dimple size and depth as the heating rate increases. The dimple size is much smaller for the samples brazed using a 2 °C/min or 5 °C/min heating rate, and in Figure 5.14b and 5.14d,

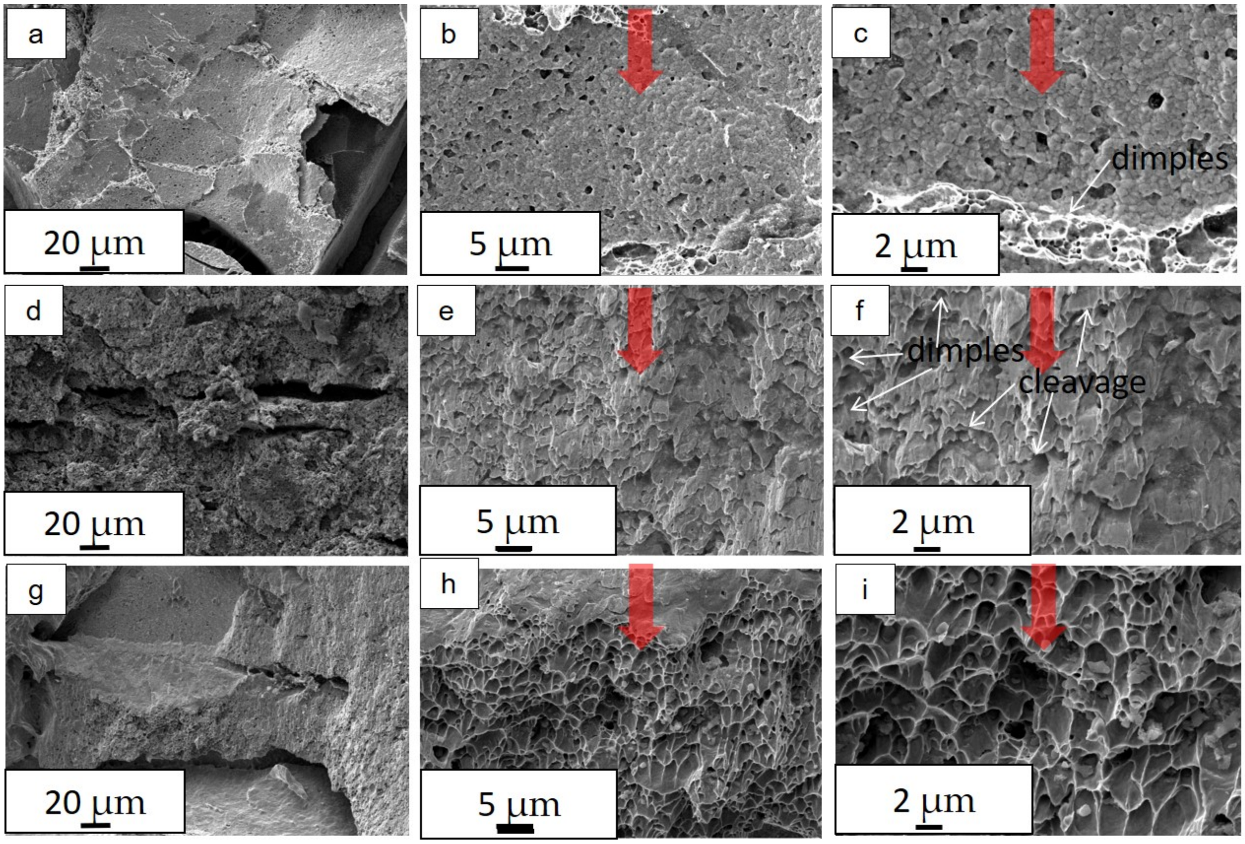

Figure 5.13: Fracture surface of lap shear joints joined at T_{max} =1050 °C and heating rate = 15 °C/min (a-c) Ni-22, (d-f) Ni-29, and (g-i) Ni-42. The red arrow indicates the loading direction of the sample [254].

(dimple diameter = 0.2-0.8 μm, dimple aspect ratio = 1.38) some of the granular morphology can still be seen. The granular morphology is more visible in the 2 °C/min fracture surface than the 5 °C/min fracture surface. In addition, there are some secondary microcracks that are normal to the fracture surface. The secondary cracks are at approximately a 40° angle of the loading direction. It is thus possible that these microcracks are formed due to the maximum principal shear strain at 45° to the tensile force. Fracture in the 2 °C/min and 5 °C/min samples occurs at the Ni-IN718 interface. In this case, the cleavage fracture is caused by the unfused particles in the joint as indicated by the red circle in Figure 5.14d [27] When the heating rate increases to 10 °C/min (Figure 5.14e-f), the fracture surface is similar to Ni-29 joint specimen with a rate of 15 °C/min in Figure 5.13c-d (dimple diameter=1.2-1.8 μm, dimple aspect ratio = 1.52). As previously mentioned, the dimples at 15 °C/min, are much rounder and deeper (dimple diameter = 1.5-3 μm, dimple aspect ratio = 1.38). The fractography exhibits some of the same tendencies with increasing temperature as it does with increasing heating rate. Fracture in the 10 °C/min and 15 °C/min samples occurs within the filler metal. The cross-section of our strongest specimens after fracture (Ni-42, 1050 °C, 15 °C/min) show that the pores are indeed elongated and slanted in the direction of the loading conditions (Figure 5.15). The massive growth in pore size (Figure 5.15b) compared to the as-joined sample (Figure 5.15a) suggests microvoid coalescence as the primary fracture

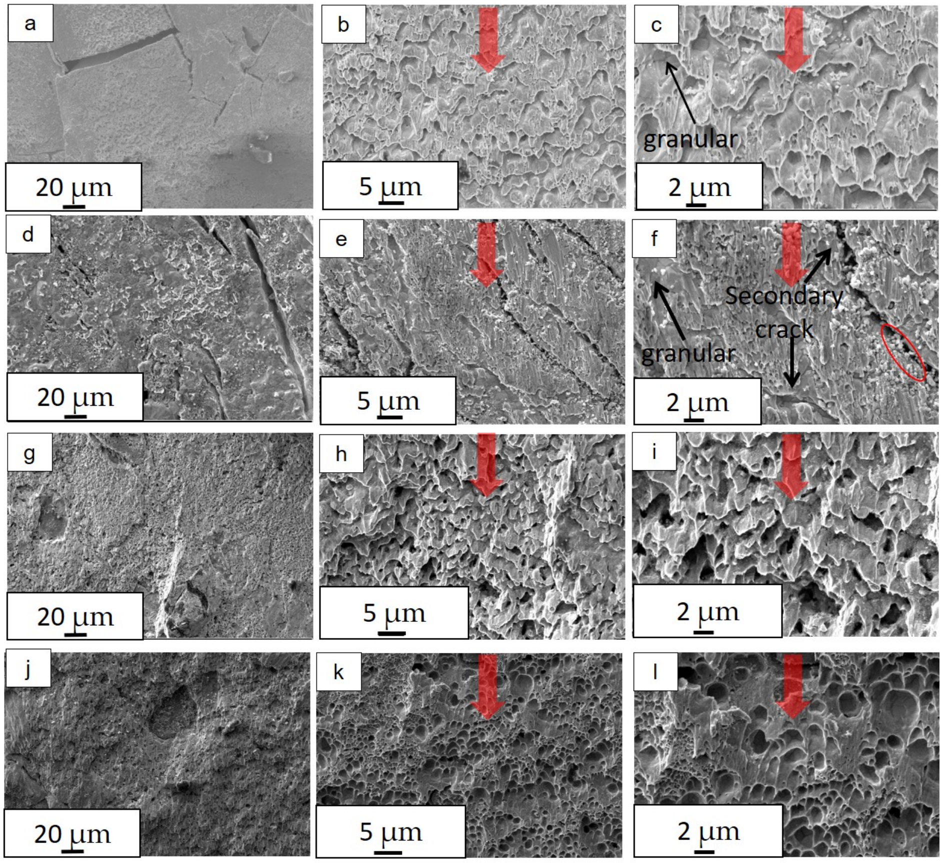

Figure 5.14: Fracture surface of lap shear joints joined at T$_{max}$ =1050 °C using Ni-42 pellets (a-c) 2 °C/min, (d-f) 5 °C/min, (g-i) 10 °C/min, (j-l) 15 °C/min. The red arrow indicates the loading direction of the sample. [254].

mechanism for the high strength joints (>100 MPa). Microvoid coalescence typically follows this process: nucleation, growth, and coalescence. The preexisting pores in the joint serve as ideal growth sites during shear loading of the joint in addition to the microvoids that nucleate during loading. As the microvoids grow coalesce, they do so according to the stress-influenced mass transport around the voids. The mass transport around the void inner surface causes the slanted shape seen in Figure 5.15b [92].

5.4 Conclusions

In this study, the Ni NPs were investigated and demonstrated to produce brazed joints up to 243 MPa bonding strength. Furthermore, the quantitative and qualitative effects of

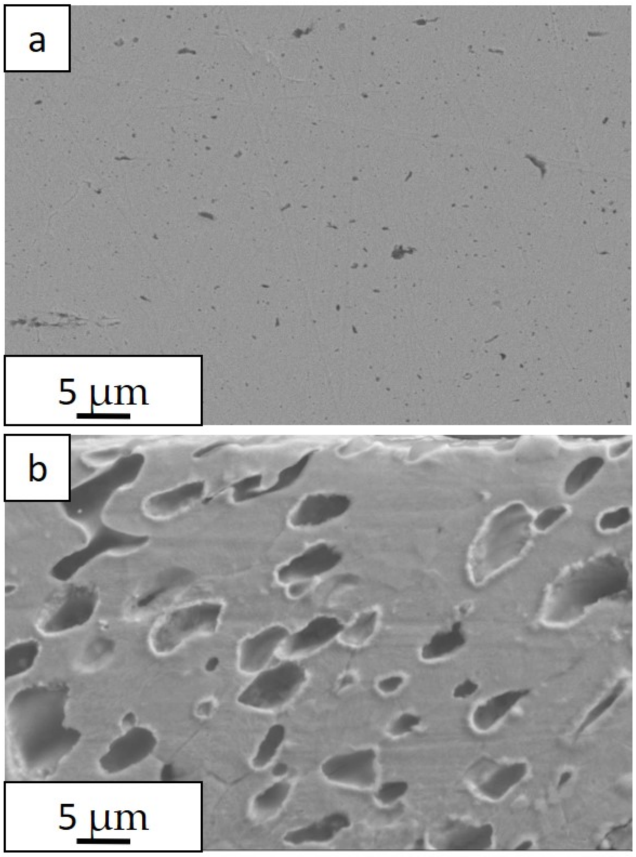

Figure 5.15: Cross-section of a Ni-42 (T_{max} =1050 °C and heating rate = 15 °C/min) joint (a) before fracture and (b) after fracture [254].

heating rate on the microstructure and mechanical properties have been elucidated. From these experiments, it was found that a faster heating rate can improve the bonding strength of IN718 brazed joints using Ni NPs by TLP bonding. The faster heating rate decreases the opportunity for solid-state sintering to occur before surface melting can take place. The microhardness testing of the joint showed the increased hardness in IN718 after TLP bonding. In practice, smaller NPs also were shown to have relatively lower bonding strength compared to larger NPs because the thicker organic layer on the surface of smaller NPs inhibits bonding. The residual organic byproducts after heating most likely segregated to the grain boundaries and contributed to the intergranular fracture that characterized these joints. The other joints had ductile fracture features and failed by microvoid coalescence. The study elucidated the processing parameters that affect the robustness of nano-joined IN718 and can be potentially applied to other nano-filler metals. From the experiments reported, we can suggest that optimum joining performance can be achieved through maximizing the heating rate, minimizing organic contamination, and controlling the maximum temperature.

Chapter 6

Wettability and Diffusion of Ni nanomaterials

6.1 Introduction

In Chapter 1, it was mentioned that wettability and diffusion are critically important processes for successful brazing. Wettability is especially important for crack repair and narrow gap brazing which are both potential applications of nanobrazing materials, particularly high temperature materials such as Ni. It has been established in multiple studies that the wettability of solders, brazes, and weldments can be enhanced with the addition of nanoparticles such as Si [97], TiC ([96]), and W ([98]). Wettability of joined nanomaterials themselves is studied only under very specific contexts such as wetting of other nanostructures. For example, Muzikansky et al. studied the dewetting tendency of Ag shells (change from wetting to non-wetting behavior) in Cu-Ag core-shell NPs at elevated temperatures [267]. And Grouchko et al. discussed the selective wettability of Ag NPs gold nanostructures [267, 268]. Our publication discusses some of the wettability characteristics of Ag NPs and Ag NWs on IN718 [195], but contact angle was not discussed. Additionally, pure Ag is not an optimum choice for joining IN718.

Diffusion is typically discussed in nanojoining studies typically in the context of understanding the phase transformations and densification that occur during joining processes. Aside from a lack of studies on high temperature nanobrazing, the interdiffusion coefficients of nanomaterials for a joining application have seldom been experimentally determined or calculated via any of the analyses discussed in Section 1.3.2. Again, the diffusion behavior was discussed on a basic level for Ag NPs and Ag NWs [195]. In that publication, the diffusion behavior of the two NMs was discussed but the interdiffusion coefficient was not calculated at that time. In this chapter, the contact angle of Ni NPs and NWs will be measured and discussed. In addition, the interdiffusion coefficients for Ni will be calculated based on experimental data and compared to bulk diffusion values and predicted NP interdiffusion coefficients. These works are of critical benefits to understanding nanobrazing and the key for the further optimization of nanobrazing of IN718 with Ni nanomaterials.

6.2 Experimental and Analytical Methods

6.2.1 Ni Nanoparticle Synthesis

The procedure for making Ni NPs is the same as the one used in Chapter 5 [254, 258].

6.2.2 Ni Nanowire Synthesis

This procedure was modified from Remadevi et al. [269] 2.9 grams of nickel chloride was added to 200 mL of an ethylene glycol-water mixture (3:1 ratio). Then, 1 g of K-30 PVP (M.W. = 40,000) was added and stirred non-magnetically until fully dissolved. The resulting solution was heated to 120 °C and 12 mL of hydrazine hydrate was added approximately 1 drop/second. The reaction was allowed to continue for 20 minutes then was allowed to cool naturally. The resulting Ni NWs were first collected by a permanent magnet then washed with ethanol via centrifugation 3 times at 8000 rpm for 5 minutes [269]. The washed Ni NWs were dried using a freeze dryer. 0.12 g of dry Ni NWs were loaded into a rectangular pellet press (12 mm × 12 mm) without any binder material and uniaxially pressed under 2 GPa of pressure.

6.2.3 Contact Angle Measurement

For contact angle measurements, IN718 was polished up to 0.25 μm diamond paste, followed by 50% HCl aqueous solution etching in preparation for Ni plating. Ni plating was done using a Woods nickel strike solution for 10 minutes (67 mA/cm^2) followed by a modified Watts nickel plating solution (0.684 M nickel sulfate hexahydrate, 0.467 M ammonium chloride, and 0.485 M boric acid) for 10 minutes at (22 mA/cm^2). The resulting Ni plating was approximately 50 μm thick. Ni plating was done to improve the adhesion of Ni NMs to the IN718 surface. A Ni nanopowder pellet and uncompacted nanopowder was placed on the IN718 surface and held lightly in place by a graphite clamp (Figure 6.1). The Ni NMs were then heated up to 1100 °C using the temperature profile in Figure 5.1. The IN718 plate was then embedded in epoxy and polished up to 1 μm diamond paste to view

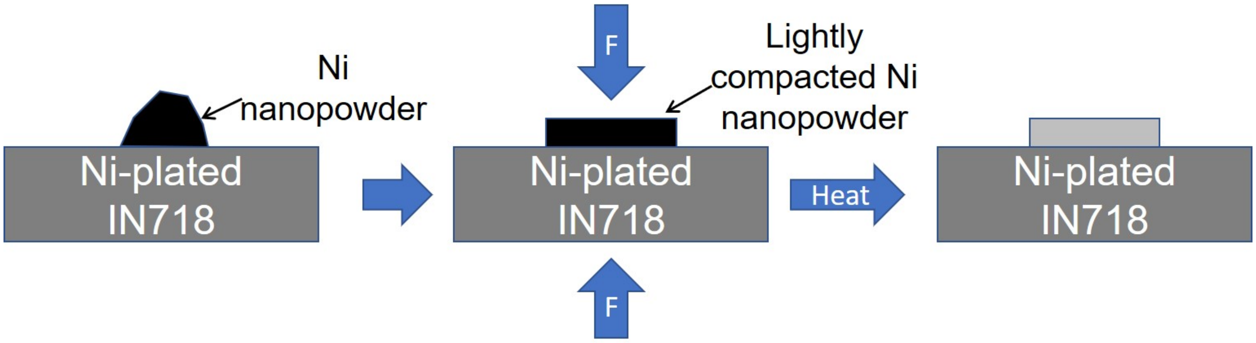

Figure 6.1: Schematic of how wettability experiments are conducted.

the cross-section. SEM images were taken on a Zeiss Auriga Scanning Electron Microscope using the secondary electron detector and the contact angle was measured using ImageJ.

6.2.4 Diffusion Analysis

First, a cross-section of the brazed joint formed using the temperature profile in Figure 5.1 was prepared. Then after cross-sectioning and polishing using the procedure detailed in Section 6.2.3, EDS measurements were conducted using a Zeiss MA15 EVO SEM equipped with a Bruker xFlash 6—30 detector. The noisy EDS data was smoothed with a SavitzkyGolay filter (Equation 6.1).

$$(y_k)_{smooth} = \frac{\sum_{i=-0.5(n-1)}^{0.5(n-1} A_i y_{k+i}}{\sum_{i=-0.5(n-1)}^{0.5(n-1)} A_i} \qquad 6.1$$

$(y_k)_{smooth}$ is the smoothed data point y_k is the raw data point. n is the number of points used for smoothing (20 points for this study). A_i is a convolution coefficient obtained from a Savitzky-Golay table. Smoothing was performed using OriginPro software. After smoothing, the concentration curve is fitted to a sigmoid function (Equation 6.2) using OriginPro with an $R^2 \geq 95\%$.

$$c(x) = \frac{A1 - A2}{1 + exp(\frac{x - x_0}{dx})} + A2 \qquad 6.2$$

c(x) is the concentration with respect to the position x. $A1$, $A2$, x_0, and dx are mathematical coefficients. Sauer-Friese analysis (Equations 1.13 to 1.15 was conducted on the fitted sigmoid function using the MATLAB code included in Appendix C to determine the concentration-dependent interdiffusion coefficient (D(c)) and the average interdiffusion coefficient for Ni, Fe, and Cr. The Ni interdiffusion coefficients determined by Sauer-Friese were compared to values from literature and values calculated using Equations 1.25 and 1.26. The values used for calculating the diffusion coefficients are listed in Table 6.1.

6.3 Results and Discussion

6.3.1 Ni Nanomaterial Characterization

As mentioned in Chapter 5, when sodium borohydride is added all at once, the average particle diameter is approximately 22 nm (Figure 6.2a-b). Figure 6.2c-d shows the SEM and accompanying size distribution of Ni NPs with an average diameter of 29 nm that were synthesized using a 1 mL/min injection rate, and Figure 6.2e-f shows the SEM and accompanying size distribution of Ni NPs (an average diameter of 42 nm) synthesized using a 0.03 mL/min injection rate. As before, the 22 nm NPs will be referred to as Ni-22, the 29

Table 6.1: Diffusion prefactor (D_0, cm^2/s), activation energy (E_A, kJ/mol), and Vibrational entropy (S_{vib}, J/mol-K) used for calculated bulk and nano diffusion coefficients

$\mathbf{D}_0^{lattice}$ [270]	$\mathbf{E}_{bulk}^{lattice}$ [270]	$\mathbf{D}_0^{GB}$ [271]	$\mathbf{E}_{bulk}^{GB}$ [271]	$\mathbf{D}_0^{surface}$ [272]	$\mathbf{E}_{bulk}^{surface}$ [272]	S_{vib} [273]
1.9	278	9.3	177	12.8	168	29.87

nm NPs will be referred to as Ni-29, and the 42 nm NPs will be referred to as Ni-42. As for the Ni NWs, they take the appearance of several Ni NPs chained together (Figure 6.2)g-h.

6.3.2 Wettability

Since the powder is not tightly compacted into a pellet like it is during normal brazing experiments [254], the Ni appears extremely porous in Figure 6.3a-b. Wetting experiments were done without Ni plating as well, however we found that the Ni did not adhere to the IN718 surface and/or points of contact between the Ni and IN718 were not found under the SEM microscope. Based on these results, Ni plating is critical to the successful wetting and bonding using the current Ni nanomaterials. As for the samples with Ni plating, the Ni NPs (Figure 6.3a) showed higher contact angles than the Ni NWs (Figure 6.3b) as seen in Table 6.2 for all sizes. When using the powder, there were several contact angles because the powder yielded a a porous Ni layer on the IN718 surface with several contact angles for measurement after joining. The Ni pellets only had contact angles for measurement at the edges of the pellet. Pellets and loose powder yielded similar wetting results. At least three contact angles were measured for each nanomaterial.

There are a few possible reasons for the Ni NWs having better wettability. The first possibility Ni NWs may generate more surface melting than the Ni NPs. The Ni NWs may have lower surface stability than Ni NPs which leads to a lower surface melting temperature. With more surface liquid, the wettability appears to be much better. This is somewhat contrary to what some people have modeled for the shape effects on the nanomaterial melting point depression. For instance, Nanda et al., Qi and Wang, and X. Zhang et al. predict that NWs have slightly less of a melting point depression than spherical NPs (Figure 6.4,

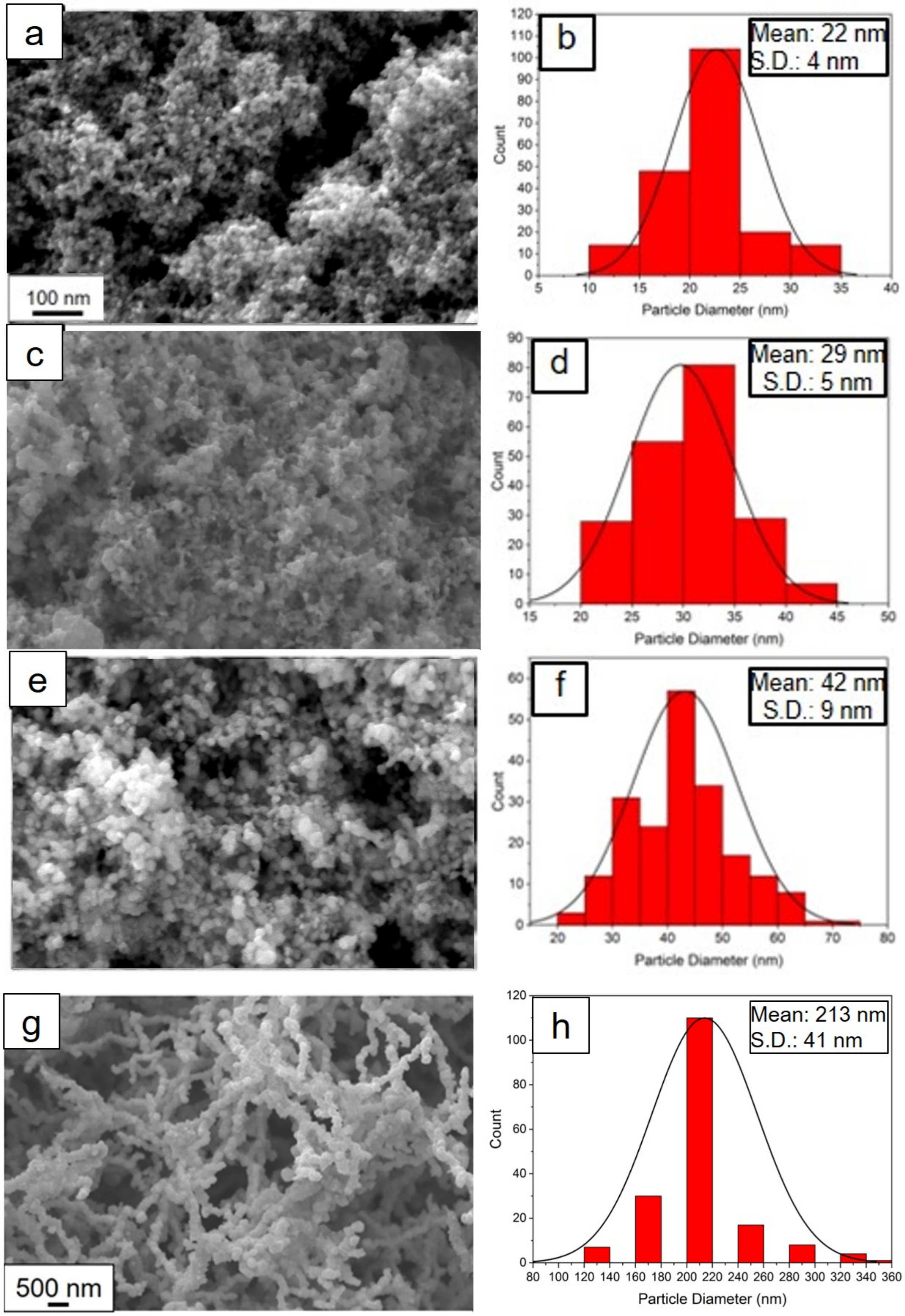

Figure 6.2: SEM and size distribution (histogram and distribution curve) of Ni NPs synthesized at 120 °C with the sodium borohydride added (a-b) rapidly, (c-d) dropwise added approximately 1 mL/min and (e-f) dropwise added approximately 0.03 mL/min. The SEM and size distribution of Ni NWs is also included (g-h). The mean and standard deviation (S.D.) are also listed in the figure.

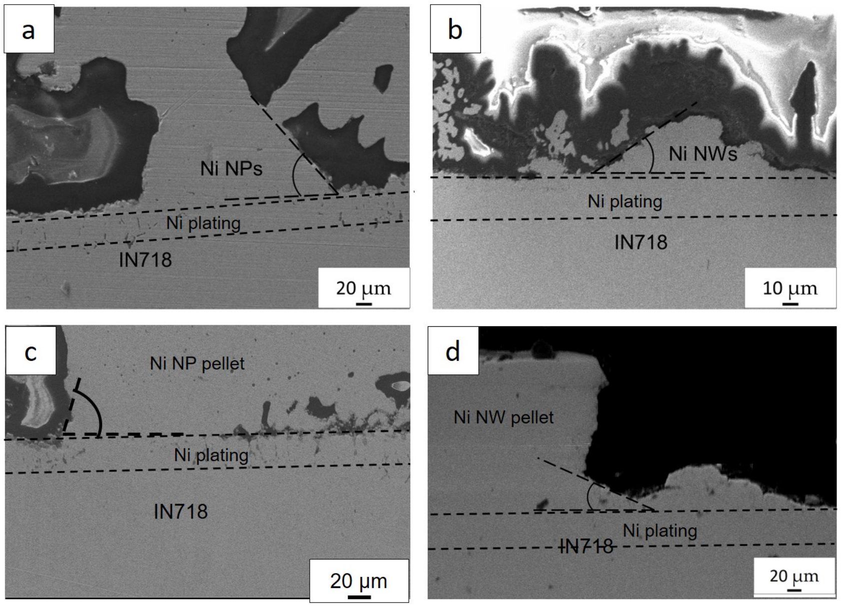
a
Ni NPs
Ni plating
IN718
20 μm
b
Ni NWs
Ni plating
IN718
10 μm
c
Ni NP pellet
Ni plating
IN718
20 μm
d
Ni NW pellet
Ni plating
IN718
20 μm

Figure 6.3: Example of the contact angle measurements for Ni NP powder (a) and pellet (c). As well as for Ni NWs (b) powder and (d) pellet

Equations 1.18 and 1.19) [102, 103, 274].

There are a few experimental studies that support shape dependency on melting point depression. For example, according to Thouy et al. and Volk et al., the thermal instability of NWs and other thin, one-dimensional nanostructures results in nanowires fragmenting and coalescing into chains of nanodroplets during melting (also known as Rayleigh breakup) [275, 276]. Marzbanrad et al. reported a similar phenomenon with pentagonal Ag NWs; despite Ag NWs not fully melting at 300 °C experienced Rayleigh breakup only within the surface melting regime [277]. Therefore, based on the present data and past reports, we deduce that Ni NWs exhibit more surface melting than Ni NPs due to the higher thermal instability of Ni NWs. Another complimentary reason is lower liquid vapor surface energy (γ_{lv}) due to the larger diameter of the Ni NWs. This is in agreement with prevailing models of melting of NMs as well as the general tendency for the surface energy of nanomaterials to be inversely size dependent [278].

Table 6.2: Contact angle for Ni nanomaterials heated to 1100 °C

Material	Average Contact Angle	Range
Ni-22 NPs	$64.7 \pm 7.4°$	44-71°
Ni-29 NPs	$58.6 \pm 8.9°$	53-72°
Ni-42 NPs	$66.4 \pm 14.3°$	55-81°
Ni NWs	$29.2 \pm 13.2°$	15-45°

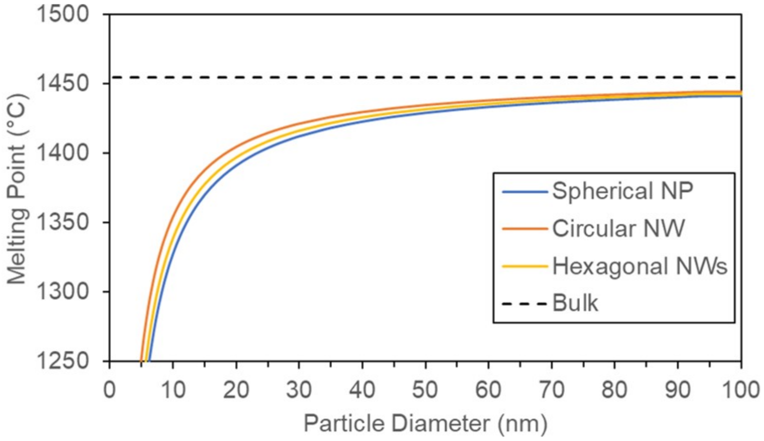

Figure 6.4: Liquid drop model for spherical Ni NPs according to Nanda et al (Equation 1.18) and NWs with different cross-sectional shapes according to Qi et al. [102, 103]

6.3.3 Diffusion

An example of one of the fitted curves for the EDS line scan is shown in Figure 6.5. The interdiffusion coefficients of spherical NPs was calculated as a function of particle size (Equations 1.25 and 1.26) and compared to the bulk interdiffusion coefficients. Grain boundary diffusion is typically 3-5 orders higher than lattice diffusion because the activation energy is much lower. For example, self-interdiffusion coefficient for lattice interdiffusion coefficient ($D_{Lattice}$) and grain boundary interdiffusion coefficient (D_{GB}) of Ni is 1.59×10^{-11} cm^2/s and 2.01×10^{-6} cm^2/s at 1050 $°C$ [270]. Surface diffusion is even higher than grain boundary diffusion; Maiya and Blakely report the surface self-interdiffusion coefficient of Ni to be 1.5-3.1 $\times 10^{-5}$ cm^2/s depending on the crystallographic plane. In nanomaterials,

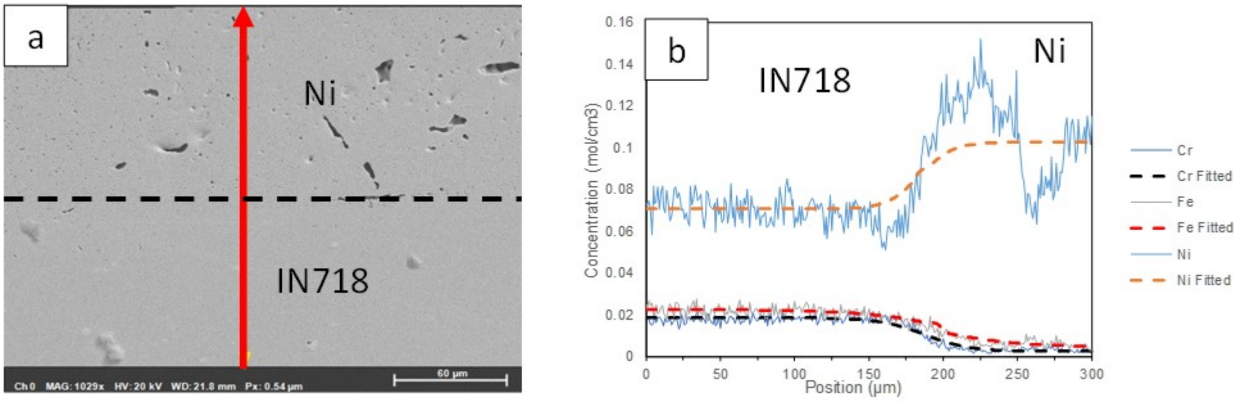

Figure 6.5: Example of (a) an EDS line scan and (b) the fitting of the raw EDS data for Sauer-Friese analysis

surface diffusion and grain boundary diffusion will be extremely prominent, especially in the early stages of brazing due to the high surface-area-to-volume (SAV) ratio and small grain size once the particles are initially joined [279]. The effective interdiffusion coefficient D_{eff} is calculated using the Hart's equation [280]:

$$D_{eff1} = \frac{3\delta}{d}D_{GB} + (1 - \frac{3\delta}{d})D_{Lattice} \tag{6.3}$$

δ is the grain boundary thickness which is assumed to be 0.5 nm and d is the grain diameter. In Figure 6.6a, d is assumed to be 950 nm based on the overall average grain size of the Ni grains according to EBSD measurements in Figure 5.9. Based on our current knowledge of nanojoining, surface diffusion is active in particle-particle and particle- BM surface joining. Furthermore, surface diffusion should primarily be active in diffusion along the NM surface and the Ni-IN718 interface. Trans-interfacial diffusion is traditionally driven by lattice and grain boundary diffusion. However, to reiterate, surface diffusion should not be ignored because surface diffusion has some influence on mass transfer during NM densification and transport of NM adatoms to the IN718 surface. To give a rough estimate of the effective diffusion coefficient Equation 6.4 was developed.

$$D_{eff2} = \beta D_{Surface} + (1-\beta)(\frac{3\delta}{d}D_{GB} + (1-\frac{3\delta}{d})D_{Lattice}) \qquad 6.4$$

$$\beta = LhS \qquad 6.5$$

β is a prefactor meant to account for the percentage of atoms that participate in surface diffusion. L is the number of atomic layers that participate in surface diffusion. We assume L=3 for the calculation in this study. We chose L=3 because this is the number of atomic layers that comprise the surface layer of a NP based on other studies [108, 279, 281], however this number is open to revision based on the results of further studies. h is the atomic diameter and S is the particle SAV ratio. Equation 6.4 assumes the three diffusion processes have no effect on each other because at this time it is unknow the connection between surface diffusion and the other two types of diffusion in a nanojoining context.

As seen in Figure 6.6a, the experimentally determined D_{eff} for the Ni NMs is not very close to the calculated values for nanoparticle D_{eff1}. Furthermore, the calculated D_{eff1} is roughly 2 orders lower than the experimentally determined D_{eff} which proves that lattice diffusion and grain boundary diffusion are insufficient on their own in explaining the Ni NM interdiffusion behavior. When surface diffusion is accounted for according to Equation 6.4 (D_{eff2}), this serves as a much better predictor for the effective interdiffusion coefficient than Equation 6.3. The experimentally determined D_{eff} is 1-2 orders of magnitude lower than the bulk surface diffusion coefficient. For Ni-22 NPs and Ni NWs, there seems to be more disparity between the calculated value and the measured value. For Ni-22 NPs, this is likely the result of the thicker organic layer on these two nanoparticles compared to Ni-29 and Ni-42 NPs. That organic surface layer will certainly hinder interdiffusion of Ni [219]. For Ni NWs, D_{eff} is nearly one order of magnitude higher than predicted. One possible reason for the higher than predicted D_{eff} could be that Ni NWs experience more liquid phase diffusion due to more surface melting than Ni NPs as previously mentioned. The measured nanoparticle interdiffusion coefficient seems to obey the Arrhenius-type behavior with respect to temperature as seen in Figure 6.6b. And the experimentally determined interdiffusion coefficient is still close to our calculated D_{eff2}. The interdiffusion coefficients of Ni, Fe, and Cr as a function of heating rate are included in Figure 6.7. The bulk interdiffusion coefficients for Cr and Fe in Ni superalloys are 9×10^{-11} cm^2/s, and 0.3 x 10^{-11} cm^2/s, respectively [282]. The measured interdiffusion coefficients for Fe and Cr, however, are on the same order of magnitude as the nano Ni interdiffusion coefficients. Fe interdiffusion coefficient seems to be mostly unaffected by the heating rate. Ni and Cr have increasing interdiffusion coefficients as the heating rate increases. However, Cr tends to have similar or higher interdiffusion coefficient than Ni and Fe. The interdiffusion coefficients increase as the heating rate increases because, as mentioned in the previous chapter, the faster heating rate helps mitigate sintering at lower temperatures and preserves the particle size and curvature [254]. By extension, the high size-dependent interdiffusion coefficient is also preserved. It is important to note that EDS is typically reveals microscale diffusion behavior and generally only in one dimension. If a higher resolution technique such as atom probe tomography is used to determine the elemental distribution, the interdiffusion coefficient calculation will be even more accurate and the three dimensional elemental distribution may give some insight

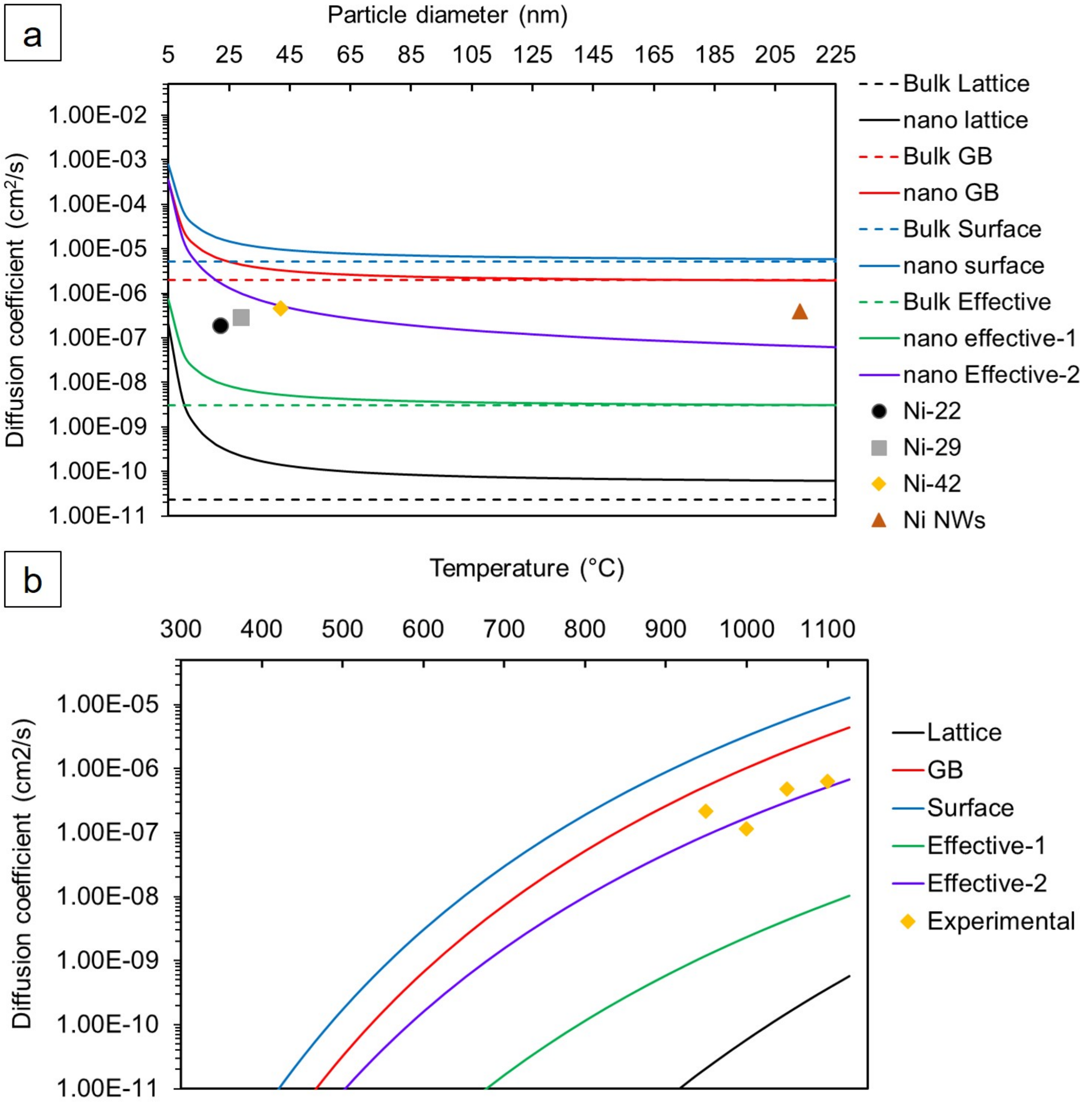

Figure 6.6: Ni interdiffusion coefficients (a) as a function of particle diameter as calculated by Jiang et al.'s equation [112] as well as the experimentally calculated interdiffusion coefficients for Ni NPs and Ni NWs joined at 1050 °C and 15 °C/min. The bulk interdiffusion coefficients for Ni are also shown for 1050 °C. (b) Ni interdiffusion coefficients as a function of temperature for Ni-42 NPs is also shown

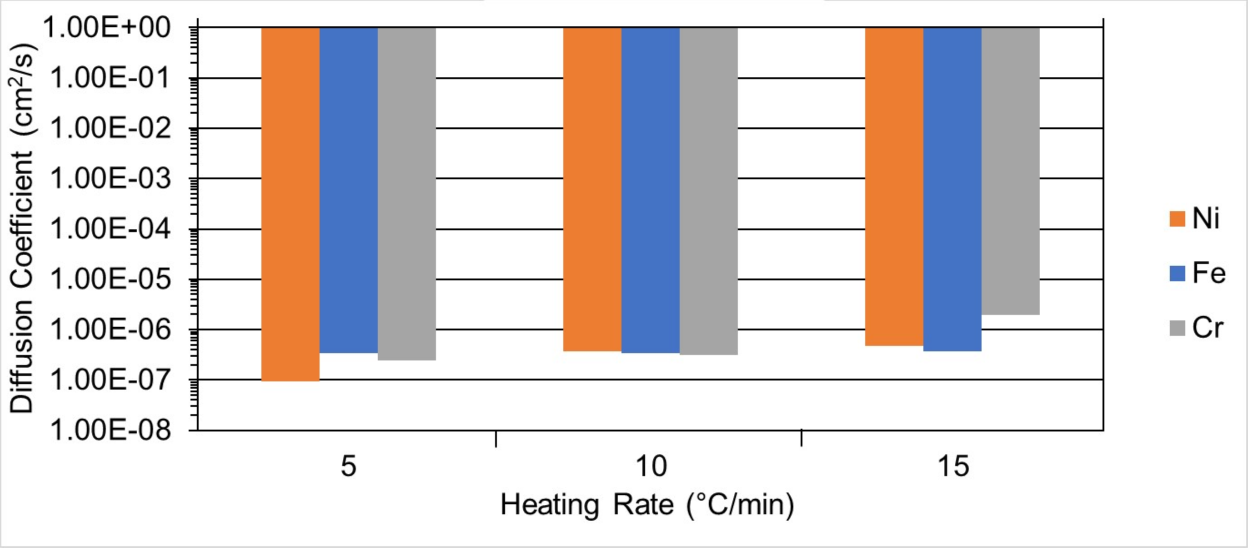

Figure 6.7: Calculated interdiffusion coefficients of key elements (Ni, Cr and Fe) in Ni-42 joints, processed with the three (3) different nano-brazing heating rates. These calculations are based on Sauer-Friese analysis of EDS data

to surface diffusion behavior of NMs. Additionally, atom probe tomography is sensitive enough for us to track lower concentration elements in IN718 such as Nb, Al, and Ti.

6.4 Conclusions

This study demonstrates that the wettability of Ni NWs outpaces the wettability of Ni NPs. The suspected reason for the lower contact angle for Ni NWs is that the lower surface energy in solid form due to the larger radius results in a lower γ_{lv} during surface melting. According to Young's equation (Equation 1.5), this leads to a lower contact angle. The interdiffusion coefficients for NMs in a joining context are seldom reported and they are investigated in detail in this chapter. The calculated effective interdiffusion coefficients are several orders higher than the lattice interdiffusion coefficients predicted using Equations 1.25 and 1.26, suggesting that grain boundary diffusion and surface diffusion are major contributors to the overall diffusion behavior in Ni NMs. The interdiffusion coefficients of Fe and Cr are also significantly enhanced. As the heating rate increases, the diffusivity also increases as a result of mitigating sintering at low temperatures.

Chapter 7

Conclusions and Outlook

7.1 Conclusions

Considering the lack of studies investigation nanobrazing materials, some of the fundamental aspects of nanobrazing needed to be investigated. Furthermore, in this dissertation, I discussed the performance of nanobrazing materials with respect to commercially available brazing alloys. I also discussed what the key factors would be in the success or failure of nanobrazing joints. First, Cu-Ag and Ag nanomaterials demonstrated higher strength compared to BAg-8 (the commercially available equivalent) by laser brazing with the implication that Hall-Petch strengthening even at the subgrain level is one of the factors of success. An investigation of the effect of particle shape on wetting and diffusion behavior showed that nanowires exhibited better diffusion and wetting behavior. The advantage of wetting and diffusion led to the Ag nanowires having higher strength than Ag nanoparticles. The addition of Ag NPs seems to make the joint more reliable while the Ag NWs lower the laser power threshold. The Ni-Mn-Fe-Co-Cu HEA investigated in Chapter 3 demonstrated good mechanical performance as a brazing filler metal for IN71. However, the phase separation experienced by HEA nanoparticles led to a weaker joint, even though it was demonstrated that the minimum brazing temperature is decreased by over 100 °. The self-powered brazing using Ni/Al RMFs demonstrated that reactive exothermic materials can be used for brazing, however a lack of diffusion between the RMF and the BAlSi-4 material and the brittleness of the AlNi reaction product resulted in a low bonding strength. The reaction temperature was clearly enough to melt the BAlSi-4 material. In Chapters 5 and 6, heating rate was identified as a new critical factor for maximizing joint strength. Hall-Petch strengthening was identified as the strengthening mechanism at the Ni-IN718 interface. Ni nanomaterials do not completely melt in the temperature ranges examined, but through diffusion and surface melting, a dense joint is formed without complete melting. However, surface melting has yet to be experimentally observed. Also, the diffusivity of Ni nanoparticles and nanowires was experimentally calculated in a joining context and grain boundary and surface diffusion was found to be major contributors to the overall interdiffusion behavior of Ni NMs. In summary, the findings of each chapter firmly support one or both of the hypotheses stated in Chapter 1.

Therefore, the main discoveries during my Ph.D. studies can be summarized as follows:

1. Cu-Ag nanobrazing materials exhibit higher strength compared to bulk brazing materials due to Hall-Petch strengthening.

2. High entropy alloy nanoparticles successfully demonstrate lower brazing temperature at the cost of phase stability.

3. Reactive multilayer films can successfully melt low melting temperature brazing materials, but due to a lack of diffusion the high strength is not achieved.
4. High strength joining using Ni nanomaterials can be achieved by relying on surface melting and diffusion processes. Increasing the heating rate also produces Hall-Petch strengthened joints.
5. Ni and Ag nanowires exhibit more favorable wetting properties over their respective nanoparticle counterparts and diffusion in nanomaterials is primarily driven by grain boundary diffusion.

7.2 Outlook

As mentioned in the previous section, surface melting in Ni-based nanomaterials has yet to be experimentally observed and ratified through repetition. Observing and mathematically modeling the surface melting temperature of nanomaterials through experimental determination is the next fundamental step in nanobrazing technology. Additionally, the effective diffusion coefficient of nanomaterials in a joining context needs to be repeated and ratified under different experimental conditions and base materials. For instance, the IN718 used ins in this dissertation is polycrystalline and hence grain boundary diffusion can be exploited. Performing the same diffusion analysis and brazing experiments on a single crystal alloy can help firmly establish the lattice diffusion coefficient of nanobrazing materials. Furthermore, an informed study of the nanoscale phase transformations can aid in the design of multicomponent nanobrazing materials especially those prone to phase separation. For nanomaterials that do not fully melt, maximizing the initial green density and densification process prior to brazing will be extremely helpful and can potentially push high melting metal nanoparticles such as Ni to exceed the maximum achievable strength of BNi brazing materials without the use of melting point depressants. One such way to accomplish both is to mix Ni nanowires and nanoparticles to balance maximizing green density (Figure 7.1) and improving densification.

Modeling of the nanobrazing process will additionally be a highly useful tool enhancing understanding. Phase field modeling in particular can model the particle-particle and particle-base material joining procedures [283, 284] and different phase transformations [84, 283, 285, 286]. Phase field modeling can be combined with Park and Lees CALPHAD method for nanoalloy phase diagrams to build a comprehensive model that incorporates solid-state sintering, surface melting, and complete melting of NPs. Solid-state sintering, surface melting, melting, and solidification of elemental and nanoalloy NPs are frequently an atomistic perspective by molecular dynamics, density functional theory, or Monte Carlo [104, 287]. However, most MD, DFT, and MC calculations are limited to NPs with a diameter less than 20 nm which is smaller than what can be used practically in brazing experiments. Molecular dynamics, density functional theory and Monte Carlo are also limited to small systems due to the large amount of computational resources needed to handle a large system. Phase field modeling is better equipped for modeling the melting, solidification, and microstructure evolution of NPs in a larger system because PF modeling is a continuum-based technique and hence does not have to bear to computational burden of millions or billions of atoms, unlike molecular dynamics, density functional theory, or Monte Carlo. PF modeling can also address both the thermodynamics and kinetics of sintering, melting, solidification, and microstructure evolution, unlike CALPHAD which only addresses the thermodynamics

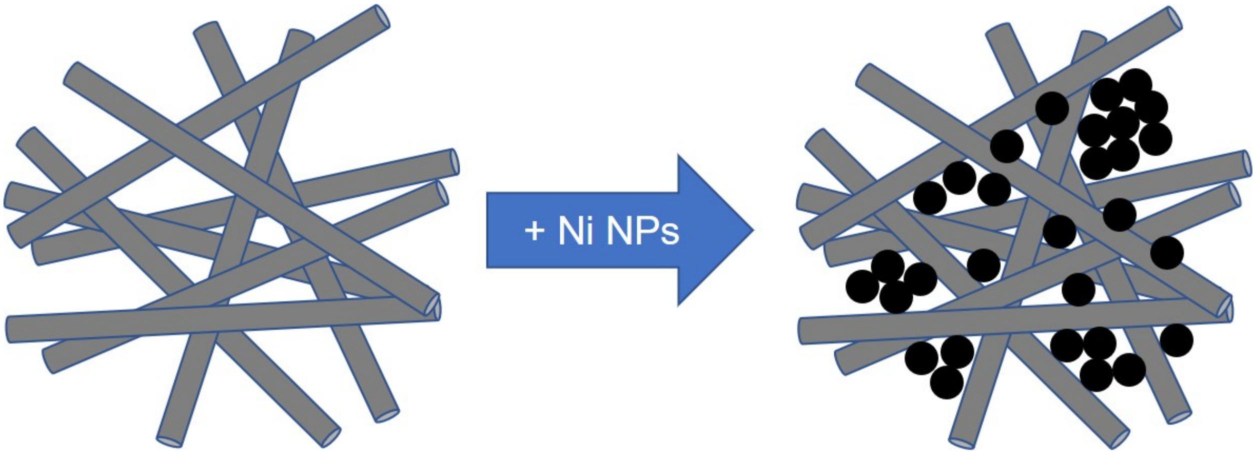

Figure 7.1: Schematic of showing how the initial density of a pure Ni NW pellet (left) can be increased by adding Ni NPs (right).

of melting and solidification (Figure 7.2). The general form of the governing equation of the thermo-kinetic approach to PF modeling is as follows:

$$F = \int_v \, [f(\phi_1,\ \phi_2,\ \phi_3, \ldots, \phi_N) + \frac{1}{2}\sum_{i=1}^{N} \kappa_i \left|\nabla\phi_i\right|^2] dv \qquad 7.1$$

F is the total free energy, f($\phi_1,\ \phi_2,\ \phi_3, \ldots$) is the free energy density of the system as a function of phase field order parameter ϕ_i. PF variables are designed to smoothly connect two or more different states or phases. For example, a PF variable used to describe melting can equal ranges from 0 (100% liquid) to 1 (100% solid) [285]. Values between 0 and 1 are metastable states between solid and liquid such as with surface melting. The graphical representation of a PF variable typically looks like a sigmoid curve, sinusoidal wave, or damped sinusoidal wave. The model will be thoroughly validated through several brazing experiments and subsequent microstructural analysis. These modeling efforts will provide the foundation developing time-temperature-transformation and continuous cooling transformation diagrams for nanojoining processes. Furthermore, using phase field modeling

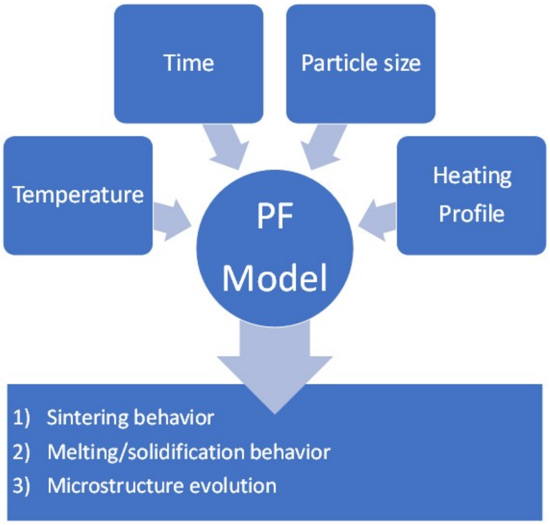
Time
Particle size
Temperature
Heating Profile
PF Model
1) Sintering behavior
2) Melting/solidification behavior
3) Microstructure evolution

Figure 7.2: Flow chart of the input parameters and projected output of the proposed phase field modeling.

to incorporate thermodynamics and kinetics into the study of nanojoining behavior can help modify existing equations for melting temperature and diffusion in nanoparticles to account for heating rate and other kinetic processes.

As for self-powered brazing, an alternative solution is to strengthen the bonding through the direct contact of brazing materials as opposed to using the RMFs as the sole joining layer. Ni/Al RMFs could be embedded within a trenched BAlSi-4 brazing layer (Figure 7.3). When the RMF is ignited, the reaction heat will result in an RMF-BAlSi-4 interface like the ones described in this study. Additionally, the reaction heat will melt the corners of the BAlSi-4 (indicated by arrows in Figure 7.3) and will fuse to the opposing BAlSi-4 surface. Ideally the union of two BAlSi-4 surfaces will be much stronger than the union of Ni/Al RMF and BAlSi-4. The AlNi intermetallic compound will serve as a strengthening precipitate instead of the primary load-bearing layer. For a large brazing area, multiple ignition points can be used to ensure that the reaction is not quenched before completion.

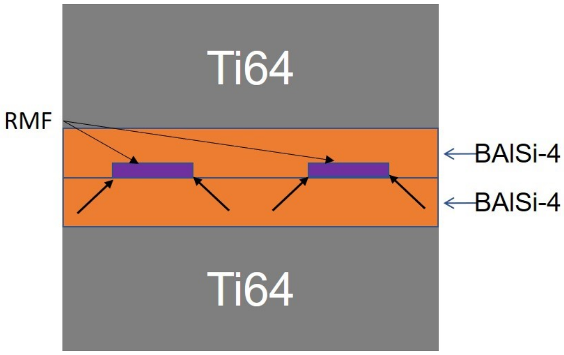

Figure 7.3: Suggested embedded RMF joining schematic; arrows indicate where the adjacent BAlSi-4 surfaces would fuse together [232].

Lastly, characterization of the thermomechanical properties of the RMF-brazed joint will also need to be conducted.

References

References

[1] Hertzberg, R. W. *Deformation and fracture mechanics of engineering materials.* John Wiley & Sons, Ltd, Canada, 4 edition, (1996). 2, 5, 87, 138

[2] Hansen, N. *Scripta Materialia* **51**(8), 801 – 806 (2004). Viewpoint set no. 35. Metals and alloys with a structural scale from the micrometer to the atomic dimensions. 3

[3] Trelewicz, J. R. and Schuh, C. A. *Acta Materialia* **55**(17), 5948 – 5958 (2007). 4

[4] Schuh, C., Nieh, T., and Yamasaki, T. *Scripta Materialia* **46**(10), 735 – 740 (2002). 4

[5] Lesuer, D., Syn, C., and Sherby, O. *Materials Science and Engineering: A* **463**(1), 54 – 60 (2007). TMS 2006, Mukherjee Symposium. 4, 84

[6] Sherby, O. D., Klundt, R. H., and Miller, A. K. *Metallurgical Transactions A* **8**(6), 843–850 Jun (1977). 4

[7] Chua, B. W., Lu, L., and Lai, M. O. *Materials research bulletin* **41**(11), 2102–2110 (2006). 4

[8] Wang, Y., Chen, M., Zhou, F., and Ma, E. *Nature* **419**(6910), 912–5 (2002). 4

[9] Li, Y., Zeng, X., and Blum, W. *Acta Materialia* **52**(17), 5009 – 5018 (2004). 4

[10] Rogers, D. J., Sandana, V. E., Teherani, F. H., Razeghi, M., and Drouhin, H. J. *Zinc Oxide Materials and Devices Iv* **7217** (2009). 4

[11] Benjamin, J. S. *Metallurgical Transactions* **1**(10), 2943–2951 Oct (1970). 5

[12] Doi, M., Miki, D., Moritani, T., and Kozakai, T. *Superalloys 2004* , 109–114 (2004). 5, 12

[13] Slama, C. and Abdellaoui, M. *Journal of Alloys and Compounds* **306**(1), 277 – 284 (2000). xv, 5, 6, 12, 136

[14] Zhang, Z. and Chen, D. *Scripta Materialia* **54**(7), 1321 – 1326 (2006). 5

[15] Ferguson, J. B., Schultz, B. F., Venugopalan, D., Lopez, H. F., Rohatgi, P. K., Cho, K., and Kim, C.-S. *Metals and Materials International* **20**(2), 375–388 Mar (2014). 5, 21

[16] Hu, A., Bridges, D., Zhang, S., and Feng, Z. *Advanced Materials & Processes* **175**(7), 25–29 (2017). xv, 8, 9, 23

[17] Anderson, D. L. *New Theory of the Earth.* Cambridge University Press, 2 edition, (2007). 9

[18] Stout, R. T., Ott, C. W., Pense, A. W., Snyder, D. J., Somers, B. R., and Somers, R. E. *Weldability of Steels.* Welding Research Council, New York, N.Y., 4th edition, (1987). 9, 10, 18, 20, 24

[19] Maalekian, M. Report, Christian Doppler Laboratory for Early Stages of Precipitation, October 2007 (2007). 9

[20] Inc., C. T. (2011). xv, 10, 11

[21] Emami, S., Saeid, T., and Khosroshahi, R. A. *Journal of Alloys and Compounds* **739**, 678 – 689 (2018). 10

[22] Huo, S., Qian, M., Schaffer, G., and Crossin, E. In *Fundamentals of Aluminium Metallurgy,* Lumley, R., editor, Woodhead Publishing Series in Metals and Surface Engineering, 655 – 701. Woodhead Publishing (2011). 10, 29

[23] Jose Roberto Costa Guimarases, P. R. R. *Materials Research* **18**, 595 – 601 06 (2015). xv, 10

[24] Kim, D., Jang, C., and Ryu, W. S. *Oxidation of Metals* **71**(5-6), 271–293 (2009). 11

[25] Heckl, A., Neumeier, S., Gken, M., and Singer, R. *Materials Science and Engineering: A* **528**(9), 3435 – 3444 (2011). 11

[26] Harrison, N. J., Todd, I., and Mumtaz, K. *Acta Materialia* **94**, 59 – 68 (2015). 11

[27] Mishima, Y., Ochiai, S., and Suzuki, T. *Acta Metallurgica* **33**(6), 1161 – 1169 (1985). 12, 140

[28] Smith, G. D. and Patel, S. J. In *Superalloys 718, 625, 706 and Derivatives*, 135–154. The Minerals, Metals & Materials Society, (2005).

[29] Li, J. and Wang, H. *Materials Science and Engineering: A* **527**(18), 4823 – 4829 (2010). 12, 13

[30] Amato, K., Gaytan, S., Murr, L., Martinez, E., Shindo, P., Hernandez, J., Collins, S., and Medina, F. *Acta Materialia* **60**(5), 2229 – 2239 (2012). 12, 120

[31] Reddy, G. M., Murthy, C. V. S., Rao, K. S., and Rao, K. P. *International Journal of Advanced Manufacturing Technology* **43**(7-8), 671–680 (2009). 12

[32] Ye, X., Hua, X., Wang, M., and Lou, S. *Journal of Materials Processing Technology* **222**, 381–390 (2015). 12, 18, 45

[33] Bouse, G. K. *Superalloys 1996* , 163–172 (1996). 12

[34] Shankar, V., Rao, K. B. S., and Mannan, S. *Journal of Nuclear Materials* **288**(2), 222 – 232 (2001). 12

[35] Schwartz, M. *Brazing Fundamentals*, volume 2. ASM International, Materials Park, Ohio (2003). 12, 119, 122, 131

[36] Mignanelli, P., Jones, N., Pickering, E., Mess, O., Rae, C., Hardy, M., and Stone, H. *Scripta Materialia* **136**, 136 – 140 (2017). xvi, 13

[37] Gangwar, K. and Ramulu, M. *Materials & Design* **141**, 230 – 255 (2018). 13, 18

[38] Ruirun, C., Deshuang, Z., Tengfei, M., Hongsheng, D., Yanqing, S., Jingjie, G., and Hengzhi, F. *Scientific Reports* **7**, 41463 (2017). 13

[39] Khorasani, A. M., Goldberg, M., Doeven, E. H., and Littlefair, G. *Journal of Biomaterials and Tissue Engineering* **5**(8), 593–619 (2015). 13

[40] Zhang, C., Robson, J., and Prangnell, P. *Journal of Materials Processing Technology* **231**, 382 – 388 (2016). 14

[41] Atieh, A. M. and Khan, T. I. *Journal of Materials Science* **49**(22), 7648–7658 (2014). 14, 38

[42] Pardal, G., Ganguly, S., Williams, S., and Vaja, J. *International Journal of Advanced Manufacturing Technology* **86**(5-8), 1139–1150 (2016). 14, 20

[43] Simoes, S., Ramos, A. S., Viana, F., Vieira, M. T., and Vieira, M. F. *Metals* **6**(5), 96 (2016). 96

[44] Kumar, R. and Balasubramanian, M. *Defence Technology* **11**(1), 65–75 (2015). 14

[45] Ahmed, T. and Rack, H. *Materials Science and Engineering: A* **243**(1), 206 – 211 (1998). 14

[46] In *Introduction to Aerospace Materials,* Mouritz, A. P., editor, 202 – 223. Woodhead Publishing (2012). 14, 15

[47] Smallman, R. and Ngan, A. In *Modern Physical Metallurgy (Eighth Edition),* Smallman, R. and Ngan, A., editors, 529 – 569. Butterworth-Heinemann, Oxfordeighth edition edition (2014). titanium. 15

[48] Boyer, R. R. *JOM* **32**(3), 61–65 Mar (1980). 15

[49] Rhodes, C. G. and Paton, N. E. *Metallurgical Transactions A* **8**(11), 1749 Nov (1977). 15

[50] Shi, X., Zeng, W., Sun, Y., Han, Y., Zhao, Y., and Guo, P. *Journal of Materials Engineering and Performance* **24**(4), 1754–1762 Apr (2015). xvi, 15

[51] Tsai, M.-H. and Yeh, J.-W. *Materials Research Letters* **2**(3), 107–123 (2014). 15, 79

[52] Bridges, D., Zhang, S., Lang, S., Gao, M., Yu, Z., Feng, Z., and Hu, A. *Materials Letters* **215**, 11–14 (2018). xx, xxi, 15, 16, 77, 82, 83, 85, 87, 88, 90

[53] Murali, M., Babu, S. P. K., Krishna, B. J., and Vallimanalan, A. *Progress in Natural Science: Materials International* **26**(4), 380–384 (2016). 15

[54] Yeh, J. W., Chen, S. K., Lin, S. J., Gan, J. Y., Chin, T. S., Shun, T. T., Tsau, C. H., and Chang, S. Y. *Advanced Engineering Materials* **6**(5), 299–303 (2004). 15

[55] Gurao, N. P. and Biswas, K. *Journal of Alloys and Compounds* **697**, 434–442 (2016). 15

[56] Hsu, U. S., Hung, U. D., Yeh, J. W., Chen, S. K., Huang, Y. S., and Yang, C. C. *Materials Science and Engineering: A* **460**, 403–408 (2007). 16

[57] Yeh, J. W. *Jom* **65**(12), 1759–1771 (2013). 16

[58] Gludovatz, B., Hohenwarter, A., Catoor, D., Chang, E. H., George, E. P., and Ritchie, R. O. *Science* **345**(6201), 1153–8 (2014).

[59] Rao, J. C., Diao, H. Y., Ocelk, V., Vainchtein, D., Zhang, C., Kuo, C., Tang, Z., Guo, W., Poplawsky, J. D., Zhou, Y., Liaw, P. K., and De Hosson, J. T. M. *Acta Materialia* **131**, 206–220 (2017). 16

[60] Tung, C. C., Yeh, J. W., Shun, T., Chen, S. K., and Huang, Y. S. *Materials letters* **61**(1), 1–5 (2007). 16

[61] Santodonato, L. J., Liaw, P. K., Unocic, R. R., Bei, H., and Morris, J. R. *Nature Communications* **9**(1), 4520 (2018). 16

[62] Lin, C., Shiue, R.-K., Wu, S.-K., and Huang, H.-L. *Entropy* **21**(3), 283 (2019). 16

[63] Chikova, O. A., Tsepelev, V. S., Vyukhin, V. V., and Shmakova, K. Y. *Metallurgist* **59**(5-6), 435–440 (2015). 16

[64] Tsao, T.-K., Yeh, A.-C., Kuo, C.-M., Kakehi, K., Murakami, H., Yeh, J.-W., and Jian, S.-R. *Scientific reports* **7**(1), 12658 (2017). 16

[65] Mller, F. and Thomy, C. In *Lasers in Manufacturing Conference*, volume 41, 81–89, (2013). 18

[66] Liu, W. C., Yao, M., Chen, Z. L., and Wang, S. G. *Journal of Materials Science* **34**(11), 2583–2586 (1999). 18

[67] Wu, P. H., Liu, N., Zhou, P. J., Peng, Z., Du, W. D., Wang, X. J., and Pan, Y. *Materials Science and Technology* , 1–5 (2016). 18

[68] Zhang, L.-C., Liu, Y., Li, S., and Hao, Y. *Adv. Eng. Mater.* **20**(5), 1700842 March (2018). 18

[69] Eluri, R. and Paul, B. K. *Materials & Design* **36**, 13–23 (2012). 18, 38

[70] Charles, A. and Taylor, C. *Development of a Method to Repair Gas Turbine Blades using Electron Beam Melting Additive Manufacturing Technology.* Thesis, KTH Royal Institute of Technology, (2016). 19, 23

[71] Hawk, C. *WIDE GAP BRAZE REPAIRS OF NICKEL SUPERALLOY GAS TURBINE COMPONENTS.* Thesis, (2016).

[72] Huang, X. and Miglietti, W. *Journal of Engineering for Gas Turbines and Power* **134**, 10801 (2012). 19, 23

[73] Chen, B., Xiong, H. P., Mao, W., Cheng, Y. Y., and Wu, X. *Welding in the World* **59**(6), 911–915 (2015). 20

[74] Ma, Y., Bridges, D., Yu, Y., Han, J., Li, H., and Hu, A. *Applied Sciences* **9**(2) (2019). 20, 96

[75] Massalski, T. B., Murray, J. L., Bennett, L. H., and Baker, H. *Binary alloy phase diagrams*, volume 2. American Society for Metals, Metals Park, Ohio, (1986). 21, 56, 120

[76] Khorram, A. and Ghoreishi, M. *Optics & Laser Technology* **68**, 165–174 (2015). 21, 45, 119

[77] Khorram, A., Fakhraei, O., and Torkamany, M. J. *The International Journal of Advanced Manufacturing Technology* **88**(5), 2075–2084 (2017). xvii, 21, 45, 46, 119

[78] Hebda, M., Kaczor, P., and Miernik, K. *Archives of Metallurgy and Materials* **64**(1), 5–11 (2019). 22

[79] Stroppa, D. G., Unfried, J., Hermenegildo, T., and Ramirez, A. J. *Welding Journal* **89**(3), 47–49 (2010). 23

[80] Solomon, H. D., Delair, R. E., and Thyssen, J. *Welding Journal* **82**(10), 278s–287s (2003). 23

[81] den Broeder, F. *Scripta Metallurgica* **3**(5), 321 – 325 (1969). 24, 25

[82] Glicksman, M. E. *Diffusion in Solids: Field Theory, Solid-State Principles, and Applications.* John Wiley & Sons, Inc., Canada, (2000). 25

[83] elik, C. and Duman, M. *Journal of Computational Physics* **231**(4), 1743 – 1750 (2012). 26

[84] Plapp, M. *Phase-Field Models*, volume 538, 129–175. (2012). 26, 162

[85] Zhang, R., Jing, T., Jie, W., and Liu, B. *Acta materialia* **54**(8), 2235–2239 (2006). 26

[86] Ye, X., Hua, X. M., Wu, Y. X., and Lou, S. N. *Journal of Materials Processing Technology* **217**, 13–20 (2015). 26, 119

[87] Ma, Y., Li, H., Yang, L., and Hu, A. *Journal of Materials Processing Technology* **262**, 204–209 (2018). 27, 96, 99

[88] Arafin, M. A., Medraj, M., Turner, D. P., and Bocher, P. *Materials Science and Engineering A* **447**(1-2), 125–133 (2007). 27, 45

[89] West, D. R. F. *Ternary equilibrium diagrams.* Chapman and Hall, London ; New York, 2nd edition, (1982). 27, 135

[90] Herzog, D., Seyda, V., Wycisk, E., and Emmelmann, C. *Acta Materialia* **117**, 371 – 392 (2016). 28

[91] Li, R. Z., Hu, A., Zhang, T., and Oakes, K. D. *ACS Appl Mater Interfaces* **6**(23), 21721–9 (2014). xvii, 28, 37, 38, 50

[92] Li, R. Z., Hu, A., Bridges, D., Zhang, T., Oakes, K. D., Peng, R., Tumuluri, U., Wu, Z., and Feng, Z. *Nanoscale* **7**(16), 7368–77 (2015). 28, 35, 37, 136, 139, 142

[93] Yu, Y., Chen, M., Wang, S., Hill, C., Joshi, P., and Hu, A. *Journal of Laser Applications* **30**(3), 032605 (2018). 28

[94] Yu, Y., Chen, M., Wang, S., Hill, C., Joshi, P., Kuruganti, T., and Hu, A. *Journal of The Electrochemical Society* **165**(3), A584–A592 (2018). 28

[95] Vyatskikh, A., Delalande, S., Kudo, A., Zhang, X., Portela, C. M., and Greer, J. R. *Nature Communications* **9**(1), 593 February (2018). 28

[96] Sokoluk, M., Cao, C., Pan, S., and Li, X. *Nature Communications* **10**(1), 98 (2019). 29, 144

[97] Hdz-Garca, H., Martinez, A., Muoz-Arroyo, R., Acevedo-Dvila, J., Garca-Vzquez, F., and Reyes-Valdes, F. *Journal of Materials Science and Technology* **30**(3), 259–262 (2014). 29, 105, 144

[98] Hdz-Garca, H. M., Muoz-Arroyo, R., Martinez, A. I., Gonzlez, M. A., Granda-Gutirrez, E. E., Acevedo-Dvila, J. L., Castro-Roman, M., and Garca-Vzquez, F. *Journal of Nanomaterials* **2016**, 1–7 (2016). 29, 144

[99] Lipowsky, R. *Physics Review Letters* **49**(21), 1575–1578 (1982). 29, 30

[100] Makkonen, L. *Langmuir* **16**(20), 7669–7672 October (2000). 30

[101] Andrews, D. H. *J. Chem. Educ.* **6**(3), 591 March (1929). 30, 194

[102] Nanda, K. K., Sahu, S. N., and Behera, S. N. *Physical Review A* **66**(1) (2002). xxiii, xxvi, 30, 126, 128, 151, 152

[103] Qi, W. H. and Wang, M. P. *Materials Chemistry and Physics* **88**(2-3), 280–284 (2004). xxvi, 30, 151, 152

[104] Wang, J. Q., Shin, S. H., and Hu, A. M. *Journal of Physical Chemistry C* **120**(31), 17791–17800 (2016). 31, 58, 62, 67, 162

[105] Wang, J., Shin, S., Hu, A., and Wilt, J. K. *Computational Materials Science* **152**, 228–235 (2018). 127

[106] Alarifi, H. A., Atis, M., Ozdogan, C., Hu, A., Yavuz, M., and Zhou, Y. *Journal of Physical Chemistry C* **117**(23), 12289–12298 (2013). 31, 40, 67, 133

[107] Zhang, K., Stocks, G. M., and Zhong, J. *Nanotechnology* **18**(28), 285703 June (2007). 31

[108] Chernyshev, A. P. *Materials Letters* **63**(17), 1525–1527 (2009). 31, 40, 127, 154

[109] German, R. *Sintering Theory and Practice.* John Wiley & Sons, Inc., New York, NY, (1996). 31, 33, 40

[110] Bridges, D., Li, R., Gao, Z., Wang, Z., Wang, Z., Hu, A., and Feng, Z. *Metallic Nanopastes for Power Electronic Packaging*, book section 10. Taylor & Francis Group, Boca Raton, Florida (2017). xvii, 31, 35, 36, 38, 39, 124

[111] Fang, Z. Z., Wang, H., and Kumar, V. *International Journal of Refractory Metals and Hard Materials* **62**, 110–117 (2017). 32, 40, 131

[112] Jiang, Q., Zhang, S. H., and Li, J. C. *Solid State Communications* **130**(9), 581–584 (2004). xxvi, 32, 156

[113] Fang, Z. Z. and Wang, H. *International Materials Reviews* **53**(6), 326–352 (2008). 33, 130

[114] Rahimian, M., Ehsani, N., Parvin, N., and Baharvandi, H. R. *Journal of Materials Processing Technology* **209**(14), 5387–5393 (2009).

[115] Buffat, P. and Borel, J.-P. *PRA* **13**(6), 2287–2298 June (1976). xvii, 33, 35

[116] Munoz, J. E., Cervantes, J., Esparza, R., and Rosas, G. *Journal of Nanoparticle Research* **9**(5), 945–950 (2007). 33, 84

[117] Amirkhanlou, S., Ketabchi, M., and Parvin, N. *Materials Letters* **86**, 122–124 (2012).

[118] Anand, K., Varghese, S., and Kurian, T. *Powder Technology* **271**, 187–192 (2015).

[119] Gunduz, I. E., Kyriakou, A., Vlachos, N., Kyratsi, T., Doumanidis, C. C., Son, S., and Rebholz, C. *Surface & Coatings Technology* **260**, 396–400 (2014). 33, 38, 96

[120] Arakelyan, S. M., Veiko, V. P., Kutrovskaya, S. V., Kucherik, A. O., Osipov, A. V., Vartanyan, T. A., and Itina, T. E. *Journal of Nanoparticle Research* **18**(6), 155 (2016). 33, 35

[121] Krishna Podagatlapalli, G., Hamad, S., Tewari, S. P., Sreedhar, S., Prasad, M. D., and Venugopal Rao, S. *Journal of Applied Physics* **113**(7), 073106 (2013). 40, 54

[122] Streubel, R., Barcikowski, S., and Gökce, B. *Opt. Lett.* **41**(7), 1486–1489 Apr (2016).

[123] DellAglio, M., Gaudiuso, R., Pascale, O. D., and Giacomo, A. D. *Applied Surface Science* **348**, 4 – 9 (2015). Advanced Synthesis of Functional Nanoparticles by Lasers in Liquids From Fundamentals to Application in Catalysis, Energy Science, and Biomedicine.

[124] Zhang, J., Chaker, M., and Ma, D. *Journal of Colloid and Interface Science* **489**, 138 – 149 (2017). Laser Synthesis. 33

[125] Lazar, K., Varga, L. K., Kis, V. K., Fekete, T., Klencsar, Z., Stichleutner, S., Szabo, L., and Harsanyi, I. *Journal of Alloys and Compounds* **763**, 759–770 (2018). 33

[126] Kotov, Y. A. *Journal of Nanoparticle Research* **5**(5-6), 539–550 (2003).

[127] Sarathi, R., Sindhu, T. K., and Chakravarthy, S. R. *Materials Characterization* **58**, 148–155 (2007).

[128] Abdelkader, E. M., Jelliss, P. A., and Buckner, S. W. *Inorganic Chemistry* **54**(12), 5897–5906 (2015).

[129] Lee, S., Kim, W., Park, J. S., Suh, C. Y., and Cho, S. W. *Materials Transactions* **52**(2), 135–138 (2011). 33

[130] Pithawalla, Y., El-Shall, M., and Deevi, S. *Scripta Materialia* **48**(6), 671 – 676 (2003). 33

[131] Glaspell, G. P., Jagodzinski, P. W., and Manivannan, A. *J. Phys. Chem. B* **108**(28), 9604–9607 July (2004). 33

[132] Cho, C., Ha, Y. C., Kang, C., Jin, Y. S., and Rim, G. H. *Journal of the Korean Physical Society* **57**(6), 1807–1810 (2010). 34

[133] Yadav, T. P., Yadav, R. M., and Singh, D. P. *Nanoscience and Nanotechnology* **2**(3), 22–48 (2012). 34

[134] Rekha, M. Y., Mallik, N., and Srivastava, C. *Sci Rep* **8**(1), 8737 (2018). 34

[135] Yao, Y., Huang, Z., Xie, P., Lacey, S. D., Jacob, R. J., Xie, H., Chen, F., Nie, A., Pu, T., Rehwoldt, M., Yu, D., Zachariah, M. R., Wang, C., Shahbazian-Yassar, R., Li, J., and Hu, L. *Science* **359**(6383), 1489–1494 (2018).

[136] Wu, Q. F., Wang, Z. J., He, F., Wang, L. L., Luo, J., Li, J. J., and Wang, J. C. *Metallurgical and Materials Transactions a-Physical Metallurgy and Materials Science* **49a**(10), 4986–4990 (2018). 34

[137] Bin, X. B., Chen, J. Z., and Cao, H. *Turkish Journal of Chemistry* **35**(2), 181–188 (2011). 35
[138] Zheng, X. W. *Journal of Nano Research* **4**, 145–152 (2008).
[139] Basts, N. G., Comenge, J., and Puntes, V. *Langmuir* **27**(17), 11098–11105 September (2011). 35, 124
[140] Bai, S., Lin, Y.-H., Zhang, X.-P., Zhou, W.-P., Chen, T., Ma, Y., Hou, T.-X., Bridges, D., Oakes, K. D., and Hu, A. *Plasmonics* **10**(6), 1675–1685 (2015). 35
[141] Li, R.-Z., Zhang, T., Hu, A., and Bridges, D. *Materials Transactions* **56**(7), 984–987 (2015). 35, 37, 72
[142] Singh, M. and Tlali, S. *Journal of Taibah University for Science* **11**(6), 1–8 (2016). 63
[143] Ghasemi, M., Zanolli, Z., Stankovski, M., and Johansson, J. *Nanoscale* **7**(41), 17387–96 (2015).
[144] Bridges, D., Ma, C., Palmer, Z., Wang, S., Feng, Z., and Hu, A. *Journal of Materials Processing Technology* **249**, 313–324 (2017). xvii, xviii, xix, xx, 35, 43, 52, 54, 55, 56, 57, 59, 64, 66, 68, 69, 70, 71, 72, 73
[145] Suramwar, N. V., Thakare, S. R., and Khaty, N. T. *Synthesis and Reactivity in Inorganic, Metal-Organic, and Nano-Metal Chemistry* **43**(1), 57–62 (2013). 35
[146] Xu, S. L., Sun, X., Ye, H., You, T., Song, X. Y., and Sun, S. X. *Materials Chemistry and Physics* **120**(1), 1–5 (2010).
[147] Gong, J., Luo, L., Yu, S.-H., Qian, H., and Fei, L. *J. Mater. Chem.* **16**(1), 101–105 (2006). 35
[148] Sharma, V., Chotia, C., Tarachand, Ganesan, V., and Okram, G. S. *Phys. Chem. Chem. Phys.* **19**, 14096–14106 (2017). 35
[149] Verma, A. D., Mandal, R. K., and Sinha, I. *Catalysis Letters* **145**(10), 1885–1892 (2015). 35
[150] Sarkar, A., Mukherjee, T., and Kapoor, S. *Journal of Physical Chemistry C* **112**(9), 3334–3340 (2008).
[151] Yang, C. C., Wang, Y. Y., and Wan, C. C. *Journal of the Electrochemical Society* **152**(2), C96–C100 (2005). 35
[152] Tang, X.-F., Yang, Z.-G., and Wang, W.-J. *Colloids and Surfaces A: Physicochemical and Engineering Aspects* **360**(1-3), 99–104 (2010). 35
[153] Wu, C. J., Chen, S. M., Sheng, Y. J., and Tsao, H. K. *Journal of the Taiwan Institute of Chemical Engineers* **45**(5), 2719–2724 (2014). 35
[154] Kim, C. K., Lee, G. J., Lee, M. K., and Rhee, C. K. *Powder Technology* **263**, 1–6 (2014). 35, 55
[155] Lin, J. and Guliants, V. *Applied Catalysis a-General* **445**, 187–194 (2012).
[156] Lee, C., Kim, N. R., Koo, J., Lee, Y. J., and Lee, H. M. *Nanotechnology* **26**(45) (2015). 48
[157] Kim, T. G., Park, H. J., Woo, K., Jeong, S., Choi, Y., and Lee, S. Y. *ACS Appl Mater Interfaces* **10**(1), 1059–1066 (2018). 35
[158] Miyakawa, M., Hiyoshi, N., Nishioka, M., Koda, H., Sato, K., Miyazawa, A., and Suzuki, T. M. *Nanoscale* **6**(15), 8720–8725 (2014). 36
[159] Chen, Z., Mochizuki, D., Maitani, M. M., and Wada, Y. *Nanotechnology* **24**(26), 265602 (2013).

[160] Yamauchi, T., Tsukahara, Y., Sakata, T., Mori, H., Yanagida, T., Kawai, T., and Wada, Y. *Nanoscale* **2**(4), 515–23 (2010).

[161] Eluri, R. and Paul, B. *Materials Letters* **76**, 36 – 39 (2012). 36

[162] Zhang, P., He, J., Ma, X. B., Gong, J. L., and Nie, Z. H. *Chemical Communications* **49**(10), 987–989 (2013). 36

[163] Xu, H. and Suslick, K. S. *ACS Nano* **4**(6), 3209–3214 June (2010).

[164] Zin, V., Brunelli, K., and Dabal, M. *Materials Chemistry and Physics* **144**(3), 272 – 279 (2014). 36

[165] Levi, S., Rousse, C., Mancier, V., Michel, J., and Fricoteaux, P. *Journal of Materials Research* **30**(22), 3518–3527 (2015). 36

[166] Sofiah, A. G. N., Kananathan, J., Samykano, M., Ulakanathan, S., Lah, N. A. C., Harun, W. S. W., Sudhakar, K., Kadirgama, K., Ngui, W. K., and Siregar, J. P. *IOP Conference Series: Materials Science and Engineering* **257**, 012032 oct (2017).

[167] Gao, F. and Gu, Z. *Nanotechnology* **21**(11), 115604 feb (2010). 36, 40

[168] Ma, Y., Li, H., Bridges, D., Peng, P., Lawrie, B., Feng, Z., and Hu, A. *RSC Advances* **6**(79), 75916–75936 (2016). 36, 96

[169] Yang, C., Wong, C. P., and Yuen, M. M. F. *Journal of Materials Chemistry C* **1**(26), 4052 (2013).

[170] Siow, K. S. *Journal of Alloys and Compounds* **514**, 6–19 (2012).

[171] Liu, X., Wang, C., Liu, W., Zheng, Z., and Li, M. *Journal of Materials Science: Materials in Electronics* **28**(7), 5446–5451 (2017). xvii, 47, 48

[172] McCoppin, J., Reitz, T. L., Miller, R., Vijwani, H., Mukhopadhyay, S., and Young, D. *Journal of Electronic Materials* **43**(9), 3379–3388 (2014).

[173] Hu, A., Guo, J. Y., Alarifi, H., Patane, G., Zhou, Y., Compagnini, G., and Xu, C. X. *Applied Physics Letters* **97**(15), 153117 (2010). 40

[174] Fu, S., Mei, Y., Lu, G.-Q., Li, X., Chen, G., and Chen, X. *Materials Letters* **128**, 42–45 (2014). 36, 46

[175] Manikam, V. R., Razak, K. A., and Cheong, K. Y. *Microelectronics Reliability* **53**(3), 473–480 (2013). 37, 137

[176] Deng, Y., Bai, Y., Yu, Y., Deng, S., Tian, Y., Zhang, G., Zheng, C., Wu, J., and Hu, A. *Journal of Laser Applications* **31**(2), 022414 (2019). 37, 40

[177] Peng, P., Hu, A. M., Gerlich, A. P., Zou, G. S., Liu, L., and Zhou, Y. N. *Acs Applied Materials & Interfaces* **7**(23), 12597–12618 (2015). 37

[178] Wang, S., Li, M., Ji, H., and Wang, C. *Scripta Materialia* **69**(11-12), 789–792 (2013). 38

[179] Eluri, R. and Paul, B. *Journal of Nanoparticle Research* **15**(8) (2013). 38

[180] Tiwari, S. K. *Nickel Nanoparticles-Assisted Diffusion Brazing of Stainless Steel 316 for Microfluidic Applications*. Thesis, Oregon State University, (2010). 38, 40

[181] Zhao, W., Rovere, T., Weerawarne, D., Osterhoudt, G., Kang, N., Joseph, P., Luo, J., Shim, B., Poliks, M., and Zhong, C. J. *ACS Nano* **9**(6), 6168–77 (2015). 38

[182] Phillip, V. August (2008). 38, 40

[183] Veiko, V. P., Shishkovsky, I., Scherbakof, V., Volyansky, I., and Vartanyan, T. A. **9065**, 90650I (2013). 40

[184] Krishnan, S., Haseeb, A. S. M. A., and Johan, M. R. *IEEE Transactions on Components, Packaging and Manufacturing Technology* **2**(4), 587–592 (2012).

[185] Yu, E. K., Piao, L., and Kim, S. H. *Bulletin of the Korean Chemical Society* **32**(11), 4099–4102 (2011).

[186] Sabbah, W., Azzopardi, S., Buttay, C., Meuret, R., and Woirgard, E. *Microelectronics Reliability* **53**(9-11), 1617–1621 (2013). 40

[187] Hsel, M. and Krebs, F. C. *Journal of Materials Chemistry* **22**(31), 15683 (2012). 40

[188] Duan, X., Huang, Y., Agarwal, R., and Lieber, C. M. *Nature* **421**(6920), 241–245 January (2003). 40

[189] Tian, B., Kempa, T. J., and Lieber, C. M. *Chem Soc Rev* **38**(1), 16–24 (2009).

[190] Xu, S., Qin, Y., Xu, C., Wei, Y., Yang, R., and Wang, Z. L. *Nature Nanotechnology* **5**, 366 March (2010). 40

[191] Liu, L., Huang, H., Hu, A., Zou, G., Quintino, L., and Zhou, Y. *Nano-Micro Letters* **5**(2) (2013). 40

[192] Ma, C., Xue, S., Bridges, D., Palmer, Z., Feng, Z., and Hu, A. *Journal of Alloys and Compounds* **721**, 431–439 (2017). 40, 49, 67, 72

[193] Sopousek, J., Vrestal, J., Pinkas, J., Broz, P., Bursik, J., Styskalik, A., Skoda, D., Zobac, O., and Lee, J. *Calphad* **45**, 33–39 (2014). 39

[194] Park, J. and Lee, J. *Calphad* **32**(1), 135–141 (2008). 39

[195] Bridges, D., Ma, C., Zhang, S., Xue, S., Feng, Z., and Hu, A. *Welding in the World* **62**(1), 169–176 (2017). xix, 44, 61, 62, 145

[196] Pouranvari, M., Ekrami, A., and Kokabi, A. H. *Materials Science and Technology* **30**(1), 109–115 (2014). 45

[197] Jamaloei, A. D., Khorram, A., and Jafari, A. *Journal of Manufacturing Processes* **29**, 447–457 (2017). 45, 119

[198] Riggs, B., Alexandrov, B., Benatar, A., and Xu, R. *Science and Technology of Welding and Joining* **22**(3), 227–235 (2016). 45

[199] Hokita, Y., Kanzaki, M., Sugiyama, T., Arakawa, R., and Kawasaki, H. *ACS Appl Mater Interfaces* **7**(34), 19382–9 (2015). 46

[200] Kahler, J., Heuck, N., Wagner, A., Stranz, A., Peiner, E., and Waag, A. *IEEE Transactions on Components, Packaging and Manufacturing Technology* **2**(10), 1587–1591 (2012). 46

[201] Sheng, W. and Colino, R. *Power Electronic Modules — Design and Manufacture*. CRC Press, Boca Raton, 1st edition, (2004). xvii, 47

[202] Tsai, C. H., Chen, S. Y., Song, J. M., Chen, I. G., and Lee, H. Y. *Corrosion Science* **74**, 123–129 (2013). 47

[203] Chen, J., Chen, J., Li, Y., Zhou, W., Feng, X., Huang, Q., Zheng, J., Liu, R., Ma, Y., and Huang, W. *Nanoscale* **7**(40), 16874–16879 (2015). 47

[204] Zhang, X., Zhang, D., Ni, X., and Zheng, H. *Solid State Communications* **139**(8), 412–414 (2006). 50

[205] Grouchko, M., Kamyshny, A., and Magdassi, S. *Journal of Materials Chemistry* **19**(19), 3057 (2009). 50

[206] Zhao, J., Zhang, D., and Zhang, X. *Surface and Interface Analysis* **47**(4), 529–534 (2015). 50

[207] Spechler, J. A. and Arnold, C. B. *Applied Physics a-Materials Science & Processing* **108**(1), 25–28 (2012). 52

[208] Klinger, L., Kraft, O., and Rabkin, E. *Acta Materialia* **83**, 180–186 January (2015). 53

[209] Fan, H. J., Gsele, U., and Zacharias, M. *Small* **3**(10), 1660–1671 May (2019). 53

[210] Wang, R. L. and Ruan, H. B. *Journal of Alloys and Compounds* **656**, 936–943 (2016). 54

[211] Wei, Y., Chen, S., Lin, Y., Yang, Z. M., and Liu, L. *Journal of Materials Chemistry C* **3**(37), 9594–9602 (2015). 54

[212] Tang, X. L. and Tsuji, M. *Nanowires Science and Technology* , 25–42 (2010). 54

[213] Wazzan, A. R., Tung, P., and Robinson, L. B. *Journal of Applied Physics* **42**(13), 5316–5320 (1971). 59, 60

[214] G. Neumann, M. Pfundstein, P. R. *Physica Status Solidi a-Applied Research* **64**(1), 225–232 (1981). 60

[215] Hirano, K.-I., Cohen, M., and Averbach, B. L. *Acta Metallurgica* **11**(5), 463–466 May (1963). 60

[216] Zhan, H., Gu, Y., Yarlagadda, P. K. D. V., and Yan, C. In *2012 12th IEEE International Conference on Nanotechnology (IEEE-NANO)*, 1–5, (2012). 60, 63

[217] Sansoz, F., Huang, H. C., and Warner, D. H. *Jom* **60**(9), 79–84 (2008). 60

[218] Oura, K., Lifshifts, V., Saranin, A., Zotov, A., and Katayama, M. *Surface Science: An Introduction*. Advanced Texts in Physics. Springer-Verlag Berlin Heidelberg, Berlin, Germany, (2003). 60

[219] Wang, T., Zhao, M. H., Chen, X., Lu, G. Q., Ngo, K., and Luo, S. F. *Journal of Electronic Materials* **41**(9), 2543–2552 (2012). 62, 155

[220] Wang, J. and Shin, S. *Journal of Nanoparticle Research* **19**(2) (2017). 63, 67

[221] Stacey, F. D. and Irvine, R. D. *Australian Journal of Physics* **30**(6), 631 (1977). 63

[222] Guo, W., Zhang, H. Q., Zhang, X. Y., Liu, L., Peng, P., Zou, G. S., and Zhou, Y. N. *Journal of Alloys and Compounds* **690**, 86–94 (2017). 71

[223] Tsai, M.-H. *Entropy* **18**(7), 252 (2016). 79

[224] Gao, M. *Development of new high entropy alloys for brazing of Ni-base superalloys*. Master of science, (2017). 80, 81, 89

[225] Cook, G. O. and Sorensen, C. D. *Journal of Materials Science* **46**(16), 5305–5323 (2011). 85, 119

[226] Gao, M., Yeh, J., Liaw, P., and Zhang, Y. *High-Entropy Alloys: Fundamentals and Applications*. Springer International Publishing, (2016). 86

[227] Zhang, Y., Zuo, T. T., Tang, Z., Gao, M. C., Dahmen, K. A., Liaw, P. K., and Lu, Z. P. *Progress in Materials Science* **61**, 1–93 (2014). 87, 92

[228] Hull, D. *Fractography: observing, measuring and interpreting fracture surface topography*. Fractography: observing, measuring and interpreting fracture surface topography. Cambridge University Press, Cambridge, United Kingdom, (1999). 87

[229] Liang, R., Ji, Y., Wang, S., and Liu, S. *Metals* (2016). 88

[230] Munitz, A., Kaufman, M. J., and Chandler, J. P. *Materials Science and Engineering A* **560**, 633–642 (2013). 89

[231] Guo, W., Dmowski, W., Noh, J. Y., Rack, P., and Liaw, P. K. *Metallurgical and Materials Transactions A* **44A**, 1994–1997 (2013). 89

[232] Bridges, D., Rouleau, C., Gosser, Z., Smith, C., Zhang, Z., Hong, K., Cheng, J., Bar-Cohen, Y., and Hu, A. *Applied Sciences* **8**(6), 985–998 (2018). xiv, xxii, xxiii, xxvii,

93, 99, 101, 102, 104, 105, 106, 107, 108, 110, 111, 112, 115, 165

[233] Bridges, D., Ma, Y., Rouleau, C., Gosser, Z., Hong, K., Cheng, J., Zhang, Z., Smith, C., Bar-Cohen, Y., and Hu, A. In *International Manufacturing Science and Engineering Conference*. ASME, (2018). xiv, xxii, 93, 104, 105, 109, 110, 114

[234] Bar-Cohen, Y., Olorunsola, A. K., Badescu, M., Bao, X., and Sherrit, S. *NASA Tech Briefs* **32**(12), 38–40 (2008). 95

[235] Sen, S., Lake, M., Wilden, J., and Schaaf, P. *Thin Solid Films* **631**, 99–105 (2017). 96

[236] Adams, D. P. *Thin Solid Films* **576**, 98–128 (2015). 96, 99, 111

[237] Longtin, R., Hack, E., Neuenschwander, J., and Rusch, J. *Advanced Materials* **23**(48), 5812–5816 (2011). 96

[238] Qiu, X. and Wang, J. *Sensors and Actuators A: Physical* **141**(2), 476–481 (2008). 96

[239] Swiston, A. J., Hufnagel, T. C., and Weihs, T. P. *Scripta Materialia* **48**(12), 1575–1580 (2003). 96

[240] Hooper, R. J., Adams, D. P., Hirschfeld, D., and Manuel, M. V. *Journal of Electronic Materials* **45**(1), 1–11 (2016). 96

[241] Weihs, T. P. *Fabrication and characterization of reactive multilayer films and foils*, 160–243. Woodhead Publishing Limited (2014). xiii, 96, 98, 99

[242] Resnik, D., nik, V. D., i, A. U., Mozek, M., Peni, S., and Amon, S. *Microelectronic Engineering* **85**(7), 1603–1607 (2008). 99

[243] Fritz, G. M., Jr, S. J., Grapes, M. D., and Weihs, T. P. *Journal of Applied Physics* **113**(1), 14901 (2013). 99

[244] Miura, S., Ohashi, T., and Mishima, Y. *Intermetallics* **5**(1), 45–59 (1997). 104

[245] Turlo, V., Politano, O., and Baras, F. *Journal of Applied Physics* **121**(5), 55304 (2017). 104

[246] Rogachev, A. S., Vadchenko, S. G., Baras, F., Politano, O., Rouvimov, S., Sachkova, N. V., and Mukasyan, A. S. *Acta Materialia* **66**, 86–96 (2014). 104

[247] Fujiwara, K. and Horita, Z. *Acta materialia* **50**(6), 1571–1579 (2002). 107

[248] Janssen, M. M. P. *Metallurgical Transactions* **4**, 1623–1633 (1973). 107

[249] Pochapsky, T. E. *Acta Metallurgica* **1**(6), 747–751 (1953). 110

[250] Buyco, E. H. and Davis, F. E. *Journal of Chemical & Engineering Data* **15**(4), 518–523 (1970).

[251] Chase, M. W. *NIST-JANAF Themochemical Tables*. Journal of Physical Chemistry Reference Data, Washington D.C., USA, fourth edition, (1998). 110

[252] Bartsch, H., Manuel, J. M., and Grieseler, R. *Technologies* **5**(4), 79 (2017). 111

[253] Wang, J., Besnoin, E., Knio, O. M., and Weihs, T. P. *Acta Materialia* **52**(18), 5265–5274 (2004). 113

[254] Bridges, D., Xu, R., and Hu, A. *Materials & Design* **174**, 107784 (2019). xxiii, xxiv, xxv, 117, 122, 125, 126, 127, 130, 132, 134, 135, 137, 138, 140, 141, 142, 145, 149, 155

[255] Khorram, A., Ghoreishi, M., Torkamany, M. J., and Bali, M. M. *Optics & Laser Technology* **56**, 443–450 (2014). 119

[256] Knorovsky, G. A., Cieslak, M. J., Headley, T. J., Romig, A. D., and Hammetter, W. F. *Metallurgical Transactions A* **20**(10), 2149–2158 (1989). 119

[257] Tiwari, J. N., Pan, F. M., Chen, T. M., Tiwari, R. N., and Lin, K. L. *Journal of Power Sources* **195**(3), 729–735 (2010). 120

[258] Bridges, D., Xu, R., and Hu, A. In *47th North American Manufacturing Research Conference*. ASME. 122, 145

[259] Blaber, J., Adair, B., and Antoniou, A. *Experimental Mechanics* **55**(6), 1105–1122 (2015). 124

[260] Jackson, C. L. and Mckenna, G. B. *Journal of Chemical Physics* **93**(12), 9002–9011 (1990). xxiii, 126, 128

[261] Zhang, H., Kalvapalle, P., and Douglas, J. F. *Soft Matter* **6**, 5944–5955 (2010). 127

[262] Shukla, S., Seal, S., Vij, R., and Bandyopadhyay, S. *Nano Letters* **3**(3), 397–401 (2003). 132

[263] Kferstein, R., Walther, T., Hesse, D., and Ebbinghaus, S. G. *Journal of Solid State Chemistry* **213**, 57 – 64 (2014). 135

[264] Stanciu, L. A., Kodash, V. Y., and Groza, J. R. *Metallurgical and Materials Transactions A* **32**(10), 2633–2638 Oct (2001). 136

[265] Lim, L. and Watanabe, T. *Acta Metallurgica et Materialia* **38**(12), 2507 – 2516 (1990). 136

[266] Kuo, C.-M., Yang, Y.-T., Bor, H.-Y., Wei, C.-N., and Tai, C.-C. *Materials Science and Engineering: A* **510-511**, 289 – 294 (2009). 11th International Conference of Creep and Fracture of Engineering Materials and Structures, CREEP 2008. 138

[267] Muzikansky, A., Nanikashvili, P., Grinblat, J., and Zitoun, D. *Journal of Physical Chemistry C* **117**(6), 3093–3100 (2013). 144, 145

[268] Grouchko, M., Roitman, P., Zhu, X., Popov, I., Kamyshny, A., Su, H., and Magdassi, S. *Nature Communications* **5**, 2994 January (2014). 145

[269] Remadevi, A., Kesavapillai Sreedeviamma, D., and Surendran, K. P. *ACS Omega* **3**(10), 14245–14257 (2018). 146

[270] Wazzan, A. R. *Journal of Applied Physics* **36**(11), 3596–3599 (1965). 148, 152

[271] Herzig, C. and Divinski, S. V. *Materials Transactions* **44**(1), 14–27 (2003). 148

[272] Maiya, P. S. and Blakely, J. M. *Journal of Applied Physics* **38**(2), 698–704 (1967). 148

[273] Jian, Z. Y., Kuribayashi, K., and Jie, W. Q. *Materials Transactions* **43**(4), 721–726 (2002). 148

[274] Zhang, X., Li, W., Wu, D., Deng, Y., Shao, J., Chen, L., and Fang, D. *Journal of Physics: Condensed Matter* **31**(7), 075701 dec (2018). 151

[275] Thouy, R., Olivi-Tran, N., and Jullien, R. *Phys. Rev. B* **56**, 5321–5327 Sep (1997). 151

[276] Volk, A., Knez, D., Thaler, P., Hauser, A. W., Grogger, W., Hofer, F., and Ernst, W. E. *Phys Chem Chem Phys* **17**(38), 24570–5 (2015). 151

[277] Marzbanrad, E., Hu, A., Zhao, B., and Zhou, Y. *J. Phys. Chem. C* **117**(32), 16665–16676 August (2013). 151

[278] Molleman, B. and Hiemstra, T. *Phys. Chem. Chem. Phys.* **20**, 20575–20587 (2018). 151

[279] Alarifi, H. *Ag Nanoparticles and their Application in Low-Temperature Bonding of Cu.* Thesis, (2013). 153, 154

[280] Wang, Y.-J., Gao, G.-J. J., and Ogata, S. *PHYSICAL REVIEW B* **88**(11), 115413 September (2013). 153

[281] Shi, F. G. *Journal of Materials Research* **9**(05), 1307–1314 (2011). 154

[282] Fu, C. L., Reed, R., Janotti, A., and Krcmar, M. *Superalloys 2004* , 867–876 (2004). 155

[283] Biswas, S., Schwen, D., Wang, H., Okuniewski, M., and Tomar, V. *Computational Materials Science* **148**, 307–319 (2018). 162

[284] Chockalingam, K., Kouznetsova, V. G., Sluis, v. O., and Geers, M. G. D. *Computer Methods in Applied Mechanics and Engineering* **312**, 492–508 (2016). 162

[285] Boettinger, W. J., Warren, J. A., Beckermann, C., and Karma, A. *Annual Review of Materials Research* **32**(1), 163–194 (2002). 162, 163

[286] Kundin, J., Mushongera, L., and Emmerich, H. *Acta Materialia* **95**, 343–356 (2015). 162

[287] Li, S. Q., Qi, W. H., Peng, H. C., and Wu, J. Z. *Computational Materials Science* **99**, 125–132 (2015). 162

Appendices

Appendix A

Acronyms

BCC	body-centered cubic
BFM	brazing filler material
BM	base material
CSNWs	core-shell nanowires
CTE	coefficient of thermal expansion
DAZ	diffusion-affected zone
DIC	digital image correlation
e-beam	electron beam physical vapor
EBSD	electron backscattered diffraction
EDS	Energy Dispersive X-ray Spectroscopy
FCC	face-centered cubic
HCP	hexagonal closed-packed
HEAs	high entropy alloys
IN718	Inconel 718
MIG	metal inert gas
MPD	melting point depressant
NMs	nanomaterials
NP	nanoparticle
NPA	nanopaste
NPs	nanoparticles
NWs	nanowires
RMF	reactive multilayer film

SAV	surface-area-to-volume
SPR	surface plasmon resonance
Ti64	Ti-6Al-4V
TIG	tungsten inert gas
TLP	transient liquid phase
XRD	X-ray diffraction

Appendix B

Denzel Bridges Publication list

First-Author Publications

1. Bridges, D., Xu, R. & Hu, A. in 47th North American Manufacturing Research Conference. (ASME).
2. Bridges, D., Xu, R. & Hu, A. Microstructure and mechanical properties of Ni nanoparticle-bonded Inconel 718. Mater Design 174, 107784, (2019).
3. Bridges, D., Zhang, S., Lang, S., Gao, M., Yu, Z., Feng, Z. & Hu, A. Laser brazing of a nickel-based superalloy using a Ni-Mn-Fe-Co-Cu high entropy alloy filler metal. Materials Letters 215, 11-14, (2018).
4. Bridges, D., Rouleau, C., Gosser, Z., Smith, C., Zhang, Z., Hong, K., Cheng, J., Bar-Cohen, Y. & Hu, A. Self-powered brazing of Ti-6Al-4V using Ni/Al Reactive Multilayer Films. Applied Sciences 8, 985-998, (2018).
5. Bridges, D., Ma, Y., Rouleau, C., Gosser, Z., Hong, K., Cheng, J., Zhang, Z., Smith, C., Bar-Cohen, Y. & Hu, A. in International Manufacturing Science and Engineering Conference. (ASME).
6. Bridges, D., Ma, C., Zhang, S., Xue, S., Feng, Z. & Hu, A. Diffusion and wetting behaviors of Ag nanoparticle and Ag nanowire pastes for laser brazing of Inconel 718. Welding in the World 62, 169-176, (2017).
7. Bridges, D., Ma, C., Palmer, Z., Wang, S., Feng, Z. & Hu, A. Laser brazing of Inconel 718 using Ag and Cu-Ag nanopastes as brazing materials. Journal of Materials Processing Technology 249, 313-324, (2017).
8. Bridges, D., Li, R., Gao, Z., Wang, Z., Wang, Z., Hu, A. & Feng, Z. in Semiconductor Nanocrystals and Metal Nanoparticles: Physical Properties and Device Applications (eds Tupei Chen & Yang Liu) Ch. 10, (Taylor & Francis Group, 2017).

Co-Author Publications

1. Wu, J., Xue, S., Bridges, D., Yu, Y., Zhang, L., Pooran, J., Hill, C., Wu, J. & Hu, A. Fe-based ceramic nanocomposite membranes fabricated via e-spinning and vacuum filtration for Cd2+ ions removal. Chemosphere 230, 527-535, (2019).
2. Ma, Y., Bridges, D., Yu, Y., Han, J., Li, H. & Hu, A. Joining of Carbon Fiber Reinforced Plastic to Aluminum Alloy by Reactive Multilayer Films and Low Power Semiconductor Laser Heating. Applied Sciences 9, (2019).
3. Wu, J., Xue, S., Bridges, D., Yu, Y., Smith, C., Hong, K., Hill, C., Zhang, Z., Feng, Z. & Hu, A. Electrophoretic Deposition and Thermo-Chemical Properties of Al/Fe2O3 Nanothermite Thick Films. Engineered Science, (2018).
4. Feldman, M. A., Dumitrescu, E. F., Bridges, D., Chisholm, M. F., Davidson, R. B., Evans, P. G., Hachtel, J. A., Hu, A., Pooser, R. C., Haglund, R. F. & Lawrie, B. in Conference on Lasers and Electro-Optics. FTu3H.4 (Optical Society of America).
5. Feldman, M. A., Dumitrescu, E. F., Bridges, D., Chisholm, M. F., Davidson, R. B., Evans, P. G., Hachtel, J. A., Hu, A., Pooser, R. C., Haglund, R. F. & Lawrie, B. in Conference on Lasers and Electro-Optics (OSA, 2018).
6. Bar-Cohen, Y., Sekulic, D. P., Pan, R., Babu, S. S., Hu, A., Bridges, D., Bao, X., Badescu, M., Hyeong, J. L., Sherrit, S. & Firdosy, S. A. in Advances in Manufacturing and Processing of Materials and Structures (ed CRC Press - Taylor & Francis) Ch. 12, (CRC Press, 2018).
7. Wang, S., Yu, Y., Ma, D., Bridges, D., Feng, G. & Hu, A. High performance hybrid supercapacitors on flexible polyimide sheets using femtosecond laser 3D writing. Journal of Laser Applications 29, 022203, (2017).
8. Ma, C., Xue, S., Bridges, D., Palmer, Z., Feng, Z. & Hu, A. Low temperature brazing nickel with Ag nanoparticle and Cu-Ag core-shell nanowire nanopastes. Journal of Alloys and Compounds 721, 431-439, (2017).
9. Hu, A., Bridges, D., Zhang, S. & Feng, Z. Nanobrazing for turbine blade and vane repair. Advanced Materials & Processes 175, 25-29 (2017).
10. Zhou, W., Bridges, D., Li, R., Bai, S., Ma, Y., Hou, T. & Hu, A. Recent progress of laser micro-and nano manufacturing. Science Letters Journal 5, 228 (2016).
11. Ma, Y., Li, H., Bridges, D., Peng, P., Lawrie, B., Feng, Z. & Hu, A. Zero-dimensional to three-dimensional nanojoining: current status and potential applications. Rsc Adv 6, 75916-75936, (2016).
12. Li, R.-Z., Peng, R., Kihm, K., Bai, S., Bridges, D., Tumuluri, U., Wu, Z., Zhang, T., Compagnini, G., Feng, Z. & Hu, A. High-rate in-plane micro-supercapacitors scribed onto photo paper using in situ femtolaser-reduced graphene oxide/Au nanoparticle microelectrodes. Energy & Environmental Science 9, 1458-1467, (2016).

13. Hu, A., Li, R., Bridges, D., Zhou, W., Bai, S., Ma, D. & Peng, P. Photonic nanomanufacturing of high performance energy devices on flexible substrates. Journal of Laser Applications 28, 022602, (2016).

14. Zhou, W., Hu, A., Bai, S., Ma, Y. & Bridges, D. Anisotropic optical properties of large-scale aligned silver nanowire films via controlled coffee ring effects. Rsc Adv 5, 39103-39109, (2015).

15. Shi, X., Zhou, W., Ma, D., Ma, Q., Bridges, D., Ma, Y. & Hu, A. Electrospinning of Nanofibers and Their Applications for Energy Devices. J Nanomater 2015, 1-20, (2015).

16. Li, R.-Z., Zhang, T., Hu, A. & Bridges, D. Ag Nanowire and Nanoplate Composite Paste for Low Temperature Bonding. Materials Transactions 56, 984-987, (2015).

17. Li, R.-Z., Zhang, T., Hu, A. & Bridges, D. Ag Nanowire and Nanoplate Composite Paste for Low Temperature Bonding. Materials Transactions 56, 984-987, (2015).

18. Li, R. Z., Hu, A., Bridges, D., Zhang, T., Oakes, K. D., Peng, R., Tumuluri, U., Wu, Z. & Feng, Z. Robust Ag nanoplate ink for flexible electronics packaging. Nanoscale 7, 7368-7377, (2015).

19. Hou, T., Zheng, C., Bai, S., Ma, Q., Bridges, D., Hu, A. & Duley, W. W. Fabrication, characterization, and applications of microlenses. Appl Opt 54, 7366-7376, (2015).

20. Bai, S., Lin, Y.-H., Zhang, X.-P., Zhou, W.-P., Chen, T., Ma, Y., Hou, T.-X., Bridges, D., Oakes, K. D. & Hu, A. Two-Step Photonic Reduction of Controlled Periodic Silver Nanostructures for Surface-Enhanced Raman Spectroscopy. Plasmonics 10, 1675-1685, (2015).

Appendix C

MATLAB Codes

RMF High Speed Camera

Image extraction

```
        %TIFF Frame Extractor
%by Cary Smith, graduate student, University of Tennessee

        %Code description: this script automatically extracts images from 16-bit
%multiframe TIFF files and writes them as individual TIFFs with color
%added. The script is designed to be used with raw image data created by
%the TSI PowerView HS-650 high-speed camera. Image frame timestamps are
%shown at the top of the image.

%Instructions: %1. put tifframeextractor.m in the same directory as the raw TIFFs
%2. assign name of raw file to be processed to variable fn
%3. write name of new folder to be created for processed images after
% command mkdir; new folder will be created automatically in the same
% directory as the raw images
%4. assign colormap to variable map

        close all
clear all
fn = ’samplefilename.tif’; %name of raw file to be processed
mkdir samplefoldername; %name of directory to be created for processed images
map = hot; %desired colormap

k = numel(imfinfo(strcat(fn,’.tif’))); %Number each individual image in directory

maxes = zeros(1,k);

for i = 1:k
```

```
A = imread(strcat(fn,'.tif'),i);
Aa = imcrop(A,[0 20 1024 1280]);
maxes(i) = max(max(Aa));
img{i} = A;
end

for i = 1:k
img{i} = double(img{i})/max(maxes);
img{i} = gray2ind(img{i});
end

for i = 1:k
imwrite(img{i},map,strcat(fn,'/',fn,'-',num2str(i),'.tif'));
end
```

Temperature Calibration

```
    %HS camera temperature calibrator

close all
fn = '800C-200ms_exp';
brightness800 = 0; %initialize the brightness value
for i = 27:75
A = imread(strcat(fn,'.tif'),i);
I=imcrop(A,[265 265 27 25]);
brightness800= brightness800+mean2(I);
end
brightness800 = brightness800/49;

fn = '850C-200ms_exp';
brightness850 = 0; %initialize the brightness value
for i = 1:14
A = imread(strcat(fn,'.tif'),i);
I=imcrop(A,[438 268 38 28]);
brightness850= brightness850+mean2(I);
end
brightness850 = brightness850/14;

fn = '900C-200ms_exp';
brightness900 = 0; %initialize the brightness value
for i = 1:14
A = imread(strcat(fn,'.tif'),i);
I=imcrop(A,[438 268 38 28]);
brightness900= brightness900+mean2(I);
end
```

```
brightness900 = brightness900/14;

fn = ’950C-200ms_exp’;

A = imread(strcat(fn,’.tif’),14);
I=imcrop(A,[438 268 38 28]);
brightness950= mean2(I);

fn = ’RMF_bonding-2’;
A = imread(strcat(fn,’.tif’),1);
I=imcrop(A,[346 318 40 40]);
brightness20= mean2(I);

brightness = [brightness20 brightness800 brightness850 brightness900 brightness950]’;
temperature = [20 735 785 835 885]’;
plot(brightness, temperature, ’gx’)
hold on
TvB_power = fit(brightness, temperature, ’power2’);
TvB_exp = fit(brightness, temperature, ’exp2’);
testB= 820:10:2.5E4;
plot(testB, TvB_power(testB), testB, TvB_exp(testB))
legend(’data’, ’fit1’, ’fit2’, ’Location’,’southeast’)

fn = ’RMF_bonding-2’;
TRMF1 = zeros(1,36);
TRMF2 = zeros(1,36);
errTRMF1=zeros(1,36);
errTRMF2=zeros(1,18);
overlay=zeros(1,18);
time = 0:977:34195;
time2 = zeros(1,18);
for i = 11:46
A = imread(strcat(fn,’.tif’),i);
I=imcrop(A,[285 135 9 5]);
brightnessRMF= mean2(I);
TRMF1(i-10) = TvB_power(brightnessRMF);
errTRMF1(i-10)=TvB_power(brightnessRMF+std2(I))-TRMF1(i-10);
TRMF2(i-10) = TvB_exp(brightnessRMF);

if mod(i-10,2)==0
errTRMF2((i-10)/2)=((TvB_exp(brightnessRMF+std2(I)) - TRMF2(i-10)) + (TRMF2(i-
10) - TvB_exp(brightnessRMF-std2(I))))/2;
overlay((i-10)/2)=TRMF2(i-10);
time2((i-10)/2)=time(i-10);
end
```

```
end

figure
%errorbar(time,TRMF1,errTRMF1)
plot(time, TRMF2, ’k’)
hold on

errorbar(time2,overlay,errTRMF2, ’k.’,’MarkerSize’, 1)
xlim([0 3.4E4])
ylim([0 850])
%legend(’T_c’,’error’,’Location’,’east’)
avgerr=mean2(errTRMF2(7:11));
x1= xlabel(’Measured Time (\{}mus)’);
y1 =ylabel(’Measured Temperature (degC)’);
ax1=gca;
ax1.XColor = ’k’;
ax1.YColor = ’k’;
box off
% L1=legend(’Measured Temp’, ’Location’, ’southwest’);
% L1.FontSize = 12;
ax2=axes(’XAxisLocation’,’top’,’YAxisLocation’,’right’,...
’Color’,’none’);
ax2.XColor = ’r’;
ax2.YColor = ’r’;
simTime= [0 200 400 600 800 1000 1200 1400 1600 1800 2000 2200 ...
2400 2800 3200 3400];
simTemp1= [20 156 473 700 813 802 791 779 773 773 768 768 757 745 734 727]; %simulated
RMF temperature
simTemp2= [20 156 473 586.9 813 802 780 769 763 763 757 750 745 734 727 720]; %simulated
RMF-BAl temperature
simTemp3= [20 156 451 757.6 790 779 757 744 741 734 734 731 731 722 711 700]; %simulated
BAl-Ti64 interface

line(simTime, simTemp1, ’Parent’,ax2,’Color’,’blue’,’LineWidth’,1)
line(simTime, simTemp2, ’Parent’,ax2,’Color’,’red’,’LineStyle’,’–’,’LineWidth’,1)
line(simTime, simTemp3, ’Parent’,ax2,’Color’,’magenta’,’LineStyle’,’:’,’LineWidth’,1)
L=legend(’RMF center’, ’RMF-BAl interface’,’BAl-Ti64 interface’, ’Location’, ’south’);
L.FontSize = 12;
xlabel(’Simulated Time (\{}mus)’)
ylabel(’%HS camera temperature calibrator

%Calibrate analysis at 800 degrees Celsius
close all
fn = ’800C-200ms_exp’;
brightness800 = 0; %initialize the brightness value
```

```
for i = 62:75
A = imread(strcat(fn,’.tif’),i);
I=imcrop(A,[265 265 27 25]); %Snapshot chosen on visual inspection of the images before running the code
brightness800= brightness800+mean2(I); %Obtain the average brightness from each individual image of BAlSi-4
end
brightness800 = brightness800/14; %Obtain the average value

%Calibrate analysis at 850 degrees Celsius
fn = ’850C-200ms_exp’;
brightness850 = 0; %initialize the brightness value
for i = 1:14
A = imread(strcat(fn,’.tif’),i);
I=imcrop(A,[438 268 38 28]); %Snapshot chosen on visual inspection of the images before running the code
brightness850= brightness850+mean2(I); %Obtain the average brightness from each individual image of BAlSi-4
end
brightness850 = brightness850/14; %Obtain the average value

%Calibrate analysis at 900 degrees Celsius
fn = ’900C-200ms_exp’;
brightness900 = 0; %initialize the brightness value
for i = 1:14
A = imread(strcat(fn,’.tif’),i);
I=imcrop(A,[438 268 38 28]);
brightness900= brightness900+mean2(I);
end
brightness900 = brightness900/14;

    %Calibrate analysis at 950 degrees Celsius
fn = ’950C-200ms_exp’;
A = imread(strcat(fn,’.tif’),14);
I=imcrop(A,[438 268 38 28]);
brightness950= mean2(I);

    %Calibrate analysis at room temperature
fn = ’RMF_bonding-2’;
A = imread(strcat(fn,’.tif’),1);
I=imcrop(A,[346 318 40 40]);
brightness20= mean2(I);

    %Plot thermocouple temperature as a function of calculated brightness
brightness = [brightness20 brightness800 brightness850 brightness900 brightness950]’;
```

```
temperature = [20 735 785 835 885]’;
plot(brightness, temperature, ’gx’)
hold on

TvB_exp = fit(brightness, temperature, ’exp2’); %Fit temperature function as a function of brightness

fn = ’RMF_bonding-2’;
%brightnessRMF = zeros(35); %initialize the brightness vector
TRMF1 = zeros(1,36);
errTRMF1=zeros(1,36);
overlay=zeros(1,18);
time = 0:977:34195; %time in microseconds
time2 = zeros(1,18);
for i = 11:46
A = imread(strcat(fn,’.tif’),i);
I=imcrop(A,[285 135 9 5]); %Crop image to only include joint area
brightnessRMF= mean2(I);
TRMF1(i-10) = TvB_exp(brightnessRMF); %evaluate temperature at the measured brightness

    if mod(i-10,2)==0
errTRMF1((i-10))=((TvB_exp(brightnessRMF+std2(I))- TRMF2(i-10)) + (TRMF2(i-10) - TvB_exp(brightnessRMF-std2(I))))/2;
end
end

    figure
plot(time, TRMF2, ’k’)
hold on
errorbar(time,errTRMF1, ’k.’,’MarkerSize’, 1)
xlim([0 3.4E4])
ylim([0 850]) Temperature (degC)’)
xlim([0 3400])
ylim([0 850])
```

Sauer-Friese Analysis

```
    % Sauer-Friese Analysis of EDS line scan data by Denzel Bridges, University of Tennessee graduate student
data=xlsread(’line1.xlsx’,2); %import fitted EDS curve
t=14512; % Total time in seconds
```

$$x, y$$

```
=size(data);
DNi=zeros(x,1); %Ni diffusion coefficient
DCr=zeros(x,1); %Cr diffusion coefficient
DFe=zeros(x,1); %Fe diffusion coefficient

%Evaluation of D(c) of Ni
cL=min(data(:,2));
cM=max(data(:,2));
%Sigmoidal function parameters c(z)
A1=0.14071;
A2=0.08858;
x0=0.00758;
dx=6.65508E-4;
syms z
c1=((A2 + (A1-A2)./(1 + exp((z-x0)./dx)))-cL)/(cM-cL); %c(z)
dc=diff(c1); % derivative of c(z)

%Sauer-Friese integral
for i=1:x
DNi(i)=abs(1/(2*t*subs(dc,z,data(i,1))*(-(1-subs(c1,z,data(i,1)) *double(int(c1, z, data(1,1),
data(i,1))) +subs(c1,z,data(i,1)*double(int((1-c1),z,data(i,1),data(x,1))))))));

end
DNi_avg=trapz(c1,DNi)/(cM-cL) % average diffusion coefficient calculation
%Evaluation of D(c) of Ni
cL=min(data(:,4));
cM=max(data(:,4));
A1=0.00252;
A2=0.03011;
x0=0.00883;
dx=9.6367E-4;
syms z

c2=((A2 + (A1-A2)./(1 + exp((z-x0)./dx)))-cL)/(cM-cL);

dc=diff(c2);
for i=1:x
DCr(i)=abs(1/(2*t*subs(dc,z,data(i,1))*(-(1-subs(c2, z, data(i,1))*double(int(c2, z, data(1,1),
data(i,1))) +subs(c2,z,data(i,1)*double(int((1-c2),z,data(i,1),data(x,1))))))));
end
DCr_avg=trapz(c2,DCr)/(cM-cL)
%Fe
cL=min(data(:,3));
cM=max(data(:,3));
A1=0.00234;
```

```
A2=0.02719;
x0=0.00837;
dx=9.86633E-4;
syms z
c3=((A2 + (A1-A2)./(1 + exp((z-x0)./dx)))-cL)/(cM-cL);
dc=diff(c2);
for i=1:x

DFe(i)=abs(1/(2*t*subs(dc,z,data(i,1))*(-(1-subs(c3,z,data(i,1))*double(int(c3, z, data(1,1),
data(i,1))) + subs(c3,z,data(i,1)*double(int((1-c3),z,data(i,1),data(x,1)))))))));

end
DFe_avg=trapz(c3,DFe)/(cM-cL)
```

Appendix D

Gibbs-Thomson Derivation

[101]

- μ_L - liquid chemical potential
- μ_S - solid chemical potential
- P_0 - pressure at which a solid melts at temperature T_{mB}
- P_2 - pressure at which a solid melts at temperature T_{MP}
- S - entropy
- $\Delta_{fus}S$ - entropy of fusion

$$\mu_L(T_{mB}) = \mu_S(T_{mB}) \tag{D.1}$$

$$\mu_L(T_{MP}) = \mu_S(T_{MP}, P_2) \tag{D.2}$$

$$\mu_L(T_{mB}) + \partial\mu = \mu_S(T_{MP}) + +\partial\mu \tag{D.3}$$

$$\partial\mu = -\overline{S}dT + \overline{V}dP \tag{D.4}$$

$$\mu_L(T_m) + \int_{T_{mB}}^{T_{MP}} -\overline{S_L}dT = \mu_S(T_m) + \int_{T_{mB}}^{T_{MP}} -\overline{S_S}dT + \int_{P_0}^{P_2} \overline{V_S}dP \tag{D.5}$$

$$-\int_{T_{mB}}^{T_{MP}} (\overline{S_L} - \overline{S_S})dT = \int_{P_0}^{P_2} \overline{V_S}dP \tag{D.6}$$

$$\overline{S_L} - \overline{S_S} = \Delta_{fus}S \tag{D.7}$$

$$-\int_{T_{mB}}^{T_{MP}} \Delta_{fus}SdT = \overline{V_S}\int_{P_0}^{P_2} dP \tag{D.8}$$

$$\Delta_{fus}S(T_{MP} - T_{mB}) = -\overline{V_S}\Delta P \tag{D.9}$$

$$\Delta_{fus}S(T_{MP} - T_{mB}) = \frac{-\overline{V_S}2\gamma_{sl}}{R} \tag{D.10}$$

$$T_{MP} = T_{mB} - \frac{\overline{V_S}2\gamma_{sl}}{R\Delta_{fus}S} \tag{D.11}$$

$$T_{MP} = T_{mB} - \frac{2\overline{V_S}T_{mB}\gamma_{sl}}{RH_f} \tag{D.12}$$

$$T_{MP}(d) = T_{mB} - \frac{4\overline{V_S}T_{mB}\gamma_{sl}}{H_f d} \tag{D.13}$$

$$T_{MP}(d) = T_{mB} - \frac{4\sigma_{sl}T_{mB}}{H_f \rho_s d} \tag{D.14}$$

$$T_{MP}(d) = T_{mB}(1 - \frac{4\sigma_{sl}}{H_f \rho_s d}) \tag{D.15}$$

Vita

Denzel Bridges was born in Riverside, California in 1991. He began attending Cornell University in 2009 and received his Bachelor of Science degree in Materials Science and Engineering, Cornell University in 2014. Immediately after graduating, he joined the University of Tennessee: Knoxville as a Ph.D. candidate in Mechanical Engineering. During his five years of Ph.D. work, he published 5 publications, two conference proceedings, and one book chapter as a first-author in addition to twenty-one co-authored publications.